

# Radiative Effect of Mixed Mineral Dust and Biomass Burning Aerosol in the Thermal Infrared

Von der Fakultät für Physik und Geowissenschaften

der Universität Leipzig

genehmigte

D I S S E R T A T I O N

zur Erlangung des akademischen Grades

doctor rerum naturalium

(Dr. rer. nat.)

vorgelegt

von Dipl. Phys. Claas H. Köhler

geboren am 23.02.1981 in Bünde

Gutachter: Prof. Dr. Thomas Trautmann  
Prof. Dr. Manfred Wendisch

Tag der Verleihung: 16.12.2013

## Wissenschaftlicher Werdegang

06/2000	Abitur am Freiherr-vom-Stein Gymnasium in Bünde
10/2001–10/2003	Grundstudium der Physik an der Universität Bayreuth Abschluss: Vordiplom in Physik
10/2003–10/2005	Hauptstudium der Physik an der Universität Göttingen Schwerpunkte: Strömungsphysik und Geophysik
10/2005–10/2006	Diplomarbeit am Institut für Theoretische Physik der Universität Göttingen zum Thema <i>Einfluss des Excluded Volume Effekts auf die Viskosität von Polymergelen</i> Betreuerin: Prof. Dr. Annette Zippelius
11/2006	Abschluss des Studiums als Diplomphysiker
05/2007–10/2011	Wissenschaftlicher Mitarbeiter am Deutschen Zentrum für Luft- und Raumfahrt in Oberpfaffenhofen am Institut für Methodik der Fernerkundung in der Abteilung Atmosphärenprozessoren mit dem Ziel der Promotion zum Thema <i>Radiative Effect of Mixed Mineral Dust and Biomass Burning Aerosol in the Thermal Infrared</i> Betreuer: Prof. Dr. Thomas Trautmann
seit 11/2011	Wissenschaftlicher Mitarbeiter am Deutschen Zentrum für Luft- und Raumfahrt in Oberpfaffenhofen am Institut für Methodik der Fernerkundung in der Abteilung Experimentelle Verfahren zuständig für flugzeuggetragene Hyperspektralsensorik

# Bibliographische Beschreibung

Köhler, Claas H.

Radiative Effect of Mixed Mineral Dust and Biomass Burning  
Aerosol in the Thermal Infrared

Universität Leipzig, Dissertation

170 Seiten, 119 Literaturangaben, 58 Abbildungen, 3 Tabellen

Referat: This thesis treats the optical properties of mixed mineral dust and biomass burning aerosol in the thermal infrared (TIR) based on Fourier Transform infrared spectrometer (FTIR) measurements and radiative transfer simulations. The measurements were part of the Saharan Mineral Dust Experiment 2 (SAMUM-2) conducted from January to February 2008 at Praia, Cape Verde. The large amount of different instruments co-located at the main field site during the campaign resulted in a unique dataset comprising in-situ information and remote sensing data perfectly suited for column closure studies. The ultimate goal of this work is to investigate the consistency of microphysical and TIR remote sensing data. This is achieved by reproducing the measured radiances at top and bottom of the atmosphere (TOA, BOA) with a radiative transfer model, which assimilates the microphysical aerosol information gathered during SAMUM-2. The first part of the thesis describes several experimental efforts, including a novel calibration method and a drift correction algorithm for the ground-based FTIR instrument operated within the scope of SAMUM-2 by the author. The second part introduces the concurrent radiative transfer library PIRATES, which has been developed in the framework of this thesis for the analysis of TIR aerosol optical properties. The third and final part of the treatise compares measured and simulated spectra for various typical scenarios encountered during SAMUM-2. It is demonstrated in three case studies, that measured radiances in the TIR atmospheric window region ( $8 - 12\mu\text{m}$ ) can be reproduced at BOA and TOA by radiative transfer simulations assuming spheroidal model particles. Moreover, spherical particles are shown to be an inadequate model for mineral dust aerosol in this spectral region unless the aerosol optical depth is small.

*I love deadlines.*  
*I like the whooshing sound they make as they fly by.*  
DOUGLAS ADAMS



# Contents

<b>1</b>	<b>Introduction</b>	<b>3</b>
1.1	The Importance of Atmospheric Dust . . . . .	3
1.2	State of the Art . . . . .	6
1.3	Scope of Work . . . . .	10
<b>2</b>	<b>Measurements</b>	<b>13</b>
2.1	Fourier Transform Spectroscopy . . . . .	14
2.1.1	The Michelson-Interferometer . . . . .	14
2.1.2	The Fourier Transform Spectrometer . . . . .	20
2.1.3	Truncation and Sampling . . . . .	24
2.1.4	Spectral Resolution and Apodisation . . . . .	28
2.2	The Model 102 $\mu$ FTIR . . . . .	32
2.2.1	General Instrument Description . . . . .	33
2.2.2	Interferogram Post Processing . . . . .	34
2.2.3	Wavenumber Correction . . . . .	36
2.2.4	Radiometric Calibration . . . . .	37
2.2.5	Uncertainty Estimation for the Calibrated Radiances . . . . .	42
2.2.6	Wavenumber Accuracy . . . . .	44

2.2.7	Calibration Source . . . . .	49
2.2.8	Instrument Stability . . . . .	53
2.2.9	Field of View . . . . .	59
2.2.10	Detector Non-Linearity . . . . .	62
2.2.11	Instrument Validation and Error Estimation . . . . .	64
2.3	IASI . . . . .	70
2.4	Measurements during SAMUM-2 . . . . .	71
<b>3</b>	<b>Radiative Transfer Simulations</b>	<b>75</b>
3.1	Theoretical Foundations of Radiative Transfer . . . . .	76
3.1.1	The Radiative Transfer Equation . . . . .	76
3.1.2	Absorption and Emission by Gaseous Matter . . . . .	81
3.1.3	Scattering and Absorption by Small Particles . . . . .	89
3.2	Model Description . . . . .	96
3.2.1	Model Input . . . . .	98
3.2.2	Gas Absorption . . . . .	99
3.2.3	Absorption by Particulate Matter . . . . .	101
3.2.4	Discrete Ordinate Solver . . . . .	103
3.3	Model Validation . . . . .	104
3.3.1	DISORT . . . . .	104
3.3.2	Mie-Engine . . . . .	104
3.3.3	T-Matrix Engine . . . . .	105
3.3.4	Comparison to Measurements . . . . .	105
<b>4</b>	<b>Results</b>	<b>111</b>
4.1	Ingestion of Parameters . . . . .	112

4.1.1	Trace Gas Concentrations . . . . .	112
4.1.2	Aerosol Layers . . . . .	113
4.1.3	Boundary Conditions . . . . .	114
4.2	Sensitivity Studies . . . . .	117
4.2.1	Water Vapour Concentration . . . . .	117
4.2.2	Ozone Concentration . . . . .	118
4.2.3	Temperature Profile . . . . .	120
4.2.4	Surface Temperature . . . . .	122
4.3	Aerosol Signature . . . . .	123
4.4	Radiative Closure . . . . .	127
4.4.1	6 February 2008 . . . . .	128
4.4.2	29 January 2008 . . . . .	131
4.4.3	25 January 2008 . . . . .	142
4.4.4	Discussion . . . . .	146
<b>5</b>	<b>Summary and Outlook</b>	<b>149</b>



# List of Figures

1.1	Saharan Dust over Cape Verde . . . . .	4
1.2	Examples of Dust Particles . . . . .	6
1.3	Smoke and Dust Advection to Cape Verde . . . . .	11
1.4	SAMUM-2 Experimental Setup . . . . .	12
2.1	Principle Setup of a Michelson Interferometer . . . . .	14
2.2	Principle Design of a Fourier Transform Spectrometer . . . . .	20
2.3	Simulated Interferogram . . . . .	23
2.4	Apodisation Functions . . . . .	31
2.5	Interferometer Core of the D&P Model 102 $\mu$ FTIR . . . . .	32
2.6	Experimental Setup of Transmission Measurements . . . . .	46
2.7	Wavenumber Correction Method . . . . .	47
2.8	Wavenumber Accuracy . . . . .	48
2.9	Black Body Homogeneity . . . . .	49
2.10	Temperature Measurements of the Black Body Surface . . . . .	51
2.11	Estimated Emissivity of Reference Black Bodies . . . . .	52
2.12	Drift Characterisation . . . . .	54
2.13	Drift Correction . . . . .	57
2.14	Validation of Drift Correction with Black Body Measurements . . . . .	58

2.15	Experimental Setup for Field of View Measurements . . . . .	60
2.16	Instrument Field of View . . . . .	61
2.17	MCT–InSb Signal Comparison for the D&P Model 102 FTIR . . . . .	63
2.18	Brightness Temperature Measurements of the UKMO Black Body . . . . .	65
2.19	Uncertainties for Measurements with the D&P Model 102 . . . . .	66
2.20	Comparison of D&P Model 102 and MAERI . . . . .	67
2.21	Comparison of Calibration Methods . . . . .	68
2.22	IASI and IIS FOV . . . . .	71
2.23	Experimental Setup during SAMUM-2 . . . . .	72
2.24	Angular Dependence of the Downwelling Radiance . . . . .	73
3.1	MTCKD Water Vapour Continuum . . . . .	88
3.2	The Scattering Problem . . . . .	89
3.3	Pforte Flow Diagram . . . . .	97
3.4	PIRATES–Mieschka T-Matrix Intercomparison . . . . .	106
3.5	PFORTE Validation against AERI Measurements . . . . .	109
4.1	Influence of the Water Vapour Profile on Simulated Radiances . . . . .	118
4.2	Influence of the Ozone Profile on Simulated Radiances . . . . .	119
4.3	Influence of the Temperature Profile on Simulated Radiances . . . . .	121
4.4	Influence of the Surface Temperature on Simulated Radiances . . . . .	122
4.5	Comparison of Measured and Simulated IASI Spectrum . . . . .	124
4.6	Spectral Signatures of Dust & Biomass at BOA . . . . .	125
4.7	Spectral Signatures of Dust & Biomass at TOA . . . . .	126
4.8	Map with Data Ingested into the Case Study for 6 February 2008 . . . . .	128
4.9	Vertical Aerosol Profile on 6 February 2008 . . . . .	129

4.10 Simulated and Measured Radiances for 6 February 2008 . . . . .	130
4.11 Map with Data Ingested into the Case Study for 29 January 2008 .	132
4.12 Vertical Aerosol Profile for 29 January 2008 . . . . .	133
4.13 Simulated and Measured Radiances for 29 January 2008 . . . . .	134
4.14 Dust Signatures for Several Internal Mixtures of Spherical Particles	135
4.15 Dust Signatures for several External Mixtures of Spherical Particles	136
4.16 Effect of Size Distribution Truncation . . . . .	137
4.17 Dust Signatures for an External Mixture of Oblate Spheroids . . . .	138
4.18 Dust Signatures for an External Mixture of Various Spheroids . . .	140
4.19 Simulated and Measured Radiances for 29 January 2008 (2) . . . .	141
4.20 Map with Data Ingested into the Case Study for 25 January 2008 .	142
4.21 Vertical Aerosol Profile for 25 January 2008 . . . . .	143
4.22 Simulated and Measured Radiances for 25 January 2008 . . . . .	144
4.23 Simulated and Measured Radiances for 25 January 2008 (2) . . . .	145





# List of Tables

1.1	Experimental Data Used in this Study . . . . .	10
4.1	Refractive Index Weighting Matrix . . . . .	115
4.2	Refractive Index Literature . . . . .	116



# Chapter 1

## Introduction

### 1.1 The Importance of Atmospheric Dust

Every year 1000 – 2200 Tg (IPCC, 2007, chapter 2.4) of mineral dust are entrained into the Earth atmosphere, thereby making it the most abundant of all aerosol types. The sources from which the dust is regularly activated are predominantly located in a broad 'dust belt' extending from North Africa over the Middle East towards China. According to De Longueville et al. (2010) the Saharan Desert contributes up to 1100 Tg of particulate matter to the annual dust budget, thereby making it the most active among all source regions worldwide.

While gravitational settling effectively removes large particles from the atmosphere shortly after their activation, smaller particles with diameters of less than ten microns may stay airborne for several days (Goudie and Middleton, 2006) and are subject to considerable deposition during this time. Mineral Dust originating from the Sahara is e.g. regularly transported to central Europe, middle Asia or the Caribbean. Figure 1.1 shows an image of the Cape Verde Islands off the West African coast during the overpass of a typical low level dust cloud observed by the Moderate Resolution Imaging Spectroradiometer (MODIS).

Once the dust returns to the surface due to atmospheric downdrafts or wash-out by precipitation, it may interact with the local ecosystem. Shinn et al. (2000) present evidence that coral reef decline in the Caribbean may be linked to the advection of Saharan soil, while other authors (Das, 1988, Martin et al., 1991, Swap et al., 1992) identified a beneficial effect on the local flora, as the dust serves as nutrient for plants and algae. Moreover, mineral aerosols have been found to impair human health both directly and indirectly: Kar and Takeuchi (2004) report that Yellow



Figure 1.1: Saharan dust aerosol observed on 5 March 2004 over Cape Verde by MODIS on-board the Terra satellite. The lower-lying islands towards the east are almost entirely obscured by dust, while the peaks of the volcanic islands protrude from the dust layer. Notice the complex aerodynamic flow of air around the islands, which is visualised by the dust. (Source: [http://visibleearth.nasa.gov/view\\_rec.php?id=6480](http://visibleearth.nasa.gov/view_rec.php?id=6480))

dust from the arid areas in China regularly causes traffic incidents due to reduced visibility and they draw a connection between the occurrence of respiratory disease among the local population and the exposure to aeolian particles.

Another motive for the investigation of mineral dust is related to the energy budget of the Earth. Since the exchange of energy between the Earth and the rest of the universe predominantly occurs in form of electromagnetic radiation, the balance of absorbed solar and emitted terrestrial radiation critically affects the climate on our planet. Following the Fourth Assessment Report on Climate Change (IPCC, 2007) published by the Intergovernmental Panel on Climate Change (IPCC), it is common to distinguish between a direct and an indirect aerosol radiative effect. The direct radiative effect (DRE) encompasses the interaction of aerosols with electromagnetic radiation from ultraviolet (UV) to thermal infrared (TIR). Airborne dust particles e.g. scatter and absorb solar and terrestrial radiation and emit thermal radiation and thus exert a complex DRE. The indirect radiative effect comprises changes in the radiation budget entailed by aerosol induced modifications of microphysical cloud properties. Dust particles may e.g. act as cloud condensation nuclei, thereby altering the cloud droplets and eventually the cloud's ability to form precipitation. The resulting modified lifetime and altered optical

properties of the cloud contribute to the indirect aerosol radiative effect. Currently there still exists a considerable lack of understanding regarding both direct and indirect radiative effect. As climate change has become a central issue in politics and science, it is desirable to advance the capabilities of current climate models to treat the aerosol effect. A thorough investigation of the associated processes is a prerequisite to reach this goal.

Apart from the DRE and its connection to climate on Earth, there exists another important motivation to advance the understanding of the way aerosols interact with radiation: Over the last decades remote sensing, i.e. the process of measuring physical quantities from a large distance, has critically altered our perception of Earth and other planets. Be it the discovery of the ozone hole, the monitoring of the polar ice caps, accurate weather forecasts or the search of life on foreign planets: they all depend upon remote sensing techniques, which ultimately require the capability to measure and predict electromagnetic radiation. In fact the vast majority of remote sensing instruments shares a common fundamental measurement principle, no matter whether they are ground based, airborne or spaceborne: They infer quantities of physical interest, such as trace gas concentrations or sea surface temperature (SST) from a comparison of electromagnetic radiation measurements with a predicted result. Since the methods employed to extract the desired information comprise elaborate algorithms and complex physical modelling, a simplified example will be provided to demonstrate, how advancing the understanding of the aerosol's interaction with electromagnetic radiation improves the quality of remote sensing products.

Imagine a satellite instrument designed to measure SST. Such an instrument will likely record the amount of TIR radiation emitted at the surface due to Planck's law. For simplicity it shall be assumed, that this is done in a spectral interval where gaseous absorption can be ignored, e.g. in a suitable microwindow. It is then possible to deduce the surface temperature by an inversion of Planck's law based on the emissivity of water and the amount of radiation measured at top of the atmosphere (TOA). The presence of an atmospheric dust cloud however will complicate matters. Since the aerosol typically absorbs and scatters in the entire TIR spectral region, it is usually impossible to find a spectral interval not affected by the dust particles. Thus the amount of radiation reaching the instrument at TOA is reduced, because the dust absorbs part of the terrestrial radiation. Ignoring this during the inversion will lead to a cool bias in the retrieved SST, because the amount of radiation leaving the surface is underestimated. The only possibility to infer a correct SST in the presence of aerosols is thus to simulate the amount of radiation absorbed by the particles and to add it to the measured radiation before the inversion.

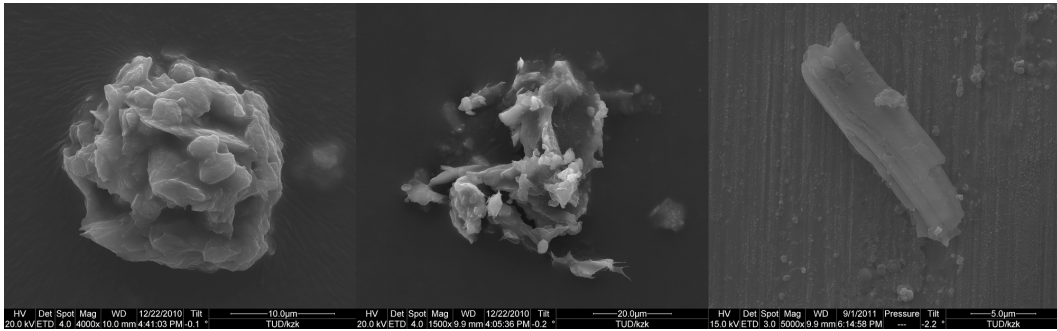


Figure 1.2: TEM images of several dust particles collected during SAMUM-2 (Images courtesy of K. Kandler)

This example clarifies, that the capability to model aerosol optical parameters is a prerequisite for accurate remote sensing products in the presence of aerosols even if the quantity of interest by itself is not aerosol-related. Needless to say, that the capability to model the interaction of radiation with particulate matter is essential, if the aim is to infer information about any aerosols. Most likely politicians and scientists will be forced to decide upon strategies to mitigate the human impact on our ecosystem in the upcoming years. Taking into account that their decisions will be based to a large extent upon simulations and remote sensing data, the motivation to advance the understanding in this particular field of research becomes even more apparent.

## 1.2 State of the Art

At this point the question might arise, why the treatment of particulate matter poses so many problems compared to the relatively well understood properties of gaseous matter. From a theoretical point of view the solution of the problem is straight forward at first glance: Given a plane wave incident on a particle of arbitrary shape, the Maxwell-Equations guarantee a unique solution of the scattered and absorbed fields, if the complex refractive index (or equivalently the dielectric function) of the particle is known. Unfortunately the solution of the Maxwell Equations is a challenging issue and solutions in closed form are known for only a handful of highly symmetric geometries, such as spheres or infinite cylinders.

The simplicity of the geometries for which analytical solutions exist is contrasted by the complexity of particles typically encountered in atmospheric aerosols. These customarily consist of agglomerates of different materials displaying highly irregular shapes and it is not uncommon for them to contain coatings or inclusions

(see figure 1.2). Although the continuously increasing processing power of modern computer systems would foster the hope to solve the problem numerically, it has to be stated that current algorithms still require a considerable amount of time to produce a solution and –which is even worse– are not guaranteed to converge for arbitrary shapes and particle sizes.

In the face of these difficulties it is tempting to proceed similar to statistical gas theory and assume that a distribution of randomly oriented particles with a variety of geometries behaves similar to a distribution of isotropic particles, i.e. spheres. Unfortunately this approximation is often inappropriate due to the non-linearity of the scattering problem. In other words, the average over all solutions generally differs (sometimes quite substantially) from the solution for an average geometry.

Owing to the fact, that the rigorous treatment of light scattering by aerosol particles poses so many challenges, several approximations have been developed, which enable the inclusion of aerosols into radiation models for remote sensing applications or climate simulations. These models constitute a trade-off between precision and computational efficiency, since the constraints on computation time are often a limiting factor in both applications. Such simplifications may consist of e.g. look-up tables, neural networks or approximations in terms of simple analytic functions depending on a reduced number of parameters. In order to develop or tune these models, however, it is necessary to have a benchmark model at ones disposal, which is based on solid physical grounds and reduces empirical approximations to a minimum.

Unfortunately no commonly accepted benchmark model for mineral dust in the TIR exists so far. This may be attributed to the fact, that the radiative properties of aerosols in this spectral region have received comparatively little attention compared to the ultraviolet and visible spectral domain (UV/Vis) until recently. A possible explanation for this lack of interest might be that measurements in the TIR often require more complex instrumentation or that the impact of aerosols within this spectral region has been underestimated for a long time.

Although Hoidale and Blanco (1969) report TIR measurements of dust aerosol and identify a distinct spectral signature, it took quite a while until Sokolik et al. (1998) revived the topic with simulation studies addressing the radiative forcing of mineral dust aerosols in the TIR atmospheric window region. They stress the strong dependence of aerosol optical properties on particle refractive index and conclude, that since the mineral composition of dust is likely to vary with source region, it would be advantageous to assume a source dependent bulk refractive index instead of a global dust model. The question how exactly such a bulk refractive index is obtained (e.g. by measurements of dust samples or by calculation

from the refractive indices of pure mineral constituents) is left open, as is the validity of the assumption of spherical model particles.

Highwood et al. (2003) present airborne high spectral resolution measurements over a Saharan dust layer and confirm the theoretical predictions of a distinct spectral signature. They further conclude, that ground based measurements of the downwelling radiation might be better suited for closure studies, since simulated radiances are affected to a far lesser extent by uncertainties in the surface properties (temperature, emissivity) in this case. A detailed simulation study by Hollweg et al. (2006) confirms this presumption. Their analysis of the error budget for ground based Fourier Transform infrared spectrometer (FTIR) measurements including the uncertainties of radiative transfer simulations indicates that the aerosol optical depth commonly encountered in the vicinity of source regions should be detectable with state-of-the art instrumentation and radiative transfer modelling.

These findings motivated the investigations presented in this thesis. The ultimate goal was to develop a benchmark aerosol model suitable for TIR radiative transfer simulations including the validation against bottom of the atmosphere (BOA) and TOA measurements. A number of field experiments dedicated at least partly to mineral dust aerosol have been conducted since. The following paragraphs are used to summarise briefly the key results of these campaigns as far as they bear relevance to the thesis at hand.

Hansell et al. (2008) analyse ground based measurements of downwelling radiation recorded in 2004 with the AERI instrument during the UAE<sup>2</sup> campaign close to Abu Dhabi, United Arab Emirates. They present a method to retrieve dust aerosol optical depth (AOD) from atmospheric emitted radiance interferometer (AERI) measurements. Based on brightness temperature difference (BTD) between different AERI channels, the AOD is chosen from a set of pre-calculated values, such that the associated simulated BTD optimally matches the observed BTD. The simulations are performed with the refractive index model of Volz (1973). In a later paper (Hansell et al., 2010) the AOD retrieval described above is applied to AERI spectra measured during the 2006 NAMMA campaign, which was conducted on the island of Sal, Cape Verde, in parallel to the African monsoon multidisciplinary analysis (AMMA) project.

Turner (2008) retrieves dust composition and size distribution from AERI measurements obtained during the 2006 AMMA campaign in Niamey, Niger. The author models the dust aerosol with a three component external mixture of spherical particles formed of either kaolinite, quartz or gypsum. It is concluded from the observations that kaolinite and gypsum are the most abundant minerals while



quartz seems to play a minor role. The retrieval is based on an optimal estimation strategy using microwindows distributed over the spectral region  $770 - 1200 \text{ cm}^{-1}$  excluding the interval  $980 - 1080 \text{ cm}^{-1}$ , where a strong ozone absorption band disturbs the retrieval, as the author states.

Thomas and Gautier (2009) performed TIR absorption measurements within the scope of AMMA at M'Bour, Senegal. The AOD derived from their observations displays a spectral red shift of approximately  $40 \text{ cm}^{-1}$  compared to simulations assuming spherical model particles. The shift is most prominent in the spectral interval  $1000 - 1100 \text{ cm}^{-1}$  and is shown to occur for several different refractive index models including internal and external mixtures. The authors speculate, that the inconsistencies between modelled and measured data are likely attributable to the non-sphericity of the aerosol particles. Their assumption is based on laboratory measurements on synthetic model aerosols conducted by Hudson et al. (2008) and Mogili et al. (2008). Therein the authors report similar red shifts of the main absorption peak for several pure mineral dust constituents. A reanalysis of this data by Kleiber et al. (2009) reveals, that a mixture of spheroids with different aspect ratios yields a much better agreement between measured and simulated AOD. According to their simulations, the required aspect ratios depend on the aerosol forming material and exceed the values obtained in microscopic observations by a factor of approximately 10.

The findings of Kleiber et al. (2009) are basically confirmed by Boer (2010), who compares the airborne measurements of Highwood et al. (2003) to radiative transfer simulations. In contrast to the work of Kleiber et al. (2009), an external mixture of oblate spheroids with aspect ratio 5 is assumed independent of the particle mineralogy. As demonstrated by the author, it is possible to reproduce measured dust signatures in the TIR with this model, if mineral composition and size distribution are fitted by a simple least-squares approach. However, no attempts are made to validate the such obtained aerosol number concentration and mineral composition versus in-situ measurements.

All of the aforementioned measurements investigate the optical properties of mineral dust aerosol in the TIR. However, none of them is a rigorous closure study in the sense, that the complete input data required for the radiative transfer simulations is derived from measurements. The only exception are the laboratory studies of Kleiber et al. (2009), but the latter exclusively focus on pure minerals instead of real-world dust mixtures. Furthermore the aerosols examined within the scope of their studies lacked a substantial amount of larger particles typically observed in the atmosphere. The essence of the works presented above is twofold: Firstly most of these measurements seemingly indicate, that particle non-sphericity has to be taken into account for mineral dust aerosols in TIR radiative transfer. Secondly it

Quantity	Instrument	Location	Reference
downwelling radiance	D&P Model 102	Praia	this work
upwelling radiance	IASI	MetOp	EUMETSAT (2011)
p, T, RH profiles	Radiosonde	Praia	Knippertz et al. (2011)
vertical aerosol structure	LIDAR	Praia Praia D-CMET	Tesche et al. (2011a) Groß et al. (2011a) Weinzierl et al. (2011)
aerosol size distribution	Filter, Impactor CPC,DMA,OPC	Praia D-CMET	Kandler et al. (2011a) Weinzierl et al. (2011)
Particle composition& shape	offline analysis	Praia D-CMET	Kandler et al. (2011b) Lieke et al. (2011)

Table 1.1: Experimental Data Used in this Study

has been demonstrated, that it is possible, to reproduce measured radiances with those models, if several input parameters such as mineral composition and particle size are fitted to the data. The validation of the such obtained microphysical aerosol parameters with in-situ observations however still remains an open issue.

### 1.3 Scope of Work

As indicated before, the ultimate goal of this thesis is a column closure of mixed mineral dust and biomass burning aerosol in the TIR. To achieve this goal, measured spectra recorded at BOA and TOA are going to be compared to simulated radiances. The influence of several typical aerosol models on the simulated radiances is going to be scrutinized including different choices for the bulk refractive index and particle geometry. A prerequisite for such an investigation is the availability of accurate measurements with well characterised and validated instruments. The quantities of interest are not limited to the upwelling and downwelling radiances, but comprise a manifold of input data entering the simulations.

The extensive amount of data required to complete the study at hand (ref. table 1.1) could not have been gathered without the support of many colleagues, who participated in the SAharan Mineral dUst experiMent (SAMUM). SAMUM is a research project funded by the German Research Foundation (DFG) which included two major field campaigns: The first phase (SAMUM-1) featured a large field experiment at Morocco and was dedicated to the optical and micro-physical properties of pure mineral dust aerosol directly after its entrainment into the atmosphere. The second phase (SAMUM-2) focused on the optical and microphysical properties

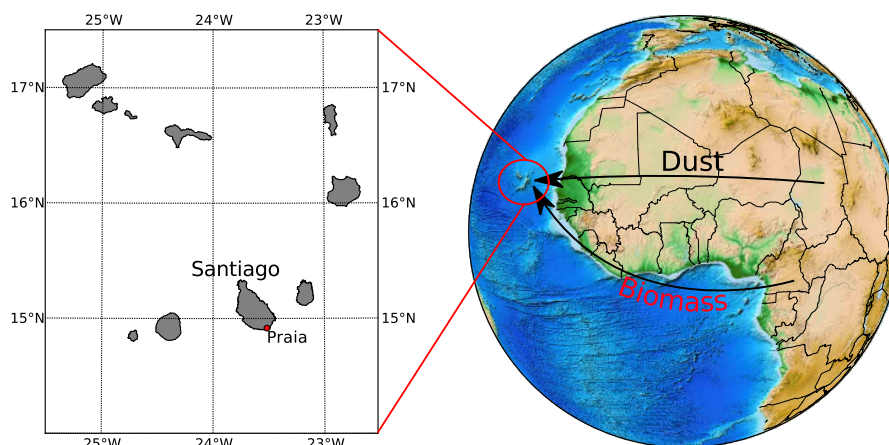


Figure 1.3: Expected transport routes of biomass burning aerosol and mineral dust during SAMUM-2.

of mineral dust and biomass burning aerosols. As this thesis was prepared within the scope of SAMUM-2, the interested reader is referred to Heintzenberg (2009) for an overview of SAMUM-1.

SAMUM-2 took place on the Island of Santiago, Cape Verde, in January and February 2008. This location was chosen due to a complex mixture of mineral dust and biomass burning aerosol typically observed there during the (northern hemisphere) winter months. While the dust is usually advected from the Saharan Desert, the biomass aerosol customarily originates from fires distributed over Central Africa. Both aerosols are predominantly subject to westward transport by the north-easterly trade winds and typically mix over Cape Verde (figure 1.3). The main field site for ground-based instrumentation was located at Praia airport, from where the German Aerospace Center (DLR) operated its research aircraft D-CMET during the campaign. More detailed information about SAMUM-2 can be found in the summary compiled by Ansmann et al. (2011).

Figure 1.4 summarises the third-party measurements most relevant for this work in graphical form. The vertical structure of the aerosol layers is derived from Light detection and ranging (LIDAR) measurements performed from both the Praia field site and the D-CMET. Additionally in-situ size distribution measurements are conducted on-board the D-CMET and at the surface. Chemical composition and geometry of the aerosol particles are inferred from the offline analysis of aerosol samples collected by aircraft. Radiosondes launched from Praia airport deliver vertical profiles of atmospheric pressure, temperature and relative humidity. For a detailed description of any of these measurements please refer to the respective reference provided in table 1.1.

The remaining chapters of this thesis treat the TIR aerosol optical properties during SAMUM-2. After a detailed presentation of the FTIR measurements performed by the author within the scope of SAMUM-2, an aerosol model for the TIR will be developed based on state-of-the-art radiative transfer tools. In particular the following tasks will be addressed:

- Characterise stability and accuracy of the D&P Model 102 FTIR in terms of typical core quantities
- Develop and validate a method to measure downwelling atmospheric radiances with defined uncertainties using the D&P Model 102 FTIR
- Set-up a simulation environment capable to compute the atmospheric radiation at BOA and TOA in the presence of aerosols with benchmark accuracy
- Identify a microphysical aerosol model suited to reproduce the measured radiation at BOA and TOA with special attention to refractive index and particle shape.

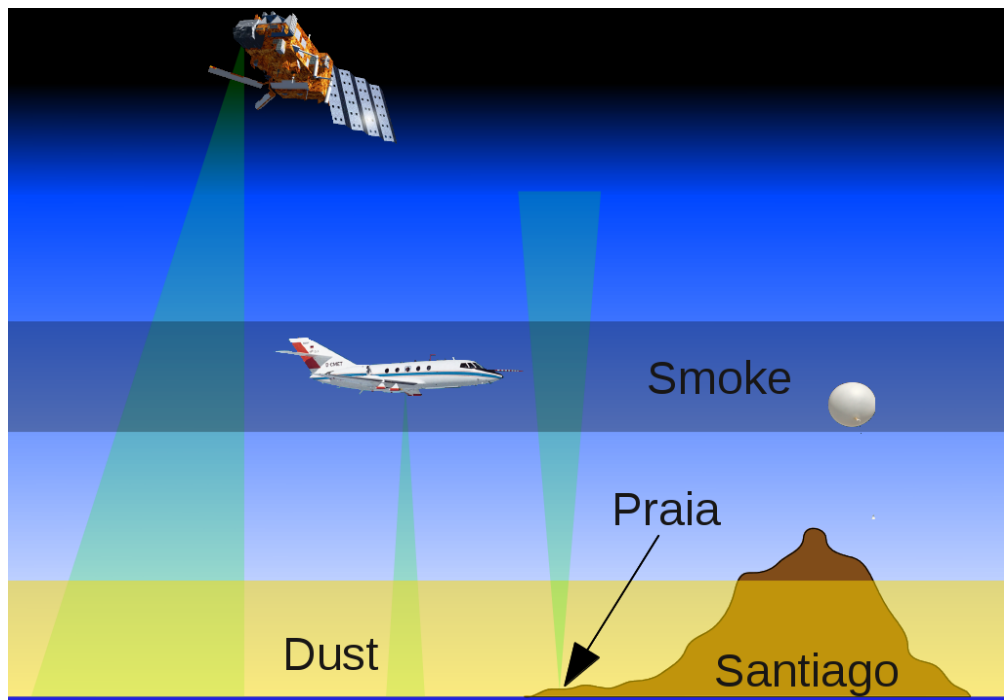


Figure 1.4: Sketch of the SAMUM-2 instrumentation contributing data to this thesis. Green shaded areas depict the field of view for remote sensing instruments.

# Chapter 2

## Measurements

This chapter treats the experimental work performed within the scope of SAMUM-2 and is organised in four sections. Section 2.1 summarises the theoretical concepts necessary to understand the basic features of Fourier Transform spectroscopy (FTS). Section 2.2 treats the D&P Model 102  $\mu$ FTIR, a commercially manufactured instrument employed for the ground based radiance measurements conducted as part of this work. After a brief description of the unique instrument design, the main experimental results prepared within the scope of this thesis are presented in this section. Apart from a thorough instrument characterisation this includes an improved calibration method and a drift correction for the instrument. Furthermore a detailed analysis of the overall measurement uncertainty is performed based on the results of the instrument characterisation. The section concludes with a validation of the calibrated spectra versus measurements of a benchmark instrument for atmospheric TIR radiation to demonstrate the benefits of the newly developed calibration and drift correction algorithms. Since the ground-based measurements will be complemented by space-borne measurements of the upwelling radiation, section 2.3 contains a concise introduction of the space-borne Infrared Atmospheric Sounding Interferometer (IASI). The final section 2.4 provides a detailed description of the experimental setup chosen for the ground based measurements during the SAMUM-2 campaign upon which the following chapters of this thesis are build.

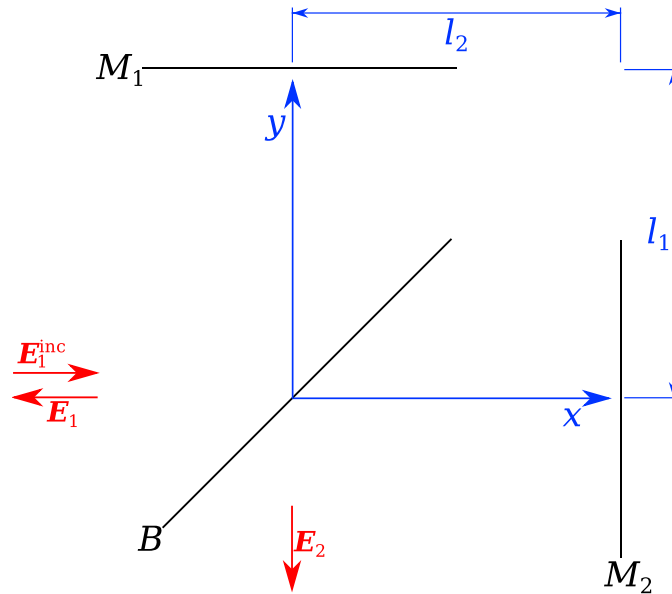


Figure 2.1: Principle setup of a Michelson Interferometer consisting of a beamsplitter ( $B$ ) and two mirrors ( $M_1$ ,  $M_2$ ). Arrows indicate the direction of propagation of the waves rather than the field vectors.

## 2.1 Theoretical Foundations of Fourier Transform Spectroscopy

This section constitutes a recapitulation of the physics behind FTS and its mathematical formalisation. It is intended to introduce a common notation and to provide the unfamiliar reader with the necessary theoretical concepts to understand the development of the instrument specific algorithms for calibration, drift correction and uncertainty estimation presented later. For a more detailed treatise of the matter the interested reader is referred to the works of Kauppinen and Partanen (2001) and Beer (1991), upon which most of this section is based.

### 2.1.1 The Michelson-Interferometer

The Michelson-Interferometer is a good starting point for an introduction to FTS. The idealised set-up depicted in figure 2.1 reduces the optical components to the absolute minimum: a beam splitter  $B$  and two mirrors  $M_1$  and  $M_2$ . To mathematically model the interferometer, a cartesian coordinate system is introduced, such that the beam splitter, which is modelled as plane containing the  $z$ -axis, cuts

the  $yz$ -plane at a  $45^\circ$  angle. The mirrors  $M_1$  and  $M_2$  are modelled as planes normal to the  $x$ - and  $y$ -axis, respectively. The distance of mirror  $M_i$  from the origin is labelled  $l_i$  (for  $i = 1, 2$ ). Note that the beam splitter separates the  $xy$ -plane into a half-space containing the positive  $y$ -axis (labelled half-space 1) and a half-space containing the positive  $x$ -axis (labelled half-space 2). The ultimate goal is to calculate the electric field at the points  $r_1 = (x_1, 0, 0)$  and  $r_2 = (0, y_2, 0)$ , which are commonly referred to as ports of the interferometer. In the following sections indices identify the half-space or port of the associated quantities.

In order to discuss the working principle of the Michelson-Interferometer, it is necessary to introduce some fundamental electrodynamic quantities. The electrical field of a plane electromagnetic wave travelling in the direction of the unit vector  $\hat{\mathbf{q}}$  is written as<sup>1</sup>

$$\mathbf{E}(\mathbf{r}) = \mathbf{E}_0 e^{i2\pi(\nu \hat{\mathbf{q}}\mathbf{r} - ft)}$$

with time  $t$ , wavenumber  $\nu$ , frequency  $f$ , position vector  $\mathbf{r}$  and electric field  $\mathbf{E}_0$  at the origin at  $t = 0$ . Obviously propagation of the wave from an arbitrary point  $\mathbf{r}$  to a point  $\mathbf{r} + l\hat{\mathbf{q}}$  can be expressed in terms of a multiplication, since

$$\mathbf{E}(\mathbf{r} + l\hat{\mathbf{q}}) = \mathbf{E}(\mathbf{r}) e^{i2\pi(\nu l)}.$$

Thus it is convenient to introduce the function

$$p(l) := \exp(i2\pi\nu l),$$

which propagates the wave in the direction of travel by a length  $l$ . Furthermore reflection is formalised in terms of a complex-valued reflection coefficient  $\rho = |\rho| \exp(i\phi_\rho)$ . The norm  $0 \leq |\rho| \leq 1$  controls the intensity of the reflected wave, while the angle  $\phi_\rho$  contains information about the phase shift caused by the reflection. The Fresnel equations allow to calculate this coefficient for a single plane interface. For an infinite metallic plate one obtains e.g.  $\rho = \exp(i\pi) = -1$ . The unity norm implies the absence of absorption and the phase angle  $\phi_\rho = \pi$  is the phase shift of the reflected wave. In a similar manner transmission can be written as a complex transmission coefficient  $\tau$ . In the following paragraph the passage of a plane electromagnetic wave through the Michelson-Interferometer will be discussed using the formalism introduced above.

Imagine a plane wave travels in the direction of the positive  $x$ -axis through  $r_1$  and enters the interferometer through the beam splitter, where it is split into two

---

<sup>1</sup>This thesis adopts the complex notation found in many textbooks on electrodynamics, which expand real-valued physical quantities to the complex plane by adding a suitable imaginary part. Thus complex quantities should be thought of as implicitly reduced to their real part, as far as measurable physical quantities are concerned.

waves. One wave travels back and forth the interferometer arms in half-space 1, the other wave propagates through the corresponding interferometer arm in half-space 2. Finally both waves exit the interferometer through the beam splitter. The mathematical formulation of this process involves expressing the electrical field  $\mathbf{E}_2$  of the outgoing wave at port 2 in terms of the incident field  $\mathbf{E}_1^{\text{inc}}$  at port 1. The superposition principle for electromagnetic waves allows to calculate the field at port 2 as sum of the fields exiting the two interferometer arms:

$$\mathbf{E}_2(\mathbf{r}_2) = (\alpha_2 + \beta_2 e^{i2\pi\nu\Delta}) \mathbf{E}_1^{\text{inc}}.$$

Three new quantities were introduced for brevity in the last equation: the optical path difference  $\Delta = 2(l_2 - l_1)$ , which relates  $p(x_1)$  and  $p(y_2)$  via

$$p(y_2) = p(x_1) e^{i2\pi\nu\Delta}$$

and two complex coefficients

$$\begin{aligned} \alpha_2 &= p(x_1)p(2l_1)p(y_2)\rho_1\rho_{M1}\tau_1 \\ \beta_2 &= p(x_1)p(2l_1)p(y_2)\tau_1\rho_{M2}\rho_2 \end{aligned}$$

summarising the various transmission and reflection coefficients.  $\rho_i$  indicates reflection at the beam splitter in half-space  $i$ ,  $\tau_i$  is the transmission coefficient from half-space  $i$  to half-space  $3 - i$  through the beam splitter and  $\rho_{Mi}$  symbolises reflection at the mirror in half-space  $i$ . Since common practise is to measure radiant energy and not fields, it is necessary to calculate the radiant flux  $d\Phi_2^{\text{out}}$  through a surface element  $d\mathbf{A} = -\hat{\mathbf{y}} dA$  of size  $dA$  normal to the  $y$ -axis at  $\mathbf{r}_2$ .

$$d\Phi_2^{\text{out}} = \langle \mathbf{S}(\mathbf{r}_2) \cdot d\mathbf{A} \rangle_t = |\alpha_2 + \beta_2 e^{i2\pi\nu\Delta}|^2 I_1^{\text{inc}} dA, \quad (2.1)$$

where  $\mathbf{S}$  is the Poynting vector,  $\langle \cdot \rangle_t$  indicates the temporal average and

$$I_1^{\text{inc}} = \frac{1}{2} |\mathbf{E}_1^{\text{inc}}|^2 \sqrt{\frac{\varepsilon_0}{\mu_0}}$$

is the irradiance of the incident plane wave. Note that the explicit dependence on wavenumber is used to discriminate the spectral irradiance  $I(\nu)$  and the spectral flux  $\Phi(\nu)$  from the irradiance  $I$  and the flux  $\Phi$ , respectively. Irradiance and flux are related to their spectral counterparts via

$$\begin{aligned} I &= \int_0^{\infty} I(\nu) d\nu \\ \Phi &= \int_0^{\infty} \Phi(\nu) d\nu. \end{aligned}$$



It is convenient to separate the fraction  $d\tilde{\Phi}_2^{\text{out}}$  of the flux depending on the path difference  $\Delta$  from the total flux via

$$d\Phi_2^{\text{out}} = d\bar{\Phi}_2^{\text{out}} + d\tilde{\Phi}_2^{\text{out}}(\Delta).$$

Evaluating equation 2.1 the fluxes  $d\bar{\Phi}_2^{\text{out}}$  (often called DC part) and  $d\tilde{\Phi}_2^{\text{out}}$  (also called the AC part) can be expressed in terms of the complex coefficients  $\alpha_2$  and  $\beta_2$  and the path difference  $\Delta$ :

$$d\bar{\Phi}_2^{\text{out}} = (|\alpha_2|^2 + |\beta_2|^2) I_1^{\text{inc}} dA \quad (2.2)$$

$$d\tilde{\Phi}_2^{\text{out}}(\Delta) = 2\Re \{ \alpha_2^* \beta_2 e^{i2\pi\nu\Delta} \} I_1^{\text{inc}} dA. \quad (2.3)$$

In addition to the flux at  $\mathbf{r}_2$ , the incident wave causes an outgoing wave at  $\mathbf{r}_1$ , too. As before, AC and DC parts of the outgoing flux at  $\mathbf{r}_1$  can be written as

$$d\bar{\Phi}_1^{\text{out}} = (|\alpha_1|^2 + |\beta_1|^2) I_1^{\text{inc}} dA \quad (2.4)$$

$$d\tilde{\Phi}_1^{\text{out}}(\Delta) = 2\Re \{ \alpha_1^* \beta_1 e^{i2\pi\nu\Delta} \} I_1^{\text{inc}} dA \quad (2.5)$$

with complex coefficients

$$\alpha_1 = p(2x_1)p(2l_1)\rho_1\rho_{M1}\rho_1$$

$$\beta_1 = p(2x_1)p(2l_1)\tau_1\rho_{M2}\tau_2.$$

In an ideal Michelson interferometer all optical components are non-absorbing. Thus energy conservation requires the accumulated outgoing fluxes to equal the incident flux:

$$d\Phi_1^{\text{inc}} = d\Phi_1^{\text{out}} + d\Phi_2^{\text{out}}. \quad (2.6)$$

This equation can be used to derive constraints on the complex reflection and transmission coefficients. Since energy conservation must hold independently of the optical path difference  $\Delta$ , AC part and DC part must each fulfill equation 2.6 separately, which after insertion of 2.2-2.5 yields

$$1 = |\alpha_1|^2 + |\beta_1|^2 + |\alpha_2|^2 + |\beta_2|^2$$

$$0 = \Re \{ \alpha_1^* \beta_1 \alpha_2^* \beta_2 \}.$$

Focussing on the properties of the beam splitter, it is advantageous to simplify the problem by assuming two identical ideal mirrors with  $\rho_{M1} = \rho_{M2} = -1$  and a symmetric beam-splitter with  $\rho_1 = \rho_2 := \rho$  and  $\tau_1 = \tau_2 := \tau$ . Inserting the definitions of the complex coefficients  $\alpha_i$  and  $\beta_i$  with the above mentioned simplifications results in

$$1 = 2(|\rho|^4 + |\tau|^4) \quad (2.7)$$

$$0 = (\rho^* \tau)^2 + |\rho|^2 |\tau|^2. \quad (2.8)$$

As the beam splitter is required to be non-absorbing, the accumulated fluxes of reflected and transmitted beam must equal the incident flux, i.e.  $|\rho|^2 + |\tau|^2 = 1$ . Substitution of this relation in equation 2.7 then yields the magnitude of the reflection and transmission coefficient

$$|\rho| = |\tau| = \frac{1}{\sqrt{2}}. \quad (2.9)$$

This result inserted into equation 2.8 finally leads to

$$(\rho^* \tau)^2 = -\frac{1}{2}$$

or equivalently

$$\phi_\rho - \phi_\tau = \pm \frac{\pi}{2}. \quad (2.10)$$

Since  $\rho$  and  $\tau$  are material constants of the beam splitter, their values remain unchanged if the properties of the interferometer change, e.g. if the mirrors  $M_1$  and  $M_2$  have finite reflectivity. The essential constraint on the beam splitter is to be symmetric and non-absorbing.

Due to the symmetry of the interferometer set-up, it is clear that similar results are obtained, if the incident plane wave enters through port 2 instead of port 1. As the waves entering through different ports have no fixed phase-relation, the resulting flux leaving the interferometer through a surface element  $dA = -\hat{x}dA$  at  $\mathbf{r}_2$  is obtained as sum of the individual fluxes:

$$\begin{aligned} d\bar{\Phi}_2^{\text{out, tot}} &= (|\alpha_2|^2 + |\beta_2|^2) I_1^{\text{inc}} dA + (|\alpha'_2|^2 + |\beta'_2|^2) I_2^{\text{inc}} dA \\ d\tilde{\Phi}_2^{\text{out, tot}}(\Delta) &= 2\Re \left\{ (I_1^{\text{inc}} \alpha_2^* \beta_2 + I_2^{\text{inc}} \alpha_2'^* \beta_2') e^{i2\pi\nu\Delta} \right\} dA \end{aligned}$$

where  $I_2^{\text{inc}}$  is the intensity of the incident plane wave at port 2 and

$$\begin{aligned} \alpha'_2 &= p(2y_2)p(2l_1)\tau_2\rho_{M1}\tau_1 \\ \beta'_2 &= p(2y_2)p(2l_1)\rho_2\rho_{M2}\rho_2 \end{aligned}$$

are the respective complex coefficients. In the special case of the absorption-free interferometer with symmetric beamsplitter the expressions for the fluxes can be simplified:

$$\begin{aligned} d\bar{\Phi}_2^{\text{out, tot}} &= \frac{I_1^{\text{inc}} + I_2^{\text{inc}}}{2} dA \\ d\tilde{\Phi}_2^{\text{out, tot}}(\Delta) &= \frac{I_1^{\text{inc}} - I_2^{\text{inc}}}{2} \cos(2\pi\nu\Delta) dA. \end{aligned}$$

Thus the DC part of the flux is obtained as the accumulated intensity of the incident waves, while the AC part depends on the difference of the incident intensities.

Up to this point the incident radiation has been restricted to monochromatic plane waves. However, it is straightforward to generalise the theory to the more practical case of a polychromatic collimated beam. Approximating the beam as ensemble of plane waves without a fixed phase relation, the spectral irradiance  $I_1^{\text{inc}}(\nu)$  of the incident collimated beam can be interpreted as the intensity of a plane wave with wavenumber  $\nu$  and the total flux through a surface element at port 2 is obtained after integrating over all wavenumbers and the beam cross-section  $A$ :

$$\begin{aligned}\bar{\Phi}_2^{\text{out, tot}} &= \int_0^\infty \int_A (|\alpha_2|^2 + |\beta_2|^2) I_1^{\text{inc}}(\nu) + (|\alpha'_2|^2 + |\beta'_2|^2) I_2^{\text{inc}}(\nu) dA d\nu \\ \tilde{\Phi}_2^{\text{out, tot}}(\Delta) &= 2 \int_0^\infty \int_A \Re \{ (I_1^{\text{inc}}(\nu) \alpha_2^* \beta_2 + I_2^{\text{inc}}(\nu) \alpha_2'^* \beta_2') e^{i2\pi\nu\Delta} \} dA d\nu.\end{aligned}$$

Expanding all wavenumber-dependent quantities to the domain of negative wavenumbers by defining  $f(-\nu) := f^*(\nu)$  for each quantity  $f$  (which is possible without loss of generality, since all physical quantities are restricted to positive wavenumbers), the equations can be written as

$$\bar{\Phi}_2^{\text{out, tot}} = \int_{-\infty}^\infty \int_A \frac{|\alpha_2|^2 + |\beta_2|^2}{2} I_1^{\text{inc}}(\nu) + \frac{|\alpha'_2|^2 + |\beta'_2|^2}{2} I_2^{\text{inc}}(\nu) dA d\nu \quad (2.11)$$

$$\tilde{\Phi}_2^{\text{out, tot}}(\Delta) = \int_{-\infty}^\infty \int_A (I_1^{\text{inc}}(\nu) \alpha_2^* \beta_2 + I_2^{\text{inc}}(\nu) \alpha_2'^* \beta_2') dA e^{i2\pi\nu\Delta} d\nu. \quad (2.12)$$

where the optical path difference  $\Delta$  has been assumed to be constant over the whole beam cross-section. Equation 2.12 is the basic equation of FTS, since it relates the energy flux leaving the interferometer through port 2 and the mean of the incident intensity over the beam cross-section in terms of a Fourier Transform pair.

While the theory derived so far is based on the simplest interferometer model thinkable, it can be generalised to more realistic cases in a straight forward manner. Real beam splitters e.g. typically consist of a multi-layered coating applied to some substrate and are thus not directly representable in terms of a single interface. Nonetheless the reflection and transmission coefficients of the individual interfaces can be combined to a single transmission/reflection coefficient for the

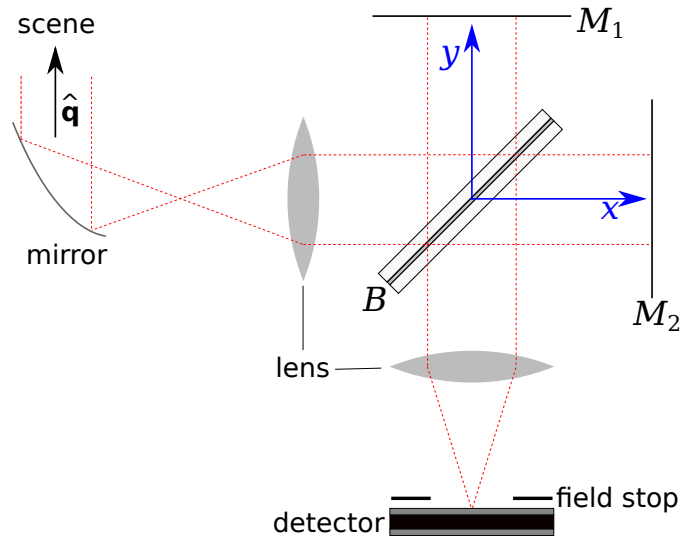


Figure 2.2: Principle design of a Fourier Transform Spectrometer

whole beam splitter assembly. Hamilton (2000) examines several more realistic beam splitter models and uses energy conservation and the Stokes principle to constrain magnitude and phase of the reflection and transmission coefficients. If the refractive index of the medium differs from unity, this can be accounted for multiplying the lengths  $l_1$ ,  $l_2$ ,  $x_1$  and  $y_2$  by the (possibly complex) refractive index  $\mathcal{N}$  of the respective medium. Furthermore additional optical elements, such as focusing lenses or mirrors can be introduced through appropriate additional reflection and transmission coefficients. Although these changes affect the values of the coefficients, they do not fundamentally alter the resulting equations 2.11 and 2.12. It has to be taken into account, though, that the introduction of a wavenumber dependent refractive index will cause the optical path difference to depend on wavenumber, too. The consequences this has on the measured fluxes will be discussed in chapter 2.2.3.

### 2.1.2 The Fourier Transform Spectrometer

This section shows how to develop the Michelson-Interferometer discussed in the previous section into a Fourier Transform spectrometer. As a first step let the optical path difference  $\Delta$ , which is a constant in the Michelson-Interferometer, be variable. This is achieved by allowing either one or both of the mirrors  $M_1$  and  $M_2$  to move back and forth in the direction of their respective surface-normal. In order to be able to measure the outgoing radiation at port 2, a detector with

suitable optics (lens, fieldstop) is installed at  $\mathbf{r}_2$ , such that the detector records the focussed radiation passing through the field stop. Finally a collimator consisting of a parabolic mirror and a lens is installed in front of port 1 to convert the incident radiation to a collimated beam. This typical set-up of a FTS is shown in figure 2.2. Assuming both detector and associated electronics to be linear, the output voltage  $U$  depends linearly on the incident spectral flux:

$$U = \int_0^{\infty} \gamma \Phi(\nu) d\nu \quad (2.13)$$

$\gamma$  is the (possibly wavenumber dependent) response function of the combined detector assembly including electronics. It is feasible to divide the voltage into an AC part  $\tilde{U}$  and a DC part  $\bar{U}$  part in complete analogy to the fluxes. At this point the choice of the terms AC part and DC part for the fluxes becomes apparent, since the latter are indeed related to alternating and direct currents, respectively. Note that the DC part does not contribute any additional information to the AC signal<sup>2</sup>. As a consequence it is typically removed from the interferogram using an electronic filter to exploit the full dynamic range of the analog to digital converter (ADC) employed for data-recording. Using equation 2.12, the AC part can be written as

$$\tilde{U}(\Delta) = \int_{-\infty}^{\infty} [r(\nu) L(\nu) + g(\nu)] e^{i2\pi\nu\Delta} d\nu, \quad (2.14)$$

where

$$L(\nu) = \frac{1}{\Omega_{\text{FOV}}} \int_{\Omega_{\text{FOV}}} L^{\text{scene}}(\nu, \hat{\mathbf{q}}') \hat{\mathbf{q}}' \cdot \hat{\mathbf{q}} d^2q' \quad (2.15)$$

is the mean scene radiance over the instrument field of view  $\Omega_{\text{FOV}}$ ,

$$r(\nu) = \Omega_{\text{FOV}} \int_A \gamma \alpha_2^* \beta_2 dA \quad (2.16)$$

is the instrument response function and

$$g(\nu) = \int_A \gamma \left( \alpha_2^* \beta_2 I_1^{\text{bg}}(\nu) + \alpha_2'^* \beta_2' I_2^{\text{bg}}(\nu) \right) dA \quad (2.17)$$

is the instrument radiation. The latter contains the newly introduced spectral irradiance  $I_2^{\text{bg}}(\nu) = I_2^{\text{inc}}(\nu)$  emitted by spectrometer components in half-space 2

---

<sup>2</sup>This is true for linear detectors/electronics only. If the output voltage depends non-linearly on the incident flux, the DC part of the flux can be employed for a non-linearity correction

and the instrument background  $I_1^{\text{bg}}(\nu)$  in half-space 1, i.e.

$$I_1^{\text{inc}}(\nu) = \Omega_{\text{FOV}} L(\nu) + I_1^{\text{bg}}(\nu).$$

The function  $\tilde{U}(\Delta)$  is called the interferogram in the context of FTS. Equation 2.14 relates the interferogram with the scene radiance  $L$  in terms of a Fourier Transform pair, which allows to reconstruct the scene radiance from the interferogram, if the instrument functions  $r$  and  $g$  are known. While it is theoretically possible to calculate them based on the theory derived above, it is not practical to do so, since neither the various reflection and transmission coefficients nor the radiation emitted by the instrument are typically known. Furthermore the instrument radiation is mainly caused by thermal emission of individual interferometer components and thus changes whenever the temperature of the instrument changes. Additionally the instrument response is subject to change, if optical components deteriorate or if the interferometer alignment is altered. As a consequence it is preferable to determine  $r$  and  $g$  experimentally. This process is called radiometric calibration and will be discussed in chapter 2.2.4.

Before proceeding to the next section, it is instructive to take a closer look at the instrument function  $r$  and  $g$  for a loss-less interferometer with symmetric beam splitter. Insertion of equations 2.9 and 2.10 into equations 2.16 and 2.17 yields

$$r(\nu) = \Omega_{\text{FOV}} \int_A \frac{\gamma}{4} dA$$

$$g(\nu) = \int_A \gamma \frac{I_1^{\text{bg}}(\nu) - I_2^{\text{bg}}(\nu)}{4} dA.$$

Note that both instrument functions are real in this special case and consequently the interferogram equation 2.14 becomes

$$\tilde{U}(\Delta) = \int_0^\infty \int_A \frac{\gamma}{2} dA \left[ \Omega_{\text{FOV}} L(\nu) + I_1^{\text{bg}}(\nu) - I_2^{\text{bg}}(\nu) \right] \cos(2\pi\nu\Delta) d\nu. \quad (2.18)$$

Observe that the interferogram described by equation 2.18 is axis-symmetric around  $\Delta = 0$ , as can be seen in the left hand panel of figure 2.3, which shows a synthetic interferogram for a hypothetic black body at 300 K.  $\Delta = 0$  is often called ZPD and from equation 2.18 immediately follows that

$$\|U(0)\| > \|U(\Delta)\| \quad \forall \Delta \neq 0. \quad (2.19)$$

In other words, the ZPD peak (also referred to as centreburst) is higher than all other peaks and can be conveniently used to identify the ZPD. Additionally

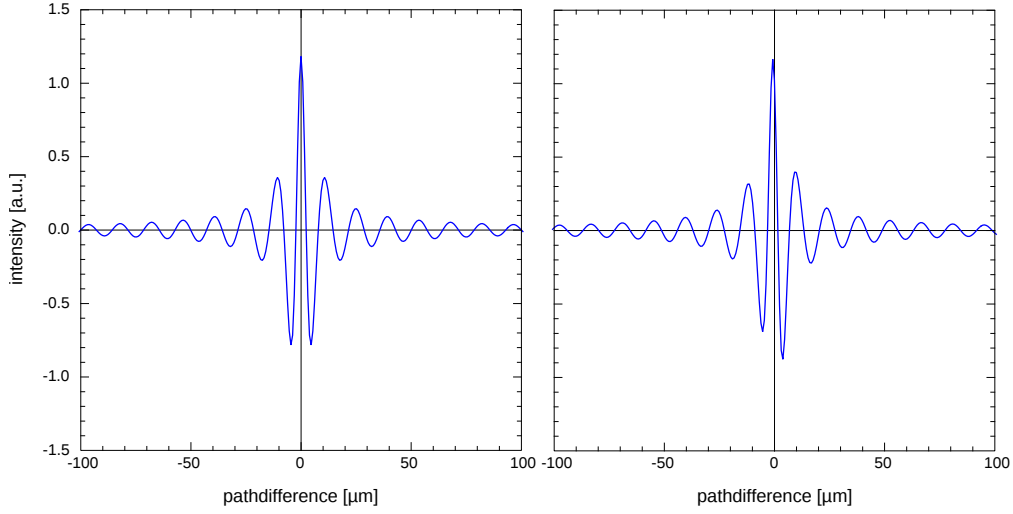


Figure 2.3: Visualisation of the influence of a complex valued response function: Both plots show the same synthetic interferogram for an ideal black body at 300 K. The left hand panel assumes a constant, real-valued response, while the right hand panel uses the same response with an additional phase shift of  $30^\circ$  in the complex plane. Note the asymmetry and the apparent shift of the ZPD introduced by the imaginary fraction of the response.

observe that  $U(0)$  can be negative, if

$$\int_0^{\infty} \Omega_{\text{FOV}} L(\nu) + I_1^{\text{bg}}(\nu) d\nu < \int_0^{\infty} I_2^{\text{bg}}(\nu) d\nu \quad (2.20)$$

Thus the centreburst can be inverted, if the accumulated intensity entering through port 1 is less than the intensity entering from the opposite side of the beam-splitter. Note however, that the considerations above are strictly valid only if the instrument functions  $r$  and  $g$  are real-valued. This is visualised by the right-hand panel in figure 2.3, where a  $30^\circ$  phase shift has been introduced into the response function  $r$ , leading to an asymmetric interferogram with a seemingly shifted ZPD.

Although scene radiance and interferogram must be real-valued measurable quantities, the instrument functions may be complex-valued. Any non-zero imaginary part in the instrument functions incurs sine contributions from the complex exponential during Fourier Transform (equation 2.14). These add point symmetric components to the interferogram. Thus asymmetries in the interferogram are a mere indication of non-zero imaginary parts in the instrument functions. Consequently instrument functions and Fourier Transform must be treated in the complex plane.

### 2.1.3 Truncation and Sampling

As shown in the previous section, interferogram and incoming radiance form a Fourier Transform pair. It is straight forward to solve equation 2.14 for the radiance:

$$\int_{-\infty}^{\infty} \tilde{U}(\Delta) e^{-i2\pi\nu\Delta} d\Delta = r(\nu)L(\nu) + g(\nu) \quad (2.21)$$

This equation however idealises in two important ways: First it is impossible to measure the interferogram for an infinite range of path differences  $\Delta$  and secondly the interferogram has to be sampled at discrete points. The effects caused by truncation and sampling are conveniently investigated using basic properties of the Fourier Transform. A prerequisite for this is the formalisation of truncation and sampling in terms of mathematical expressions. The necessary theory is going to be recapitulated in the following paragraph for the reader's convenience and for the sake of a consistent notation. Due to the general mathematical nature of most expressions, the path-difference  $\Delta$  is replaced by  $x$  as argument in the spatial domain to comply with most textbooks covering the matter. The boxcar function

$$\square_{2a}(x) := \begin{cases} 0 & \text{if } |x| > a \\ 1 & \text{if } |x| \leq a \end{cases}$$

constitutes the formalisation of truncation. It is straightforward to show (Kaupinen and Partanen, 2001), that its Fourier Transform leads to the modified sinc function

$$\text{sinc}_a(x) := \begin{cases} a & \text{if } x = 0 \\ \frac{\sin(a\pi x)}{\pi x} & \text{if } x \neq 0 \end{cases}.$$

Introducing the Fourier Transform operator

$$\mathcal{F}\{f\}(\nu) := \hat{f}(\nu) := \int_{-\infty}^{\infty} f(x) e^{-i2\pi\nu x} dx$$

$$\mathcal{F}^{-1}\{\hat{f}\}(x) = f(x) = \int_{-\infty}^{\infty} \hat{f}(\nu) e^{i2\pi\nu x} d\nu$$

for an arbitrary integrable function  $f : \mathbb{R} \rightarrow \mathbb{C}$  (Kerner and von Wahl, 2006), this relation can be written as

$$\mathcal{F}\{\square_a\} = \text{sinc}_a.$$



Defining the convolution by

$$(f * g)(x) := \int_{-\infty}^{\infty} f(y)g(x-y) dy$$

it can be shown (Kerner and von Wahl, 2006) that the so-called convolution theorem

$$\mathcal{F}\{f * g\} = \hat{f} \cdot \hat{g} \quad (2.22)$$

holds for any two integrable functions  $f, g : \mathbb{R} \rightarrow \mathbb{C}$ . As a consequence any finite integral may be expressed in terms of the boxcar function or the sinc function

$$\int_{-a}^a f(x)e^{-i2\pi\nu x} dx = \mathcal{F}\{\Pi_{2a} \cdot f\}(\nu) = [\text{sinc}_{2a} * \hat{f}](\nu). \quad (2.23)$$

Sampling is typically formalised by the delta comb  $\text{III}_{\Delta x}$  (also called sampling function), which is defined as

$$\text{III}_{\Delta x}(x) := \sum_{j=-\infty}^{\infty} \delta(x - j\Delta x).$$

Since the delta comb is obviously periodic with period  $\Delta x$ , it can be developed into a Fourier series (Bronstein et al., 2001):

$$\text{III}_{\Delta x}(x) = \sum_{j=-\infty}^{\infty} c_j e^{i2\pi jx/\Delta x}$$

with coefficients

$$c_j = \frac{1}{\Delta x} \int_{-\Delta x/2}^{\Delta x/2} \text{III}_{\Delta x}(x) e^{-i2\pi jx/\Delta x} dx = \frac{1}{\Delta x} \int_{-\Delta x/2}^{\Delta x/2} \delta(x) e^{-i2\pi jx/\Delta x} dx = \frac{1}{\Delta x}.$$

Thus the delta comb can be expressed as

$$\text{III}_{\Delta x}(x) = \frac{1}{\Delta x} \sum_{j=-\infty}^{\infty} e^{i2\pi jx/\Delta x} = \text{III}_{\Delta x}^*(x) = \frac{1}{\Delta x} \sum_{j=-\infty}^{\infty} e^{-i2\pi jx/\Delta x}.$$

Comparing the infinite sum to the Fourier Transform of the delta comb

$$\mathcal{F}\{\text{III}_{\Delta x}\}(\nu) = \sum_{j=-\infty}^{\infty} e^{-i2\pi\nu j\Delta x} = \Delta x \text{III}_{1/\Delta x}(\nu)$$

it becomes apparent that the Fourier Transform of a delta comb is a scaled delta comb with inverse spacing.

Having thus formalised truncation and sampling it is possible to discuss their respective effects in combination with the Fourier Transform. The influence of truncation in the Fourier domain can be observed regarding a truncated delta comb

$$\text{III}_{\Delta x}^M := \square_{2M} \cdot \text{III}_{\Delta x}.$$

Application of the convolution theorem 2.22 yields

$$\mathcal{F}\{\text{III}_{\Delta x}^M\}(\nu) = \Delta x \text{sinc}_{2M}(\nu) * \text{III}_{1/\Delta x}(\nu) = \Delta x \sum_{j=-\infty}^{\infty} \text{sinc}_{2M}\left(\nu - \frac{j}{\Delta x}\right). \quad (2.24)$$

Thus truncation causes the original spectrum of infinitely narrow lines to be transformed into a series of sinc functions with finite width. In other words, truncation in the signal domain causes a reduction of spectral resolution in the Fourier domain as individual peaks become inseparable if their full width at half maximum (FWHM) is less than the peak-distance  $\Delta x^{-1}$ . In order to investigate sampling, consider a function  $f: \mathbb{R} \rightarrow \mathbb{C}$  sampled at equal-spaced points  $x_j = j\Delta x$ . Let

$$f_{\Delta x}(x) := \sum_{j=-\infty}^{\infty} f_j \delta(x - j\Delta x) = f(x) \text{III}_{\Delta x}(x)$$

be the discrete approximation with  $f_j := f(x_j)$ . Application of the convolution theorem 2.22 to the Fourier Transform yields

$$\hat{f}_{\Delta x}(\nu) = \Delta x \hat{f}(\nu) * \text{III}_{1/\Delta x}(\nu) = \Delta x \sum_{j=-\infty}^{\infty} \hat{f}\left(\nu - \frac{j}{\Delta x}\right).$$

Obviously this function is periodic with period  $\Delta x^{-1}$ , since shifting  $\nu$  by this amount is equivalent to an index shift in the infinite sum, implying that the Fourier Transform of any discrete signal is periodic. If  $\hat{f}$  is band limited with maximum frequency  $F$  such that  $2F \leq \Delta x^{-1}$ , only one term in the infinite sum can be non-zero at a time and consequently the Fourier Transform of  $f$  is related to the Fourier Transform of its discrete approximation

$$\hat{f}(\nu) = \Delta x^{-1} \hat{f}_{\Delta x}(\nu) \quad \forall \quad \nu \in \left[-\frac{1}{2\Delta x}, \frac{1}{2\Delta x}\right).$$

Furthermore the multiplication with a boxcar function of width  $2F$  is an identity operation for the band limited function  $\hat{f}$ :

$$\hat{f} = \square_{2F} \hat{f}.$$

Thus application of the inverse Fourier Transform to  $\hat{f}$  yields

$$f = \mathcal{F}^{-1} \left\{ \square_{2F} \hat{f} \right\} = \Delta x^{-1} \mathcal{F}^{-1} \left\{ \square_{2F} \hat{f}_{\Delta x} \right\} = \Delta x^{-1} \text{sinc}_{2F} * f_{\Delta x}$$

In other words: a function with band-limited spectrum can be fully reconstructed from a discrete set of sampling points, if the sampling interval  $\Delta x$  and the spectral bandwidth  $F$  satisfy

$$F \cdot \Delta x \leq \frac{1}{2}. \quad (2.25)$$

This is the well known Nyquist or sampling theorem.

Let  $\hat{f}^M$  be a spectrum obtained by coarsening the resolution of  $\hat{f}(\nu)$  through convolution

$$\hat{f}^M := \text{sinc}_{2M} * \hat{f}.$$

From the convolution theorem (2.22) obviously follows

$$f^M = \mathcal{F} \left\{ \hat{f}^M \right\} = \square_{2M} \cdot f.$$

Since  $f^M$  is band-limited with bandwidth  $M$ , the Nyquist theorem states that its Fourier Transform  $\hat{f}^M$  is reconstructible from the discrete spectrum

$$\hat{f}_{\Delta\nu}^M(\nu) := \sum_{j=-\infty}^{\infty} \hat{f}_j^M \delta(\nu - j\Delta\nu)$$

(with  $\hat{f}_j^M := \hat{f}^M(\nu_j)$ ) if the sampling width  $\Delta\nu$  is chosen such that

$$\Delta\nu \leq \frac{1}{2M}.$$

Introducing  $N \in \mathbb{N}$  with  $M = N\Delta x$  this becomes

$$\Delta\nu \Delta x \leq \frac{1}{2N}.$$

If the maximum possible sampling width  $\Delta\nu = \Delta x/(2N)$  is chosen, the coefficients  $\hat{f}_k^M$  can be related to the coefficients  $f_j$  by a discrete Fourier Transform:

$$\hat{f}_k^M = \Delta x^{-1} \hat{f}_{\Delta x}^M(\nu_k) = \Delta x^{-1} \sum_{j=-N}^{N-1} f_j e^{-i\pi jk/N} \quad \forall k = -N \dots N-1. \quad (2.26)$$

Equation 2.26 can be conveniently evaluated with the numerically efficient and stable fast Fourier Transform (FFT) algorithm first suggested by Cooley and Tukey

(1965). In fact, this algorithm in combination with the advent of modern personal computers fostered the evolution of FTS, since it provides a convenient method to numerically evaluate the integrals occurring in equation 2.21. Throughout this work the open source implementation of Frigo and Johnson (2005) is used, which has been optimised for modern processors.

The detectors built into FTIR instruments are typically receptive to electromagnetic radiation only in a finite spectral interval, so that  $r$  and  $g$  are guaranteed to have compact support, which in turn results in a band limited right hand side in equation 2.21. Assuming  $\nu_{\max}$  to be the upper cut-off frequency of the detector, the Nyquist theorem 2.25 states, that the original spectrum is fully reconstructible from a finite interferogram sampled at equal spaced path differences, if the stride  $\Delta x$  satisfies

$$\Delta x \leq \frac{1}{2\nu_{\max}}. \quad (2.27)$$

The maximum optical path difference (MOPD)  $M = N\Delta x$  at which the interferogram is truncated defines the optimal sampling interval  $\Delta\nu = (2M)^{-1}$  of the spectrum, thereby limiting its resolution. As a consequence the optimally sampled spectrum is fully defined by an interferogram recorded at  $2N$  equal-spaced path differences.

### 2.1.4 Spectral Resolution and Apodisation

As shown in the previous section, truncation of an interferogram at MOPD  $M$  determines the optimal sampling distance  $\Delta\nu$  of the associated spectrum.  $\Delta\nu$  is sometimes referred to as the resolution of a spectrometer, although it actually constitutes a theoretical upper limit of the maximum possible resolution. In order to quantify spectral resolution, recall that an ideal delta-comb spectrum transforms into a sequence of equally spaced sinc functions, if the associated interferogram is truncated with a rectangle function (equation 2.24). Since the peaks of the individual sinc functions become inseparable, if their FWHM exceeds their distance, the spectral resolution  $\delta\nu$  is defined here as FWHM of the sinc

$$\delta\nu := \frac{1}{\pi M} h_{\text{sinc}}$$

where  $h_{\text{sinc}}$  is defined by

$$\sin(h_{\text{sinc}}) = \frac{h_{\text{sinc}}}{2}.$$

Insertion of the optimal sampling distance  $\Delta\nu = (2M)^{-1}$  yields

$$\delta\nu = \frac{2h_{\text{sinc}}}{\pi} \Delta\nu$$

which leads to the definition of the resolution factor  $\eta$

$$\eta := \frac{\delta\nu}{\Delta\nu}$$

as quotient of the spectral resolution and the optimal sampling distance. In case of the sinc function the resolution factor is

$$\eta_{\text{sinc}} = \frac{2h_{\text{sinc}}}{\pi} \approx 1.21.$$

The concept of truncation can be generalised, if the boxcar function multiplied with the interferogram is replaced with another function  $A : [-M, M] \rightarrow \mathbb{R}$ , where  $A$  is usually required to be symmetric, i.e.  $A(x) = A(-x) \forall x \in [-M, M]$ . The multiplication of the interferogram with  $A$  is termed apodisation and  $A$  is called apodisation function. Since multiplication in the interferogram domain is equivalent to convolution in the spectral domain, apodisation is equivalent to a convolution of the spectrum with the convolution kernel  $K = \mathcal{F}\{A\}$ . Due to the multitude of different apodisation functions found in literature, it is beyond the scope of this thesis to present a comprehensive overview. Instead only those apodisation functions appearing in the context of this work are going to be discussed briefly in the following paragraphs.

The main incentive to use an apodisation function different from the boxcar function is the latter's discontinuity at the boundary, which causes a relatively slow decay of the associated convolution kernel with increasing distance from the centre peak. In an attempt to remove the discontinuity at the boundary one arrives at the triangle function  $\Lambda_a$

$$\Lambda_a(x) := \begin{cases} 1 - \frac{|x|}{a} & \text{if } |x| \leq a \\ 0 & \text{if } |x| > a \end{cases},$$

which has a squared sinc as Fourier Transform (Kauppinen and Partanen, 2001)

$$\mathcal{F}\{\Lambda_a\} = \frac{1}{a} \text{sinc}_a^2,$$

and resolution factor

$$\eta_{\text{sinc } 2} = \frac{4h_{\text{sinc } 2}}{\pi} \approx 1.77.$$

$h_{\text{sinc } 2}$  is the half width at half maximum (HWHM) of the squared sinc satisfying

$$\sin(h_{\text{sinc } 2}) = \frac{h_{\text{sinc}}}{\sqrt{2}}.$$

Comparing the resolution factors of  $\text{sinc}^2$  and  $\text{sinc}$  it becomes apparent, that resolution has to be sacrificed to force a faster decay of the convolution kernel with increasing distance from the centre peak.

Finally the Gaussian apodisation function is defined as

$$A_G(x) := \begin{cases} \exp\left[-\frac{\pi^2}{4\ln 2}(\delta\nu x)^2\right] & |x| \leq M \\ 0 & |x| > M. \end{cases}$$

This choice is motivated by an infinite Gaussian convolution kernel with FWHM  $\delta\nu$

$$K_{G0}(\nu) = \sqrt{\frac{4\ln 2}{\pi\delta\nu^2}} \exp\left[-4\ln 2\left(\frac{\nu}{\delta\nu}\right)^2\right]$$

which is equivalent to the apodisation function

$$A_{G0}(x) = \exp\left[-\frac{\pi^2}{4\ln 2}(\delta\nu x)^2\right].$$

Since  $A_{G0}$  does not have compact support, it has to be truncated at  $x = \pm M$  in order to be of practical use. Thus  $\delta\nu$  and  $M$  can be chosen independently of each other. It should be taken into account though, that truncation means multiplication with a boxcar function, which results in the modified convolution kernel

$$K_G = K_{G0} * \text{sinc}_{2M},$$

which converges to an ideal  $\text{sinc}$  as  $\delta\nu$  approaches zero. Thus  $M$  has to be chosen large enough for a given resolution  $\delta\nu$ , if the Gaussian shape of the convolution kernel shall be preserved. A measure for an appropriately chosen cut-off  $M$  is the discontinuity  $\epsilon$  of the apodisation function at the truncation point  $M$ :

$$\epsilon := \exp\left[-\frac{\eta_G^2 \pi^2}{16\ln 2}\right],$$

where

$$\eta_G = \frac{\delta\nu}{2M}$$

is the resolution factor of the (infinite) Gaussian apodisation function  $A_{G0}$ . In practice it is advantageous to prescribe a sufficiently small  $\epsilon > 0$  and then choose resolution and cut-off such that

$$\eta_G \geq \frac{4}{\pi} \sqrt{-\ln(2) \ln \epsilon}.$$

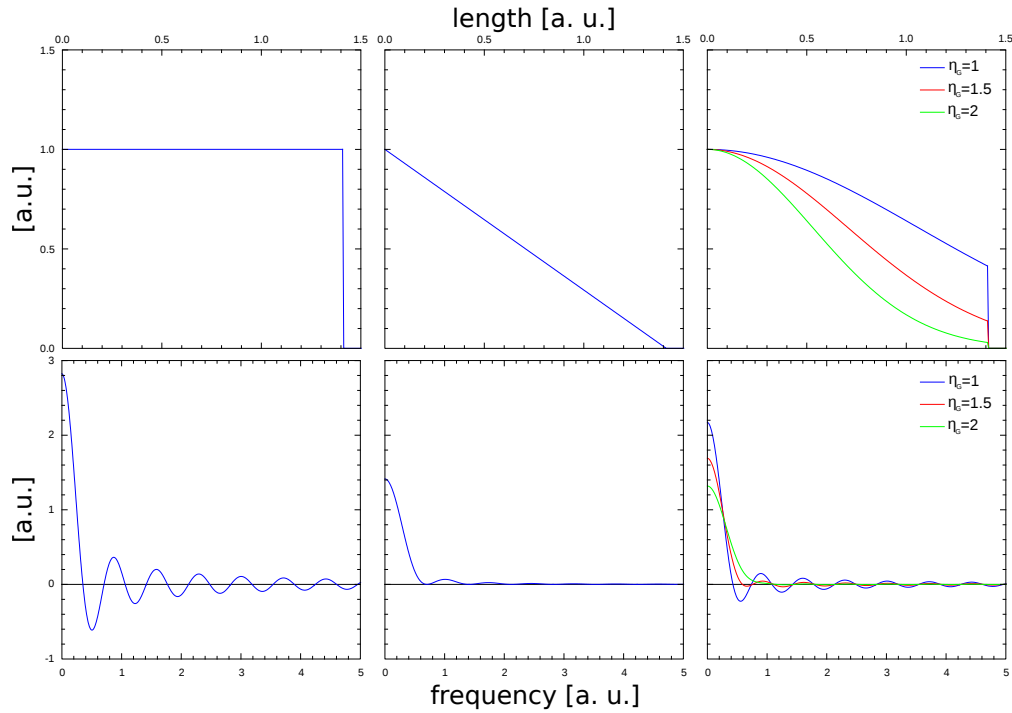


Figure 2.4: Comparison of the rectangle, triangle and gaussian apodisation function (from left to right) for identical MOPD  $M$ . Shown is the apodisation function (top row) with the respective convolution kernel directly below. Since the resolution factor  $\eta_G$  of the Gaussian can be chosen independently of  $M$ , three different values were chosen to visualise its influence. Owing to the axes symmetry of all functions, the plots are restricted to positive ordinate values.

Figure 2.4 provides an overview over the apodisation functions discussed above and their respective convolution kernels. Observe how the discontinuity of the rectangle function causes a slow decay of the associated convolution kernel in the spectral domain. This ringing is drastically reduced when using the triangle function at the cost of a lower spectral resolution (i.e. a larger HWHM of the convolution kernel). As the resolution factor  $\eta_G$  is an additional free parameter for the Gaussian apodisation function, it can be used to select a compromise between spectral resolution and ringing.

## 2.2 The Model 102 $\mu$ FTIR

The D&P Model 102  $\mu$ FTIR is a commercially available off-the-shelf instrument manufactured by Design and Prototypes. Its target customers are mainly geologists, who desire to perform field measurements of land surface and rock samples. Since the instrument was not designed with atmospheric measurements in mind, an extensive characterisation is necessary to ensure the required data quality. This section is dedicated to the verification and –where necessary– amendment of the instrument characterisation provided by Korb et al. (1996) as far as it is relevant for the measurements conducted within the scope of this thesis. The goal is to demonstrate, that the Model 102 is a cost effective alternative for atmospheric measurements if mobility is of paramount importance. Furthermore it will be shown, that radiometric accuracy and spectral resolution, although partly sacrificed for the compact design, are still sufficient to measure the effect of mineral dust aerosols in the atmosphere.

After a brief general description of the instrument in chapter 2.2 the algorithms for data evaluation and post-processing will be introduced. This most notably includes a novel algorithm for radiometric calibration (chapter 2.2.4) and a method for drift correction (chapter 2.2.8), which mitigate the instrument specific bias for measured radiances caused by the compact instrument design. Additionally this section contains a detailed description of all experimental work performed within the work of this thesis including experimental setup and practical execution.

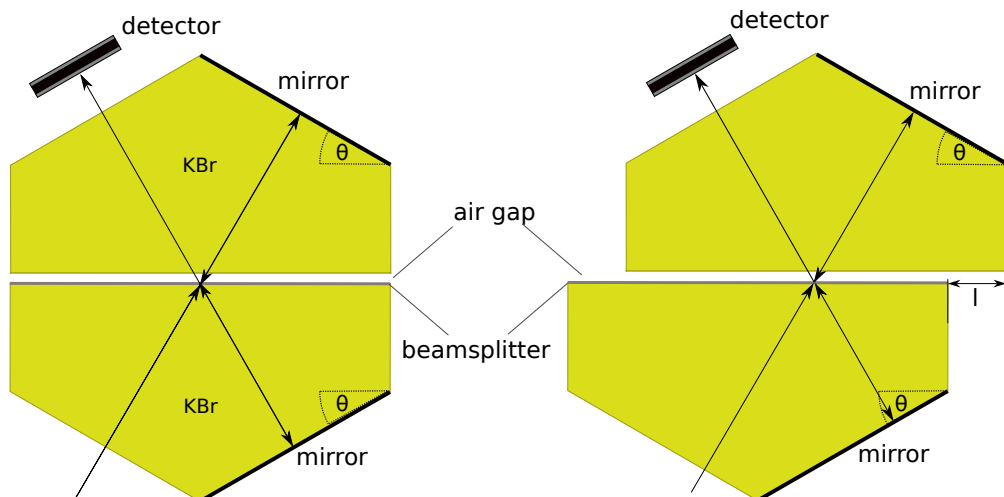


Figure 2.5: Interferometer Core of the D&P Model 102  $\mu$ FTIR



### 2.2.1 General Instrument Description

Figure 2.5 depicts the principle design of the interferometer, which consists of two laterally moving KBr prisms. Beamsplitter and mirrors are coated onto the faces of the prisms thereby minimising the number of adjustable components. The result is a very compact and rugged instrument perfectly suited to withstand the adverse conditions typically encountered in the field. Apart from the robustness against large amounts of dust and sea salt expected during SAMUM-2, portability was another core criterion for the selection of the instrument, since the complete equipment could be conveniently shipped in three small transport boxes. Compared to other benchmark instruments, which typically require one whole sea-freight container, this drastically reduces complexity and costs of campaign logistics. Furthermore the instrument's mobility is increased by its low power consumption, which allows battery based operation for several hours. An additional asset of the instrument is the rotatable fore-optics permitting observations at arbitrary zenith angles.

The radiative flux leaving the interferometer is registered by a sandwich-type indium antimonide (InSb)/ mercury cadmium telluride (MCT) detector covering the spectral range from  $600 - 3000 \text{ cm}^{-1}$  ( $3.33\text{-}16.6 \mu\text{m}$ ). The AC-coupled signals of both detectors are electrically added and digitised by one ADC. This may be a disadvantage, if the interferogram of only one of the detectors is required (e.g. for a non-linearity correction), because a separation of the interferograms by detector may be cumbersome in this case.

A temperature adjustable black body covering temperatures in the range  $3 - 63^\circ\text{C}$  is shipped with the instrument for radiometric calibration. The black body has to be attached to the instrument fore-optics manually, which requires an operator to be present for calibration. Black-body and instrument are operated by a proprietary software installed on the integrated computer system. Each individual measurement consists of a user definable number of up to 100 coadded interferograms (or coadds), which are stored in a single file on the computer's hard drive. Start of each measurement and the selection of the associated output file has to be performed manually by the operator. As a consequence the instrument is not suitable for automated recording of long time series.

From figure 2.5 it is deduced that an increment  $dl$  in relative lateral position leads to an associated optical path difference of  $d\Delta = 2n(\nu) \sin(\theta)dl$ , where  $n(\nu)$  is the refractive index of KBr. Note that the dispersion of KBr causes the optical path difference at fixed displacement to be wavenumber dependent. Furthermore the air gap is similar to an uncompensated beamsplitter substrate because it is located

in only one of the two interferometer arms. As a consequence, the ZPD is not necessarily found at  $l = 0$  and may change slightly with wavenumber.

As discussed in section 2.1.3, the interferogram has to be sampled at equal-spaced optical path differences. The sampling points are found with the help of a frequency stabilised diode laser and a separate detector recording the laser signal emerging from the interferometer. Approximating the laser spectrum  $I_{\text{laser}}$  by a Dirac delta function

$$I_{\text{laser}} = I_{0,\text{laser}}\delta(\nu - \nu_{\text{laser}}) \quad (2.28)$$

the resulting AC voltage at the reference laser detector is obtained from equation 2.14

$$\tilde{U}(x) \sim \cos(2\pi\nu_{\text{laser}}x + \varphi_0) \quad (2.29)$$

under the assumption of negligible background radiation at the laser wavelength.  $x = \Delta(\nu_{\text{laser}})$  is the optical path difference at the laser wavenumber and  $\varphi_0$  is a constant phase shift caused by the complex valued transmission and reflection coefficients. Note that  $\tilde{U}$  is a harmonic signal with period  $\nu_{\text{laser}}^{-1}$ , which can be utilised as trigger to sample the output interferogram on a regular grid with spacing  $\Delta x = \nu_{\text{laser}}^{-1}$ . Neglecting dispersion, equation 2.27 in combination with the reference laser wavelength  $\Delta x = 857 \text{ nm}$  yields the approximate Nyquist wavenumber  $\nu_{\text{max}} \approx 5834 \text{ cm}^{-1}$ .

## 2.2.2 Interferogram Post Processing

Although the proprietary software delivered with the Model 102 FTIR is able to convert the measured interferograms to spectral radiances, the author elected to employ a selection of command-line tools developed by DLR for the Michelson Interferometer with ROTating Retroreflector (MIROR) (Haschberger and Tank, 1993). This so-called MIROR library offers enhanced functionality and finer grained control over the calibration process compared to the D&P software. Furthermore the graphical user interface of the latter is not suitable for batch processing, which makes the calibration of large amounts of data a tedious task.

As described in the previous section, the built-in reference laser diode provides an accurate measure of relative path differences. However, the lack of an obvious origin prevents the determination of absolute distances. A common practise is to construct the required reference point from the recorded interferogram by identifying the origin with the centreburst. It has been discussed in chapter 2.1.2, that this method delivers accurate results for a symmetric, non-dispersive interferometer, although it typically requires re-sampling of the interferogram, since the centreburst

does not lie on the sampling grid, if the zero-crossing of the reference laser signal is used as trigger (which is located at  $\pm\Delta x/2$  for a symmetric interferometer). This method, however, is not suited for dispersive, non-symmetric interferometer set-ups, such as the Model 102, where the wavenumber dependent ZPD causes the centreburst to be found at varying  $x$  values, depending on the spectral distribution of the measured radiation. This makes the centreburst a poor choice for a universal reference point. It is still possible though, to employ it as common origin for coadded interferograms belonging to one measurement, where the individual interferograms are expected to differ little from each other. The determination of the centreburst from a filtered interferogram can yield satisfactory results, if the measured spectra show similarities in a sufficiently large band. This has been demonstrated in an earlier work (Koehler et al., 2009) for atmospheric measurements in the water absorption band between  $1300 - 1600 \text{ cm}^{-1}$ . As a consequence a band-pass filter of  $700 - 3000 \text{ cm}^{-1}$  is applied to reduce spectral noise before the ZPD is set to the centreburst of the interferogram corresponding to the water absorption band. The centreburst is found by sinc-interpolation of the interferogram followed by a shift of the sampling grid such that the ZPD is located on a sampling point. The necessary interpolation is performed with the FFT based method described by Yaroslowsky (2003). The lack of a universally valid reference point is addressed in section 2.2.4, where a modified calibration algorithm capable of re-constructing the origin from arbitrary spectra will be introduced.

During normal operation the Model 102 records an interferogram in each scan direction of the prisms (forward and backward) and stores all interferograms of one measurement into a single file. Unfortunately the scan direction is not stored along with the interferograms, so that it has to be determined during post-processing. An accurate determination of the scan direction is necessary, because spectra with different scan directions differ enough to require an independent calibration of forward and backward spectra. Although the task would seem straightforward, as each forward interferogram should follow a backward interferogram and vice versa, it turns out that interferograms may erroneously be skipped (e.g. if the build-in CPU is under high load). Thus a clustering algorithm is employed, which sorts all interferograms of one measurement into two clusters of similar interferograms, where similarity is determined by the sum squared difference of an individual interferogram from the average of all interferograms in the respective cluster. The scan direction of each cluster is then determined by looking at the average position of the centreburst relative to the first sampling point of the interferogram.

In a final post-processing step all coadds belonging to one measurement are trimmed such that they have a common number of sampling points symmetric with respect to the ZPD. The such obtained discrete interferogram is denoted  $\{\tilde{u}_k\}_{k=-N}^{N-1}$  with

$\tilde{u}_k := \tilde{U}(k\Delta x)$  and  $\tilde{U}$  as defined in equation 2.14. Zeroes are appended to the interferogram as necessary to increase  $2N$  to an integer power of two.

### 2.2.3 Wavenumber Correction

As discussed in section 2.1.3, the truncation of the interferogram  $\tilde{U}$  at MOPD  $\Delta_{\max}$  equals a convolution in the Fourier domain. In combination with equation 2.14 this motivates the definition of the ideal raw spectrum  $s$

$$s(\nu) := 2\Delta_{\max} \operatorname{sinc}(2\Delta_{\max}\nu) * [r(\nu)L(\nu) + g(\nu)]$$

or under the approximation that  $r$  and  $g$  vary only slowly with wavenumber

$$s(\nu) \approx r(\nu)2\Delta_{\max} \operatorname{sinc}(2\Delta_{\max}\nu) * L(\nu) + g(\nu). \quad (2.30)$$

As stated earlier, the optical path difference  $\Delta$  is wavenumber dependent. Furthermore it may be reduced by a finite divergence of the beam inside the interferometer (cf. chapter 6.4 in Kauppinen and Partanen, 2001). To take these effects into account, let  $\phi(\nu) := x^{-1}\Delta(\nu)$ , thereby relating the optical path difference at wavenumber  $\nu$  to the optical path difference  $x$  at the reference laser wavelength. Substitution of  $\Delta$  by  $x\phi$  in equation 2.14 results in the definition of the measured raw spectrum  $\tilde{s}$ :

$$\tilde{s} := \mathcal{F} \{ \Gamma_{2\Delta_{\max}} U(x\phi) \}$$

or equivalently

$$\tilde{s}(\nu) = \int_{-\infty}^{\infty} \int_{-\infty}^{\infty} s(\tilde{\nu}) e^{i2\pi(\tilde{\nu}\phi(\tilde{\nu}) - \nu)x} d\tilde{\nu} dx = \int_{-\infty}^{\infty} s(\tilde{\nu}) \delta(\tilde{\nu}\phi(\tilde{\nu}) - \nu) d\tilde{\nu}. \quad (2.31)$$

Under the assumption that  $\nu\phi(\nu)$  is invertible it is convenient to introduce the effective wavenumber  $\nu_e$  satisfying

$$\nu_e \phi(\nu_e) = \nu.$$

Thus equation 2.31 can be rewritten

$$\tilde{s}(\nu) = \frac{s(\nu_e)}{|\phi(\nu_e) + \nu_e \phi'(\nu_e)|}.$$

Note that the chain rule of the Dirac delta distribution was applied, which states that for an invertible function  $f : \mathbb{R} \rightarrow \mathbb{R}$  with root  $x_0$  and  $f'(x_0) \neq 0$ , the following equation holds

$$\delta(f(x)) = \frac{\delta(x - x_0)}{|f'(x_0)|}.$$

Observe that the reconstructed spectrum  $\tilde{s}$  is scaled and shifted in wavenumber space compared to the original spectrum  $s$ . While  $\nu_e$  could theoretically be inferred from the refractive index of the interferometer components and the aperture angle of the beam inside, it is more convenient to fit a parametrised function to experimental data. For the Model 102 the manufacturer suggests a function of the form

$$\nu_e \approx \nu + \Delta\nu_0 + 10^{\alpha\nu+\beta} \quad (2.32)$$

where the parameters  $\Delta\nu_0$ ,  $\alpha$  and  $\beta$  are provided by D&P for each instrument. Two different methods to derive them from measured spectra are presented in section 2.2.6.

The data processing proceeds as follows: first the discrete interferogram  $\{\tilde{u}_k\}_{k=-N}^{N-1}$  introduced in section 2.2.2 is transformed to wavenumber space by FFT. According to the theory developed in section 2.1.3 this is equivalent to the numerical evaluation of the integral in equation 2.31 and thus results in the complex valued discrete spectrum  $\{\tilde{s}_k\}_{k=0}^N$  with  $\tilde{s}_k = \tilde{s}(k\Delta\nu)$  and  $\Delta\nu := (2N\Delta x)^{-1}$ . Subsequently the effective wavenumber  $\nu_e$  is calculated for each wavenumber  $k\Delta\nu$  using equation 2.32 to obtain the wavenumber corrected raw spectrum. Finally the wavenumber corrected raw spectrum is interpolated onto a regular grid by linear interpolation and the resulting discrete raw spectrum is denoted  $\{s_k\}_{k=0}^N$ .

## 2.2.4 Radiometric Calibration

The goal of radiometric calibration is to convert the wavenumber corrected raw spectrum  $\{s_k\}_{k=0}^N$  into spectral radiances  $\{L_k\}_{k=0}^N$ , where

$$L_k := 2\Delta_{\max} \text{sinc}(2\Delta_{\max}\nu_k) * L(\nu_k).$$

Solving equation 2.30 for the radiance obviously yields

$$L_k = \frac{s_k - g_k}{r_k}$$

with discrete response  $r_k := r(\nu_k)$  and offset  $g_k := g(\nu_k)$ . This result allows the conversion of an arbitrary measured raw spectrum  $s$  to calibrated radiances, provided instrument response and offset are known. Thus radiometric calibration mainly includes the calculation of the quantities  $r_k$  and  $g_k$ . For two ideal blackbodies  $B_1$  and  $B_2$  with temperatures  $T_1$  and  $T_2$ , respectively, the emitted radiance is given by Planck's Law

$$B_\alpha(\nu) := L(T_\alpha, \nu) = 2hc^2\nu^3 \left[ \exp\left(\frac{hc\nu}{k_B T_\alpha}\right) - 1 \right]^{-1}, \quad \alpha = 1, 2$$

Insertion of  $B_{\alpha k} := B_{\alpha}(\nu_k)$  for the radiance into equation 2.30 results in the following expression for the measured raw spectrum  $\{s_{\alpha k}\}_{k=0}^N$  of the ideal black body  $B_{\alpha}$ :

$$s_{\alpha k} = r_k B_{\alpha k} + g_k. \quad (2.33)$$

This is a system of  $2(N + 1)$  equations for  $2(N + 1)$  unknowns, which uniquely determines the coefficients  $r_k$  and  $g_k$ :

$$r_k = \frac{s_{1k} - s_{2k}}{B_{1k} - B_{2k}} \quad (2.34)$$

$$g_k = \frac{s_{2k} B_{1k} - s_{1k} B_{2k}}{B_{1k} - B_{2k}}. \quad (2.35)$$

If measurements of black bodies at more than two temperatures are available, then the system of equations becomes overdetermined and the additional information can be employed to reduce errors in the calibration parameters. Lindermeir (1994) demonstrates, how black body measurements at three different temperatures can lead to a notable reduction in calibration uncertainties, if the additional information is used to fit the black body temperatures. The remainder of this section describes a modification of this algorithm capable of overcoming the difficulties associated with the lack of a universal reference point for the path difference discussed previously in section 2.2.2.

Assume a set of  $M > 2$  black body measurements sampled at  $N$  spectral points each. For any two complex valued vectors  $\mathbf{a}, \mathbf{b} \in \mathbb{C}^M$  and a real valued diagonal weighting matrix  $\mathbf{W} \in \mathbb{R}^{M \times M}$ , the scalar product  $\langle \cdot, \cdot \rangle_W : \mathbb{C}^M \rightarrow \mathbb{C}$  defined as

$$\langle \mathbf{a}, \mathbf{b} \rangle_W \mapsto \sum_{\alpha=1}^M \sum_{\beta=1}^M a_{\alpha}^* W_{\alpha\beta} b_{\beta}$$

induces the norm  $\|\cdot\|_W : \mathbb{C}^M \rightarrow \mathbb{R}$ ,  $\mathbf{a} \mapsto \sqrt{\langle \mathbf{a}, \mathbf{a} \rangle_W}$ . As before the measured black body radiances are written as  $\mathbf{B}_k \in \mathbb{R}^M$ ,  $\mathbf{B}_k := (B_{1k}, B_{2k}, \dots, B_{Mk})^T$  and  $\mathbf{s}_k \in \mathbb{C}^M$ ,  $\mathbf{s}_k := (s_{1k}, s_{2k}, \dots, s_{Mk})^T$  are the associated measured raw spectra. Furthermore let  $\boldsymbol{\mu}_k \in \mathbb{R}^M$

$$\boldsymbol{\mu}_k := [\text{Tr } \mathbf{W}(\nu_k)]^{-1} (1, 1, \dots, 1)^T,$$

which allows to express the weighted average over the components of any vector  $\mathbf{a} \in \mathbb{C}^M$  by  $\langle \boldsymbol{\mu}_k, \mathbf{a} \rangle_W$ . Note that the weighting matrix  $W(\nu)$  may depend on

wavenumber, although this dependence is omitted when  $W$  is used as an index to keep the notation simple. Introducing

$$\begin{aligned}\mathbf{x}_k &:= \mathbf{B}_k - \langle \boldsymbol{\mu}_k, \mathbf{B}_k \rangle_W \text{Tr } \mathbf{W}(\nu_k) \boldsymbol{\mu}_k \\ \mathbf{y}_k &:= \mathbf{s}_k - \langle \boldsymbol{\mu}_k, \mathbf{s}_k \rangle_W \text{Tr } \mathbf{W}(\nu_k) \boldsymbol{\mu}_k\end{aligned}$$

which obviously satisfy  $\langle \boldsymbol{\mu}_k, \mathbf{x}_k \rangle_W = \langle \boldsymbol{\mu}_k, \mathbf{y}_k \rangle_W = 0$  for all wavenumbers  $\nu_k$ , ( $k = 1 \dots N$ ), the calibration equation 2.33 can be expressed in the simple form

$$\mathbf{y}_k = r_k \mathbf{x}_k. \quad (2.36)$$

Note that this equation does not contain the offset  $g$ , which may be obtained after averaging 2.33 over all measurements:

$$g_k = \langle \boldsymbol{\mu}_k, \mathbf{s}_k \rangle_W - \frac{\langle \boldsymbol{\mu}_k, \mathbf{B}_k \rangle_W}{r_k}.$$

Requiring the solution  $r$  to satisfy equation 2.36 in a least squares sense, the remaining task is to minimise the so-called cost function  $\Phi : \mathbb{R}^N \rightarrow \mathbb{R}$ ,

$$\Phi = \sum_{k=1}^N F_k^2,$$

where  $\mathbf{F} : \mathbb{R}^n \rightarrow \mathbb{R}^N$  maps the vector  $\mathbf{X} \in \mathbb{R}^n$ ,  $\mathbf{X} := (X_1, \dots, X_n)^T$  of fit parameters to the residual  $\mathbf{F} := (F_1, F_2, \dots, F_N)^T$ ,

$$F_k := \|\mathbf{y}_k - r_k \mathbf{x}_k\|_W.$$

The minimisation can be performed numerically using e.g. the improved Levenberg-Marquardt algorithm described by Moré (1978), which has been chosen throughout this study unless stated otherwise.

The theory presented up to this point is a formalisation of the work of Lindermeir (1994), who proceeds by choosing the fit parameters  $X_\alpha = T_\alpha$  ( $\alpha = 1 \dots M$ ) to be the temperatures of the black bodies and  $X_{M+k} = r_k$  ( $k = 1 \dots N$ ) to be the calibration constants, resulting in a total of  $n = M + N$  fit parameters. In the following, a refinement of this algorithm will be presented, which allows to fit the unknown position of the ZPD. The basic idea underlying the new algorithm is to take the linear dependence of  $F_k$  on  $r_k$  into account. This allows to minimise each  $F_k^2$  individually using linear regression for  $k = 1 \dots N$  (Bronstein et al., 2001):

$$X_{M+k} = r_k = \frac{\langle \mathbf{x}_k, \mathbf{y}_k \rangle_W}{\langle \mathbf{x}_k, \mathbf{x}_k \rangle_W}.$$

Thus  $X_{M+k}$ ,  $k = 1 \dots N$  are eliminated from the fit vector  $\mathbf{X}$  and only the non-linear parameters remain to be fitted. The weighting matrix  $W(\nu_k)$  is chosen to contain the uncertainty  $\sigma_\alpha(\nu_k)$  of the measured raw spectra

$$W_{\alpha\beta}(\nu_k) = \frac{1}{\sigma_\alpha(\nu_k)} \delta_{\alpha\beta}.$$

The uncertainty is defined as the sample standard deviation over all coadded spectra  $s^{(i)}$  included in the average raw spectrum:

$$\sigma_\alpha(\nu_k) = \frac{1}{\sqrt{N_{\text{coadds}} - 1}} \sqrt{\sum_{i=1}^{N_{\text{coadds}}} \left( s_{\alpha k}^{(i)} - s_{\alpha k} \right)^2}$$

Apart from the cost function  $\Phi$ , the Levenberg-Marquardt algorithm requires the Jacobian  $\nabla \mathbf{F}$  of  $\mathbf{F}$ ,

$$(\nabla \mathbf{F})_{kj} := \frac{\partial F_k}{\partial X_j}.$$

Using

$$\nabla \langle \mathbf{x}_k, \mathbf{y}_k \rangle_W = \nabla \mathbf{x}_k^\dagger \cdot \mathbf{W}(\nu_k) \cdot \mathbf{y}_k + \mathbf{x}_k^\dagger \cdot \mathbf{W}(\nu_k) \cdot \nabla \mathbf{y}_k$$

and

$$\begin{aligned} \nabla \mathbf{x}_k &= \left( \mathbf{1} - \text{Tr}(\mathbf{W}(\nu_k)) \boldsymbol{\mu}_k \otimes \boldsymbol{\mu}_k^\dagger \cdot \mathbf{W} \right) \cdot \nabla \mathbf{B}_k \\ \nabla \mathbf{y}_k &= \left( \mathbf{1} - \text{Tr}(\mathbf{W}(\nu_k)) \boldsymbol{\mu}_k \otimes \boldsymbol{\mu}_k^\dagger \cdot \mathbf{W} \right) \cdot \nabla \mathbf{s}_k, \end{aligned}$$

where  $\otimes$  is the dyadic product and  $^\dagger$  symbolises the conjugate transpose, the  $k$ -th row of the Jacobian can be calculated from

$$\nabla F_k = \frac{1}{F_k} \Re \left\{ \left( \nabla \mathbf{s}_k^\dagger - r_k^* \nabla \mathbf{B}_k^\dagger \right) \cdot \mathbf{W}(\nu_k) \cdot \left( \mathbf{y}_k - r_k \mathbf{x}_k \right) \right\}.$$

As mentioned before, it is intended to employ the additional information provided by an extra black body measurement to remedy the lack of precision in ZPD localisation. To do so, assume that the inverse Fourier Transformation of the interferogram was performed with respect to an origin shifted by an arbitrary fraction  $p$  of one sampling interval, i.e.  $x \rightarrow x + p\Delta x$ . The shift theorem of the Fourier Transform (Kauppinen and Partanen, 2001) applied to equation 2.31 then yields the distorted spectrum

$$\tilde{s}^p(\nu) := \tilde{s}(\nu) e^{-i2\pi p\nu\Delta x}$$



and the wavenumber corrected raw spectrum becomes

$$s_{\alpha k} = s_{\alpha}^p(\nu_k) \exp [i2\pi p_{\alpha} \nu_k \phi(\nu_k) \Delta x].$$

The uncorrected wavenumber  $\nu\phi(\nu)$  is obtained from numerical inversion of equation 2.32.

Choosing  $X_{\alpha} = p_{\alpha}$  for  $\alpha = 1 \dots M$  obviously enables fitting displacements instead of temperatures. Although it is tempting to fit the black body temperatures as well, it should be taken into account, that the temperatures must be sufficiently far apart for the fit to be stable. If this is not the case, the variation of the Planck function with temperature is sufficiently linear to be compensated by the instrument response  $r_k$ , thereby destabilising the fit. Since the calibration temperatures selected within the scope of this work are typically no more than 10 K apart, the fitted quantities are restricted to the interferogram displacements  $p_{\alpha}$ . Since the parameters  $p_{\alpha}$  describe the relative shift between two interferograms, the calibration is invariant under a common shift of all ZPDs by the same amount. Thus an arbitrary offset  $p_0$  can be added to each  $p_{\alpha}$  without altering the calibrated radiances. As a consequence the displacement  $p_M$  of the black body with highest temperature is constrained to zero without loss of generality resulting in a total of  $M - 1$  fit parameters for  $M$  black body measurements.

After the calibration constants  $r_k$  and  $g_k$  have been determined from the fit, any given raw spectrum  $s$ , can be calibrated, provided its ZPD shift with respect to the reference black body (of highest temperature) is zero. As this is generally not the case, an unknown shift  $p$  is assumed for the uncalibrated raw spectrum. Since the radiance  $L$  is a measurable physical quantity and thus constrained to the domain of real numbers, the shift  $p$  can be determined by minimisation of the imaginary part of the calibrated radiance. As before the minimisation is performed using the Levenberg-Marquardt algorithm with cost function  $\tilde{\Phi} : \mathbb{R}^N \rightarrow \mathbb{R}$ ,

$$\tilde{\Phi} = \sum_{k=1}^N \tilde{F}_k^2,$$

where the components of  $\tilde{\mathbf{F}} : \mathbb{R} \rightarrow \mathbb{R}^N$ ,  $\tilde{\mathbf{F}} := (\tilde{F}_1, \tilde{F}_2, \dots, \tilde{F}_N)^T$ , are defined in terms of the imaginary part of the calibrated radiance weighted by its uncertainty:

$$\tilde{F}_k := \Im \left\{ \frac{r_k}{\sigma(\nu_k)} \right\} \Im \left\{ \frac{s_k^p - g_k}{r_k} \right\}.$$

### 2.2.5 Uncertainty Estimation for the Calibrated Radiances

This section discusses the different sources of uncertainty affecting the calibrated radiances and estimates their respective contribution to the total error budget. As the ZPD positions are known after radiometric calibration, the uncertainties are derived from the simple equations (2.34, 2.35) for two calibration sources ignoring all but the hottest and coldest black body measurement.

Insertion of the afore mentioned equations into the calibration equation 2.30 yields

$$L = \frac{B_1 - B_2}{s_1 - s_2} s - \frac{s_2 B_1 - s_1 B_2}{s_1 - s_2},$$

where the explicit wavenumber dependence has been omitted to keep the notation concise. Furthermore the shift factor  $p$  is assumed to be identical for the spectra  $s_1$ ,  $s_2$  and  $s$ . As suggested by the Joint Committee for Guides in Metrology (2008), the total uncertainty  $\sigma_L$  of the radiance is calculated in terms of the uncertainties  $\sigma_i$  of the individual input quantities  $q_i$  by Gaussian error propagation:

$$\sigma_L = \sqrt{\sum_{i=1}^N \left( \frac{\partial L}{\partial q_i} \right)^2 \sigma_i^2 + 2 \sum_{i=1}^{N-1} \sum_{j=i+1}^N \frac{\partial L}{\partial q_i} \frac{\partial L}{\partial q_j} \Sigma_{ij}} \quad (2.37)$$

with covariance  $\Sigma_{ij}$  of the quantities  $q_i$  and  $q_j$ . The covariance vanishes if the associated quantities  $q_i$  and  $q_j$  are uncorrelated.

In particular the following quantities influence the overall uncertainty of the calibrated radiance: the measured black body temperatures  $T_1$  and  $T_2$ , the corrected wavenumber  $\nu$  and the measured raw spectra  $s_1$ ,  $s_2$  and  $s$ . The partial derivatives of the radiance with respect to these quantities are obtained by straight forward calculation:

$$\begin{aligned} \frac{\partial L}{\partial T_1} &= \frac{L - B_2}{B_1 - B_2} \frac{\partial B_1}{\partial T_1} \\ \frac{\partial L}{\partial T_2} &= \frac{B_1 - L}{B_1 - B_2} \frac{\partial B_2}{\partial T_2} \\ \frac{\partial L}{\partial \nu} &= \frac{L - B_2}{B_1 - B_2} \frac{\partial B_1}{\partial \nu} + \frac{B_1 - L}{B_1 - B_2} \frac{\partial B_2}{\partial \nu} \\ \frac{\partial L}{\partial s_1} &= \frac{B_2 - L}{B_1 - B_2} r^{-1} \\ \frac{\partial L}{\partial s_2} &= \frac{L - B_1}{B_1 - B_2} r^{-1} \\ \frac{\partial L}{\partial s} &= r^{-1} \end{aligned}$$

Note that the derivatives by  $s_1$ ,  $s_2$  and  $s$  may be complex valued, resulting in complex valued uncertainties, although the radiance  $L$  is a measurable physical quantity and must be real valued. As complex calculus is employed to calculate the radiance however, it may be interpreted as complex quantity with the constraint, that the associated imaginary part vanishes within the measurement uncertainty. Thus a complex valued uncertainty is well justified here.

Since equation 2.37 is limited to real quantities, it has to be generalised to the complex domain. Interpreting the complex plane as two dimensional real space, any complex number  $z = x_1 + ix_2$  can be mapped to a two dimensional real vector  $\mathbf{x} := (x_1, x_2)$ . Similarly a complex function  $f : \mathbb{C} \rightarrow \mathbb{C}$ ,  $f(z) \mapsto f_1(x_1, x_2) + if_2(x_1, x_2)$  constitutes a real vector with components  $f_1, f_2 : \mathbb{R}^2 \rightarrow \mathbb{R}$ . The uncertainty  $\sigma_f \in \mathbb{R}^2$  of  $\mathbf{f}$  can then be expressed in terms of the uncertainty  $\sigma := (\sigma_1, \sigma_2)$  of  $\mathbf{x}$  by

$$\sigma_f := \begin{pmatrix} \sqrt{\left(\frac{\partial f_1}{\partial x_1}\right)^2 \sigma_1^2 + \left(\frac{\partial f_1}{\partial x_2}\right)^2 \sigma_2^2} \\ \sqrt{\left(\frac{\partial f_2}{\partial x_1}\right)^2 \sigma_1^2 + \left(\frac{\partial f_2}{\partial x_2}\right)^2 \sigma_2^2} \end{pmatrix}$$

if real and imaginary part of  $z$  are uncorrelated. Taking into account that all functions appearing in the calibration are holomorphic, the Cauchy-Riemann differential equations must hold:

$$\begin{aligned} \Re \frac{df}{dz} &= \frac{\partial f_1}{\partial x_1} = \frac{\partial f_2}{\partial x_2} \\ \Im \frac{df}{dz} &= \frac{\partial f_2}{\partial x_1} = -\frac{\partial f_1}{\partial x_2}. \end{aligned}$$

Thus the complex uncertainty can be written as

$$\sigma_f = \sqrt{\partial f_1^2 \sigma_1^2 + \partial f_2^2 \sigma_2^2} + i \sqrt{\partial f_2^2 \sigma_1^2 + \partial f_1^2 \sigma_2^2}, \quad (2.38)$$

where the complex derivative

$$\partial f := \partial f_1 + i \partial f_2 := \frac{\partial f}{\partial z}$$

has been introduced.

Note that real and complex part of the function  $f$  must be uncorrelated for the above derivations to hold. Since this constraint is not obviously fulfilled, the correlation of real and imaginary part must be calculated. Assume a time averaged interferogram  $\langle I(x) \rangle_t$  with time-dependent noise  $\delta I(x, t)$ , i.e.

$$I(x, t) = \langle I(x) \rangle_t + \delta I(x, t).$$

The noise  $\delta I(x, t)$  is characterised by its mean

$$\langle \delta I(x, t) \rangle_t = 0$$

and covariance

$$\langle \delta I(x, t) \delta I(x', t') \rangle_t = \sigma^2 \delta(x - x') \delta(t - t').$$

As before the raw spectrum  $s(\nu, t)$  is obtained as Fourier Transform of the interferogram

$$s(\nu, t) = \int_{-\infty}^{\infty} A(x) I(x, t) e^{-i2\pi\nu x} dx$$

with an arbitrary real symmetric apodisation function  $A$ . The mean spectrum is defined as

$$\langle s(\nu) \rangle_t = \left\langle \int_{-\infty}^{\infty} A(x) I(x, t) e^{-i2\pi\nu x} dx \right\rangle_t = \int_{-\infty}^{\infty} A(x) \langle I(x) \rangle_t e^{-i2\pi\nu x} dx$$

and the correlation of real and imaginary part is obtained from

$$\begin{aligned} & \langle \Re \{s(\nu, t) - \langle s(\nu) \rangle_t\} \Im \{s(\nu', t') - \langle s(\nu') \rangle_{t'}\} \rangle_t \\ &= -i \frac{\sigma^2}{4} \delta(t - t') \int_{-\infty}^{\infty} \int_{-\infty}^{\infty} A(x) A(y) \left( e^{i2\pi\nu x} + e^{-i2\pi\nu x} \right) \left( e^{i2\pi\nu' y} - e^{-i2\pi\nu' y} \right) \delta(x - y) dx dy \\ &= -i \frac{\sigma^2}{4} \delta(t - t') \int_{-\infty}^{\infty} (A^2(x) - A^2(-x)) \left( e^{i2\pi(\nu+\nu')x} + e^{i2\pi(\nu-\nu')x} \right) dx = 0. \end{aligned}$$

In other words, real and imaginary part of the raw spectrum are not correlated and equation 2.38 applies.

## 2.2.6 Wavenumber Accuracy

As discussed in detail in section 2.2.3, the wavenumbers  $\nu$  measured with the D&P Model 102 FTIR are shifted compared to the effective values  $\nu_e$  due to dispersion of the interferometer components. This section describes two different methods used for wavenumber correction and compares the results to benchmark measurements performed with a high-precision FTIR for validation. In principle the wavenumber correction requires a benchmark object with distinct spectral features at well-known positions in wavenumber space, e.g. a transparent solid with

absorption features measured by a highly precise instrument. A comparison of the individual spectral features obtained from a measurement with the respective literature values then yields the spectral shift  $\nu_e - \nu$  for a discrete set of wavenumbers. Using a suitable interpolation technique, the shift can be computed at an arbitrary wavenumber between the measured nodes.

Within the scope of this thesis a transmission spectrum of Polystyrol and a measurement of downwelling atmospheric radiances were used as reference spectra. Polystyrol was chosen, since it has a number of very well known absorption bands and is beyond that easy to handle and comparatively cheap. However, since the number of peaks is relatively small, these measurements were amended with atmospheric measurements displaying a larger number of distinct absorption features, which are also well characterised due to a multitude of different laboratory studies. It has to be taken into account though, that the atmospheric measurements require a radiative transfer tool, since the observed radiance spectrum depends on the atmospheric state (e.g. vertical profiles of temperature, pressure and gas concentration). As a consequence this procedure is less direct and introduces additional uncertainties due to the larger number of input quantities.

Figure 2.6 depicts a sketch of the experimental set-up for the Polystyrol transmission measurements. The D&P Model 102 is aligned such that it views the black body through a frame holding the removable Polystyrol film. Four spectra of the black body are recorded at two different temperatures  $T_1$  and  $T_2$ , such that one measurement with and without foil is obtained per temperature. Designating the resulting spectra by  $s_i^+$  and  $s_i^-$  for measurements at temperature  $T_i$  with and without foil, respectively, the transmission  $T$  can be calculated from the following formula:

$$T(\nu) = \frac{s_2^+(\nu) - s_1^+(\nu)}{s_2^-(\nu) - s_1^-(\nu)}.$$

Note that no radiometric calibration is required, because instrument response  $r$  and background  $g$  (needed for a conversion to radiances) cancel out in the expression above. The reference measurement of the Polystyrol transmission was performed with a Bruker IFS 120 HR (Birk, personal communication).

The atmospheric measurements used for wavenumber correction were selected from the measurements conducted within the scope of SAMUM-2 in pristine conditions (i.e. negligible aerosol content and no clouds). A detailed description of these measurements is presented in chapter 2.4. The reference spectra were obtained using the PIRATES software package introduced in chapter 3 based on radiosonde observations performed during SAMUM-2. Detailed information on the ingestion of the radiosonde data into the model can be found in chapter 4.1.

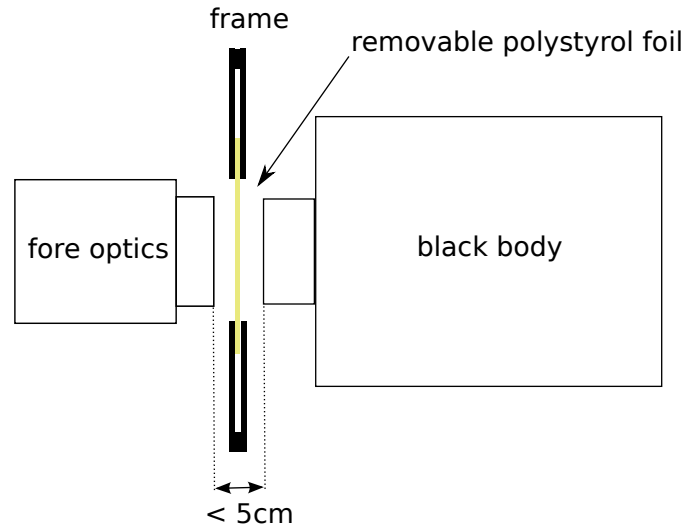


Figure 2.6: Experimental setup for transmission measurements with the D&P Model 102 FTIR

To validate the desired quality of the wavenumber correction for the intended atmospheric measurements, downwelling radiance measurements conducted with the D&P Model 102 FTIR are compared to coincident observations of the Marine Atmospheric Emitted Radiance Interferometer (MAERI) (Minnett et al., 2001). A more detailed report on these measurements follows in section 2.2.11. Since the MAERI interferometer and calibration sources are identical to those of the AERI, which according to Knuteson et al. (2004) has an estimated wavenumber accuracy of  $\Delta\nu \leq 0.01 \text{ cm}^{-1}$  over the entire recorded spectrum, the MAERI can be safely regarded as reference instrument for this comparison.

Figure 2.7 summarises the wavenumber correction process: Polystyrol transmission (blue, bottom left) and downwelling atmospheric radiance (blue, top left) are compared to their respective reference spectra (red) to obtain the wavenumber shift  $\nu_e - \nu$  at a set of discrete wavenumbers. The resulting data-set is shown in the diagram on the right hand side, where blue crosses symbolise data points derived from the atmospheric measurement and red crosses indicate data points obtained from the Polystyrol transmission measurements. Assuming the parametrised functional relationship proposed by the manufacturer (equation 2.32), an optimal choice of the parameters  $\alpha$ ,  $\beta$  and  $\nu_0$  can be made, by minimising the sum of squared deviations of the parametrised model from the measured data points. The resulting curve (continuous black) is shown along with the default wavenumber correction provided by D&P (dotted black). The latter seems to consistently underestimate the measured wavenumber shift, leading to rather substantial deviations beyond

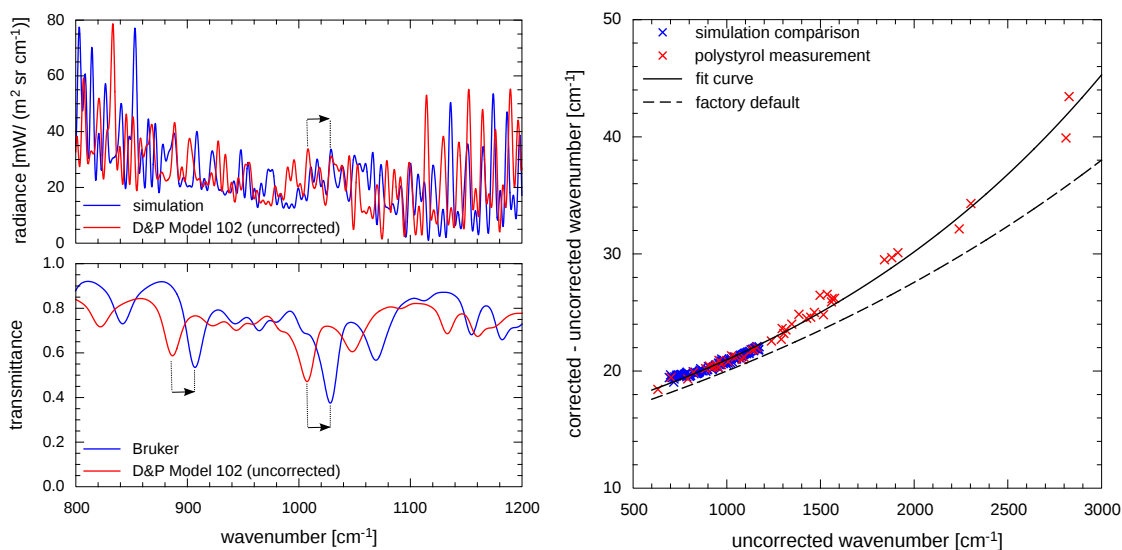


Figure 2.7: Wavenumber correction procedure: Peaks and troughs of reference spectra are compared to measured spectra (left). The differences between measurement and reference allow to fit an analytical correction function (right).

$2000\text{ cm}^{-1}$ . Note that the data points obtained from atmospheric measurements are so close in wavenumber space, that it is actually possible to use linear interpolation between neighbouring nodes instead of the empirically chosen functional relationship proposed by the manufacturer. This method could provide an advantage if the actual wavenumber shift deviates from the simple empirical model in a repeatable fashion.

In order to choose the optimal wavenumber correction method for the intended application, downwelling atmospheric radiance measurements conducted with the D&P Model 102 FTIR are compared to coincident observations of the MAERI (Minnett et al., 2001). The validation measurements were recorded on 14 May 2009 during clear-sky conditions and are described in detail in section 2.2.11. Thus only the core characteristics of the MAERI concerning wavenumber accuracy are mentioned here. The MAERI interferometer and calibration sources are identical to those of the AERI, which according to Knuteson et al. (2004) has an estimated wavenumber accuracy of  $\Delta\nu \leq 0.01\text{ cm}^{-1}$  at a theoretical maximum resolution (inverse MOPD) of  $M^{-1} = 1\text{ cm}^{-1}$  over the entire recorded spectrum. This is sufficiently accurate to regard the MAERI as reference for the following validation. In the following comparison “factory default” designates the wavenumber correction shipped with the instrument, “linear interpolation” means linear interpolation of the wavenumber shift derived from measured atmospheric and Polystyrol transmission and the fit of the empirical model (equation 2.32) to the same data is

referred to as “empirical model”.

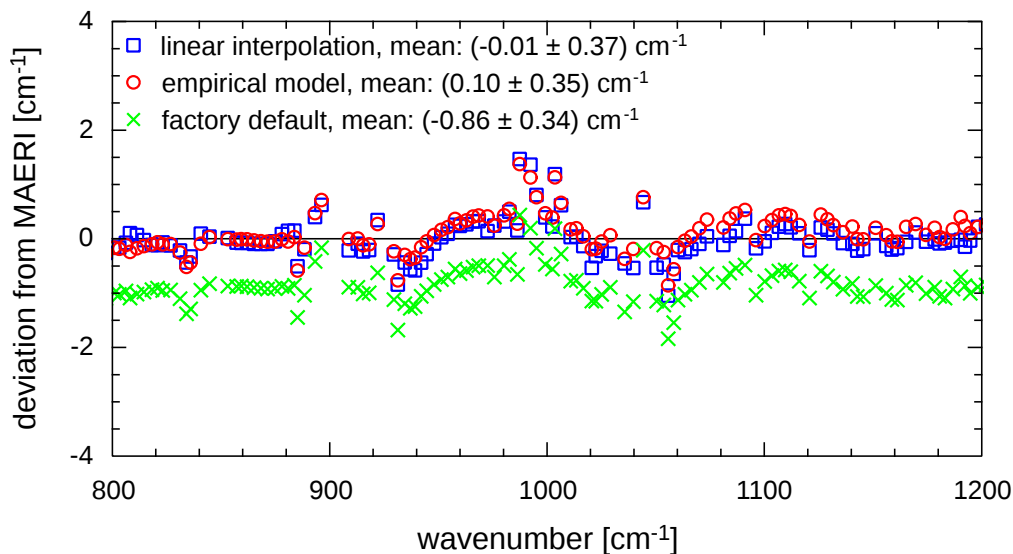


Figure 2.8: Comparison of the default wavenumber correction (green crosses) versus measured data with linear interpolation (blue boxes) and fitted empirical model (red circles). Numbers in brackets indicate mean and standard deviation of the respective dataset.

For the validation, the interferograms measured with the D&P instrument are calibrated using each of the three wavenumber correction methods described above. Then a number of distinct atmospheric features visible in all spectra is selected and the position in wavenumber space of each such feature is determined for the Model 102 and MAERI spectra. Figure 2.8 shows the resulting deviation from the MAERI reference wavenumber at a discrete set of positions. As before, the wavenumbers obtained with the factory default correction are on average  $0.86 \text{ cm}^{-1}$  too small. The wavenumbers obtained with both linear interpolation and empirical model perform much better and display no bias within their respective estimated uncertainties. Both methods indicate an approximate wavenumber uncertainty of  $\sigma_\nu = 0.4 \text{ cm}^{-1}$ . Although the mean deviation of the linear interpolation is one order of magnitude smaller than that of the empirical model, both values are zero within their respective uncertainties. Thus none of the two methods can be preferred over the other. Since a choice has to be made, the linear interpolation is applied for the rest of this thesis. It is noteworthy to observe that the wavenumber uncertainty of  $\sigma_\nu = 0.4 \text{ cm}^{-1}$  equals 8% of the maximum theoretical resolution  $M^{-1} \approx 5 \text{ cm}^{-1}$  for the D&P Model 102 FTIR. Although this value seems comparatively large compared to the 1% for the MAERI, it is actually quite good taking into account that the dispersive interferometer core of the D&P causes by design much greater



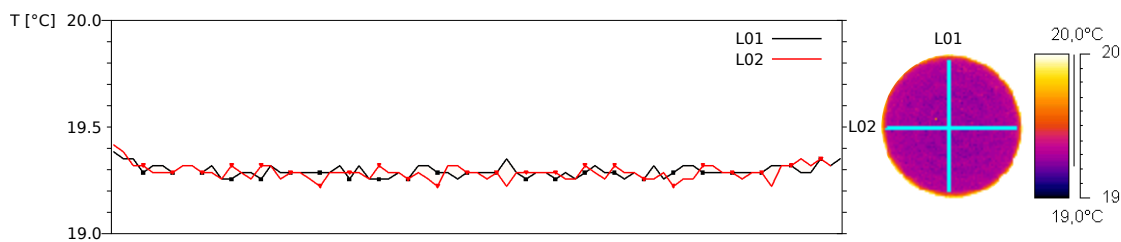


Figure 2.9: Infrared image of the black body taken with an infrared camera (left) along with resulting temperature profiles evaluated over the turquoise lines drawn in horizontal (red) and vertical (black) direction over the black body surface.

wavenumber shifts than a non-dispersive interferometer such as the MAERI.

## 2.2.7 Calibration Source

One accessory shipped with the D&P Model 102  $\mu$ FTIR is a temperature controlled black body built around a circular grooved emitting surface with a diameter of 2 cm, which is coated with an infrared black finish. Its emissivity is specified to be greater than 0.99 and its temperature is electronically controlled by a thermoelectric cooler mounted to the backside. A 100  $\Omega$  platinum resistive thermometer (Pt 100) located below the black body surface monitors the temperature at all times and serves as input to a control loop stabilising the black body at any user-defined setpoint in the range 3 – 80°C with a manufacturer specified accuracy of 0.1 K.

The properties of the calibration source are of vital importance for radiance measurements, since the radiation emitted by the latter couples the raw digital numbers measured by the instrument to standardised physical quantities. The quality of a black body is mainly expressed in terms of its absolute temperature accuracy, its emissivity, its stability, and its homogeneity over the emitting surface. These quantities are assessed in the laboratory to ensure their compliance with the specifications provided by the manufacturer.

For the purpose of these measurements, the black body is mounted facing upwards with power supplied by the FTIR instrument. A FLIR Merlin infrared camera is installed above the black body at a distance of 0.6 meters and a handheld pyrometer is used as an additional reference for the absolute temperature. Although the camera is limited to the wavenumber interval 2000 – 3333  $\text{cm}^{-1}$  and thus does not cover the whole spectral range of the FTIR, it may still be used to detect inhomogeneities of the black body surface. Figure 2.9 displays a picture of the black

body taken by the infrared camera (right) along with a plot of the temperatures along the turquoise lines evaluated using the software package included with the camera. The temperatures are corrected for atmospheric effects, assuming an ambient temperature of 23°C and an atmospheric transmission of 0.97. Obviously the black body surface is homogeneous within the relative uncertainty of the camera specified as 0.1 K by FLIR.

Furthermore the same experimental setup and equipment described above is employed to monitor the temperature stability of the black body and the time it requires to equilibrate after selection of a new setpoint. The main conclusion drawn from these measurements is, that the black body surface reaches thermal equilibrium with the internal temperature sensor almost instantaneously. Hence the black body temperature displayed by the D&P software gives good indication whether the calibration source has reached thermal equilibrium or not. It could be occasionally observed however, that the temperature seemed to have reached the set-point and then changed about 0.1 K approximately 15 – 30 seconds later. This effect –likely caused by the internal temperature control loop– can be easily counteracted by waiting another 30 seconds after the temperature has stabilised. The maximum time span observed for the black body to re-equilibrate (cooling from 80°C to 5°C) is 4.5 minutes. No discernible drift in black body temperature is observed within the scope of these investigations for up to 20 minutes.

In an attempt to verify the absolute temperature accuracy of the calibration source, the emitted radiation is measured with the calibrated IR camera and a pyrometer (*IMPAC IN 15 plus*) at different temperature setpoints. In contrast to the IR camera, which measures the spectral interval 3000 – 3333 cm<sup>-1</sup>, the pyrometer operates in the spectral interval 720 – 1250 cm<sup>-1</sup>. The pyrometer measurements have to be performed with a lens attached to the fore optics to limit the field of view to the black body surface. The transmission of the lens is assumed to be unity for this survey as is the black body emissivity. Figure 2.10 depicts the resulting black body temperature obtained from the internal temperature sensor (abscissa) and the difference between pyrometer/ IR camera measurement and internal sensor reading (ordinate). The deviations of the individual measurements from each other are remarkable: Although the IR camera has a specified accuracy of 2 K and thus agrees with the internal Pt 100 temperature measurements within this error, it produces a considerable drift over the measured temperature range. The pyrometer, on the other hand, does not indicate a similar drift, but seems to be biased towards lower values compared to the internal Pt 100. Again the measurements agree within the specified error of 1 K, but due to the fact that the differences between all temperature readings are fairly large compared to the accuracy of the internal temperature sensor, it is not possible to conclude upon

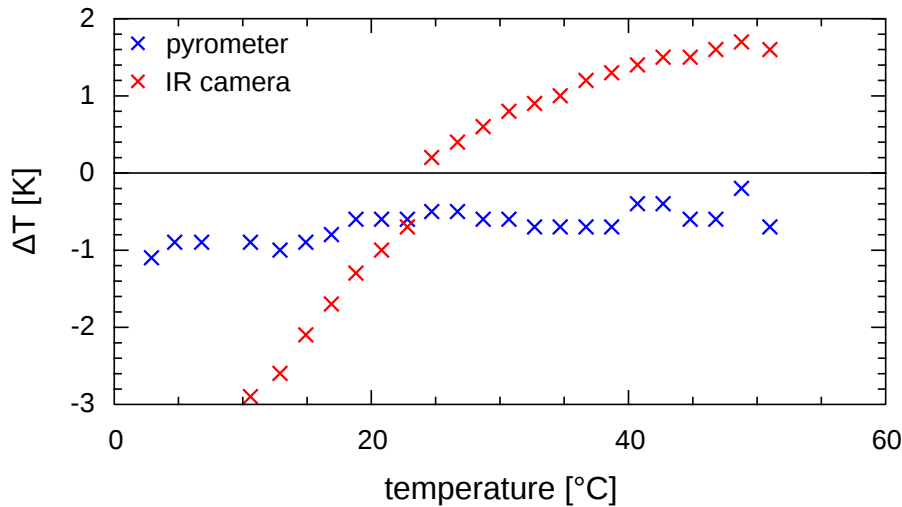


Figure 2.10: Comparison of black body surface temperature measured with different instruments: the abscissa of the plotted points is the temperature measured by the internal Pt 100 temperature sensor. The ordinate is the deviation of the pyrometer (blue) and IR camera (red) readings from the internal Pt 100 measurement

the absolute temperature accuracy of the black body from these measurements.

In the absence of a more precise measurement, a temperature uncertainty of 0.1 K is assumed for the Pt 100 thermistor in accordance with literature values. The absolute temperature uncertainty of the black body surface is estimated to be  $\sigma_T = 0.2$  K, owing to the fact, that the temperature sensor is located below the emitting surface and may thus differ in temperature from the actual surface temperature due to convection over the surface or due to heat conduction.

The remaining task is to verify that the black body meets the manufacturer's specifications on emissivity (better than 0.99). To do so, measurements of three reference cavity black bodies at 10°C, 20°C and 30°C are analysed, which were kindly provided by the United States National Institute of Standards and Technology (NIST), the Rosenstiel School of Marine and Atmospheric Science (RSMAS) and the United Kingdom Met Office (UKMO). The calibration sources of NIST and RSMAS were measured as part of an instrument intercomparison organised by the Committee for Earth Observation Satellites (CEOS) described in section 2.2.8, while the cooperation with UKMO in Exeter aimed at an investigation of the Model 102 FTIR in terms of detector non-linearity as discussed in section 2.2.10.

Figure 2.11 shows the ratio of radiance measured by the D&P Model 102 FTIR (calibrated with the D&P black body) and the radiance predicted by Planck's

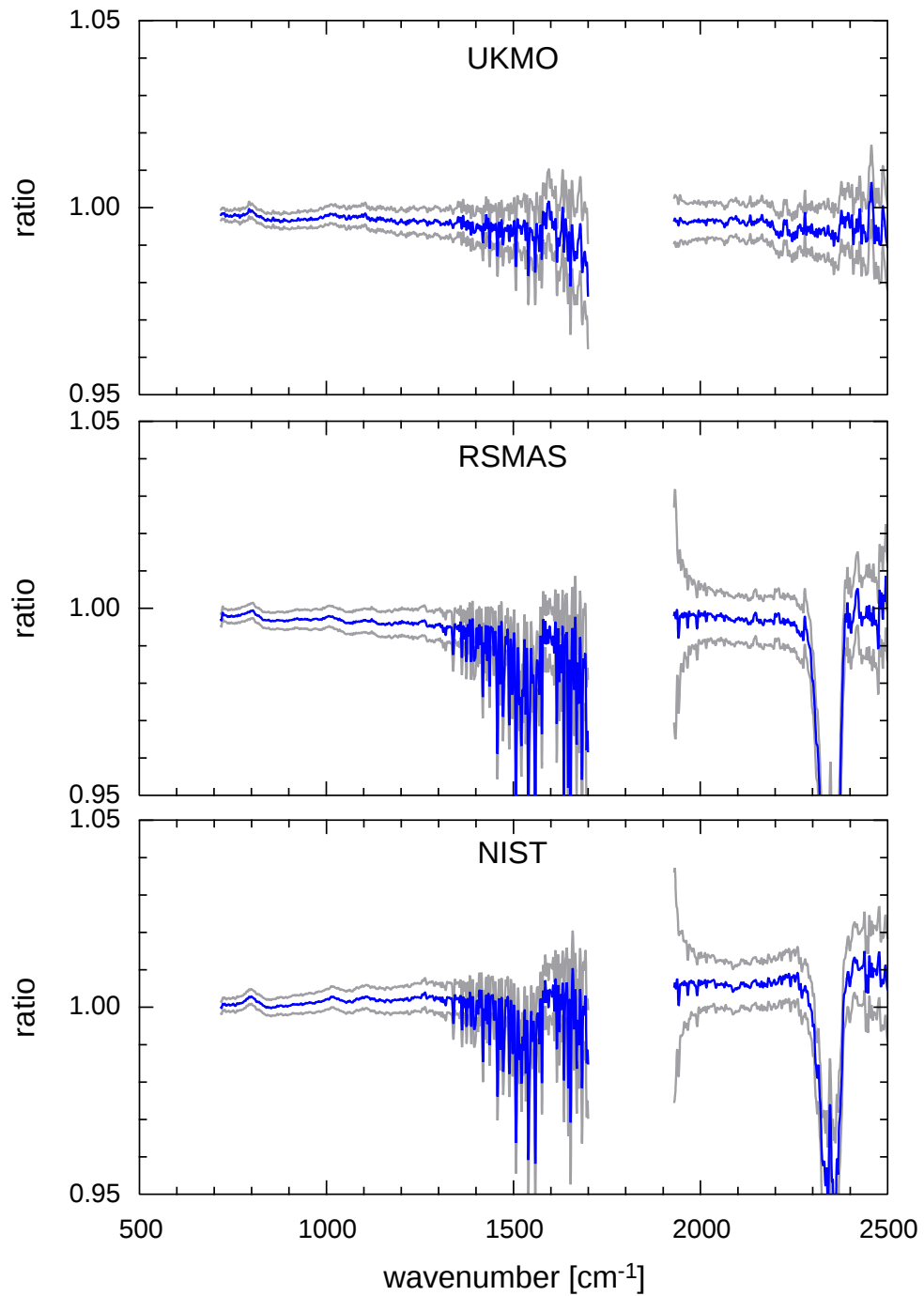


Figure 2.11: Estimated emissivity (blue) of the black bodies of UKMO (10°C), RSMAS (20°C) and NIST (30°C) determined from measurements with the D&P FTIR. The grey lines indicate the measurement uncertainty of one standard deviation.

law at the temperature measured by the internal thermistors of the respective black body. This value is a proxy for the emissivity of the black body, provided the fraction of reflected radiation leaving the black body is negligible. This assumption is valid for the three black bodies at hand, because their cavity design attenuates any radiation entering the black body to a negligible level by multiple reflections before it can leave the black body. Since the emissivity of the reference black bodies is equal to unity within the estimated measurement uncertainty for all measurements and does not vary among the measurements, it is safe to conclude that the D&P black body can be regarded as ideal within the measurement tolerances as well. The absence of the two notable absorption bands caused by water ( $1350-1700\text{ cm}^{-1}$ ) and carbon dioxide ( $2300-2400\text{ cm}^{-1}$ ) in the UKMO spectrum is explained by the fact, that the respective measurements were conducted in a pure Nitrogen atmosphere.

### 2.2.8 Instrument Stability

This section examines the stability of the D&P Model 102 FTIR, i.e. its capability to reproduce successive measurements of a stable source. This quantity is of special interest, since the non-continuous modus operandi of the instrument might prevent thermal equilibration. The prisms forming the interferometer core move only during data acquisition resulting in a non-continuous energy flow into the spectrometer caused by friction. This dissipation potentially disturbs thermodynamic equilibrium if the associated local temperature increase is not sufficiently compensated by the internal temperature control loop. Hence the efficiency of the regulation greatly determines the stability of the instrument.

The following investigations are performed on a set of black body measurements obtained during the 2009 workshop on brightness temperature (BT) retrieval organised by the CEOS Working Group on Calibration and Validation (WGCV), which has been conducted in May 2009 in cooperation with RSMAS at the University of Miami. The ultimate goal was a cross-comparison of several ground based instruments applied in SST sounding for satellite calibration and validation. As described in detail by Theocharous et al. (2010), the workshop comprised laboratory and field measurements, which took place at the Miami RSMAS site. The laboratory measurements are conducted with two liquid cooled/ heated cavity calibration sources provided by RSMAS and NIST. An in-depth description of these black bodies has been provided by Fowler (1995). Since these reference sources are very stable in temperature they allow to exclusively attribute any temporal variance in the recorded spectra to the instrument.

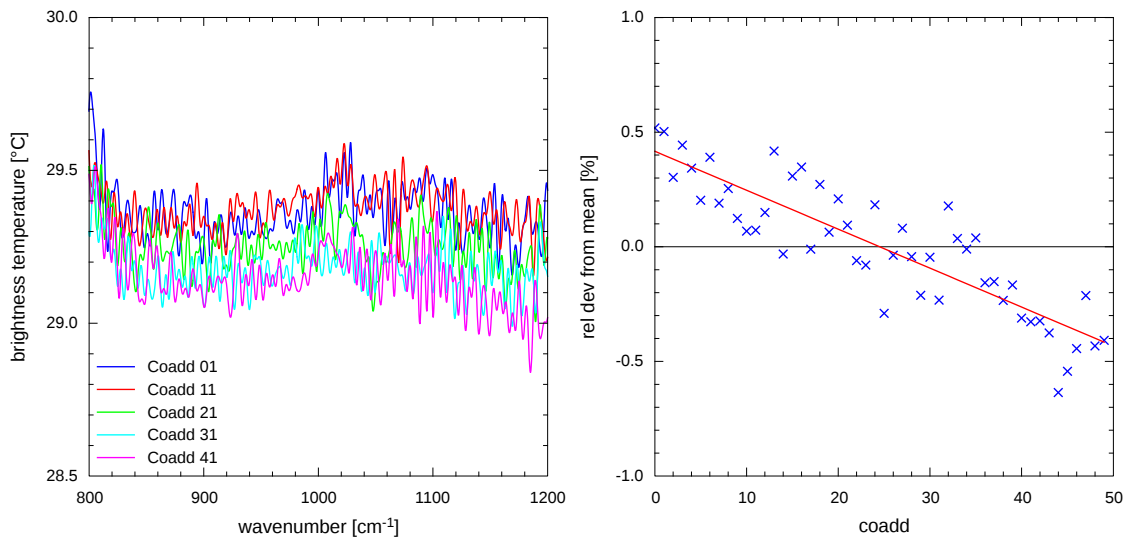


Figure 2.12: Left: Brightness temperature spectrum of every 10th coadd for a measurement of the NIST black body at 30°C. Right: Relative deviation from mean of the raw signal at 1200 cm<sup>-1</sup> for every coadd (blue) with regression line (red)

Figure 2.12 (left) shows a brightness temperature spectrum in the atmospheric window region for every 10th coadd of a measurement consisting of 100 coadds equivalent to an integration time of 100 seconds. The Model 102 was looking into the NIST black body stabilised at a constant temperature of 30°C during the entire measurement. Yet a trend towards lower temperatures with increasing coadd number is discernible from the plot. The trend becomes obvious in the right hand panel of figure 2.12, which depicts the relative deviation of the raw spectrum at 1200 cm<sup>-1</sup> from its mean (blue crosses) along with a regression line (red). The visible linear drift has already been reported by Engelbrecht (2010), who suggests to mediate the problem by ignoring all but the first ten coadds, which is equivalent to restricting the maximum number of coadds to ten. This however requires, that the instrument returns to its initial state after a measurement, which is unlikely if the relaxation time between successive measurements is small. Furthermore it is desirable to allow for a larger number of coadds to increase the signal to noise ratio.

In the following paragraphs a correction is presented, which reduces the influence of the drift by predicting the associated bias using a simple model function. Although figure 2.12 seemingly suggests a linear model at first glance, this choice has to be rejected from a physical point of view, as the following considerations reveal. Imagine the instrument to be in thermal equilibrium with the interferometer core

standing still. If a measurement is started, the system is driven out of its current thermodynamic state, as apparent in figure 2.12. If, however, the measurement was continued for a sufficient amount of time, it should asymptotically approach a new equilibrium. This asymptotic behaviour however cannot be captured by a linear model and consequently requires a slightly different approach.

In order to capture the required asymptotic behaviour, the measured raw spectrum  $s$  at time  $t$  is assumed to be representable in terms of an exponential function

$$s(\nu, t) = s_\infty(\nu)(1 + e^{-\alpha t}). \quad (2.39)$$

Here  $s_\infty(\nu)$  is the asymptotic raw spectrum obtained after running the interferometer for an infinitely long time and  $\alpha$  is a dampening constant controlling the equilibration speed. Furthermore the relative deviation at a given wavenumber with respect to an arbitrary reference time  $t_0$  is defined by

$$f(\nu, t) = \frac{s(\nu, t)}{s(\nu, t_0)} - 1. \quad (2.40)$$

A measurement  $M$  consisting of  $n$  coadds  $M = \{s_i(\nu) | i = 1 \dots n\}$  is represented as a set of data points  $(x_i, y_i)$  for each each wavenumber with

$$x_i = i - \frac{n+1}{2} \quad (2.41)$$

$$y_i = \frac{s_i(\nu)}{s(\nu, t_0)} - 1. \quad (2.42)$$

Since two consecutive interferograms of the same scan direction are approximately two seconds apart, time  $t$  and  $x$  are linearly related, i.e.  $t \sim x\Delta t$ , where  $\Delta t = 2s$  is the time period per scan. As will become clear shortly, it is advantageous to designate the time half in between first and last coadd of measurement  $M$  as  $t_0$ , which is obviously equivalent to the definition  $t = t_0 + x\Delta t$ . Owing to the similar form of equations 2.40 and 2.42, it is natural to assume a functional relationship  $f$  of the form

$$y_i = f(\nu, t_0 + x_i\Delta t) + \xi(\nu, t_0 + x_i\Delta t),$$

where  $\xi$  symbolises the statistical noise of the measured spectrum. As indicated by figure 2.12 it is intended to fit a straight line  $g : x \mapsto ax + b$  through the data points  $(x_i, y_i)$  to obtain the coefficients  $a$  and  $b$  by means of linear regression (Bronstein et al., 2001):

$$a(\nu) = \frac{\sum_{i=1}^n (x_i - \langle x \rangle) (y_i - \langle y \rangle)}{\sum_{i=1}^n (x_i - \langle x \rangle)^2} = \frac{\sum_{i=1}^n x_i y_i}{\sum_{i=1}^n x_i^2}$$

$$b(\nu) = \langle y \rangle - a \langle x \rangle = 0$$

where

$$\begin{aligned}\langle x \rangle &= \frac{1}{n} \sum_{i=1}^n x_i = 0 \\ \langle y \rangle &= \frac{1}{n} \sum_{i=1}^n y_i = \frac{1}{n} \sum_{i=1}^n \frac{s_i(\nu)}{s(\nu, t_0)} - 1 = 0.\end{aligned}$$

The choice  $\langle y \rangle = 0$  is equivalent to the definition

$$s(\nu, t_0) = \frac{1}{n} \sum_{i=1}^n s_i(\nu) \quad (2.43)$$

which follows the interpretation of  $g$  as first order approximation to  $f$  in  $t = t_0$ , thereby constraining slope  $a$  and offset  $b$ :

$$a(\nu) = \left. \frac{\partial f}{\partial t} \right|_{t=t_0} = \frac{-\alpha e^{-\alpha t_0}}{1 + e^{-\alpha t_0}} \quad (2.44)$$

$$b(\nu) = f(\nu, t_0) = 0. \quad (2.45)$$

Solving equation 2.44 for  $t_0$  results in

$$t_0 = -\frac{1}{\alpha} \ln \left( \frac{-a(\nu)}{\alpha + a(\nu)} \right)$$

which can be inserted into equation 2.40 to eliminate  $t_0$

$$f(\nu, t) = \frac{a(\nu) + \alpha}{\alpha} (1 + e^{-\alpha t}) - 1.$$

This result in combination with equation 2.39, 2.40 and 2.43 finally yields the desired asymptotic signal  $s_\infty$

$$s_\infty(\nu) = \lim_{t \rightarrow \infty} s(\nu, t) = \left( \lim_{t \rightarrow \infty} f(\nu, t) + 1 \right) s(\nu, t_0) = \left( 1 + \frac{a(\nu)}{\alpha} \right) s(\nu, t_0).$$

The uncertainty of the drift adjusted mean signal  $s_\infty$  can be derived from the uncertainties in slope and intercept of  $g$  (Bronstein et al., 2001)

$$\sigma_a^2(\nu) = \frac{1}{n-2} \frac{\sum_{i=1}^n (y_i - a(\nu)x_i - b(\nu))^2}{\sum_{i=1}^n (x_i - \langle x \rangle)^2} \quad (2.46)$$

$$\sigma_b^2(\nu) = \frac{\sigma_a^2(\nu)}{n} \sum_{i=1}^n x_i^2 = \frac{n^2 - 1}{12} \sigma_a^2(\nu). \quad (2.47)$$



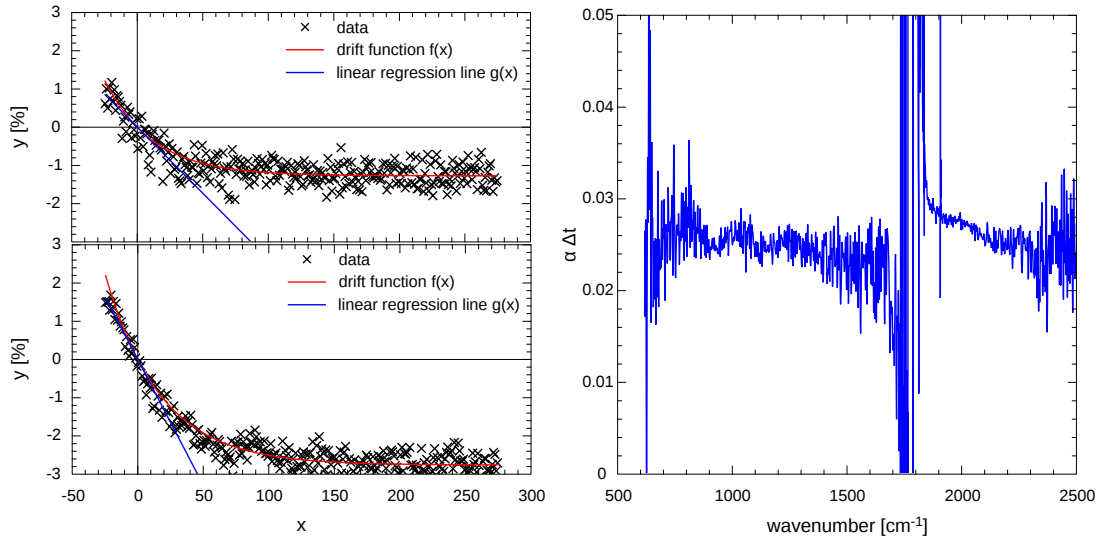


Figure 2.13: Left: Linear least squares fit of the drift function at  $800 \text{ cm}^{-1}$  (top) and  $1200 \text{ cm}^{-1}$  (bottom).

Right:  $\alpha\Delta t$  as determined from a least squares fit over the whole wavenumber range. The large variations in the spectral interval  $1700 - 1900 \text{ cm}^{-1}$  can be ignored, since this interval is of no practical use due to the MCT-InSb detector gap.

Since  $s_i(\nu) = (y_i + 1)s(\nu, t_0)$  the associated variance is obtained from

$$\sigma_s^2 = \frac{1}{n} \sum_{i=1}^n (s_i(\nu) - s(\nu, t_0))^2 = s^2(\nu, t_0) \sigma_y^2,$$

where  $\sigma_y^2 = \sigma_b^2$  is the variance of the intercept  $b$ , because  $\langle y \rangle = a\langle x \rangle + b = b$ . Application of Gaussian error propagation in accordance with the Joint Committee for Guides in Metrology (2008) yields the uncertainty  $\sigma_\infty$  of the corrected mean:

$$\sigma_\infty = s(\nu, t_0) \sqrt{\frac{\sigma_a^2(\nu)}{\alpha^2} + \left(1 + \frac{a(\nu)}{\alpha}\right)^2 \sigma_b^2(\nu) + \frac{a^2(\nu)}{\alpha^4} \sigma_\alpha^2}$$

The theory derived so far allows the estimation of the drift corrected signal  $s_\infty$  from the coadds  $s_i$ , provided the constant coefficient  $\alpha$  is known. In order to determine the yet unknown value of  $\alpha$ , a sequence of six measurements (á 100 coadds each) taken on May 15th between 1304 – 1316 universal time coordinated (UTC) is analysed. The measurements were obtained by pointing the D&P FTIR at the RSMAS black body operated at a temperature of  $20^\circ\text{C}$ . The time between

individual measurements is regarded as negligible, so that the observed instrument drift over all six measurements is interpreted as drift observed in a hypothetical single measurement with 600 coadds. Figure 2.13 (left panel) depicts a plot of the resulting drift function  $f$  at two wavenumbers along with the respective regression line  $g$ . The black crosses mark the individual xy-data points and the red line is the result of a least squares fit of equation 2.40 with  $\alpha$  as free parameter. The right panel of figure 2.13 shows the product  $\alpha\Delta t$  obtained from the fit for each wavenumber  $\nu$ . Since the plot indicates no spectral variation apart from what appears to be noise, a constant value  $\alpha = (0.0125 \pm 0.001) \text{ s}^{-1}$  is assumed. Note that  $\alpha$  is assumed to be a constant of the interferometer and thus needs to be determined only once.

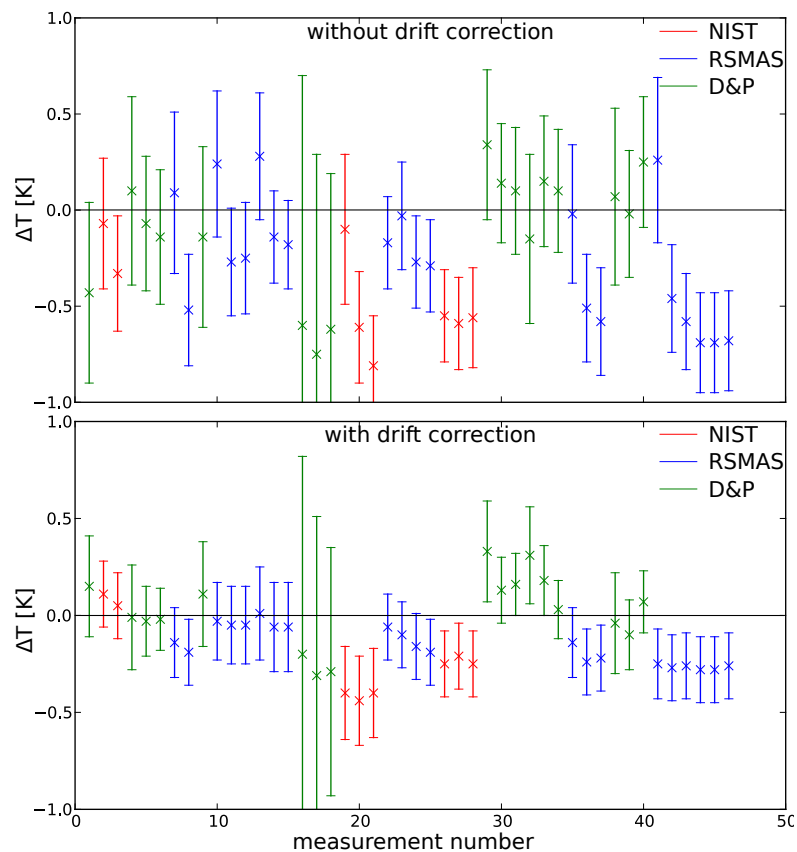


Figure 2.14: Deviation of measured temperature from nominal temperature for measurements taken during the CEOS intercomparison. Shown are results for NIST, RSMAS and D&P black body with (bottom) and without (top) drift correction. Error bars indicate the  $1\sigma$  confidence interval

Before proceeding to the next section, the improvement achieved with the suggested drift correction shall be illustrated for the ensemble of black body measurements conducted within the scope of the CEOS campaign. To allow for a convenient visualisation, the mean temperature is introduced as the mean brightness temperature over the spectral interval  $800 - 1200 \text{ cm}^{-1}$ . Figure 2.14 shows the deviation of the such defined mean temperature from the nominal black body temperature determined by the internal temperature sensors for each measurement of the CEOS comparison. Error bars indicate the  $1\sigma$  confidence interval. Obviously the drift correction discernibly reduces the measurement uncertainty in all cases and causes the majority of mean temperatures to move closer to the nominal values. This is especially true for consecutive measurements taken in rapid sequence, which customarily display a considerable drift. A closer look at the drift corrected mean temperatures of the high-precision black bodies provided by NIST (red) and RSMAS (blue), reveals a small bias towards lower values, i.e. the temperature measured with the D&P FTIR is lower than the nominal black body temperature. However, since all measured temperatures agree within two standard deviations with the nominal value, no further correction is attempted.

Note that these measurements allow to trace the absolute temperature of the D&P black body to the NIST black body, the accuracy of which was monitored with the NIST TXR transfer radiometer as described in Theocharous et al. (2010). Hence they belatedly confirm previous estimates of the D&P black body's absolute temperature accuracy presented in section 2.2.7 and moreover provide traceability to NIST standards.

### 2.2.9 Field of View

As part of the instrument characterisation laboratory measurements were conducted to determine the relative response over the entire field of view (FOV), which according to the manufacturer has a total size of  $4.8^\circ$  or equivalently 84 mrad.

The experimental setup is depicted in figure 2.15 with the FTIR residing on a standard tripod to measure the radiation emerging from a collimator mounted to an optical bench. The collimator exit is 122 mm in diameter with an aperture angle of  $0.32^\circ$ . FOV of collimator and FTIR are indicated using dashed lines in figure 2.15. Collimator and FTIR are aligned with the aid of a laser illuminating the collimator through the entrance iris. Collimator and FTIR are then positioned, such that the laser beam passes through the centres of collimator entrance, collimator exit and FTIR entrance optics, respectively.

After completion of the alignment the laser is mounted at the back of the collimator

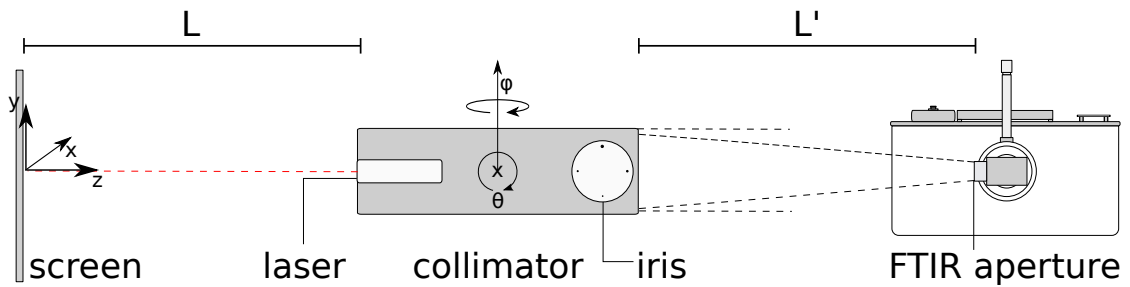


Figure 2.15: A sketch of the experimental setup for the field of view measurements: the collimator is rotated around the  $x$  and  $y$ -axis with respective angles  $\phi$  and  $\theta$ . A black body (not shown) with temperature  $T=700$  °C is mounted in front of the iris

as shown in figure 2.15 and a black body is placed in front of the collimator illuminating the entrance aperture iris. The black body is stabilised by an internal controller at a temperature of  $700^{\circ}\text{C}$  to ensure a sufficiently high intensity of the collimated beam. The origin of the coordinate system is chosen at the point, where the maximum intensity is measured with the FTIR. The orientation of the collimator at defined angles is achieved by pointing the laser to the nodes of a regular grid drawn on the screen. For each grid node an average interferogram consisting of 10 coadds is recorded and the voltage at the centreburst is logged. Since the screen is too small to cover the entire field of view in  $x$ -direction, two separate measurements were performed for the positive and negative half-plane. The distance  $L$  for both measurements is 303 cm, whereas  $L'$  changed from 59 cm in the first measurement to 17.5 cm in the second measurement.

A contour plot of the centreburst voltage normalised by its maximum over all measurements summarises the results in figure 2.16. Obviously the size of the FOV in  $x$ -direction exceeds its extent in  $y$ -direction. A similar result has previously been reported by Korb et al. (1996). In contrast to their results, however, figure 2.16 seems to exhibit a slight counter-clockwise rotation, which might be caused by a rotation of the detector compared to the outside geometry of the instrument.

A total FOV of  $7.5^{\circ}$  in  $x$ - and  $6^{\circ}$  in  $y$ -direction is inferred from these measurements with the zero intensity line as border. Although this value is slightly larger than specified, it does not incur any problems, since all optical components are laid out about a factor of two larger than needed for the specified field of view according to Korb et al. (1996). Additionally the interferometer FOV is completely covered by the FOV of the pointing optics, which allows for a sufficiently accurate alignment for all measurements performed within the scope of this thesis.

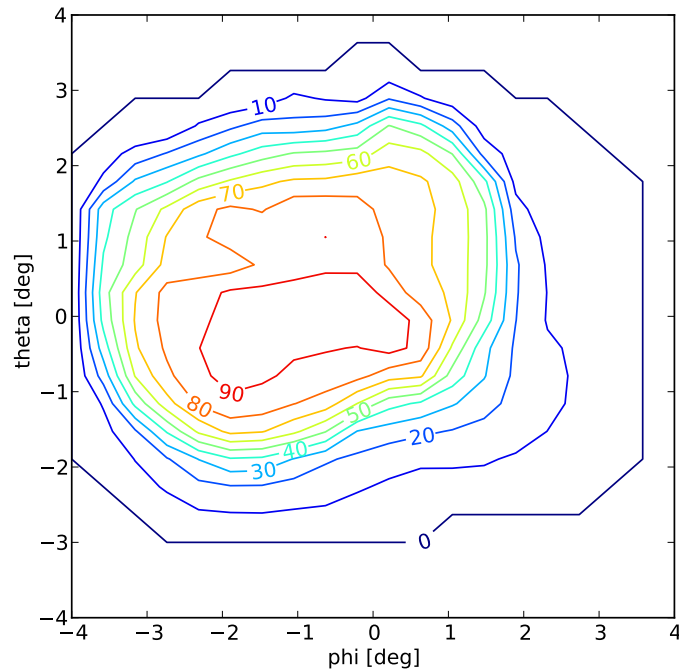


Figure 2.16: Contour plot of the relative ZPD peak voltage measured in % of the maximum peak voltage for different angle combinations  $(\phi, \theta)$

Furthermore it should be noted, that the measurements were intended to deliver a rough estimate of the FOV and offer room for improvements. First of all the data evaluation disregards the fact, that the measurement of each half-plane took approximately three hours and a perceivable instrument drift is probable during this time span. Additionally it is possible, that the iris of the collimator is heated by the black body in the course of the experiment leading to additional thermal emission and an effectively broadened collimator FOV. Finally no attempts are made to investigate the homogeneity of the collimated beam, which –if insufficient– could cause a variation of the measured FOV with changing distance  $L'$  between collimator and FTIR.

Since the following investigations are limited to scenes homogeneous over the entire field of view, the remaining uncertainties do not warrant the effort of more elaborate measurements. The most important conclusion drawn from the investigations presented above is, that although the FOV is likely larger than specified, it is still bounded by the FOV of the pointing optics, which consequently allow the selection of homogeneous fractions from inhomogeneous scenes (e.g. clear-sky patches from cloudy sky) as long as they are homogeneous over the entire optical FOV.

### 2.2.10 Detector Non-Linearity

As has been shown in section 2.2.7, radiometric calibration with the D&P black body yields good results for measurements of different reference black bodies at room temperature. When observing downwelling atmospheric radiances however, it is usually inevitable to extrapolate the instrument response function to lower voltages, since the necessary dynamic range would require a cold calibration source kept at approximately 220 K. Such a source is difficult to set up in the lab and almost impossible to maintain in the field. Besides from cooling the black body to well below ambient temperature and achieving high temperature stability at the same time, condensation and icing of atmospheric water vapour constitute the main challenges. As a consequence field calibration sources are typically operated above dew point necessitating extrapolation of the calibration constants well outside the calibrated dynamic range. This may result in large errors, if the detector output changes non-linearly with the incoming flux.

Especially MCT detectors are well known to display non-linear behaviour (Abrams et al., 1994) and a number of methods to correct for the resulting effects have been proposed (e.g. Knuteson et al., 2004, Fiedler et al., 2005, Kleinert et al., 2007). A typical approach is to express the corrected interferogram  $I_{\text{true}}$  in terms of the measured interferogram  $I_{\text{meas}}$  by means of a Taylor series:

$$I_{\text{true}} = \sum_{m=0}^M \alpha_m I_{\text{meas}}^m, \quad (2.48)$$

where  $M \leq 3$  is the maximum order of the non-linearity. The raw spectrum is obtained as Fourier transform of the corrected interferogram. As shown by Fiedler et al. (2005), the higher order terms cause artefacts in the spectrum, which appear as signal outside the wavenumber range covered by the detector (so called out-of-band signal). Hence the coefficients  $\alpha_m$  may be obtained by minimising the out-of-band signal for a given interferogram. Figure 2.17 displays the Fourier transform of the observed interferogram (without any filtering) for a black body measurement at 30°C. The measurement has been conducted once with each detector while the respective other detector was disconnected from the ADC to isolate the output interferograms of the individual detectors. It can be observed that the MCT detector displays out-of-band signal below 500  $\text{cm}^{-1}$  and between 1900–2000  $\text{cm}^{-1}$ . Note that the magnitude of the MCT out-of-band signal approximately equals the InSb signal strength beyond 2500  $\text{cm}^{-1}$ , which makes the InSb-MCT combination virtually unusable beyond this threshold for targets with similar spectral intensity distribution.

The potential non-linearity of the MCT indicated by figure 2.17 was investigated

in cooperation with colleagues from the UKMO, who previously characterised and corrected detector non-linearities of the airborne research interferometer evaluation system (ARIES). Proceeding in complete accordance with the survey of Fiedler et al. (2005) measurements at black body temperatures in the range from  $-60^{\circ}\text{C}$  to  $+30^{\circ}\text{C}$  were collected. The resulting BT spectra (red) are displayed in figure 2.18 along with the confidence intervals (grey) and the nominal black body temperatures (black lines) determined from an internal Pt 100. Apart from the measurement at  $-60^{\circ}\text{C}$ , the measurements agree with the theoretical predictions over a large portion of the spectrum within the estimated errors. Two notable exceptions are the spectral intervals around  $800\text{ cm}^{-1}$  and  $1100\text{ cm}^{-1}$ , where the measurements display an increasing cold bias with decreasing scene temperature. Comparing the bias with the instrument background radiation (dashed blue line in figure 2.18) it becomes apparent, that the maxima of bias and background radiation are located in identical spectral regions, where the instrument radiation significantly exceeds the scene radiation. This implies that the measured signal essentially consists of background radiation making it difficult to uniquely attribute the deviations to detector non-linearity, as they could also be caused by variations in the background.

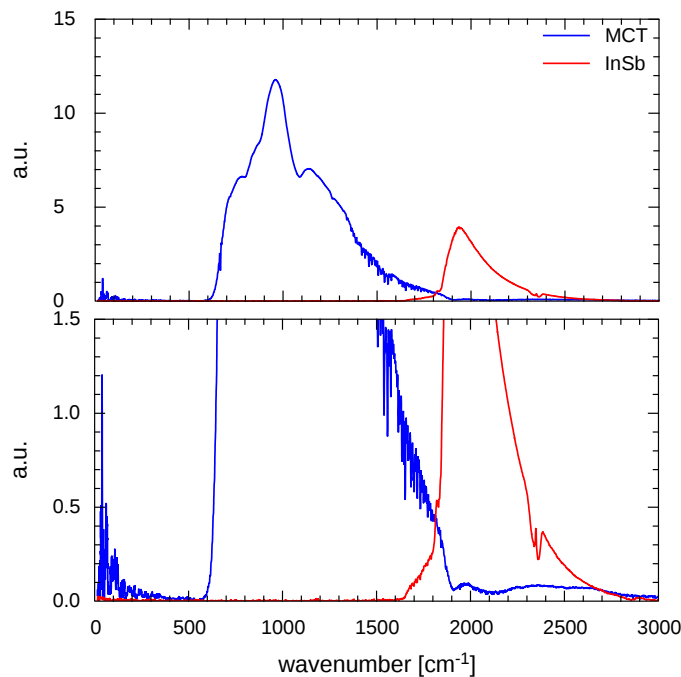


Figure 2.17: Individual raw spectra of the MCT (blue) and InSb (red) detectors viewing a  $30^{\circ}\text{C}$  black body. The upper panel shows the complete raw spectra of both detectors, while the lower figure magnifies the out-of-band signal.

Since several attempts to reduce the out-of-band signal of a single MCT interferogram taking into account non-linearities up to an order of  $M = 4$  did not lead to an improvement of the results, it was decided to accept the remaining bias without further correction. This decision is also motivated by the fact, that recorded interferograms usually consist of the combined MCT/ InSb signal, which would have to be separated before a correction could be applied, hence introducing additional uncertainties. Instead it will be demonstrated in the next section, that the undisclosed non-linearity has a relatively small impact on atmospheric observations compared to the black body measurements discussed above, because the spectrally integrated flux of the former is much greater. This entails a higher DC voltage of the interferogram which in turn moves the dynamic range of the scene closer to the range covered by the calibration.

### 2.2.11 Instrument Validation and Error Estimation

In the preceding sections a variety of different laboratory measurements have been presented, which all aim at a comprehensive characterisation of the D&P Model 102 FTIR. The results obtained from these measurements ultimately enabled the development of reliable calibration algorithms necessary to transform the raw interferograms into radiances with specified uncertainties. Figure 2.19 shows a comparison of the different uncertainties discussed in the previous chapters and the resulting total uncertainty for a measurement of the NIST black body at a temperature of approximately 300 K. This measurement was chosen, because the black body can be regarded as stable enough to trace all variations back to the instrument. Note that the statistical noise of the scene measurement (red curve) can be interpreted as noise equivalent spectral radiance (NESR) of the instrument at 300 K with an almost constant value of approximately  $0.1 \text{ mW}/(\text{m}^2 \text{ sr cm}^{-1})$  in the spectral range  $700 - 1400 \text{ cm}^{-1}$ . This value is comparable to the NESR of the AERI in this spectral region reported by Knuteson et al. (2004), a quite remarkable fact considering the large amount of drift diagnosed for the Model 102 before correction. Bear in mind though, that the AERI has an about five times higher spectral resolution when comparing these results. Furthermore it is interesting to observe, that the overall uncertainty of the calibrated radiance is dominated by the temperature uncertainty of the D&P black body, underlining the importance of the sources used for radiometric calibration.

Although the laboratory studies presented so far revealed essential information about the performance of the D&P Model 102 FTIR, they are not sufficient for a complete characterisation of a field instrument. The reason is, that laboratory measurements are typically performed under optimal conditions, while the cir-



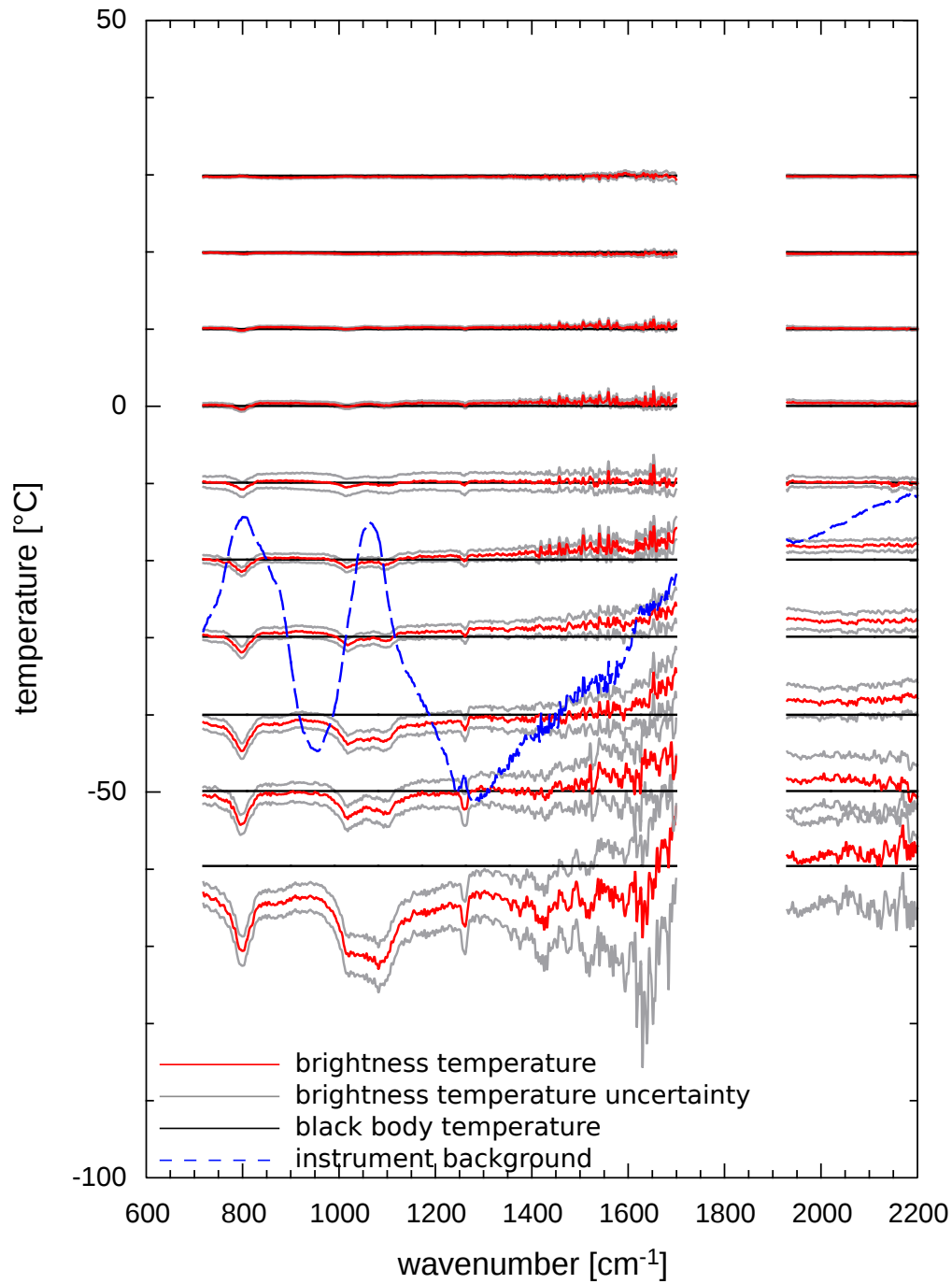


Figure 2.18: Measured brightness temperature (red) with uncertainty (grey) of the UKMO low temperature black body at different set temperatures. The solid black line indicates the black body temperature. The dashed blue line shows the magnitude of the instrument background radiation as determined during calibration.

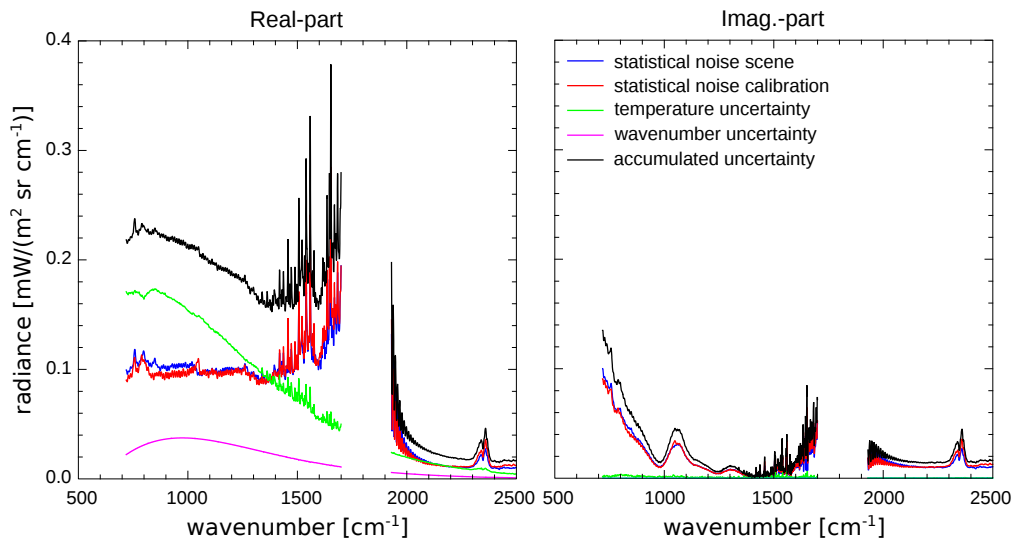


Figure 2.19: Comparison of real (left) and imaginary part (right) of the different uncertainties for a measurement of the NIST black body at 300 K: Shown are the uncertainties arising from the statistical noise in the calibration black body measurements (blue), from the statistical noise in the scene observations (red), from the temperature uncertainty of the black body (green) and from the wavenumber uncertainty (magenta). The accumulated uncertainty of the calibrated radiance is shown in black.

cumstances during field campaigns regularly present additional challenges such as wind, temperature variations, direct sun light or elevated pollution levels. To assert satisfactory instrument performance of the Model 102 under such conditions, an instrument intercomparison was conducted with a MAERI FTIR operated by RSMAS. The MAERI has a specified absolute accuracy of less than 1% of the ambient radiance over the entire spectrum at a theoretical maximum resolution of  $\Delta\nu = 0.5 \text{ cm}^{-1}$  (as defined in chapter 2.1.4). The instrument has been validated in numerous campaigns over the last decade and hence constitutes a good choice as benchmark for TIR atmospheric observations.

The intercomparison was conducted within the scope of the CEOS workshop described in section 2.2.8, when both instruments were set up side by side at a peer. The MAERI has a FOV of  $2.6^\circ$  (full angle) and recorded downwelling radiances with a scene integration time of 215 seconds. Since the workshop was mainly dedicated to SST measurements, a complete measurement cycle of the MAERI lasted about 12 minutes and consisted of a zenith view, two limb observations and a calibration with two internal black bodies. A cycle of the Model 102 comprised three scene measurements á 100 coadds (equalling an integration time of 100 s)

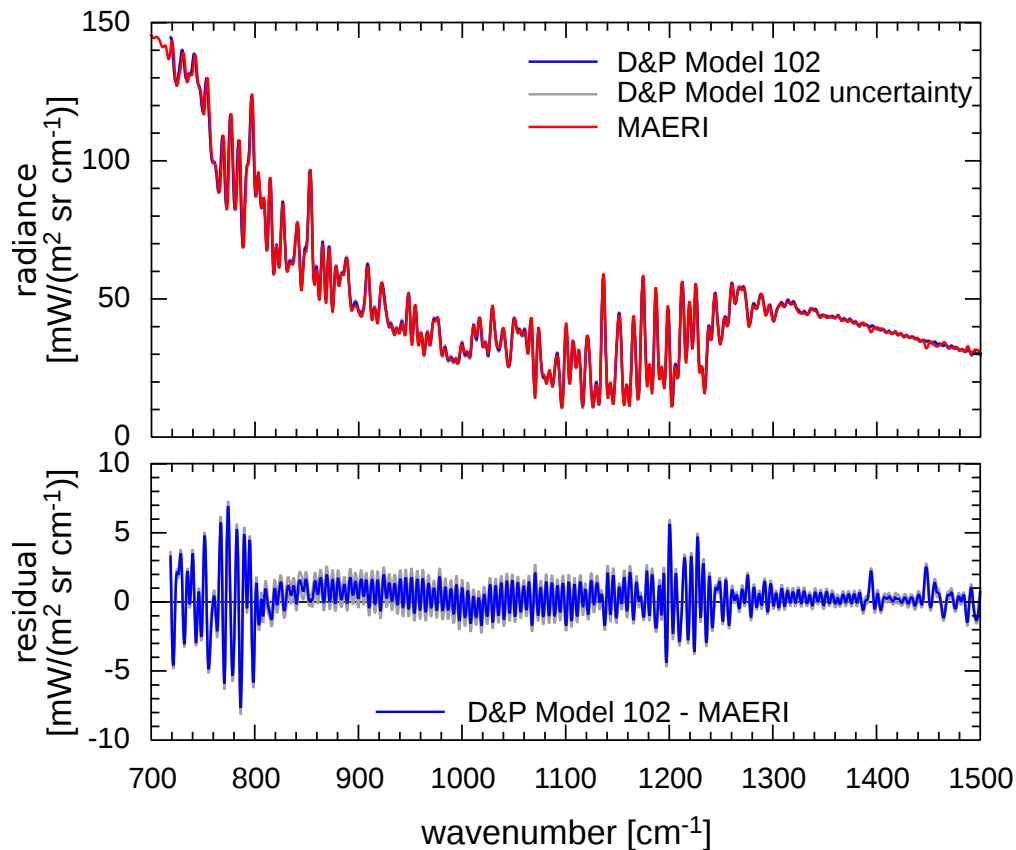


Figure 2.20: Comparison of coincident downwelling radiance observations performed with D&P Model 102 (blue) and MAERI (red). The grey lines indicate the confidence interval of the Model 102 spectrum. Shown are calibrated radiances (top) and residual with respect to MAERI (bottom).

taken in consecutive order without delay followed by a calibration with the D&P black body at temperatures of 3°C, 13°C and 23°C. In order to obtain comparable results, two consecutive zenith measurements of the D&P FTIR are averaged to simulate an integration time similar to the MAERI.

Figure 2.20 depicts a typical example of the resulting spectra for a period without clouds on May 14th, 2009 at 2055 UTC. The top panel shows the radiances measured by the D&P Model 102 FTIR (blue) with the associated  $1\sigma$ -confidence interval and the MAERI spectrum (red). The latter has been reduced to the native resolution of the D&P instrument by convolution. The bottom panel displays the residual BTD obtained after conversion of both spectra to BT followed by subtraction of the MAERI spectrum from the Model 102 spectrum. The BT at a given wavenumber is defined as the temperature of an ideal black body emitting

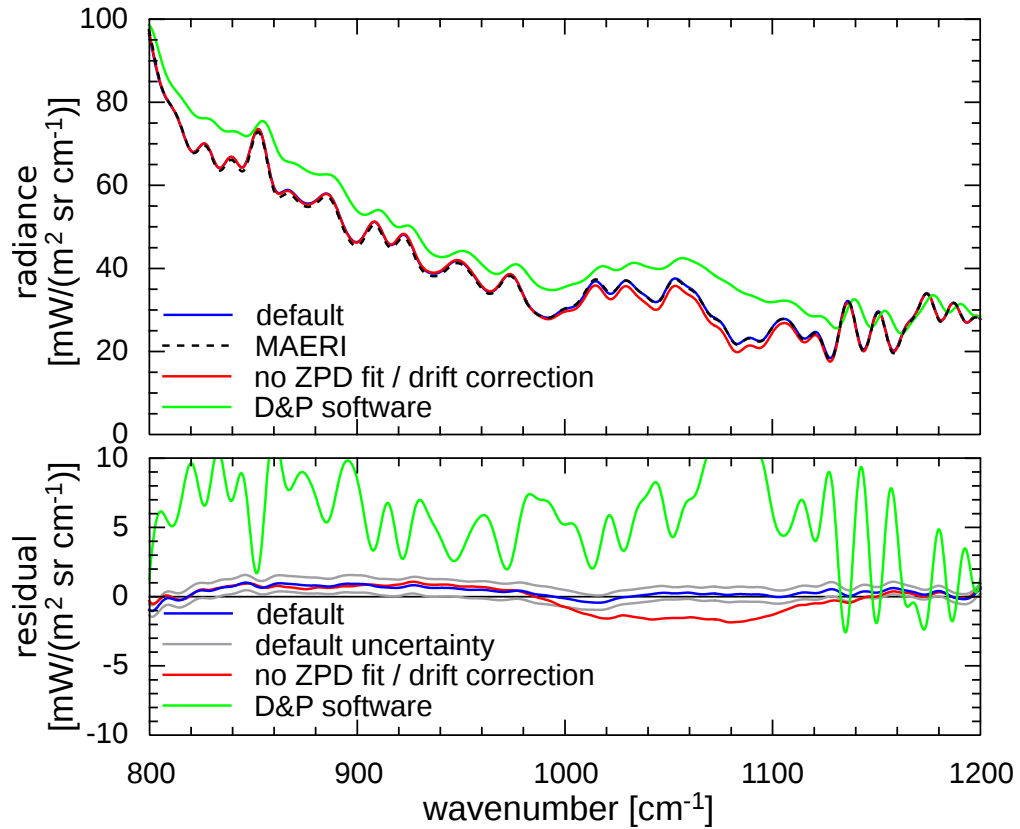


Figure 2.21: Influence of the calibration method on the spectral radiance over the atmospheric window domain at a reduced resolution of  $10 \text{ cm}^{-1}$ . The top figure shows spectral radiances and the bottom figure the residual with respect to the reference MAERI measurement. The green curve is obtained from the D&P software shipped with the Model 102. The blue and red curves are both created with the MIROR software package and illustrate the improvement achieved with the default algorithm (blue) compared to the version without ZPD fit and drift correction (red).

the same radiance at this wavenumber. It can be observed that both measurements agree well within the error bounds. The high frequency noise discernible in the BTD is caused by small shifts in position of the individual absorption line originating from an imperfect wavenumber correction of the Model 102.

The disturbing noise is suppressed in figure 2.21, where both spectra have been reduced to a spectral resolution of  $10\text{ cm}^{-1}$  and the spectral axis has been limited to the atmospheric window region. In addition to the MAERI and Model 102 spectra shown before, figure 2.21 contains a spectrum obtained from the D&P software after calibration with black bodies at  $3^\circ\text{C}$  and  $13^\circ\text{C}$  (green) and the result of a calibration with the MIROR software without drift correction and ZPD iteration (red). It is obvious that the D&P software is hardly suited to evaluate atmospheric measurements. The improvement achieved with drift correction and ZPD iteration becomes apparent in the region  $1000 - 1150\text{ cm}^{-1}$ , where the large bias of almost 4 K compared to the MAERI measurement is completely removed.

The comparison shows, that although the uncertainties are large compared to benchmark instruments such as the MAERI, the D&P Model 102 FTIR is well suited to measure downwelling atmospheric radiances with moderate spectral resolution, if the corrections described in the previous sections are applied. For completeness it has to be remarked, that the relative humidity during the measurements presented here was quite high (33 mm of precipitable water were measured by a radiosonde launched from Miami Airport at 2306 UTC). As a consequence the bias observed in the UKMO black body measurements may become more pronounced under ambient conditions featuring a drier and cooler air mass which emits less downwelling radiation.

## 2.3 IASI

Apart from the downwelling radiation at the surface, the upwelling radiation exiting the atmosphere is another key quantity determining the radiation budget of the Earth. To investigate the effect mineral dust and biomass burning aerosols have on the radiation balance, satellite measurements with the IASI FTIR are used in combination with radiative transfer simulations within the scope of this study.

IASI is a payload instrument on board the polar-orbiting MetOp satellites operated by the European Organisation for the Exploitation of Meteorological Satellites (EUMETSAT) as part of the EUMETSAT Polar System (EPS). The FTIR was developed by the French Centre National d' Études Spatiales (CNES) and the first instrument of a series of three has been launched on October 19, 2006 on MetOp-A. IASI since circles Earth in a sun-synchronous polar orbit at an altitude of 817 km with an orbital period of 100 minutes. Apart from the interferometer itself, the IASI system comprises an Integrated Imaging Subsystem (IIS), consisting of a broad band radiometer with high spatial resolution, which eases spatial co-registration with other instruments and allows for a straightforward manual cloud detection. The imager has a quadratic field of view with an opening angle of 59.63 mrad, which is recorded by a  $64 \times 64$  pixel matrix. One IASI spectrum is acquired simultaneously with every IIS image for each of four instantaneous fields of view (IFOVs), which are distributed over the IIS FOV. The respective viewing geometries of the IIS and IASI are visualised in Figure 2.22.

IASI and the IIS are both whisk broom scanners with a rotating mirror scanning in across-track direction to obtain a line of images, while the along track movement of the satellite continuously progresses the location of the scan line at the surface. Each scan line consists of 30 individual images, which are acquired at equally spaced scan angles from  $-49^\circ$  to  $49^\circ$  with respect to the nadir direction.

The interferometer covers the spectral range  $645 - 2760 \text{ cm}^{-1}$  with three individual detectors for the sub-ranges  $645 - 1210 \text{ cm}^{-1}$ ,  $1210 - 2000 \text{ cm}^{-1}$  and  $2000 - 2760 \text{ cm}^{-1}$ , respectively. The specified noise equivalent temperature uncertainty for IASI is  $0.2 - 0.32 \text{ K}$  at a spectral resolution of  $0.5 \text{ cm}^{-1}$ , while the absolute temperature accuracy amounts to  $0.5 \text{ K}$ . The Level 1C product distributed via EUMETSAT contains the calibrated radiances apodised by a truncated Gaussian function (Blumstein and Fjortoft, 2008, page 361) with a resolution of  $\delta\nu = 0.5 \text{ cm}^{-1}$  as defined in section 2.1.4.

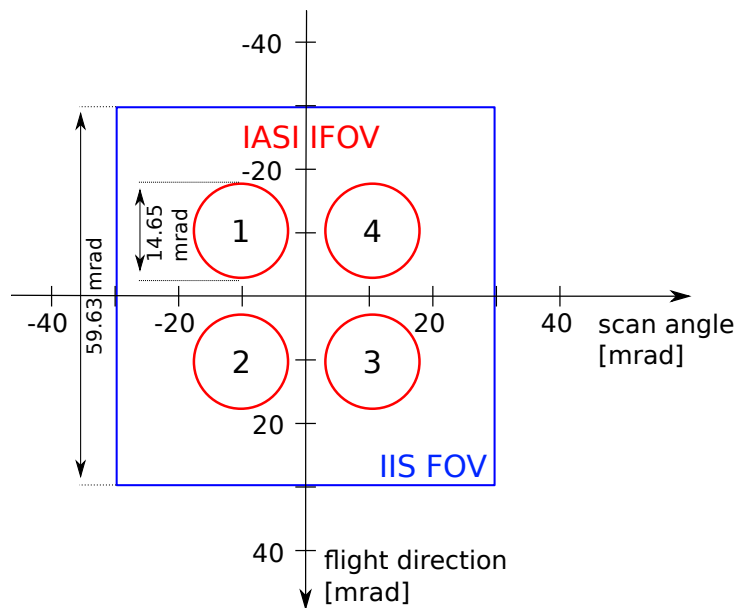


Figure 2.22: Arrangement of the four circular IASI IFOVs (red) relative to the square IIS FOV (blue). At an altitude of 817 km each IIS image covers an area of approximately  $49 \times 49 \text{ km}^2$  and each circular IASI pixel has a diameter of roughly 12 km.

## 2.4 Measurements during SAMUM-2

The D&P Model 102 FTIR was based at the SAMUM-2 main site on Praia Airport along with the other remote sensing instruments and collected data from 19 January 2008 to 6 February 2008. Figure 2.23 depicts the experimental setup used for the zenith measurements: the instrument was mounted on a standard tripod and a specially manufactured sun-shield protected it from direct sun light. The fore optic was aligned at zenith using a spirit level. An FTP server installed on the Model 102 enabled near-realtime data transfer to an additional laptop computer, which was used for data processing and data quality control. Calibration was performed every 30 – 45 minutes as described in section 2.2.4 with the black body source delivered with the instrument at temperatures of  $3^\circ\text{C}$ ,  $13^\circ\text{C}$  and  $23^\circ\text{C}$ . One measurement with 100 coadds was acquired per temperature resulting in a duration of 15 minutes per calibration cycle. Due to the fact that all measurements had to be acquired manually, the operator selected and characterised the scene for each measurement, which limited data acquisition to day time. The live data provided by the LIDAR supported the scene selection process by detecting significant changes in airmass or layer structure. All atmospheric measurements



(a) FTIR tent (lower left) and LIDAR container with radiometric instrumentation on top (b) D&P Model 102 without sun-shield

Figure 2.23: Image of the experimental setup during SAMUM-2: Overview of the measurement site (left) and a close up of the equipment deployed within the scope of this thesis (right)

were recorded with 100 coadds, leading to a measurement time of approximately 2 minutes per measurement. During night-time the instrument was stored in a sea-freight container close to the measurement site in two storage boxes especially manufactured for the instrument.

For several distinct atmospheric conditions the ability of the instrument to measure at different zenith angles was used. For this purpose the sun-shield was dismantled, since it restricts the viewing direction of the instrument to zenith. The zenith angle dependence of the radiance was measured at an azimuth angle of  $110^\circ$  east of north by taking one measurement of 100 coadds at each zenith angle from  $0^\circ$  to  $90^\circ$  in  $10^\circ$  steps. Figure 2.24 shows the results of one such scan during a day with high dust loads. The coloured curves display the radiance at different zenith angles, while the grey lines are calculated radiances for an ideal black body at the respective temperature labelled on the left. Note that the spectra closely resemble a black body spectrum at 300 K over large wavenumber ranges. This behaviour is caused by strong gas absorption bands, which limit the effective viewing distance to a few meters thereby rendering these bands useless for atmospheric observations. The spectral region  $800 - 1200 \text{ cm}^{-1}$  however displays strong variations with zenith angle and deviates significantly from an ideal black body spectrum, because it is considerably less affected by gas absorption and is consequently referred to as TIR atmospheric window, indicating its transparency



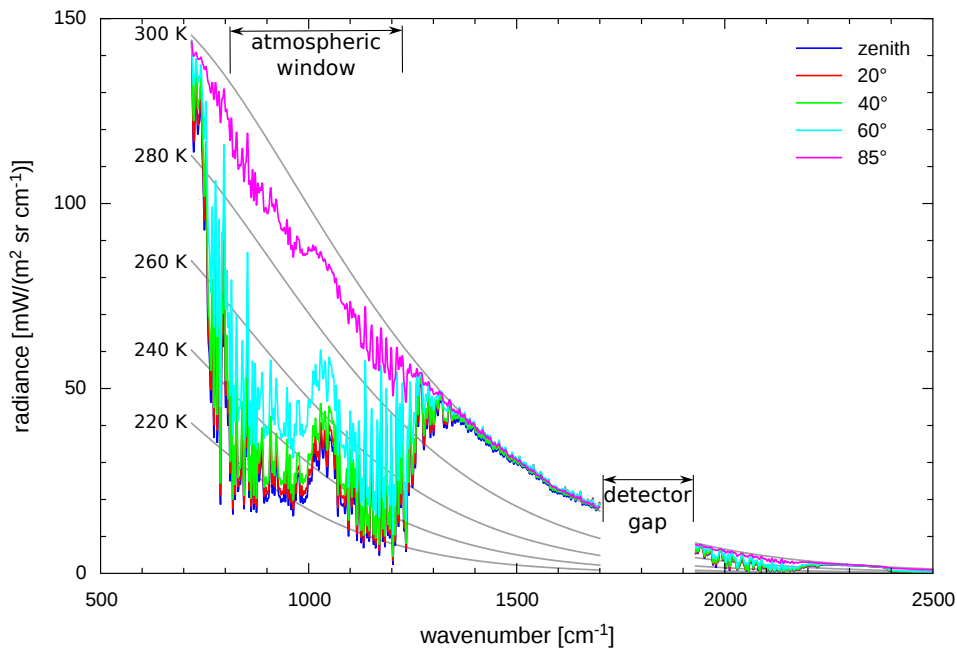


Figure 2.24: Measurements of a dusty atmosphere taken at different zenith angles on 28 January 2008 between 1415 UTC and 1430 UTC. Grey lines are theoretical black body spectra for the annotated temperatures.

for infrared radiation. As a consequence the focus lies on this spectral window region for the main part of this thesis. Furthermore figure 2.24 illustrates the difficulties associated with a column integrating instrument: the absorption and emission characteristics of all species contained in the instrument FOV between BOA and TOA are encoded in the spectrum making it virtually impossible to infer information about a single constituent without further processing. In order to separate the desired optical properties of the aerosol for example, the effect of gaseous absorption has to be remedied first, since the latter dominates the spectrum even in the atmospheric window region. Chapter 3 is entirely dedicated to the radiative transfer tools necessary to isolate the aerosol contribution from the downwelling radiance and to infer information about its physical properties.



# Chapter 3

## Radiative Transfer Simulations

As indicated in section 2.4, radiative transfer (RT) simulations are an indispensable tool for the interpretation of atmospheric radiance measurements. The need for such software arises from the column integrating nature of passive spectroscopic observations, which entwine the information of all emitting and absorbing atmospheric constituents into a single spectrum. Consequently a change in e.g. relative humidity cannot be distinguished from variations in the aerosol optical depth without further processing on the basis of RT theory. This chapter describes the RT tools developed within the scope of this thesis with the aim to evaluate the measurements discussed in chapter 2. The underlying theory and its implementation into efficient algorithms are prerequisites for the interpretation of the results to be discussed in chapter 4. However, the achievements of this work concerning RT simulations are very technical in nature in so far, as they are limited to advances in terms of implementation, rather than newly developed algorithms or fundamental theoretical concepts. Hence the intention of this chapter is to provide the essential details for the upcoming data evaluation without excessive repetition of well established theories. In an attempt to be as concise as possible without loss of information, literature providing an in-depth treatment of the topics touched in the individual sections is cited wherever possible.

Starting with an overview of the necessary foundations of radiative transfer in section 3.1 the chapter proceeds with a discussion of the respective implementation into algorithms and programs executable on modern computers in section 3.2. Finally the results obtained with the radiative transfer tools are validated against benchmark measurements and well proven independent software in chapter 3.3.

## 3.1 Theoretical Foundations of Radiative Transfer

The general goal of radiative transfer theory is to predict the radiance  $L$  at a prescribed point  $\mathbf{r}$  in space. This section summarises the required theoretical concepts in a consistent notation with the ultimate goal to express the radiance in terms of measurable quantities describing the current state of the optical medium (e.g. the Earth atmosphere). As the fundamental electromagnetic theory formulated through the Maxwell equations is quite general, several assumptions have to be made in order to arrive at a practically manageable theory. These assumptions will be addressed as well, since they typically limit the applicability of the theory to a subset of scenarios. Furthermore a sound understanding of the underlying approximations is a prerequisite to assess the results obtained from the respective theory. For a detailed treatise of any topic presented in the following sections, the textbook by Zdunkowski et al. (2007) is recommended to the interested reader including the many references therein.

### 3.1.1 The Radiative Transfer Equation

In textbooks on atmospheric radiative transfer, the radiance is typically introduced as the amount of energy  $dE$  propagating through a differential surface element  $d\mathbf{A}$  during the time  $dt$  in any direction covered by the solid angle  $d\Omega$  centred at the unit vector  $\hat{\mathbf{q}}$ :

$$dE = L(\mathbf{r}, \hat{\mathbf{q}}, t) \hat{\mathbf{q}} \cdot d\mathbf{A} d\Omega dt. \quad (3.1)$$

Interpreting the radiation as ray bundles, it is possible to derive the so-called radiative transfer equation (RTE) similar to a continuity equation based on phenomenological requirements (e.g. Zdunkowski et al., 2007, Chapter 2.1)

$$-\frac{1}{k_{\text{ext}}} \hat{\mathbf{q}} \cdot \nabla L = L - \frac{\omega_0}{4\pi} \int_{S^2} \mathcal{P}(\hat{\mathbf{q}}, \hat{\mathbf{q}}') L(\hat{\mathbf{q}}') d^2q' - \frac{1}{k_{\text{ext}}} J \quad (3.2)$$

with volume extinction coefficient  $k_{\text{ext}}(\mathbf{r}, \nu)$ , single scattering albedo  $\omega_0(\mathbf{r}, \nu)$ , scattering phase function  $\mathcal{P}(\mathbf{r}, \hat{\mathbf{q}}, \hat{\mathbf{q}}', \nu)$  and source term  $J(\mathbf{r}, \hat{\mathbf{q}}, \nu)$ . The dependence of the variables  $\mathbf{r}$ ,  $\hat{\mathbf{q}}$  and  $\nu$  has been omitted where possible without ambiguity to shorten the notation. Furthermore equation 3.2 implicitly contains the assumption of an infinite vacuum light speed  $c$ , i.e. it is obtained in the limit  $c \rightarrow \infty$ . This approximation is valid for atmospheric RT, since typical temporal variations are slow compared to the propagation of electromagnetic radiation. As a result the RTE does not explicitly depend on time, although the quantities occurring in equation 3.2 may of course be subject to temporal change. This situation can be

interpreted as a radiative equilibrium in analogy to equilibrium thermodynamics, which requires the RTE to hold for the entire medium at any fixed point in time.

It is remarkable, that the derivation of the RTE 3.2 from first principles (i.e. the Maxwell equations) is quite challenging. The main problem arises from the fact, that the energy flux in classical theory is specified through the mono-directional Poynting vector, whereas the radiance defined by 3.1 has to be known in all possible directions for a uniquely determined energy flux. Although the problem was apparently solved by Mishchenko (2002), the author argues in a later publication (Mishchenko, 2011), that the quantity  $L$  appearing in the such derived equation is not equivalent to the radiance introduced by equation 3.1. The differences however are subtle in nature and do not affect the results presented in this survey. Thus any solution to equation 3.2 is termed radiance within the following chapters and it is interpreted in accordance with equation 3.1.

Before addressing the solution of the RTE, it is insightful to take a closer look at the quantities appearing in equation 3.2. For a collimated beam of intensity  $I$  passing through a medium, the Beer-Lambert Law states, that the beam's attenuation over an infinitely small distance  $ds$  in the direction of propagation is proportional to its intensity

$$\frac{dI}{ds} = -k_{\text{ext}}I,$$

where the proportionality constant is the volume extinction coefficient  $k_{\text{ext}}(\nu, \mathbf{r})$ . Taking into account that attenuation of the beam can be caused by either scattering or absorption, it is logical to separate the respective contributions into a scattering coefficient  $k_{\text{sca}}$  and an absorption coefficient  $k_{\text{abs}}$

$$k_{\text{ext}} = k_{\text{sca}} + k_{\text{abs}}.$$

The single scattering albedo is defined as the ratio of scattering to extinction

$$\omega_0 := \frac{k_{\text{sca}}}{k_{\text{ext}}}.$$

The scattering process is formalised through the scattering phase function  $\mathcal{P}(\mathbf{r}, \hat{\mathbf{q}}, \hat{\mathbf{q}}', \nu)$ , which specifies the probability for radiation entering from a direction  $\hat{\mathbf{q}}$  to be scattered into the direction  $\hat{\mathbf{q}}'$ . Additionally it is convenient to introduce the dimensionless optical depth  $\tau(\mathbf{r}, \nu)$

$$d\tau := k_{\text{ext}} ds.$$

The source term  $J(\mathbf{r}, \hat{\mathbf{q}}, \nu)$  comprises the total amount of radiation emitted by the medium in the direction  $\hat{\mathbf{q}}$ , such as thermal emission or fluorescence.

Since analytical solutions of the RTE are generally very hard to calculate and known for only a handful of very simple cases, the equation has to be solved numerically for almost all atmospheric applications. Since even a numeric treatment of equation 3.2 can be very time consuming, an approximated version is commonly solved instead. The so-called plane-parallel approximation assumes, that the atmospheric constituents change only in vertical direction  $z$  and are homogeneous in each plane normal to  $z$ . Note that this implies a flat geometry, i.e. the curvature of Earth and atmosphere is disregarded. Furthermore all scattering media are assumed to be isotropic. As a result the scattering phase function depends solely on the product  $\hat{\mathbf{q}} \cdot \hat{\mathbf{q}}'$  of the directions of incoming and scattered radiation. It is important to state, though, that this assumption does not constrain the geometry of the individual scatterers to be spheres, but holds for arbitrary ensembles of randomly oriented particles independent of their shape.

The first step in incorporating the simplifications discussed above into the RTE is the so-called direct-diffuse splitting. The idea is to separate the radiance into a diffuse part  $L_d$  and a direct irradiance  $I$  representing the solar radiation incident on the surface in the direction  $\hat{\mathbf{q}}_0$

$$L = L_d + I\delta(\hat{\mathbf{q}} - \hat{\mathbf{q}}_0).$$

Insertion into equation 3.2 then results in an equation for the direct beam and another independent equation for the diffuse radiance. Choosing the coordinate system such that  $z = 0$  at TOA it is possible to express any unit vector in terms of the azimuthal angle  $\varphi$  with respect to the positive  $x$ -Axis and the zenith angle  $\vartheta$  with respect to the positive  $z$ -axis. Introducing the differential optical depth  $d\tau = k_{\text{ext}} dz$  allows to express the solution of the RTE for the direct beam as

$$I(\tau) = I_0 \exp\left(-\frac{\tau}{\mu_0}\right),$$

where  $I_0 = I(\tau = 0)$  is the solar constant at TOA and  $\mu_0 = \cos \vartheta_0$  is the cosine of the solar zenith angle. Limiting the emission of the medium to isotropic thermal radiation, the associated source term  $J_T$  can be written as

$$J_T := (1 - \omega_0(\tau)) B(\tau),$$

where  $B(\tau) = B(T(\tau))$  is the Planck function at temperature  $T$ . In this notation, the RTE for the diffuse radiance in the plane-parallel approximation reads as follows ( $\mu := \cos \vartheta$ ):

$$\mu \frac{d}{d\tau} L(\tau, \hat{\mathbf{q}}) = L(\tau, \hat{\mathbf{q}}) - \frac{\omega_0(\tau)}{4\pi} \int_{S^2} \mathcal{P}(\tau, \hat{\mathbf{q}} \cdot \hat{\mathbf{q}}') L(\tau, \hat{\mathbf{q}}') d^2 q' - J_T(\tau) - J_I(\tau, \hat{\mathbf{q}} \cdot \hat{\mathbf{q}}_0). \quad (3.3)$$

Observe that the index  $d$  for the diffuse radiance and the explicit wavenumber dependence of all quantities has been omitted. The additional source term

$$J_I := \frac{\omega_0(\tau)}{4\pi} \mathcal{P}(\tau, \hat{\mathbf{q}} \cdot \hat{\mathbf{q}}_0) I_0 \exp\left(-\frac{\tau}{\mu_0}\right)$$

originates from direct-diffuse splitting and describes the creation of diffuse radiation by scattering of the direct beam. Note that the  $z$ -dependence in equation 3.3 has been completely replaced by the optical depth  $\tau$ .

Since the phase function at each optical depth depends only on the vector product

$$\hat{\mathbf{q}} \cdot \hat{\mathbf{q}}' = \cos \theta := x$$

where  $\theta$  is the angle enclosed by the unit vectors, it is possible to expand  $\mathcal{P}$  into a series of Legendre Polynomials:

$$\mathcal{P}(x) = \sum_{l=0}^{\infty} (2l+1) p_l P_l(x). \quad (3.4)$$

The Legendre Polynomial  $P_l$  of order  $l$  is defined by

$$P_l(x) = \frac{1}{2^l l!} \frac{d^l}{dx^l} (x^2 - 1)^l$$

for  $|x| \leq 1$ . Introducing a scalar product

$$\langle f, g \rangle := \int_{-1}^1 f(x)g(x) dx$$

for any two square integrable functions  $f, g : [-1, 1] \rightarrow \mathbb{R}$  and the induced norm

$$\|f\|^2 := \langle f, f \rangle \quad (3.5)$$

it can be shown that the Legendre Polynomials are mutually orthogonal

$$\langle P_l, P_{l'} \rangle = \frac{2}{2l+1} \delta_{ll'}. \quad (3.6)$$

Consequently the coefficients  $p_l$  of the phase function can be calculated via

$$p_l = \frac{1}{2} \langle P_l, \mathcal{P} \rangle. \quad (3.7)$$

Using equation 3.6 it is straight forward to verify the following simple expression for the norm of the phase function

$$\|\mathcal{P}\|^2 = 2 \sum_{l=0}^{\infty} (2l+1) p_l^2.$$

Due to energy conservation the phase function must satisfy the normalisation condition

$$\frac{1}{4\pi} \int_0^{2\pi} \int_{-1}^1 \mathcal{P}(x) dx d\varphi = 1$$

leading to  $p_0 = 1$  independent of the scattering properties of the medium. The first moment  $p_1$  of the phase function is called the asymmetry parameter denoted by

$$g := \frac{1}{2} \int_{-1}^1 x \mathcal{P}(x) dx = p_1.$$

The term asymmetry parameter arises from the fact that  $g$  vanishes for any symmetric phase function  $\mathcal{P}$  satisfying

$$\mathcal{P}(x) = \mathcal{P}(-x)$$

and is thus a measure for the asymmetric fraction of the phase function. Henyey and Greenstein (1940) proposed a one parameter model for the phase function by choosing each expansion coefficient depending on the asymmetry parameter:

$$p_l = g^l.$$

The resulting phase function  $\mathcal{P}_{HG}$ ,

$$\mathcal{P}_{HG}(x) := \sum_{l=0}^{\infty} (2l+1) g^l P_l(x) = \frac{1-g^2}{(1+g^2-2gx)^{3/2}},$$

is called Henyey-Greenstein phase function. It is often used, if the exact scattering properties of a medium are not known, e.g. in cases where the asymmetry parameter has been determined experimentally for an otherwise unknown atmospheric aerosol mixture.

The development of the phase function into Legendre Polynomials lays the foundation for the solution of the RTE by means of the so-called discrete ordinate method. The fundamental idea behind this method is to express  $x$  in terms of the quantities  $\mu$  and  $\mu' = \cos \vartheta'$  determined by the angles the  $z$ -axis forms with



the unit vectors  $\hat{\mathbf{q}}$  and  $\hat{\mathbf{q}}'$ , respectively. This allows to separate the dependence on  $\varphi$  and  $\varphi'$  from the phase function. Expansion of the azimuth dependence of the radiance into a Fourier series

$$L(\tau, \hat{\mathbf{q}}) = \sum_{m=0}^{\infty} (1 - \delta_{0m}) L^m(\tau, \mu) \cos(m\varphi - m\varphi_0)$$

then leads to a system of coupled integro-differential equations for the Fourier coefficients  $L^m$ . These equations contain integrals over  $\mu'$  which can be evaluated numerically. Typically this involves Gauss-Legendre quadrature to approximate the integral over any function  $f : [-1, 1] \rightarrow \mathbb{R}$  by a weighted sum

$$\int_{-1}^1 f(x) dx \approx \sum_{i=1}^N w_i f(x_i). \quad (3.8)$$

Here each  $w_i$  is a constant weight and  $x_i$  is the  $i$ -th root of the Legendre Polynomial  $P_N$  of order  $N$ . The Gauss-Legendre quadrature can be shown to deliver exact results if  $f$  is a Polynomial of order  $M \leq 2N - 1$ . Evaluating the integrals of the RTE by the quadrature formula 3.8, one obtains a system of equations containing the radiance exclusively at discrete ordinates  $L^m(\tau, \mu_i)$ , with  $i = \pm 1, \dots, \pm N$ ,  $\mu_{-i} = -\mu_i$ . Thus the name discrete ordinate method. The  $L^m(\tau, \mu_i)$  are often referred to as streams and  $2N$  is called the number of streams. The factor of two arises from the fact, that integrals over the interval  $[-1, 1]$  are separated into two integrals over the upper and lower hemisphere to make sure that a sufficient number of streams is located close to the horizontal plane at  $\mu = 0$ . As the numerical quadrature is exact for Polynomials up to the order  $2N - 1$ , it is feasible to truncate all terms containing Legendre Polynomials of higher order from the expansion of the phase function. Stamnes et al. (1988) developed a numerically stable method to solve the resulting system of linear equations, which has been implemented in the publicly available DISORT code (see chapter 3.2.4).

### 3.1.2 Absorption and Emission by Gaseous Matter

This section describes the theory of gaseous absorption and emission. As shown previously (e.g. figure 2.20), the measured atmospheric spectra contain a variety of gas absorption/ emission features in the TIR, which are more or less hindering the planned extraction of information about the radiative properties of airborne particulate matter. In order to effectively isolate the desired properties, the gaseous absorption has to be modelled as accurately as possible, so that its effect can

be removed from the measured spectra. This section summarises the theory of gaseous absorption required to do so. Owing to the fact, that gaseous emission can be regarded as time-inverted absorption, the following discussion is limited to absorption.

### Absorption by individual transitions

Absorption of electromagnetic radiation by gas molecules is related to changes in the quantum-mechanical state of the molecules. A single photon of wavenumber  $\nu_0$  and energy  $E = hc\nu_0$  can be absorbed by a molecule, if the energy difference between initial state before the absorption and final state after the absorption satisfies

$$hc\nu_0 = E_f - E_i, \quad (3.9)$$

where  $E_i$  and  $E_f$  are the energies of lower (initial) and upper (final) state, respectively. Due to its comparatively low energy, TIR radiation typically causes transitions between different vibrational and/or rotational states of a molecule, in contrast to UV/Vis radiation, which typically excites different electronic states. In both cases it is observed in practice, that a given transition is not exclusively caused by photons with a single wavenumber  $\nu_0$  (satisfying equation 3.9). Instead, a given transition can be triggered by photons with wavenumbers located in a narrow continuous interval centred at  $\nu_0$ . This phenomenon –called line-broadening– is actually a combination of three different effects:

- Heisenberg’s uncertainty principle causes the energy of the molecule to be distributed over a finite interval due to the finite lifetime of the excited state. The process is termed natural line broadening
- The exchange of energy due to collision of neighbouring molecules during the photon-molecule interaction process can cause fluctuations in the energy levels of the quantum mechanical states leading to the so-called pressure broadening.
- At finite temperature the molecules possess kinetic energy in form of thermal motion. The associated finite speed in combination with the Doppler effect causes the energy of the photon in the reference frame of one molecule to differ from the energy perceived by another molecule at different speed. Hence molecules at different speed may absorb photons at slightly different wavenumber due to the so-called Doppler broadening.

The combination of these processes causes the spectral distribution of the absorbed energy – the line shape – to deviate from an ideal delta-shaped peak.

Before discussing the influence of the different broadening effects on the line shape, gaseous absorption is formalised with the introduction of the molecular absorption cross-section  $C_{\text{abs}}$  [cm<sup>2</sup>/molecule]:

$$k_{\text{abs}}(\nu) = n C_{\text{abs}}(\nu).$$

As before  $k_{\text{abs}}$  is the absorption coefficient and  $n$  is the molecular number density. For a gas mixture containing several species, the total absorption cross-section is obtained as sum over all species weighted by their respective volume mixing ratio  $c_m$

$$C_{\text{abs}} = \sum_{m=1}^{N_{\text{species}}} c_m C_{\text{abs}}^m$$

where  $C_{\text{abs}}^m$  symbolises the molecular absorption cross-section of molecule  $m$ . According to Van Vleck and Huber (1977) the cross-section of a given molecule can be written in the form

$$C_{\text{abs}} = \nu \tanh\left(\frac{hc\nu}{2k_B T}\right) \Phi_s(\nu). \quad (3.10)$$

Here  $\Phi_s$  is the symmetrised spectral density function

$$\Phi_s(\nu) = \sum_{l=1}^{N_{\text{lines}}} \tilde{S}_l(T) f(\nu, \nu_l).$$

The sum runs over all transitions (or lines)  $l$ , each characterised in terms of its temperature dependent intensity  $\tilde{S}_l$  [cm<sup>2</sup>/molecule] and its transition wavenumber  $\nu_l$ .  $f$  [cm] symbolises the transition independent line shape normalised to unity

$$\int_{-\infty}^{\infty} f(\nu, \nu_l) d\nu = 1.$$

Note that this normalisation condition is the reason not to include the hyperbolic tangent into the line shape function, since it typically causes the associated integral to diverge. Sometimes it is convenient, though, to introduce the intensity  $S$  [cm/molecule]

$$S_l(T) := \nu_l \tanh\left(\frac{hc\nu_l}{2k_B T}\right) \tilde{S}_l(T),$$

because the so-called radiation factor

$$R(\nu, \nu_l) = \frac{\nu \tanh\left(\frac{h\nu}{2k_B T}\right)}{\nu_l \tanh\left(\frac{h\nu_l}{2k_B T}\right)}$$

is approximately unity for wavenumbers significantly greater zero (including wavenumbers in the TIR). Thus one obtains the simpler expression

$$C_{\text{abs}} = \sum_{l=1}^{N_{\text{lines}}} S_l(T) R(\nu, \nu_l) f(\nu, \nu_l) \approx \sum_{l=1}^{N_{\text{lines}}} S_l(T) f(\nu, \nu_l)$$

for the absorption cross-section of the molecule, where the total amount of energy absorbed by a single transition over the whole spectrum is  $S_l$  and all information concerning line broadening is contained in  $f$ . The remaining task is to determine the line profile and the line intensity for each transition.

As natural line broadening is typically negligible compared to pressure and Doppler broadening under atmospheric conditions, only the latter two will be discussed here. As shown by Zdunkowski et al. (2007), pure pressure broadening results in a Lorentzian line shape of the form

$$f_L(\nu, \nu_0) = \frac{1}{\pi} \frac{\gamma_L}{(\nu - \nu_0)^2 + \gamma_L^2}$$

with HWHM  $\gamma_L$  scaling with temperature and pressure:

$$\gamma_L = \left(\frac{T_0}{T}\right)^{n_{\text{air}}} \frac{p}{p_0} [(1 - c_i)\gamma_{\text{air}} + c_i\gamma_{\text{self}}].$$

The self- and foreign broadening half-width  $\gamma_{\text{self}}$  and  $\gamma_{\text{air}}$ , respectively, are constants determined from laboratory experiments, which are available in tabulated form at a certain reference temperature  $T_0$  and reference pressure  $p_0$  for each transition. The scaling exponent  $n_{\text{air}}$  is an experimentally determined constant with a theoretical value of  $n_{\text{air}} = 0.5$  for an ideal gas. Since the measured value often deviates from this simple theoretical prediction, it is commonly tabulated for each transition, too.  $c_i$  designates the volume mixing ratio of the molecule under investigation in a mixture with foreign gases. All of the above mentioned quantities are included in the Hitran spectral database (Rothman et al., 2009) used throughout this thesis.

Since pressure broadening is caused by molecular collisions, it becomes weaker with increasing altitude as the pressure decreases and the mean free path length of the molecules increases. As a consequence Doppler broadening has to be taken into

account in the upper atmospheric regions. The profile function for pure Doppler broadening can be shown to be a Gaussian (Zdunkowski et al., 2007)

$$f_D(\nu, \nu_0) = \frac{1}{\sqrt{\pi}\gamma_D} \exp \left[ - \left( \frac{\nu - \nu_0}{\gamma_D} \right)^2 \right]$$

with HWHM (1/e decay)

$$\gamma_D = \nu_0 \sqrt{\frac{2k_B N_A T}{Mc^2}}$$

for a molecule with molar mass  $M$ . The influences of pressure and Doppler broadening can be combined into a single profile. This so-called Voigt-Line shape  $f_V$  is the convolution of the pure line shape functions for pressure and Doppler broadening

$$f_V(\nu, \nu_0) = (f_L * f_D)(\nu) = \frac{1}{\sqrt{\pi}\gamma_D} K(x, y).$$

$K(x, y)$ , defined as

$$K(x, y) = \Re w(x + iy) = \frac{y}{\pi} \int_{-\infty}^{\infty} \frac{e^{-t^2}}{y^2 + (x - t)^2} dt,$$

is the real part of the Faddeeva function  $w$  satisfying

$$w(z) = e^{-z^2} \left( 1 + \frac{2i}{\sqrt{\pi}} \int_0^z e^{t^2} dt \right).$$

The complex argument  $z = x + iy$  depends on transition wavenumber and on the half-widths of Doppler and Lorentz profile:

$$x := \frac{\nu - \nu_0}{\gamma_D}$$

$$y := \frac{\gamma_L}{\gamma_D}.$$

The relationship of the Voigt profile to the complex error function can be exploited for radiative transfer calculations, since efficient algorithms for the numerical evaluation of the complex error function are readily available. The rational approximation of Hui et al. (1977) has been chosen for the work presented in this thesis.

The final step to complete is the calculation of the line strength for every transition. This is conveniently achieved with a spectral database which contains line strengths

of all known transitions measured at a reference temperature  $T_0$ . Care has to be taken of the temperature dependence, though, which requires scaling of the tabulated values. According to Rothman et al. (1998) the line intensity can be calculated by

$$\tilde{S}(T) = \frac{8\pi^3}{3hc\varepsilon_0} \rho_l(T) d_l^2$$

with temperature independent dipole moment  $d_l$  and lower state population density

$$\rho_l(T) = g_l I_a \exp\left(-\frac{E_l}{k_B T}\right) Q^{-1}(T)$$

depending on lower state statistical weight  $g_l$ , isotopic abundance  $I_a$ , lower state energy  $E_l$  and total internal partition sum  $Q$ . The latter is obtained as product of the rotational and vibrational partition sums  $Q_{\text{rot}}$  and  $Q_{\text{vib}}$ . Thus the line intensity  $\tilde{S}(T)$  at an arbitrary temperature  $T$  is related to the value  $\tilde{S}(T_0)$  at reference temperature  $T_0$ :

$$\frac{\tilde{S}_l(T)}{\tilde{S}_l(T_0)} = \frac{\rho_l(T)}{\rho_l(T_0)} = \frac{Q_{\text{rot}}(T_0) Q_{\text{vib}}(T_0)}{Q_{\text{rot}}(T) Q_{\text{vib}}(T)} \exp\left[\frac{E_l}{k_B T_0} \left(1 - \frac{T_0}{T}\right)\right].$$

The quotient of the partition sums can be conveniently obtained using the following equations suggested by Norton and Rinsland (1991):

$$\begin{aligned} \frac{Q_{\text{rot}}(T_0)}{Q_{\text{rot}}(T)} &= \left(\frac{T_0}{T}\right)^\beta \\ \frac{1}{Q_{\text{vib}}(T)} &= \prod_{i=1}^N \left(1 - \exp\left[-\frac{hc\nu_i}{k_B T}\right]\right)^{d_i}, \end{aligned}$$

where the dimensionless scaling coefficient  $\beta$  and the vibrational state wavenumbers  $\nu_i$  with respective degeneracy  $d_i$  are constants for each isotope. According to Rothman et al. (1998) the Hitran database uses the approximation

$$\nu \tanh\left(\frac{hc\nu}{2k_B T}\right) \approx \nu_l \left[1 - \exp\left(-\frac{hc\nu_l}{k_B T}\right)\right],$$

which allows to infer the temperature scaled line intensity  $S_l$  at any given temperature  $T$  from the tabulated value at reference temperature  $T_0$  by means of the relation

$$\frac{S_l(T)}{S_l(T_0)} = \frac{\tilde{S}_l(T)}{\tilde{S}_l(T_0)} \frac{1 - \exp\left(-\frac{hc\nu_l}{k_B T}\right)}{1 - \exp\left(-\frac{hc\nu_l}{k_B T_0}\right)}.$$

### Continuum Absorption

Sometimes the line-by-line absorption theory presented in the previous sections yields unsatisfactory results for certain molecules or spectral bands when compared to benchmark spectroscopic measurements. This can e.g. be caused by transitions with a spectral line shape deviating from the assumed Voigt profile far away from the line centre. A prominent example for this behaviour is water vapour, which has long been known (Hettner, 1918) to possess a smoothly varying absorption cross-section over the atmospheric window region, which cannot be explained by line-by-line theory alone. In case of some other gases, the number of absorption lines for a small spectral interval is so large, that the resulting absorption cross-section is spectrally smooth and can be parametrised in terms of a simple analytical function depending on pressure and temperature to save computation time. In both cases it is desirable to amend line-by-line calculations with a so-called continuum or with some other form of parametrised cross-sections.

Although it is widely agreed upon, that the water vapour continuum has to be accounted for in numerous weakly absorbing bands from TIR to near infrared (NIR), it has to be stated that its origin is still a highly disputed matter. While some authors attribute its occurrence exclusively to far wing contributions of non-Lorentzian lines, others suggest a non-negligible influence of weakly bound water vapour dimers and collision induced absorption. Since a detailed discussion is beyond the scope of this thesis, the interested reader is referred to the work of Baranov and Lafferty (2012) for a detailed discussion of existing theories and recent developments.

Within this thesis the continuum formulation of Clough et al. (1989) has been adopted, which features an empirical unitless scaling function  $\chi$  to handle deviations of the actual line shape from the assumed profile function  $f$ :

$$\Phi_s(\nu) = \sum_{l=1}^{N_{\text{lines}}} \tilde{S}_l(T) \chi(\nu, \nu_l) f(\nu, \nu_l).$$

Since distortions of the Voigt line shape typically occur far from the line centre, Clough et al. (1989) proceed with the introduction of a continuum profile function

$$f_c(\nu, \nu_l) = \begin{cases} f(\nu_c, \nu_l) & |\nu - \nu_l| \leq \nu_c \\ f(\nu, \nu_l) & |\nu - \nu_l| > \nu_c \end{cases}$$

where  $\nu_c = 25 \text{ cm}^{-1}$  is the cut-off wavenumber of the assumed line profile  $f$ . The absorption cross-section of the continuum is then defined in complete analogy to

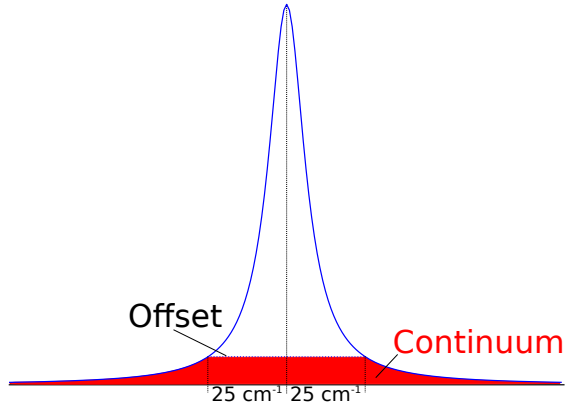


Figure 3.1: Definition of the MTCKD water vapour continuum: the red area symbolises the absorption contributed by the continuum, while the white area under the blue absorption line has to be added by line-by-line computations.

equation 3.10 with the modified continuum spectral density

$$\Phi_{\text{cont}} = \sum_{l=1}^{N_{\text{lines}}} \tilde{S}_l(T) \chi(\nu, \nu_l) f_c(\nu, \nu_l).$$

Thus the continuum amends the line-by-line calculations, in that the absorption in the spectral range  $|\nu - \nu_l| < \nu_c$  must be added separately and is not contained in the continuum. This is visualised in figure 3.1, which depicts the contribution of the continuum as red area. Note that the definition of  $f_c$  requires the offset  $f(\nu_c, \nu_l)$  to be removed from the assumed line shape  $f$  to avoid adding it twice (once by line-by-line calculations and once through the continuum). As  $\Phi_{\text{cont}}$  consists entirely of far-wing contributions, it is expected to vary slowly with wavenumber. Consequently it is sufficient to specify the continuum on a relatively coarse spectral grid, since spectral interpolation using e.g. a third order polynomial is typically very accurate. Furthermore, depending on the continuum, pressure and temperature scaling of the spectral density function can be performed using more or less heuristic simple relations, such that the number of required nodes can be further reduced, thus leading to a compact data set for the continua.



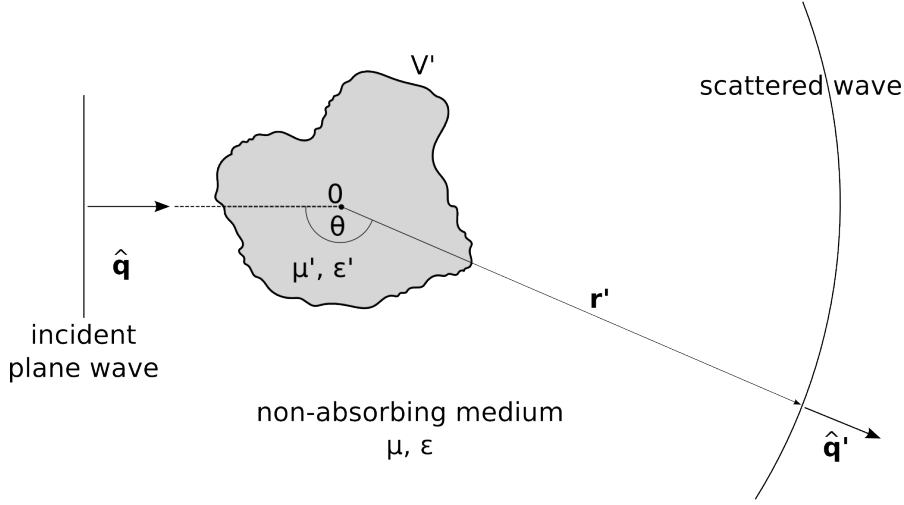


Figure 3.2: Scattering by a volume  $V'$  (grey) with permittivity  $\epsilon'$  and permeability  $\mu'$  different from the non-absorbing surrounding medium.

### 3.1.3 Scattering and Absorption by Small Particles

This section recapitulates the basic concepts needed to describe particulate matter in the context of radiative transfer theory, i.e. the scattering and absorption of electromagnetic radiation by small particles. Since entire books have been dedicated to the topic, it is beyond the scope of this thesis to provide more than a brief overview of the fundamental ideas. The interested reader is referred to the excellent textbooks of Mishchenko et al. (2002) or Bohren and Huffman (1998) for a detailed discussion of the matter.

The interaction of particulate matter with electromagnetic radiation is typically treated in form of the classical scattering problem depicted in figure 3.2: Assume a volume  $V' \subset \mathbb{R}^3$  with permittivity  $\epsilon'$  and permeability  $\mu'$  embedded in a non-absorbing volume  $V = \mathbb{R}^3 \setminus V'$  characterised in terms of permittivity  $\epsilon$  and permeability  $\mu$ . Given a homogeneous plane electromagnetic wave incident on  $V'$  in the direction of the unit vector  $\hat{\mathbf{q}}$ , find the scattered field at an arbitrary point  $\mathbf{r}'$  far away from the volume  $V'$ .

In order to tackle the problem mathematically, consider a plane electromagnetic wave

$$\mathbf{E}(\mathbf{r}, t) = \mathbf{E}_0 e^{i(k\hat{\mathbf{q}}\mathbf{r} - \omega t)},$$

with wave vector  $k = \sqrt{\epsilon\mu}\omega = 2\pi\mathcal{N}\nu$  depending on the refractive index

$$\mathcal{N} = c\sqrt{\epsilon\mu}.$$

The refractive index can be complex-valued in general and has vanishing imaginary part if and only if the scattering volume is non-absorbing. According to the Maxwell equations the vector  $\mathbf{E}_0$  is perpendicular to the direction of propagation  $\hat{\mathbf{q}}$ . Consequently it is beneficial to proceed in spherical coordinates by introducing unit vectors  $\hat{\boldsymbol{\phi}}$  and  $\hat{\boldsymbol{\theta}}$ , such that  $\hat{\mathbf{q}}$ ,  $\hat{\boldsymbol{\theta}}$  and  $\hat{\boldsymbol{\phi}}$  are mutually perpendicular. Since these requirements leave the freedom to rotate  $\hat{\boldsymbol{\theta}}$  and  $\hat{\boldsymbol{\phi}}$  around  $\hat{\mathbf{q}}$  by an arbitrary angle, the plane normal to  $\hat{\boldsymbol{\phi}}$  has to be specified for a uniquely determined orthonormal base. Common choices found in literature are either the so-called meridional plane containing the  $z$ -axis of the laboratory frame or the scattering plane spanned by incident and scattered beam.

Application of the Maxwell equations to the such described scattering problem yields a spherical wave as solution for the scattered field at any point  $\mathbf{r}' = r\hat{\mathbf{q}}'$  far away from the origin. The components  $E'_\theta$  and  $E'_\phi$  are usually defined with respect to the unit vectors  $\hat{\boldsymbol{\theta}}'$  and  $\hat{\boldsymbol{\phi}}'$  perpendicular to  $\hat{\mathbf{q}}'$ . Decomposing  $\mathbf{E}_0$  into components  $E_{0\theta}$  and  $E_{0\phi}$  in the direction of  $\hat{\boldsymbol{\theta}}$  and  $\hat{\boldsymbol{\phi}}$ , respectively, it is possible to relate scattered and incident field by means of the amplitude scattering matrix  $\mathbf{S}$

$$\begin{pmatrix} E'_\theta(r\hat{\mathbf{q}}') \\ E'_\phi(r\hat{\mathbf{q}}') \end{pmatrix} = \frac{1}{r} e^{ikr} \begin{pmatrix} S_{11} & S_{12} \\ S_{21} & S_{22} \end{pmatrix} \begin{pmatrix} E_{0\theta} \\ E_{0\phi} \end{pmatrix}. \quad (3.11)$$

The components  $S_{ij}$  of the amplitude scattering matrix depend on geometry and refractive index of the scattering medium, on the directions  $\hat{\mathbf{q}}$  and  $\hat{\mathbf{q}}'$  and on the choice of the associated reference planes for the vectors  $(\hat{\boldsymbol{\theta}}, \hat{\boldsymbol{\phi}})$  and  $(\hat{\boldsymbol{\theta}}', \hat{\boldsymbol{\phi}}')$ . Customarily the amplitude scattering matrix is specified with respect to the meridional plane. Due to the linearity of the Maxwell equations it is possible to calculate the scattered field for an arbitrary incident field expressible as superposition of plane waves by means of equation 3.11, if the amplitude scattering matrix is known.

Although the amplitude scattering matrix completely characterises the scattering process in the far-field zone, it has the disadvantage of doing so in terms of the electric fields, which are hard to measure from an experimental point of view. Instead, most optical devices measure energy fluxes proportional to quadratic combinations of the electric field. Hence it is advantageous to introduce the so-called Stokes vector  $\mathbf{I} := (I, Q, U, V)^T$  consisting of four real-valued, linearly independent components quadratic in  $E_{0\theta}$  and  $E_{0\phi}$ , which are scaled to take on the unit of a spectral energy flux:

$$\mathbf{I} = \frac{1}{2} \sqrt{\frac{\varepsilon}{\mu}} \begin{pmatrix} |E_{0\theta}|^2 + |E_{0\phi}|^2 \\ |E_{0\theta}|^2 - |E_{0\phi}|^2 \\ -2\Re\{E_{0\theta}E_{0\phi}^*\} \\ 2\Im\{E_{0\theta}E_{0\phi}^*\} \end{pmatrix}.$$

The set  $\{I, Q, U, V\}$  can be shown to form a basis of all real-valued, time-independent binary combinations constructible from the components of the incident field  $\mathbf{E}$ . This means, that any observable quadratic in the electric field (i.e. all quantities typically measured by optical instruments) can be expressed by the Stokes vector. The first component  $I$ —the intensity—is related to the three other components  $Q$ ,  $U$  and  $V$ , which describe the polarization state of the monochromatic wave, by

$$I^2 = Q^2 + U^2 + V^2.$$

Equation 3.11 can also be expressed in terms of the Stokes vectors  $\mathbf{I}$  and  $\mathbf{I}'$  of incident and scattered field:

$$\mathbf{I}' = \frac{1}{r^2} \mathbf{Z} \cdot \mathbf{I}.$$

The coefficients of the Stokes phase matrix  $\mathbf{Z} \in \mathbb{R}^{4 \times 4}$  are linear combinations of binary products of  $S_{ij}$  (Mishchenko et al., 2002, p. 51). As was the case with the amplitude scattering matrix, the coefficients of  $\mathbf{Z}$  depend on the choice of reference planes for incident and scattered beam. Typically the term phase matrix is used for the representation based on the meridional plane, while the so-called scattering matrix  $\mathbf{F}$  is customarily associated with the scattering plane. The formalism introduced up to this point allows to describe the scattering properties for an arbitrary particle in terms of either the amplitude scattering matrix  $\mathbf{S}$  or the scattering Matrix  $\mathbf{F}$ .

For a rotation averaged particle of arbitrary shape, the scattering matrix has the convenient property to consist of only six non-trivial dimensionless coefficients:

$$\mathbf{F}(\Theta) = \frac{C_{\text{sca}}}{4\pi} \begin{pmatrix} a_1(\Theta) & b_1(\Theta) & 0 & 0 \\ b_1(\Theta) & a_2(\Theta) & 0 & 0 \\ 0 & 0 & a_3(\Theta) & b_2(\Theta) \\ 0 & 0 & -b_2(\Theta) & a_4(\Theta) \end{pmatrix}.$$

The coefficients  $a_i$  and  $b_j$  depend on the scattering angle  $\Theta$  and on geometry and refractive index of the scattering medium  $V'$ . In particular,  $a_1$  is identical to the scattering phase function  $\mathcal{P}$ . It is noteworthy, that the scattering matrix for a spherical particle is similar to the scattering matrix for a rotation averaged particle with the additional constraints  $a_2 \equiv a_1$  and  $a_3 \equiv a_4$ . Consequently it is possible to distinguish spherical particles from orientation averaged non-spherical particles by means of the so-called linear depolarisation ratio

$$\delta_l := \frac{a_1(\pi) - a_2(\pi)}{a_1(\pi) + a_2(\pi)}. \quad (3.12)$$

Obviously  $\delta_l$  (which is e.g. experimentally deducible from LIDAR observations) vanishes for a mixture of spherical particles, while it is in general non-zero for an ensemble of non-spherical particles.

An elegant method to determine the scattering matrix  $\mathbf{F}$  for a particle of arbitrary shape, is the T-Matrix approach introduced by Waterman (1965). This approach involves the expansion of the time-independent part of the incoming plane wave  $\mathbf{E}$  and the scattered field  $\mathbf{E}'$  into vector spherical wave functions  $\mathbf{M}_{mn}$ ,  $Rg\mathbf{M}_{mn}$ ,  $\mathbf{N}_{mn}$ ,  $Rg\mathbf{N}_{mn}$  (c.f. Appendix C in Mishchenko et al., 2002)

$$\begin{aligned}\mathbf{E}(\mathbf{r}) &= \sum_{n=1}^{\infty} \sum_{m=-n}^n [a_{mn} Rg\mathbf{M}_{mn}(k_1\mathbf{r}) + b_{mn} Rg\mathbf{N}_{mn}(k_1\mathbf{r})] \\ \mathbf{E}'(\mathbf{r}) &= \sum_{n=1}^{\infty} \sum_{m=-n}^n [p_{mn} \mathbf{M}_{mn}(k_1\mathbf{r}) + q_{mn} \mathbf{N}_{mn}(k_1\mathbf{r})],\end{aligned}$$

where the coefficients  $a_{mn}$  and  $b_{mn}$  are obtainable analytically for a plane wave. Due to the fact that the Maxwell-Equations are linear, the coefficients  $p_{mn}$  and  $q_{mn}$ , describing the scattered field, are linearly related to the coefficients of the incident field:

$$p_{mn} = \sum_{n=1}^{\infty} \sum_{m=-n}^n [T_{mnm'n'}^{11} a_{m'n'} + T_{mnm'n'}^{12} b_{m'n'}] \quad (3.13)$$

$$q_{mn} = \sum_{n=1}^{\infty} \sum_{m=-n}^n [T_{mnm'n'}^{21} a_{m'n'} + T_{mnm'n'}^{22} b_{m'n'}] \quad (3.14)$$

The coefficients  $T_{mnm'n'}^{ij}$  form the so-called transition- or T-matrix. Converting the last equation to a generalised matrix notation, the choice of the name transition matrix becomes apparent:

$$\begin{pmatrix} \mathbf{p} \\ \mathbf{q} \end{pmatrix} = \begin{pmatrix} \mathbf{T}^{11} & \mathbf{T}^{12} \\ \mathbf{T}^{21} & \mathbf{T}^{22} \end{pmatrix} \begin{pmatrix} \mathbf{a} \\ \mathbf{b} \end{pmatrix}.$$

Note that all relevant geometric and optical properties of the scattering medium are contained in the T-Matrix, whereas it is independent of the incoming and scattered fields. This is advantageous if several computations with the same particle in different orientations have to be performed, because the T-Matrix has to be computed only once. Moreover Mishchenko (1991) proposed a method to analytically express the orientation averaged T-Matrix in terms of the T-Matrix for an arbitrarily oriented particle. This technique incurs a considerable speed up for numerical computations of orientation averaged particles. The fundamental

character of the T-Matrix formalism is underlined by the fact, that it leads to the exact solution of Mie (1908) for spherical particles.

The only major draw back of the T-Matrix approach is its numerical instability inside certain parameter regions. Typically the T-Matrix is computed from an expression of the form

$$\mathbf{T} = -(\mathbf{RgQ}) \cdot \mathbf{Q}^{-1}, \quad (3.15)$$

where the coefficients of the matrices  $\mathbf{Q}$  and  $\mathbf{RgQ}$  are defined in terms of surface integrals of products of vector spherical wave functions over the scattering volume  $\partial V'$ . Since these matrices are of infinite dimension (as is the T-Matrix), they have to be truncated at some upper limit  $n = n_{\max}$  to be of practical use. This is equivalent to a truncation of the respective sums 3.13 and 3.14. Unfortunately it turns out, that the matrix  $\mathbf{Q}$  becomes ill-conditioned for large particles or extreme choices of the refractive index. This prohibits the application of the T-Matrix approach in these cases, because the required inversion of  $\mathbf{Q}$  is numerically unstable.

Once the optical properties for a single particle have been calculated, they can be used as input to radiative transfer calculations. The latter typically require the average absorption- and scattering coefficient for an ensemble of particles, which are defined in complete analogy to gaseous absorption:

$$\begin{aligned} k_{\text{abs}} &= nC_{\text{abs}} \\ k_{\text{sca}} &= nC_{\text{sca}}, \end{aligned}$$

$C_{\text{abs}}$  [cm<sup>2</sup>/particle] and  $C_{\text{sca}}$  [cm<sup>2</sup>/particle] are the absorption- and scattering cross-section for a single particle, respectively, while  $n$  [particles/cm<sup>3</sup>] specifies the number of particles per unit volume. To allow for a generic treatment of particles with different shapes, the geometry of a particle is assumed to be representable in terms of a characteristic length  $R$  and a vector  $\boldsymbol{\xi}$  of dimensionless shape parameters. Either the radius  $R_V$

$$R_V := \left( \frac{3V'}{4\pi} \right)^{\frac{1}{3}}$$

of a sphere with same volume  $V'$  as the scatterer or the radius  $R_S$

$$R_S := \sqrt{\frac{A'}{4\pi}}.$$

of a sphere with equal surface area  $A'$  are customarily chosen as characteristic lengths.

Within the scope of this thesis all particles are assumed to be homogeneous, thus allowing to express their material properties in terms of a single complex refractive index  $\mathcal{N}$ . It turns out, that the surface integrals occurring during the computation of  $Rg\mathbf{Q}$  and  $\mathbf{Q}$  contain wavenumber and length exclusively in form of a dimensionless size parameter

$$x_V = 2\pi\nu R_V.$$

Similarly it is not the real part of the refractive index, but the quotient

$$n_r = \frac{\Re\{\mathcal{N}'\}}{\Re\{\mathcal{N}\}}$$

which determines these integrals. The introduction of the quantities  $x_V$  and  $n_r$  results in a dimensionless formulation of the entire scattering theory. The associated output quantities are the so-called scattering- and absorption efficiencies

$$Q_{\text{abs}} = \frac{C_{\text{abs}}}{\pi R_S^2}$$

$$Q_{\text{sca}} = \frac{C_{\text{sca}}}{\pi R_S^2}.$$

and the normalised phase matrix

$$\tilde{\mathbf{F}} = \frac{4\pi}{C_{\text{sca}}} \mathbf{F}.$$

Introducing the surface equivalent size parameter  $x_S$  in complete analogy to its volume equivalent counterpart  $x_V$

$$x_S = 2\pi\nu R_S,$$

absorption and scattering cross-section can be written as

$$C_{\text{abs}} = \frac{x_S^2}{4\pi\nu^2} Q_{\text{abs}}$$

$$C_{\text{sca}} = \frac{x_S^2}{4\pi\nu^2} Q_{\text{sca}}.$$

Up to this point particles have been restricted to be all of the same size, the same geometry and the same refractive index. This assumption is typically not valid for atmospheric aerosols, which differ considerably in size, composition and shape. To

formalise the treatment of such heterogeneous mixtures, let  $C_{\text{sca}}(R_V, \boldsymbol{\xi}, \mathcal{N})$  be the scattering cross-section for each individual (rotation averaged) particle included in the mixture. The average aerosol scattering cross-section is then obtained as weighted average

$$C_{\text{sca}} = \int_0^\infty \int_0^\infty \int_{\mathcal{G}} C_{\text{sca}}(R_V, \boldsymbol{\xi}, \mathcal{N}) \psi(R_V, \boldsymbol{\xi}, \mathcal{N}) d^p \xi d\mathcal{N} dR_V$$

with normalised weighting function  $\psi(R_V, \boldsymbol{\xi}, \mathcal{N})$  satisfying

$$\int_0^\infty \int_0^\infty \int_{\mathcal{G}} \psi(R_V, \boldsymbol{\xi}, \mathcal{N}) d^p \xi d\mathcal{N} dR_V = 1.$$

Here  $p$  is the number of geometry parameters contained in the vector  $\boldsymbol{\xi}$  and  $\mathcal{G}$  symbolises the  $p$ -dimensional space of all possible combinations of geometry parameters. An identical equation holds for the absorption cross-section, which is obtained by replacing  $C_{\text{sca}}$  with  $C_{\text{abs}}$  everywhere. Finally the averaged phase function is obtained from the averaged scattering matrix

$$\mathcal{P}(\Theta) = \frac{1}{C_{\text{sca}}} \int_0^\infty \int_0^\infty \int_{\mathcal{G}} C_{\text{sca}}(R_V, \boldsymbol{\xi}, \mathcal{N}) a_1(\Theta, R_V, \boldsymbol{\xi}, \mathcal{N}) \psi(R_V, \boldsymbol{\xi}, \mathcal{N}) d^p \xi d\mathcal{N} dR_V.$$

Note that the elements of the normalised scattering matrix have to be weighted by their respective scattering cross-section, since it is the absolute amount of scattered energy that has to be averaged and not the relative fraction.

## 3.2 Model Description

This section describes the RT model implemented within the scope of this thesis. The design goal was to create an object oriented, versatile and well documented radiative transfer library with special focus on concurrent processing. Naturally the question might arise, why a new implementation is necessary considering the manifold of available free and commercial codes. The main reason is, that development on most of the available codes (e.g. MODTRAN (Berk et al., 2006), LBLRTM (Clough et al., 2005), LibRadTran (Mayer and Kylling, 2005)) began fifteen or more years ago. Consequently several recent developments in both software and hardware could not be accounted for in the design phase of these models, resulting in code which is not state of the art by today's standards.

As most of the scientific programs written during their time, the available radiative transfer models have been written in either FORTRAN or C, because both languages have a reputation of being "fast". Since neither FORTRAN nor C provided support for object oriented programming when these models were designed, this programming paradigm has not been considered. In the meantime object oriented programming has become a de-facto standard for complex projects, because it fosters modular programming and data encapsulation, which both tend to increase code re-usability as well as maintenance efficiency. Since most modern compilers have improved significantly in terms of optimisation, the afore mentioned benefits are available without significant runtime overhead compared to non object oriented code.

The programming language for the implementation of the library has been chosen to be C++, mainly because of its support for templates, i.e. code blocks executed at compile time. In combination with a technique called template meta programming, this allows to write very generic and yet highly efficient code. It is e.g. possible to implement an algorithm once and then run it with any floating point type available on the respective platform from 16-bit to 128-bit precision. Without templates this task typically involves implementing the same algorithm once for each datatype. Apart from the reduction in the amount of code to maintain, template meta programming also enables the use of static polymorphism. The latter has e.g. been used excessively in the Eigen linear algebra library (<http://eigen.tuxfamily.org>), which is written exclusively in C++ and which typically yields better results in benchmark tests on execution speed than the reference FORTRAN implementations of LAPACK (<http://www.netlib.org/lapack>) and BLAS (<http://www.netlib.org/blas>).

Regarding recent developments in CPU technology it becomes apparent that ad-



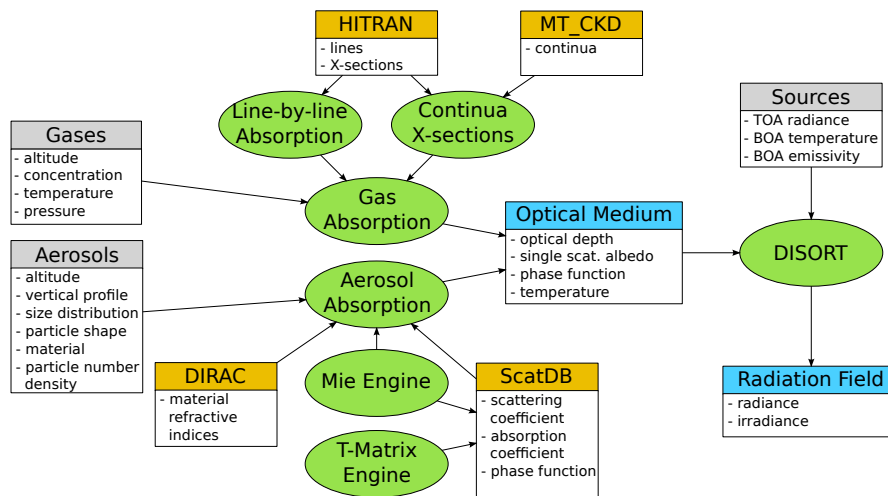


Figure 3.3: A flow diagram of the forward radiative transfer model included with PIRATES: Input quantities are shown as grey boxes, while green ellipses symbolise processing classes. Orange boxes indicate lookup tables and databases, whereas blue boxes contain output quantities storable on disk.

vances in performance are not achieved by means of an increased clock speed any more. Instead modern processors are equipped with hardware capable of performing an increased number of tasks simultaneously (concurrency) using multi-core architectures or hyper-threading (Sutter, 2005). As a result parallelization of algorithms and programs has become a major concern for software developers, since concurrent software is required to capitalise on such hardware improvements: while every program gains in terms of execution speed from a processor working at a higher clock rate, only algorithms specifically designed to distribute work among different processors can exploit advances in concurrency. Sutter (2005) pointedly summarises this recent development with the words: 'The free lunch is over'.

Based on the requirements discussed above, several algorithms for typical tasks occurring in computational radiative transfer were compiled into a library. This library was named Programmer's Interface to RAdiative TransfER algorithms (PIRATES) indicating that is rather a collection of existing algorithms under a consistent application programming interface (API) than a development of novel algorithms. Main features are

- Calculation of gas optical properties using concurrent line-by-line calculations, continua and parametrised cross-sections
- Concurrent calculation of aerosol optical properties using Mie- or T-Matrix theory

- A database containing the refractive index of a variety of different common aerosol constituents
- A database for the optical properties of non-spherical particles
- A solver for the radiative transfer equation using the discrete ordinate method

Apart from these features, which are implemented as API, a front-end consisting of a variety of small tools was added, which makes many algorithms included in the API accessible from the command line. From the beginning on, great emphasis has been placed on thorough documentation, due to the hard learned fact, that even very well written code is seldom self-explanatory.

Figure 3.3 shows a flow diagram of the PIRATES Forward Radiative Transfer Engine (PFORTE), which uses all major features provided by the library. Grey boxes indicate the input parameters describing the atmospheric state, which are forwarded to the program in form of an atmosphere file. Green ellipses symbolise functors performing data processing, such as calculation of aerosol optical properties from the input data or solution of the RTE. Orange boxes represent databases storing pre-processed or external data, such as single scattering properties of single particles or the individual transitions of each atmospheric gas required for line-by-line calculations. Blue boxes contain the output quantities of the model. In the following sections each of the different components will be briefly discussed.

### 3.2.1 Model Input

The configuration of the forward model is passed to the PFORTE executable in form of a single text file. This file contains all input options and user defined parameters as well as the path to several other input- and output files. All files except for the configuration file are stored in Version 5 of the Hierarchical Data Format (HDF5), a self-explanatory binary data format provided free of charge by the HDF group via their website <http://www.hdfgroup.org>. HDF5 allows to share binary data in a platform independent way and provides bindings for the programming languages C, C++, FORTRAN, Python and Java.

The most import among the HDF5 input files is the model atmosphere specifying the vertical distribution of aerosols and gases. Apart from vertical profiles of temperature, pressure and volume mixing ratio for each atmospheric gas, it may include an arbitrary number of aerosols and clouds. Each aerosol/ cloud is modelled as a homogeneous layer with user defined upper and lower boundary.

Furthermore particle size distribution, refractive index and particle shape can be chosen independently for each of these layers. The refractive index can be specified in form of a fixed value or in terms of a material name. In the latter case the refractive index of the respective material will be imported from the Database for the Index of Refraction of Aerosol Components (DIRAC), which consists of a single HDF5 file and contains a compilation of several published refractive index data sets including relevant meta-information such as author, publication date or measurement-technique. Several command line tools allow the manipulation of the atmosphere file e.g. by ingestion of a radiosonde profile or the creation and import of aerosols.

### 3.2.2 Gas Absorption

The gas optical depth at each wavenumber is calculated from temperature, pressure and abundance of the respective atmospheric species by either parametrised cross-sections or a combination of line-by-line and continuum absorption as described in chapter 3.1.2. The parameters for each molecular transition and the parametrised cross-sections are specified in a separate spectroscopic database file. This file currently includes the lines and infrared cross-sections provided by the high-resolution transmission molecular absorption database (HITRAN) (Rothman et al., 2009) available via <http://www.cfa.harvard.edu/hitran>. The original HITRAN data spread across different ASCII text files has been compiled into a single HDF5 file in order to speed up input- and output operations and to facilitate searching and updating the database. The conversion from native text files into the spectroscopic database format is conveniently performed by one of the command-line tools distributed with PIRATES. In addition to the parameters provided by HITRAN, the temperature scaling exponent  $\beta$  of the rotational partition sum published by Norton and Rinsland (1991) is included in the spectroscopic database file, because it is not provided by HITRAN. A Voigt line profile is assumed for all lines independent of pressure and distance from the line centre.

Since PIRATES includes an implementation of the first order and full CO<sub>2</sub> line mixing models described by Lamouroux et al. (2010), the associated additional parameters can be included in the spectroscopic database file as well. However, the influence of line mixing in the atmospheric window domain is so small, that line mixing has been disabled for all computations presented in thesis to accelerate the simulations.

In theory, line-by-line calculations require to add up the Voigt profiles for all lines of a given gas at each wavenumber and altitude (i.e. for each pressure-temperature

pair). A straightforward implementation of this procedure is typically not feasible, since the required number of Voigt function evaluations is too time consuming. Instead it is beneficial to exploit the low spectral variation of the Voigt profile far off the line centre. The so-called multi-grid technique suggested by Fomin (1995) follows this approach by calculating each part of a given absorption line on the coarsest possible spectral grid, which allows interpolation onto finer grids with a defined error. Thus the total number of necessary evaluations of the Voigt profile is reduced, leading to a considerable decrease in computational effort. PIRATES contains a variant of this multi-grid technique described by Kuntz and Hoepfner (1999), which features a more accurate estimation of the interpolation error.

In addition to the line-by-line parameters, HITRAN offers parametrised cross-sections for several larger molecules less abundant in the Earth atmosphere. These parametrisations, which consist of tabulated absorption coefficients for each gas at a number of pressure-temperature pairs, are stored in the spectroscopic database, too. They are interpolated linearly in pressure-temperature space and are added to the gas absorption using a cubic polynomial in wavenumber space. In contrast to this, the Mlawer-Tobin-Clough-Kneizys-Davies (MTCKD) coefficients of the symmetrised spectral density require more complex scaling and interpolation. Unfortunately there exists no documentation of the exact theory behind MTCKD apart from the very general description provided by Clough et al. (2005). Consequently the computation of the coefficients had to be reverse-engineered from the original source code. A re-implementation became necessary due to the fact, that the original FORTRAN code is inherently thread-unsafe and cannot be used in a concurrent implementation. It is noteworthy that the re-implementation revealed a software bug causing a  $5 \text{ cm}^{-1}$  shift in the original oxygen continuum, which has been fixed in MTCKD version 2.5.2.

Currently PIRATES includes the MTCKD continua for  $\text{H}_2\text{O}$ ,  $\text{CO}_2$ ,  $\text{N}_2$  and  $\text{O}_2$ . It has to be noted though, that in contrast to the HITRAN line parameters, which are based on very well documented laboratory studies, the continua are based on a poorly documented semi-empirical model. The parametrisation of the power spectral density function seems to depend predominantly on spectral atmospheric measurements. The extent to which biases in these measurements (e.g. due to an incorrectly modelled atmospheric state caused by the presence of aerosols) affect the continua is not clear and could introduce a non-negligible source of error. Indeed recent studies by Ptashnik et al. (2012) indicate, that the parametrisation of MTCKD deviates significantly from laboratory measurements in several NIR windows. Unfortunately MTCKD is the only publicly available continuum model the author is currently aware of, such that it is used for a lack of superior alternatives.

The entire gas absorption calculation has been implemented to allow parallel processing of different atmospheric levels using the thread model of the C++ standard library, causing a considerable increase in speed on multi-core architectures. Using e.g. an Dell PowerEdge R515 server with 12 AMD Opteron cores at 2.1 GHz, the total computation time can be decreased by a factor of twelve compared to calculations using only a single processor on the same machine. This indicates that the parallelization is achieved without noticeable overhead.

### 3.2.3 Absorption by Particulate Matter

The inclusion of aerosols into (scalar) radiative transfer requires the conversion of the microphysical description in terms of refractive index and geometry into optical properties consisting of absorption efficiency, scattering efficiency and the scattering phase function for each particle. Apart from the online calculation of these properties for spherical particles, PIRATES offers the possibility to pre-calculate optical properties of non-spherical and spherical particles and store them in a database. This is advantageous e.g. for time consuming T-Matrix calculations to avoid repetitive computations of similar particles. Although spherical particles can be stored in the database as well, there is little gain in terms of speed compared to the online calculation, because the Mie-algorithm is almost as fast as the lookup and interpolation from pre-calculated data.

The Mie-engine included in PIRATES for the processing of spherical particles is based on the algorithm of Wiscombe (1980). Since the original implementation is written in FORTRAN and does not allow for concurrent execution, it has been ported to C++ to enable the computation of several particles in parallel. Within the course of this re-implementation, the memory management has been changed from static to dynamic, which theoretically allows for the calculation of arbitrarily large particles, provided sufficient memory is available.

As mentioned before, PIRATES is capable of importing optical properties of non-spherical particles from a database. The database provides interfaces to import data from the scattering databases of Schmidt et al. (2009) and Otto (2012). Furthermore it is possible to add new data to the database with a T-Matrix engine for spherically symmetric particles (spheroids, cylinders and Chebyshev particles). The T-Matrix code is based on the algorithm of Mishchenko and Travis (1998). Again the original FORTRAN implementation has been ported to C++ for the sake of parallelization and the originally static memory management has been replaced by a dynamic one.

Within PIRATES the scattering phase function is always represented in terms

of its expansion in Legendre moments  $p_l$  as defined by equation 3.7. This has the advantage, that the phase function can be calculated at arbitrary scattering angles without the need for interpolation. With respect to the scattering database another advantage arises for small particles, which can typically be modelled using only a few moments, thus leading to a considerable decrease in required storage space. Both, the Mie code and the T-Matrix code, have the convenient property to directly deliver the expansion coefficients of the phase function. This results in a truncation of the infinite sum (3.4) at the optimal number of terms, as shown by Sekera (1952) for the Mie solution and by Mishchenko (1991) for the T-Matrix formalism.

Although the database is capable of handling arbitrary geometric shapes, it currently contains exclusively spheroids. A spheroid is a two-dimensional surface in three-dimensional euclidean space defined by the equation

$$\frac{x^2}{b^2} + \frac{y^2}{b^2} + \frac{z^2}{a^2} = 1. \quad (3.16)$$

$a$  and  $b$  are called the semi-axes of the spheroid and their ratio

$$AR = \frac{a}{b} \quad (3.17)$$

is called the aspect ratio. The Volume of a spheroid is given by

$$V = \frac{4}{3}\pi ab^2 = \frac{4}{3}\pi AR b^3. \quad (3.18)$$

In accordance with section 3.1.3 each spheroid in the database is uniquely defined in terms of its volume equivalent radius

$$R_V = b \sqrt[3]{\frac{4}{3}\pi AR} \quad (3.19)$$

and its aspect ratio  $AR$ .

As indicated in chapter 3.1.3, the single scattering properties of a single particle have to be averaged before they are passed to the radiative transfer solver. Within PIRATES, each aerosol may consist of an arbitrary number of particle ensembles, where all particles in one ensemble share the same refractive index and geometry (i.e. aspect ratio). The volume equivalent radii of particles in a given ensemble are assumed to be distributed according to a log-normal or gamma distribution.

The log-normal distribution is a single-tailed probability distribution of any random variable whose logarithm is normally distributed. The probability density

function  $\psi(x)$  for a log-normal distribution is given by the formula

$$\psi(x) = \frac{1}{x\sigma\sqrt{\pi}} \exp \left[ -\frac{1}{\sigma^2} \left( \ln \frac{x}{x_0} \right)^2 \right]. \quad (3.20)$$

The parameters  $x_0$  and  $\sigma$  define the maximum and width of the distribution, respectively.

The gamma distribution is often applied to describe the droplet number concentration in water clouds. It is defined in terms of the shape parameter  $k$  and the scale parameter  $\theta$ :

$$\psi(x) = \frac{1}{\theta \Gamma(k)} x^{k-1} \exp \left( -\frac{x}{\theta} \right)$$

where

$$\Gamma(k) = \int_0^{\infty} t^{k-1} e^{-t} dt$$

is the Gamma function.

### 3.2.4 Discrete Ordinate Solver

Once optical depth, single scattering albedo and scattering phase function have been calculated for gases and aerosols as outlined in the previous sections, the remaining task is to solve the RTE. Currently PIRATES features the discrete ordinate method described in section 3.1.1. The freely available DISORT code described in detail by Stamnes et al. (2000) has been chosen, since it emerged as one of the de-facto standards for benchmark radiative transfer computations over the last two decades. As the original code has been implemented in FORTRAN, it has been partly ported to C++, to enable dynamic memory management and to allow for concurrent invocation of the program. This allows to solve the RTE for several wavenumbers in parallel on multi-core CPUs with PIRATES. The plane-parallel approximation made by DISORT is a good approximation for the ground based measurements of the downwelling radiation and for space-borne nadir observations, since the curvature of the Earth surface and the spherical geometry of the atmosphere have a negligible effect in these cases. Since the discrete ordinate method constitutes a quasi-exact solution of the RTE for plane-parallel geometries, it is a suitable choice for benchmark computations and closure experiments, because it limits the number of computational and algorithmic uncertainties to a minimum and still offers a reasonable execution time for numeric simulations.

### 3.3 Model Validation

In order to make sure, that the results created with the PIRATES tools are accurate, a large number of unit tests has been added to the library to test each component individually. Since a discussion of each single test is far beyond the scope of this thesis, this chapter contains summarises of the most important tests, which ensure the main modules introduced in the previous sections work as expected. The tests presented in the following sections encompass purely numerical inter-simulation comparisons as well as validations against measurements with benchmark instruments.

#### 3.3.1 DISORT

The discrete ordinate solver DISORT includes a test program consisting of 13 different cases including benchmark results. The benchmark results are a combination of theoretical predictions, tabulated data found in literature and pre-calculated data created by the original developers using the FORTRAN version of the program. A wrapper for these test cases allows to call the C++ version included in PIRATES instead of the original DISORT subroutine. Thus it is possible to perform an exact comparison of both implementations. All 13 test routines agree within at least 6 decimal digits with the reference implementation, which is the expected numerical accuracy according to the documentation. Since the test cases have been designed to cover all major branches in the algorithm, the C++ re-implementation can be regarded as validated with respect to the original FORTRAN version.

#### 3.3.2 Mie-Engine

The original FORTRAN version of the Mie engine includes 19 simple scenarios with pre-defined output testing all possible branches of the algorithm. In complete analogy to DISORT, the executable used for testing the original code has been modified to invoke the ported PIRATES Mie engine instead of the reference FORTRAN implementation. Since this has been realised mainly by linking to different libraries, errors can be ruled out for these changes. The results delivered by the C++ implementation of the code agree with the output of the original version within at least 6 decimal digits. The same accuracy is achieved for the expansion coefficients of the scattering phase function and the remaining phase matrix ele-



ments. According to Wiscombe (1996) this is the estimated accuracy using 64-bit floating point arithmetic.

### 3.3.3 T-Matrix Engine

Since the original T-matrix engine ported to C++ does not contain test-cases, the validation has been performed with the independently developed database of Schmidt et al. (2009). Since a re-computation of all datasets in this database would be far too time consuming, the scattering/ absorption efficiency and the scattering phase function have been calculated for a spheroid with aspect ratio 1.5 at four different combinations of the refractive index. The relative differences of scattering/ absorption efficiency and scattering phase function are shown in figure 3.4 for different volume equivalent size parameters in the range from 0.2 to 20. The relative difference  $\Delta_{\text{rel}}$  for the phase function is defined in terms of the norm (equation 3.5)

$$\Delta_{\text{rel}} := \frac{\|\mathcal{P}_1 - \mathcal{P}_2\|}{\|\mathcal{P}_1\|}.$$

Note that the efficiencies typically agree within at least 4 decimal digits, except for the computationally least stable case with high refraction and little absorption (refractive index  $\mathcal{N} = 3 + 0.001i$ ). The relative deviation in the phase function apparently has a trend to grow with increasing particle size, but the differences are small enough to exclude serious errors in the re-implemented algorithm.

### 3.3.4 Comparison to Measurements

Up to this point, validation has been restricted to unit tests of individual PIRATES components featuring exclusively simulated data. This section complements the afore mentioned numerical studies with a validation of PFORTE against experimental observations. Compared to the previously reported validation efforts this is a more complex endeavour for two main reasons: first it involves the entire processing chain from gas absorption to radiative transfer and secondly it requires a multitude of different measurements. Apart from the downwelling radiances, which are going to be compared against their simulated counterparts, the simulations require a manifold of input parameters, e.g. the vertical profiles of gaseous atmospheric constituents and temperature and the microphysical properties of particulate matter or clouds. All input parameters have to be measured simultaneously with the downwelling radiation to capture the current atmospheric state prerequisite for a meaningful comparison.

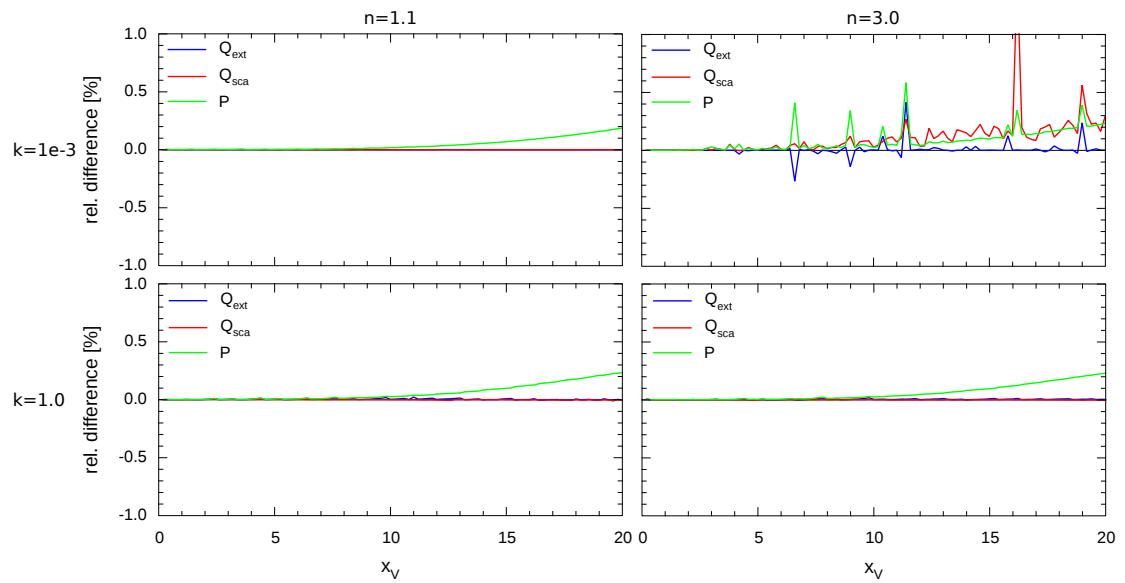


Figure 3.4: Comparison of scattering/absorption efficiency and scattering phase function calculated with the modified T-Matrix engine included in PIRATES against datasets from the scattering database of Schmidt et al. Shown are the relative differences in the size parameter range 0.2 – 20 for a spheroid of aspect ratio 1.5 with real refractive indices 1.1 (first column) and 3 (second column) and absorption 0.001 (first row) and 1 (second row)

The additional gain of a comparison against experimental results lies within its independence from simplified models and software. In this sense it constitutes an independent overall benchmark of the forward model. Since reliable experimental data is an indispensable requirement for the intended comparison, the observations provided within the scope of the Continual Intercomparison of Radiation Codes (CIRC) are going to be used here. The CIRC input data available online via <http://circ.gsfc.nasa.gov> has been acquired on three different sites of the Atmospheric Radiation Measurement (ARM) Climate Research Facility. Apart from being equipped with a manifold of different instruments, these sites are all continuously monitored and evaluated to ensure paramount data quality.

CIRC comprises seven different cases, six of which have been selected for this comparison (case 5 is a synthetic case for which no measurements exist):

- Case 1 observed on 25 September 2000, 2028 UTC, at Southern Great Plains central ARM site with low precipitable water and low aerosol loading
- Case 2 observed on 19 July 2000, 2329 UTC, at Southern Great Plains central ARM site with high precipitable water and moderately high aerosol loading
- Case 3 observed on 4 May 2000, 1548 UTC, at Southern Great Plains central ARM site with moderate precipitable water and moderately high aerosol loading
- Case 4 observed on 3 May 2004, 2209 UTC, at North Slope of Alaska (Barrow) with very low precipitable water and moderate aerosol loading
- Case 6 observed on 17 March 2000, 2029 UTC, at Southern Great Plains central ARM site with thick overcast liquid cloud and moderate precipitable water loading
- Case 7 observed on 6 July 2005, 1717 UTC, at Pt. Reyes ARM mobile facility with moderately thin overcast liquid cloud and moderate precipitable water

According to the CIRC website, the longwave aerosol optical depth for all seven cases is small enough to be neglected in TIR radiative transfer. For a more detailed report of the environmental conditions during the intercomparison and the instruments used to record the data please refer to the publication of Oreopoulos et al. (2012). In addition to the input data provided on the CIRC website, AERI measurements from each site were extracted from the ARM archive for the respective dates. All measurements within a 20 minute window centred at the observation time of the respective case were then averaged. Note that Oreopoulos et al. (2012)

mention a special treatment of these measurements to compensate for a small well known bias of the AERI (Delamere et al., 2010). While this corrected product, which is not available from the ARM archive, has been applied to produce the plots shown on the CIRC website, it was not available for this comparison. For cases 6 and 7 the water clouds were assumed to consist of spherical water droplets with a gamma size distribution as defined in chapter 3.2.3. The parameters of the size distribution and the total droplet number concentration were inferred from the CIRC data. The refractive index of Bertie and Lan (1996) is assumed for water. The conversion of liquid water content to droplet number density has been performed with the temperature dependent water density model proposed by Wagner and Pruß (2002, equation 2.6).

A comparison of the downwelling radiances observed by AERI with those simulated using PFORTE for the CIRC cases discussed above is displayed in figure 3.5. For each case the figure shows simulated (red) and measured (blue) radiance in the respective upper panel. The lower panels contain the residual (blue) obtained after subtracting the simulated radiance from the measured radiance and the root-mean-square of the measured radiance (grey) provides an estimate of the temporal scene variability. A comparison of the residuals with those provided on the CIRC website yields slightly larger discrepancies for cases 1-4. These are likely caused by the fact, that the CIRC reference data provides trace gas concentration, pressure and temperature as layer averaged quantities, while PFORTE requires level based quantities as input and performs the vertical integration internally. Consequently trace gas concentration, pressure and temperature had to be reconstructed from the layer averaged values, thereby eventually causing the small deviations. Nonetheless the differences between model and simulation are still satisfactorily small. The residuals of the cloudy cases 6 and 7 are smaller than those shown on the CIRC website, probably due to the fact, that the latter were obtained from simulations ignoring scattering, while the results shown here include scattering. Taking into account that the residual between PFORTE and AERI is smaller than the time variability of the measurements, the agreement is quite good for these cases.

Although the six cases investigated here cannot exclude model misbehaviour under all thinkable conditions, they still cover a broad variety of atmospheric states. Furthermore the cloudy cases have been calculated by the same code which calculates aerosol absorption, the model uncertainty is assumed to be in the order of magnitude as the deviations between model and measurement observed in this comparison.

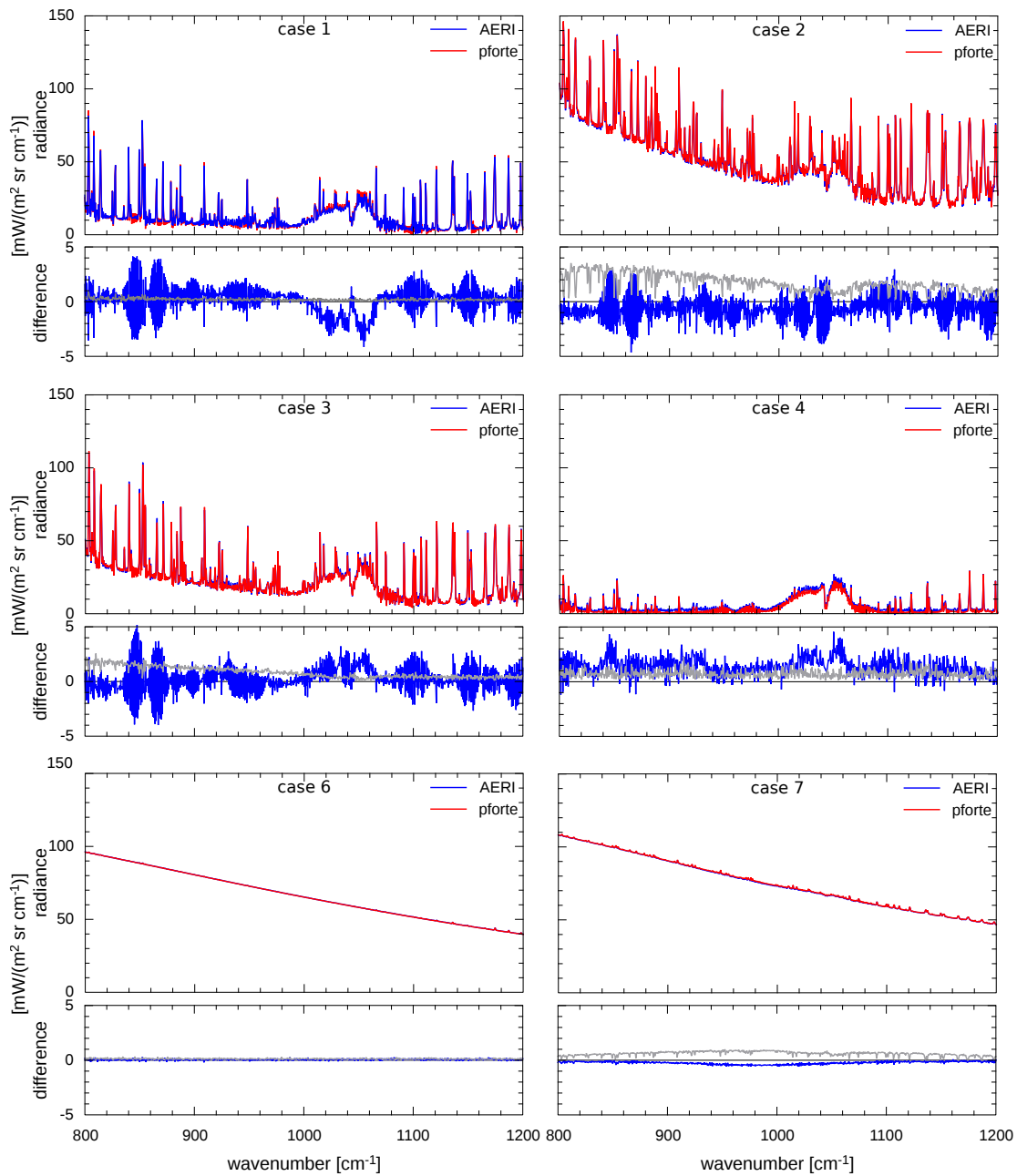


Figure 3.5: Comparison of measured and simulated downwelling radiances for 6 CIRC cases. Shown are the downwelling radiance measured by AERI (blue) and simulated radiance (red) in the respective upper panel and the AERI-pirates residual (blue) along with the standard deviation over all averaged measurements (grey) in the respective lower panel.



# Chapter 4

## Results

This chapter contains the discussion of the FTIR measurements conducted within the scope of the SAMUM-2 field campaign. The radiative transfer model PIRATES, which has been introduced in the previous chapter, is used as main tool for the data analysis. Chapter 4.1 treats the different parameters entering the simulations and explains how they were chosen based on published data and SAMUM-2 measurements. Once the origin of the input data has been presented, the propagation of the most influential uncertainties through the simulations are investigated in chapter 4.2. The discussion addresses measurement uncertainties as well as the effect of replacing missing measurements by a-priori data. Having thus characterised the error budget of the radiative transfer simulations, the spectral signature of mineral dust will be isolated from the measured spectra in chapter 4.3. A comparison with the previously derived uncertainties is employed to estimate the sensitivity of radiation measurements at BOA and TOA to different aerosol types encountered during SAMUM-2. Finally the predictions of different aerosol models will be compared to measured data in chapter 4.4. It will be examined, in how far the different models are capable to reproduce the measured aerosol signatures based on the microphysical aerosol properties gathered by the SAMUM-2 consortium. Most notably it will be shown, that a good agreement of simulated and measured dust properties requires the use of non-spherical model particles. To the best of the author's knowledge, this constitutes the first TIR column closure, demonstrating the distinct influence of non-spherical dust particles in the TIR, which comprises in-situ observations of all major microphysical aerosol parameters.

## 4.1 Ingestion of Parameters

Radiative transfer simulations require a large amount of input: gaseous absorption is characterised by the vertical profiles of temperature, pressure and each constituent's concentration, while aerosols have to be specified in terms of the refractive index and the size resolved amount of particulate matter. Since these quantities are selected in the same fashion for all simulations presented in the following chapters, the methods required to obtain the input data is presented here once instead of repeating it in each section. The information to be provided should be sufficiently accurate to allow for a reproduction of all radiative transfer simulations discussed in the further course of this document.

### 4.1.1 Trace Gas Concentrations

All atmospheric constituent profiles are based on the tropical day atmosphere described by Remedios et al. (2007), except for the ozone profile. The latter has been adopted from the tropical standard atmosphere included in the TRAVIS model of Otto et al. (2009), because it was found to yield a better agreement with radiation measurements at both TOA and BOA. The vertical carbon dioxide profile is scaled by a constant factor to a total column density of 380 ppmv reflecting the ongoing increase in atmospheric CO<sub>2</sub>. Within the scope of this study, the upper boundary of the atmosphere is set to 100 km above sea level. Beyond this altitude the optical medium is assumed to be an ideal vacuum.

Since relative humidity, temperature and pressure profiles are subject to considerable diurnal variations, these quantities are inferred from radiosonde measurements. During SAMUM-2, Vaisala RS92-SGP sondes were launched several times a day from Praia airport. It is well known (Wang et al., 2012, and references therein), that the relative humidity measured by these radiosondes exhibits a dry bias, which originates from heating of the humidity sensor through direct sunlight. According to a technical note published by Vaisala on their website, an improved humidity sensor has been introduced in 2007 with the intention to mitigate this bias. Although the serial numbers of the used sondes indicate, that they are already equipped with the improved humidity sensor, a support request at the Vaisala customer service revealed this not to be the case. To correct for the bias, the algorithms developed by Wang et al. (2012) and Cady-Pereira et al. (2008) have been applied to the measured data. Using both of these independently developed algorithms interchangeably allows to estimate the uncertainty of the corrected relative humidity.



As radiosondes have a very high vertical resolution, which is actually disadvantageous for radiative transfer simulations, the measured profiles of temperature, pressure and relative humidity are smoothed with an averaging kernel of 100 m. Subsequently, the vertical grid is coarsened, such that a linear interpolation yields a relative error of less than two percent at each node of the finer grid for each quantity except pressure, which has to satisfy the same error criterion by logarithmic interpolation. Additionally adjacent levels are constrained to differ by less than 5 K in temperature and their respective mean pressure may not exceed a ratio of 1.4. Temperature and relative humidity of the standard tropical atmosphere are appended in altitudes not covered by the radiosonde. The balloon-borne soundings during SAMUM-2 typically reached an altitude of approximately 15 km, before the balloon burst, thus limiting observations to the troposphere.

Due to a distinct  $O_3$  absorption feature in the atmospheric window region, the vertical ozone distribution has a decisive impact on the simulated spectra. To take temporal ozone variations into account, the a-priori profile is scaled by a constant factor to match the total column density measured by the GOME-2 instrument (Loyola et al., 2011) on-board MetOp-A. It should be noted though, that the retrieved values could be biased due to the presence of the intermittent high aerosol loads discussed later in this chapter.

### 4.1.2 Aerosol Layers

Within the radiative transfer simulations aerosols are modelled in terms of homogeneous layers. The optical properties of each layer are calculated on the basis of size distribution, shape and refractive index of the constituent particles. These parameters are obtained from a number of different measurements conducted by other SAMUM groups.

The altitude and vertical extent of each layer is inferred from airborne and ground based LIDAR observations described in detail by Weinzierl et al. (2011) and Tesche et al. (2011a). These measurements reveal altitude-resolved changes in the absorption coefficient, which can be associated with the total aerosol concentration. Furthermore LIDAR-ratio and depolarisation (equation 3.12) can be used to distinguish different aerosol types (Groß et al., 2011b, Tesche et al., 2011b).

The aerosol size distribution is assumed to be representable as 4-modal log-normal distribution (equation 3.20), the parameters of which have been determined by Weinzierl et al. (2011) from airborne observations. This data is amended by ground based size distribution measurements conducted by Kandler et al. (2011b) at Praia

airport, because a significant amount of larger particles is often found below 200 m above the surface, an altitude range usually inaccessible by aircraft apart from take-off and landing due to aviation safety regulations.

Since mineral dust is a complex mixture of different mineral constituents, the composition within each layer has been derived from microphysical and chemical analysis of single particles. Table 4.1 summarises the weighting factors applied to convert the thus attained information published by Lieke et al. (2011) into bulk refractive indices: For each mineral component identified therein (rows in table 4.1) the refractive indices available in the DIRAC database (columns in table 4.1) are weighted with the factor in the respective field. An 'X' indicates a weighting factor of 100%. The sources of the relevant refractive index datasets compiled in DIRAC are listed in table 4.2. Note that no refractive indices could be found in published literature for several silicate materials. Furthermore, ammonium sulfate and gypsum are the only sulfate end-members for which published optical constants could be found. As a consequence all other sulfates are assumed to be mixtures of these two sulfate representatives. Although this is probably a valid approximation, considering that absorption in the TIR atmospheric window is dominated by the  $\nu_3$  band of  $\text{SO}_4^{2-}$ , small deviations due to interactions with different cations cannot be ruled out completely. Additionally it has to be mentioned, that the refractive index data published by Aronson (1986) for orthoclase may contain typographical errors, as plotted graphs and numerical oscillator parameters provided by the author are inconsistent. The oscillator parameters have been adopted anyway for a lack of more reliable data. Another challenge consists in the multitude of modifications regularly observed among clay minerals (Kandler et al., 2011b), which hamper the unambiguous identification of end-members. This entails weighting factors, which include a certain amount of arbitrariness.

### 4.1.3 Boundary Conditions

While thermal emission at the surface has a rather negligible influence on the downwelling radiance at BOA, it is one of the determining factors for the upwelling radiance at TOA measured e.g. by satellite instruments. Although the spectral emissivity has been measured for a small patch close to the measurement site, it is not clear how characteristic this patch is for the rest of the island Santiago or even other Cape Verdian islands. Furthermore, the field of view observed by IASI is seldom entirely covered by island surface. To circumvent these problems, only pixels entirely covered by sea surface are retained. The sea surface is modelled as a flat lambertian surface with constant temperature adopted from the IASI Level 2 product. The emissivity is calculated separately for each scene depending

Component	Quartz	Kaolinite	Illite	Montmorillonite	Chlorite	Albite	Anorthite	Orthoclase	Ammonium Sulfate	Hematite	Gypsum	Sea Salt	Calcite	Soot
(NH <sub>4</sub> ) <sub>2</sub> SO <sub>4</sub>									X					
Soot														X
Soot & (NH <sub>4</sub> ) <sub>2</sub> SO <sub>4</sub>									80					20
Na <sub>2</sub> SO <sub>4</sub>									X					
Na <sub>2</sub> Ca(SO <sub>4</sub> ) <sub>2</sub>									50		50			
CaSO <sub>4</sub>											X			
other sulfates									50		50			
CaCO <sub>3</sub>													X	
CaMg(CO <sub>3</sub> ) <sub>2</sub>													X	
NaCl												X		
KCl												X		
other chlorides												X		
Fe oxides										X				
Quartz	X													
SiAl		X												
SiAlK			60					40						
SiAlNa						X								
SiAlNaCa				70			30							
SiAlNaK						50		50						
SiAlCaFeMg		40	10		5		35			10				
SiAlKFeMg		40	10		5			35		10				
FeMgSiAl					X									
MgFeSi					95					5				
MgSi					X									
mix (S+Si)	80								20					
mix (AlSi+S)		80							20					
mix (Cl+S)									20			80		
mix (NaCl+Si)	50											50		
mix (NaCl+AlSi)		50										50		
mix (Ca+Si)	50												50	
mix (Ca+AlSi)		50		4						4			50	
other Si-dominated	10	35	15	7		5		23		5				

Table 4.1: Weighting factor in percent for the transition from identified dust constituents (rows) to refractive indices (columns). 'X' symbolises 100%

<b>Mineral Species</b>	<b>Reference</b>
albite	Mutschke et al. (1998)
ammonium sulfate	Toon et al. (1976)
anorthite	Aronson and Strong (1975)
calcite	Querry et al. (1978)
chlorite	Mooney and Knacke (1985)
gypsum	Long et al. (1993)
hematite	Glotch et al. (2006) <sup>1</sup>
illite	Glotch et al. (2007)
kaolinite	Glotch et al. (2007)
montmorillonite	Glotch et al. (2007)
sea salt	Shettle and Fenn (1979)
orthoclase	Aronson (1986) <sup>1,2</sup>
quartz	Henning and Mutschke (1997)
soot	Sutherland and Khanna (1991)

Table 4.2: References for the refractive index data used to calculate bulk aerosol optical constants. (1): Averaged over principal axes of dielectric tensor, (2): Data probably contains typographical errors, but no other data available

on the observation zenith angle by application of Fresnel's formula with the water refractive index of Bertie and Lan (1996). The latter is corrected for sea water salinity following Friedman (1969). As shown by Nalli et al. (2008), this simplified water model is quite accurate for zenith angles smaller than  $45^\circ$ , but can lead to a bias of up to 0.2 K in effective SST for larger zenith angles. Compared to other uncertainties affecting the TOA observations, however, this additional uncertainty is almost negligible, so no further efforts went into the implementation of a more sophisticated model. It cannot be guaranteed though, that the IASI retrieved SST is accurate in the presence of aerosols, e.g. if atmospheric dust is not accounted for in the retrieval. The sensitivity of the upwelling radiance at TOA to SST is discussed in chapter 4.2.4 while the possibility of an aerosol induced bias of the retrieval is investigated in chapter 4.4.

## 4.2 Sensitivity Studies

This section discusses the major uncertainties of the simulated radiances at BOA and TOA in an aerosol-free atmosphere. These are entailed by an imperfectly characterised atmospheric state due to missing information or uncertainties of input quantities entering the simulations. The following results are also intended to assist the reader in developing a feeling for the overall accuracy of the radiative transfer simulations. This will prove beneficial in the discussion of the aerosol radiative impact and the closure studies presented later. All of the following results were obtained with the PIRATES model for a standard tropical atmosphere. As this thesis is restricted to the TIR atmospheric window ( $800 - 1200 \text{ cm}^{-1}$ ), all spectra are limited to this interval as well. The interested reader is also referred to the excellent treatise by Hollweg et al. (2006), which contains a variety of additional sensitivity studies addressing aerosol observations in the TIR.

### 4.2.1 Water Vapour Concentration

Condensation, convection, precipitation and advection can cause considerable diurnal changes in atmospheric humidity. Although radiosondes recorded the water vapour concentration at least twice a day during SAMUM-2, uncertainties remain due to measurement errors and temporal evolution of the atmosphere between individual observations. To assess the influence of deviations between real and assumed water vapour profile, several simulations have been carried out with manipulated atmospheric water content. The manipulations included the shift of a reference profile (standard tropical atmosphere) by 1%, 5% and 10% towards higher relative humidity. Figure 4.1 shows the modified profiles along with the deviations in upwelling and downwelling radiance compared to the reference atmosphere.

Obviously the entire atmospheric window region is affected by water vapour absorption, with a decreasing influence towards larger wavenumbers. Furthermore, the increased amount of water vapour causes a relatively high amount of additional downwelling radiation at BOA, whereas it incurs a comparatively small reduction of the upwelling radiation at TOA. Taking into account, that the majority of the water vapour is concentrated in the lower troposphere, where the temperature difference between surface and atmosphere is comparatively small, this is readily explained: the increase in absorption of terrestrial radiation due to the added water is mostly compensated for by self-emission. In contrast to this, the downwelling radiation is strongly emission dominated, i.e. the increased emission by far exceeds the amount of additionally absorbed radiation observed at the surface.

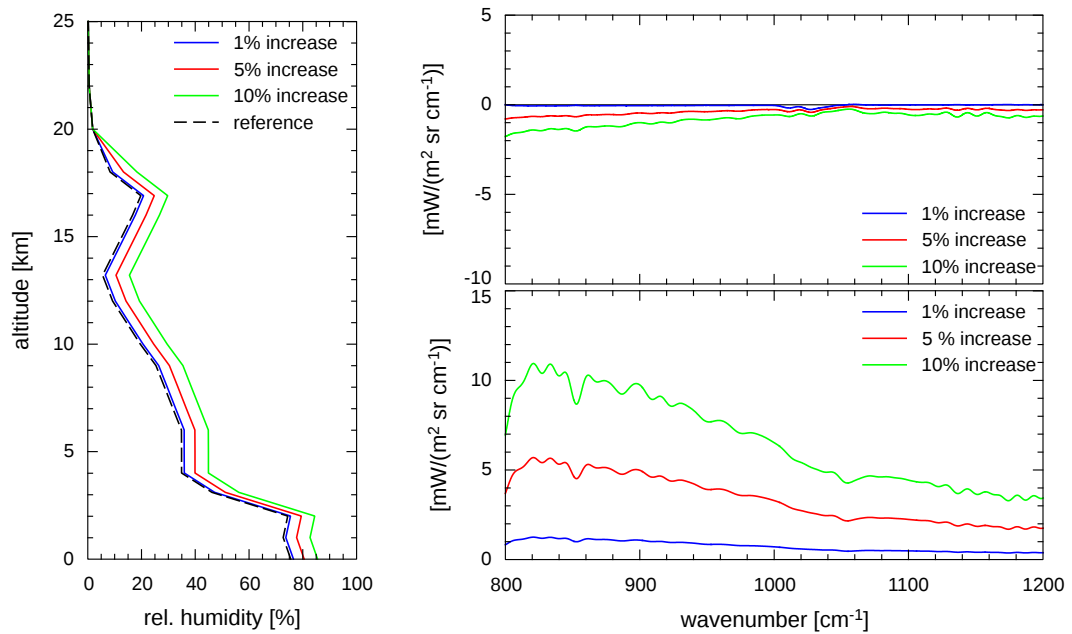


Figure 4.1: Impact of variations in the water vapour profile on the upwelling and downwelling radiation. Shown are three different water vapour profiles (left) obtained by increasing the reference relative humidity of a standard tropical atmosphere by 1%, 5% and 10%. The differences in the observed upwelling radiation at TOA (top right) and in the downwelling radiation at BOA (bottom right) compared to the reference standard profile are shown in the colour of the respective profile.

#### 4.2.2 Ozone Concentration

Apart from water vapour, ozone absorbs most significantly in the atmospheric window region between  $1000\text{ cm}^{-1}$  and  $1080\text{ cm}^{-1}$ . Due to the complex nature of upper atmospheric dynamics and photochemistry, diurnal variations in the ozone mixing ratio can be up to 8% according to Sakazaki et al. (2013). Since no in-situ measurements of the ozone profile have been performed within the scope of SAMUM-2, the assumed ozone content has been adopted from GOME-2 measurements conducted during MetOp-A overpasses. These measurements are available approximately once a day around 1100 UTC for Cape Verde. Due to the fact, that GOME-2 delivers the total column density but not the vertical profile of ozone, the dependence of the radiative transfer simulations on the assumed a-priori profile as well as the influence on changes in the total ozone column have been investigated. For this purpose, a standard tropical atmosphere with a total ozone column scaled

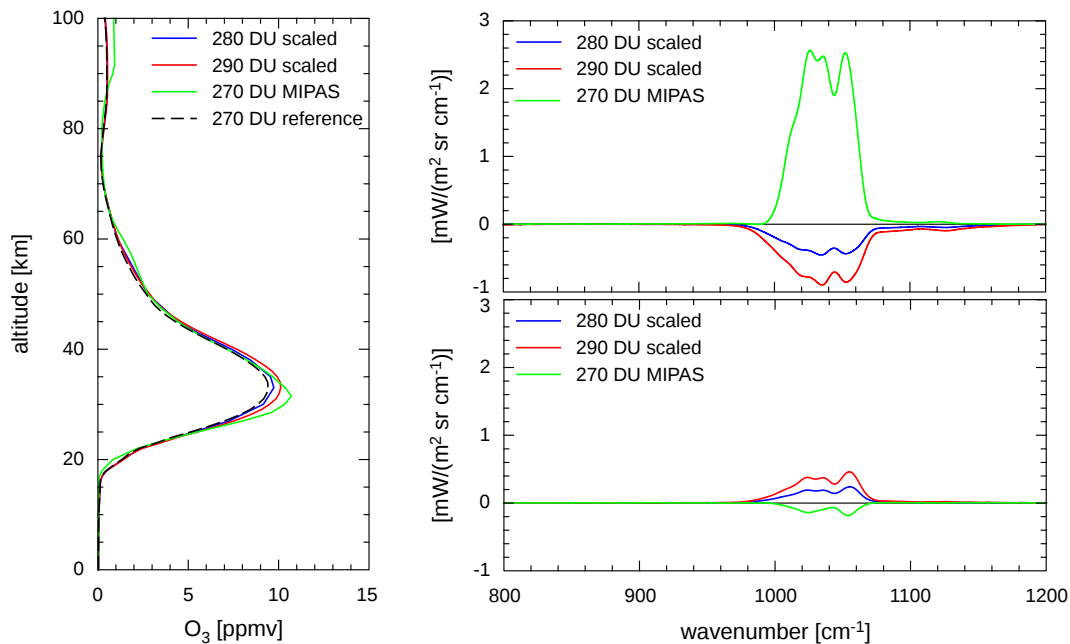


Figure 4.2: Differences in the upwelling and downwelling radiance resulting from modifications in the ozone profile. The reference ozone profile (left, dotted line) is scaled by a constant factor to increase the total column density by 10 DU (blue) and 20 DU (red). Furthermore the entire profile has been exchanged for another standard profile (green) with the same total column density. The resulting differences in upwelling radiance at TOA (top right) and downwelling radiance at BOA (bottom right) are displayed in the colour of the respective profile.

to 270 DU by a vertically constant factor has been chosen as reference. The simulated radiances thus obtained are compared against simulations featuring the same atmosphere with an increased ozone column of 280 DU and 290 DU. Additionally the entire ozone profile has been exchanged for the ozone profile of the MIPAS standard atmosphere published by Remedios et al. (2007). The latter has been scaled to a total column density of 270 DU, identical to the reference atmosphere. Figure 4.2 shows the different ozone profiles along with the residuals resulting from a comparison to the reference case at BOA and TOA.

In contrast to the water vapour profile, which mainly influences the downwelling radiance at the surface, the ozone profile has a distinct impact on the upwelling radiance. Again the explanation is connected to the vertical distribution and the associated temperature of the ozone, which is predominantly located in the middle and lower stratosphere. Since the temperatures there are low compared to the surface temperatures, the amount of absorbed upwelling radiation is much larger

than the self-emission, leading to a considerable reduction in upwelling radiation. Since the amount of downwelling radiation crossing the ozone layer is small, this has little to no effect on the radiation at the surface, which is mainly affected by the small amount of additional radiation emitted due to the increased ozone. Another interesting observation is the influence of the ozone profile on the radiation at TOA, which has a significantly greater impact than small increases in total column density. This incurs additional uncertainties in the affected spectral region due to the fact, that no information on the actual ozone profile is available for the radiative transfer simulations presented throughout this thesis. In contrast to that, the effect on the downwelling radiation at the surface is rather negligible compared to other potential error sources such as instrument noise or water vapour content.

### 4.2.3 Temperature Profile

The vertical temperature distribution decisively impacts the amount of radiation emitted by gases via Planck's law in each atmospheric level. Consequently it is one of the most critical input parameters for radiative transfer simulations in the TIR. As explained before, the temperature profile for the following case studies is obtained from radiosonde measurements. For a number of reasons, it is possible that the result of these measurements deviates from the actual atmospheric temperature. Apart from measurement errors additional uncertainties arise due to temperature variations caused by solar heating at BOA in combination with convection. Additionally the limited vertical extent of the measurements (ref. chapter 4.1.1) restricts measured values to the troposphere, thus requiring assumptions to be made for the temperature in greater heights. Although the temperature profile is assumed to be fairly stable above the troposphere, local and temporal variations cannot be ruled out completely. To quantify the resulting potential bias, a reference temperature profile (tropical standard atmosphere) has been manipulated to mimic three different scenarios: First the temperature at each altitude has been increased by a constant value of 1 K to gain a general impression about the consequences for the radiance at BOA and TOA. Secondly the temperature profile above the tropopause has been exchanged with that of the tropical day atmosphere (Remedios et al., 2007) to examine the effect of high altitude temperature variations. Finally solar heating at the surface in combination with convection has been simulated with a 5 K increase at the lowest level which linearly reduces to zero at an altitude of 1.5 km, i.e. the temperature variation  $\Delta T$  is defined as

$$\Delta T(z) = \begin{cases} 0 \text{ K}, & z > 1.5 \text{ km} \\ \frac{10}{3} \frac{\text{K}}{\text{km}} (1.5 \text{ km} - z), & 1.5 \text{ km} < z \leq 0 \text{ km}. \end{cases}$$



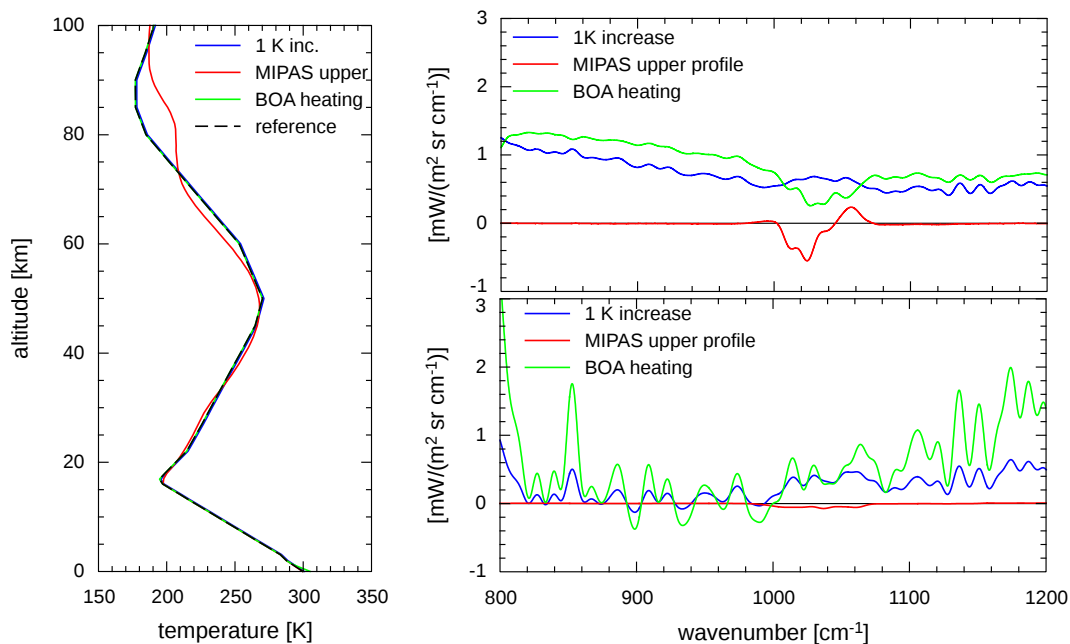


Figure 4.3: Changes in simulated radiance at TOA (top right) and BOA (bottom right) caused by replacing the reference temperature profile (left, dotted line) with a profile shifted by 1 K (blue), an alternate standard profile for the upper atmosphere (red) and a profile simulating surface heating.

Note that the temperature of the lower boundary is the same for all simulations to isolate the influence of air temperature variations. Such a scenario might e.g. be representable for an air mass heated over an island, which is successively transported over the ocean. The temperature profiles for the investigated scenarios are displayed in figure 4.3 (left).

Regarding the resulting differences compared to the reference atmosphere in figure 4.3 (right), it becomes apparent that the temperature distribution above the troposphere is of minor importance for simulations of the downwelling radiance at the surface, while a visible effect on the upwelling radiation at TOA is limited to the ozone band. This comes as no surprise, since the other major absorbers are predominantly located in the lower troposphere and consequently remain unaffected by the manipulation. The small decrease in downwelling radiation is likely attributable to the fact, that only the temperature profile has been changed without adapting the pressure accordingly to maintain hydrostatic equilibrium. This results in a small reduction in total absorbing mass, which is apparently not compensated for everywhere by the increased thermal emission caused by the elevated temperature.

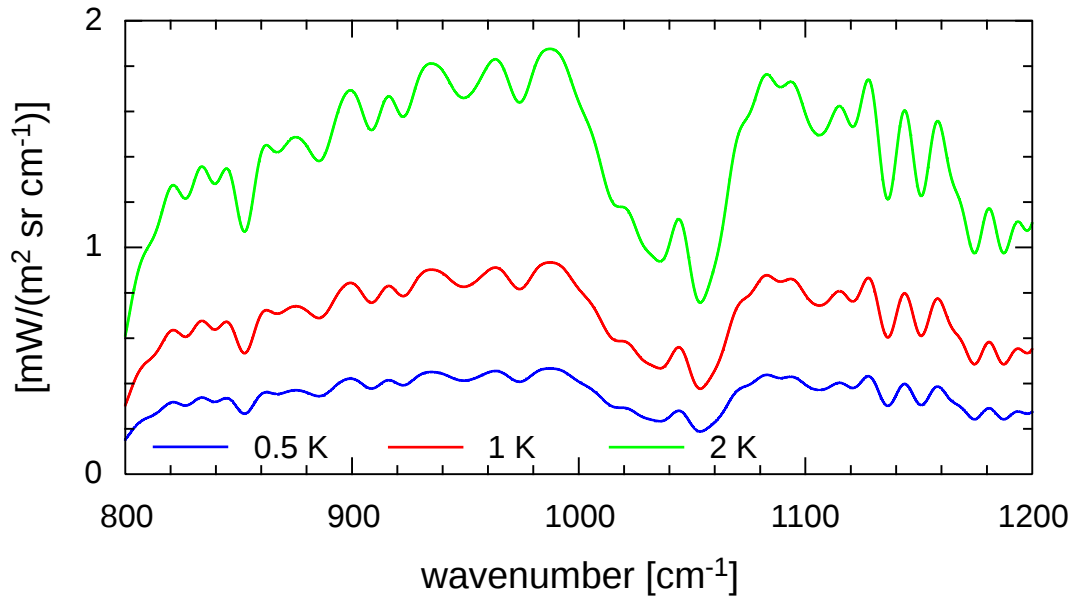


Figure 4.4: Residua in upwelling radiance at TOA due to an increase in surface temperature by 0.5 K (blue), 1 K (red) and 2 K (green), respectively.

#### 4.2.4 Surface Temperature

The Earth surface, no matter whether covered by water or dry, has a relatively high emissivity ( $\approx 0.9$ ) over most of the spectral window domain, making it the dominant contributor to the upward radiative flux in this spectral region. As the surface temperature governs the amount of energy emitted into the atmosphere due to Planck's law, it is a critical parameter for nadir observations from TOA. In contrast to that, the downwelling radiance at BOA is only indirectly affected by surface emission in the presence of aerosols or clouds scattering radiation back to the surface. Thus the following discussion is limited to upwelling radiances. For the sake of simplicity, the Earth is modelled as ideally lambertian surface with unit emissivity and a temperature of 296 K for the reference scenario. Additionally three simulations have been carried out with surface temperatures increased by 0.5 K, 1 K and 2 K, respectively. Figure 4.4 shows the residual in upwelling radiance at TOA with respect to the reference scenario.

Obviously the surface temperature affects the upwelling radiation in the entire spectral window domain and is thus a key parameter for the radiation budget. The assumed variations of up to 2 K are typical values for diurnal changes in SST, underlining the importance of this quantity for the upcoming case studies.

### 4.3 Aerosol Signature

This section discusses the radiative effect of different aerosol combinations encountered during SAMUM-2. For this purpose, PIRATES simulations are employed to isolate the aerosol signature from FTIR spectra measured at BOA and TOA. The first step of this approach involves the simulation of up- and downwelling radiances for an aerosol free (clear-sky) atmosphere with the help of radiosonde data. The assimilation of the various input parameters into the simulation is performed in accordance with the procedures described in chapter 4.1. In a second step the residual is calculated by subtracting the simulated clear-sky radiance from the measured spectrum. The such obtained aerosol signature can be compared for different atmospheric conditions, because it is considerably less affected by diurnal variations in gaseous absorption than measured radiances alone. Since it is typically not possible to entirely remove the influence of all gases, the aerosol signature is convolved with a squared sinc to reduce its spectral resolution to approximately  $10 \text{ cm}^{-1}$  in a third and final step. This effectively suppresses high frequency oscillations, which are characteristic for atmospheric gases but not for aerosols.

This three step process is illustrated by figure 4.5: a measured IASI spectrum (red) is shown in the top panel along with the associated PIRATES simulation for clear-sky conditions (blue). Owing to a small aerosol load, both curves appear to be almost equal in this depiction. Differences become more obvious in the lower panel, which shows the aerosol signature at full resolution (blue) and after convolution (red). Apparently the smoothed spectrum provides a good indication of slowly varying deviations expected in the presence of aerosols.

The following discussion focuses on convolved residuals obtained in complete analogy to the example above for a set of representative scenarios encountered during SAMUM-2. These scenarios were all selected to be cloud-free and temporally close to radiosonde observations. Furthermore IASI observations have been restricted to pixels completely covered by water, which are located within a 50 km radius around the Praia field site.

Figure 4.6 summarises the different aerosol signatures extracted from BOA measurements with the Model 102 FTIR. The legend provides the acquisition time of the spectrum and the launch time of the radiosonde ingested into the respective simulation (in brackets). Colours have been chosen according to the meteorological phase for each observation. These phases are summarised briefly in the next paragraphs. A more detailed synoptic analysis can be found in the excellent meteorological overview prepared by Knippertz et al. (2011).

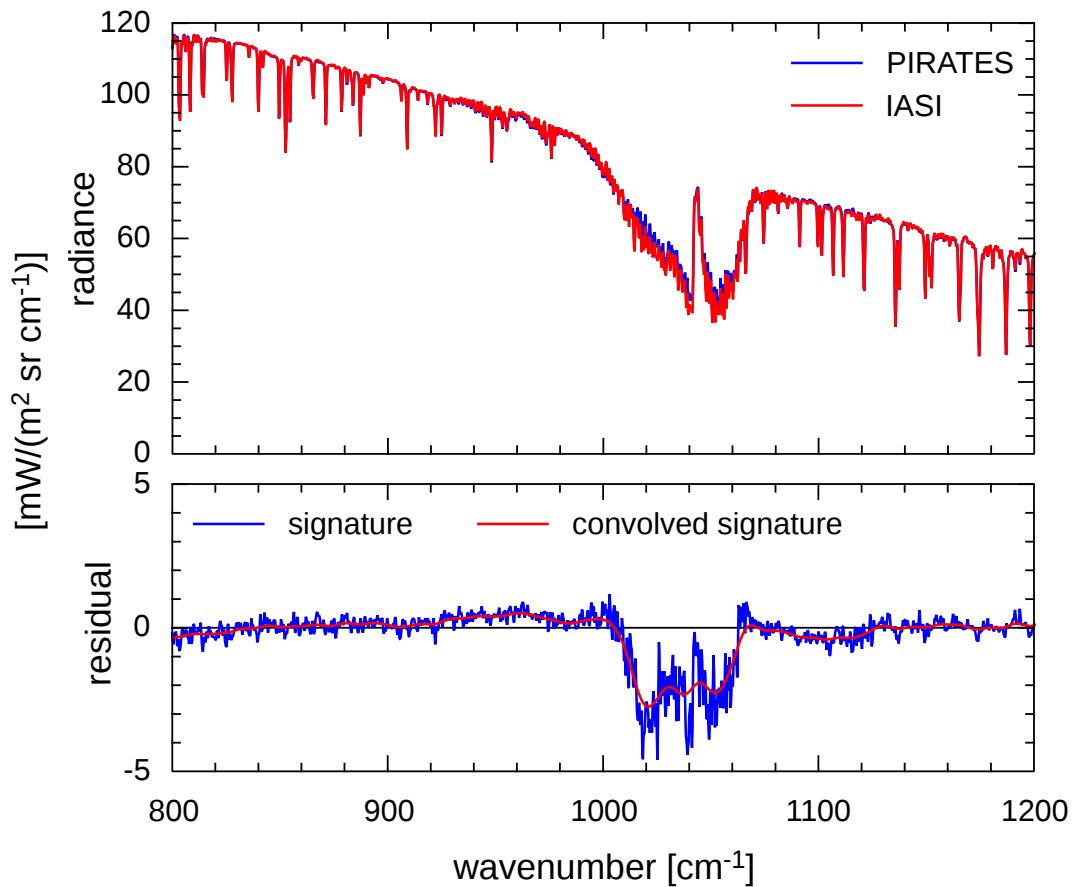


Figure 4.5: Comparison between a IASI spectrum and a PIRATES simulation neglecting aerosols for 6 February 2008. The top panel contains measured (red) and simulated (blue) radiance. The difference between the two spectra is shown in the bottom panel at full resolution (blue) and at a reduced resolution of  $10 \text{ cm}^{-1}$ .

Dust phase 2 lasted from 24 January 2008 to 26 January 2008 and was characterised by a complex mixture of mineral dust and biomass burning aerosol. After its activation in West Niger and Mali, the dust was transported westward via Mauritania and Senegal across the Atlantic Ocean towards Cape Verde. This westerly transport took approximately 3 – 5 days and was limited to atmospheric layers below 1.6 km. Above this altitude the atmospheric currents changed direction, leading to the advection of mixed biomass burning and mineral dust aerosol from Central Africa in the altitude band 1.6 – 3.6 km. Spectra observed during this period are shown in magenta in figure 4.6.

The synoptic situation during dust phase 3 (28 January 2008 to 2 February 2008) was very similar to dust phase 2 in terms of dust sources and transport routes.

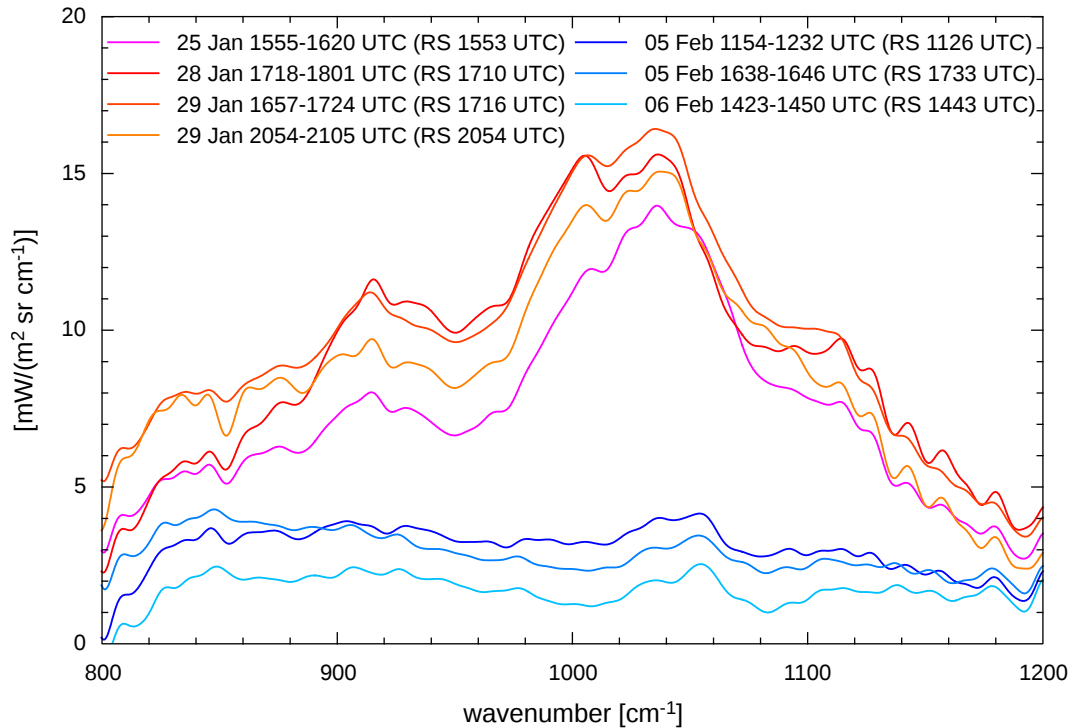


Figure 4.6: Aerosol signature inferred from BOA measurements of the downwelling radiance acquired during SAMUM-2. Time spans indicate the integration period for each measurement. The launch time of the radiosonde ingested into the respective clear sky simulation is provided in brackets.

However, this phase distinguishes itself from phase 2 in a slightly higher amount of activated dust and a more westward wind direction in upper air layers. As a consequence the lofted mixture of biomass burning aerosols and mineral dust was not observed during this period, leading to a single pure dust layer extending from the ground up to an altitude of 1.2 km. Spectra observed during dust phase 3 are shown in red and orange colours in figure 4.6. The similar shape of the residuals compared to dust phase 2 is consistent with the meteorological analysis, which reveals identical dust sources for both phases. The generally larger residual is in good agreement with in-situ observations indicating higher dust loads during this period. Only one spectrum recorded on 28 January (red curve in figure 4.6) displays a distinct behaviour in the spectral interval  $800 - 900 \text{ cm}^{-1}$ , which is likely caused by an additional maritime boundary layer detected during the afternoon hours of this day.

Within the further course of the campaign, the overall dust load steadily decreased leading to only a weak dust layer below an altitude of 0.5 km on 5 February,

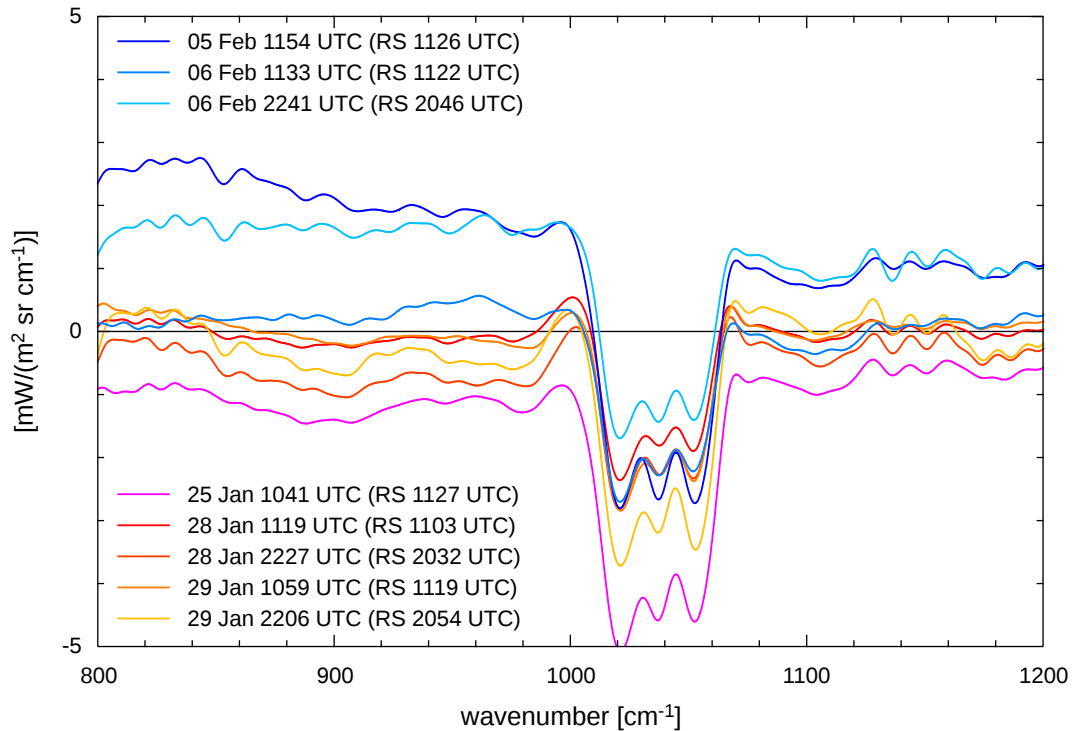


Figure 4.7: Aerosol signature inferred from IASI measurements of the upwelling radiance in complete analogy to figure 4.6.

which finally disappeared completely on 6 February. The atmospheric flow in the altitude range 3 – 5 km during this phase turned to south-easterly directions, resulting in a deep layer dominated by small smoke particles mixed with a small amount of larger mineral dust aerosol. This change in meteorological conditions is reflected by the aerosol signatures (blue curves in figure 4.6), which indicate a significantly smaller aerosol effect than observed during phases 2 and 3. Note that the signature on 6 February (light-blue curve in figure 4.6) is barely larger than the absolute instrument accuracy of the D&P Model 102 addressed in chapter 2.2.11. Taking into account the additional uncertainties arising from imperfectly characterised input quantities as discussed in chapter 4.2, it becomes evident that the signatures for these cases are close to the detection limit of the D&P FTIR and must consequently be interpreted with caution.

Figure 4.7 shows the aerosol signature at TOA as inferred from IASI observations. It is otherwise identical to figure 4.6. At first glance, the deviations in the ozone band  $1000\text{--}1080\text{ cm}^{-1}$  are the most apparent feature. A comparison of their shape with the simulated residuals discussed in chapter 4.2.2 suggests, that they are most likely caused by an inadequate a-priori ozone profile. Apart from the ozone band,

the aerosol signatures are much less pronounced than at BOA (note the different scales), making it impossible to associate them to the different dust phases. As discussed in the context of ozone sensitivity, the relatively small influence at TOA is caused by the fact, that the atmospheric dust emits almost as much radiation as it absorbs due to its low altitude and associated high temperature. The elevated mixed dust and biomass layers could be expected to have a more distinct influence, since they are cooler and thus emit less thermal radiation, but this supposition is not supported by figure 4.7. Instead it has to be concluded, that the comparatively small particles entail a small aerosol optical depth, which leads to the observed signature. Actually the spectra for 5 and 6 February (blue curves in figure 4.7) indicate positive residuals, implying an unexpected increase in TOA radiance compared to the clear-sky scenario. Keeping in mind the uncertainties associated with the (sea) surface temperature discussed in chapter 4.2.4, this might indicate errors in the retrieved SST. The coarse resemblance of the spectral signature with the simulated residuals in figure 4.7 indeed fosters this assumption. However, further simulations including aerosols are required to investigate this matter, which will be addressed in the following chapter with the help of three case studies.

## 4.4 Radiative Closure

This chapter reports on radiative closure studies for three characteristic scenarios scrutinized within the scope of SAMUM-2. Within the context of this thesis, the term radiative closure denotes the reproduction of the measured radiances at BOA and TOA using the PIRATES radiative transfer model along with the microphysical aerosol information based on in-situ and LIDAR observations. The dates for the case studies were selected to cover the different meteorological phases encountered during the campaign. Furthermore a core criterion was the availability of a complete characterisation of the vertical aerosol column above Cape Verde including radiosondes, LIDAR data and airborne in-situ measurements. Based on these requirements the following discussion starts with a case of low aerosol optical depth without pure dust layers (6 February 2008), followed by a day featuring two intense pure dust layers but no detectable biomass (29 January 2008). The chapter concludes with a complex case including multiple dust and biomass layers observed on 25 January 2008.

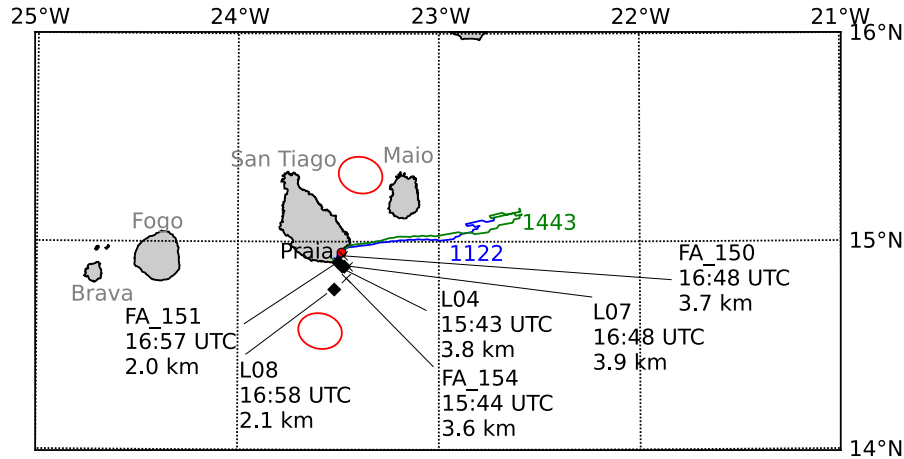


Figure 4.8: Compilation of data gathered on 6 February 2008. The map contains IASI IFOVs recorded during an overpass on 1133 UTC (red ellipses), radiosonde tracks (blue & green lines with annotated launch time), locations of in-situ particle sampling (black crosses labelled FA\_xxx) and locations of size distribution measurements (black diamonds labelled Lxx).

#### 4.4.1 6 February 2008

Figure 4.8 shows a map containing the major data sources ingested into the radiative transfer simulations in the vicinity of the field site at Praia airport (red dot). The labelling for size distribution measurements (Lxx) and samples analysed offline (FA\_xxx) are consistent with the original publications of Weinzierl et al. (2011) and Lieke et al. (2011).

Location and vertical extent of the modelled aerosol layers (figure 4.9, right) have been chosen on the basis of the extinction coefficient inferred from LIDAR measurements (figure 4.9, left). Additionally, the depolarisation ratio allows to conclude upon the aerosol type, as explained in detail by Groß et al. (2011b). Following Lieke et al. (2011) a different aerosol composition is assumed for each of three size bins symbolised by vertical black lines in figure 4.9 (right).

The fraction of accumulated aerosol surface area per size bin in each layer (provided in 4.9, right) allows for a first estimate of the associated radiative properties. Biomass aerosol is e.g. typically found to consist of particles smaller than 500 nm in diameter. This is obviously the case for the upper layers, as approximately 70% of the total aerosol surface is contributed by particles in this size range. In contrast to this, particles with diameters greater than 2.5  $\mu\text{m}$  dominate the marine boundary layer, in accordance with other studies on sea salt aerosols. It may be



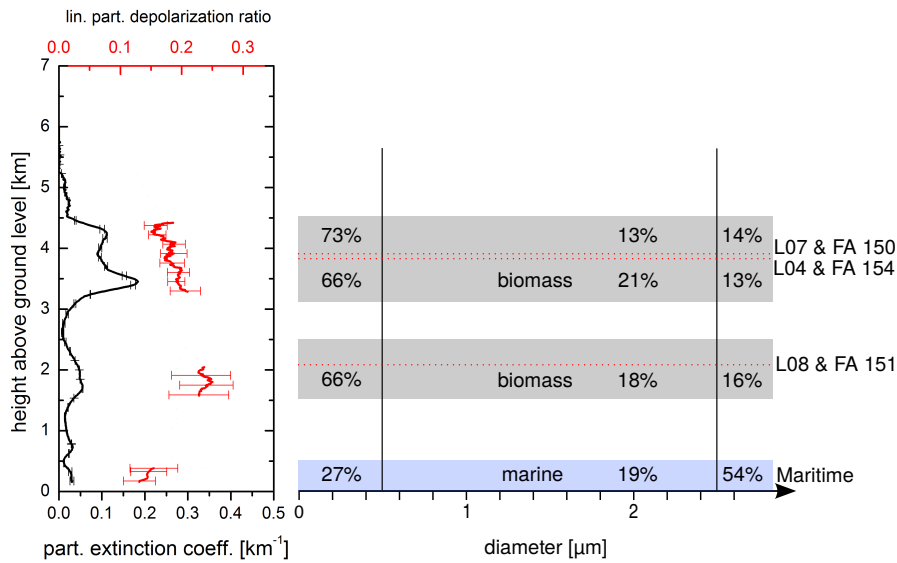


Figure 4.9: LIDAR profiles of extinction and depolarisation (left) and the derived modelled aerosol layers (right) for 6 February 2008. Percentage values indicate the fraction of total surface area contributed by each size bin (vertical black lines). Red dotted lines symbolise altitudes of airborne observations (ref. to figure 4.8). (LIDAR plot courtesy of S. Groß)

surprising though, that even in biomass layers particles larger than  $0.5 \mu\text{m}$  amount to approximately 30% of the total geometric cross-section. Lieke et al. (2011) identifies them as mineral dust aerosol probably activated along with the biomass during fire events. Taking into account, that the optical particle cross-section is the product of geometric cross-sections and absorption efficiency, it becomes apparent that large particles –although seemingly negligible in number density– potentially dominate the optical layer properties in the TIR. At least, this is a likely conclusion regarding the small size parameters of biomass particles in this spectral region.

Since no airborne measurements have been conducted inside the marine boundary layer, an average size distribution and aerosol composition is assumed based on the observations reported by Kandler et al. (2011b) for the maritime phase. Furthermore, composition and size distribution have been measured twice inside the upper biomass layer. As it turns out, either of the two measurements can be chosen to be representative for the whole layer without significantly altering the results. Thus size distribution L04 and composition FA 154 have been selected for the following simulations.

Figure 4.10 displays simulated and measured spectra at BOA (top left) and TOA (top right) along with the respective residuals (bottom row). Grey lines indicate

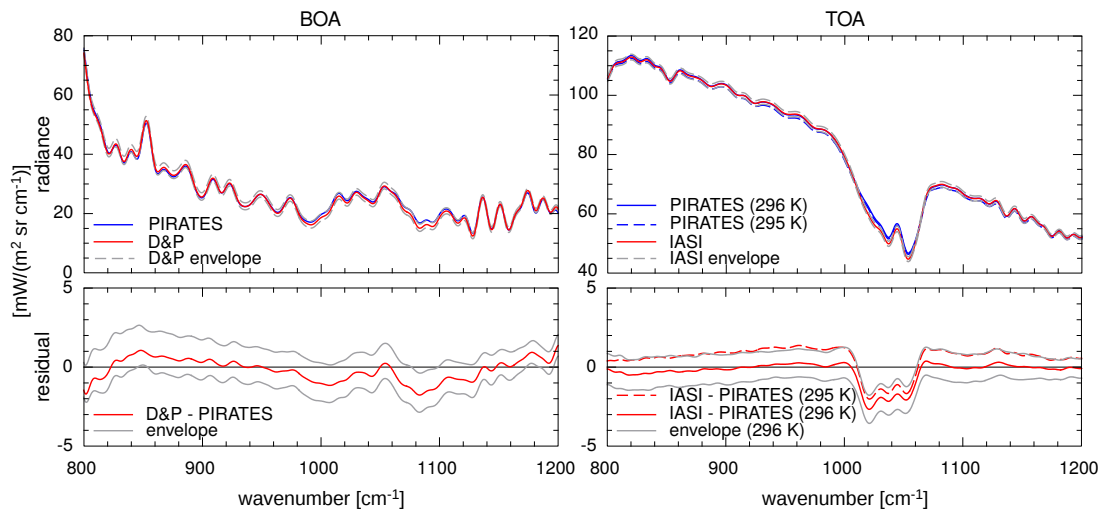


Figure 4.10: Measured (red) and simulated (blue) radiances (top row) at BOA (left) and TOA (right) along with residuals (bottom row) for 6 February 2008. BOA results are based upon the 1443 UTC radiosonde and radiance measurements averaged from 1423 UTC to 1450 UTC. TOA data include a IASI overpass at 1133 UTC and the 1122 UTC radiosonde. Annotated temperatures indicate the assumed surface temperature.

the envelope of the measured radiances including the  $1\sigma$  systematic uncertainty and the temporal variation over the observation period. A radiosonde launched at 1122 UTC has been ingested into the simulations compared to the IASI spectra, which were acquired during an overpass at 1133 UTC. The downwelling radiation at BOA has been simulated based on radiosonde data recorded at 1443 UTC for an optimal temporal proximity to the airborne in-situ observations.

Although simulated and measured downwelling radiances at BOA agree within the accumulated measurement uncertainty, the latter is quite large. A closer inspection of the data reveals, that the overall uncertainty is dominated by temporal variations of the measured spectra over the observation period. In contrast to this, the uncertainty of the IASI measurement originates to equal parts from IASI's absolute temperature accuracy of 0.5 K and from variations in the averaged spectra. Note that simulations of the upwelling radiance have been performed for two different surface temperatures of 295 K and 296 K. The former temperature has been adopted from the IASI Level 2 product for the shown pixels and yields a relatively poor agreement with the simulated data. However, this surface temperature leads to an acceptable agreement for an atmosphere without aerosols (see figure 4.5). Taking aerosols into account, however, the simulation assuming an SST of 296 K yields a much better agreement with the simulation. Either this inconsistency is

caused by the idealised handling of the sea surface in the simulation, which neglects waves and specular reflection, or it indicates, that aerosols are not accounted for in the IASI SST retrieval. In either case it has to be concluded, that even moderate aerosol loads have to be taken into account, if the SST shall be retrieved with an accuracy of better than one Kelvin.

Furthermore it is interesting to observe, that the residua at BOA and TOA are quite similar, taking into account that an overestimated aerosol optical depth leads to a positive residual at the surface due to overestimated aerosols emission, while it entails a negative residual at TOA due to an overestimated absorption of terrestrial radiation. Apparently the simulated aerosol optical depth is too high in the spectral range  $800 - 940 \text{ cm}^{-1}$  while it is seemingly underestimated in the interval  $980 - 1060 \text{ cm}^{-1}$ . The similar shape of the residua leads to the conclusion, that the deviations are dominated by a bias in the aerosol optical properties rather than being caused by measurement errors.

A bias is not unlikely, since the number of error sources is considerable: starting from unknown or possibly erroneous refractive index data, over temporal and spatial variations in the aerosol layers to eventual influences of particle non-sphericity, there exists a substantial amount of uncertainties. Furthermore the size distributions have been sampled at few discrete altitudes, which are assumed to be representative for a homogeneous layer, while LIDAR observations clearly indicate a vertical variation inside the individual aerosol layers. In light of these circumstances the overall agreement of measured and simulated spectra can be judged satisfactory for the case at hand.

In how far the above mentioned uncertainties affect the simulations is going to be investigated in the following case studies, which feature higher aerosol loads. Hence they are better suited to reveal deviations between simulated and measured radiances due to a more pronounced influence exerted by the aerosol.

#### 4.4.2 29 January 2008

Two low aerosol layers with high concentrations of mineral dust were observed over the field site on 29 January 2008. Since no additional biomass layers were present, this day allows to investigate the optical properties of pure mineral dust. Figures 4.11 & 4.12 visualise the main input data ingested into the radiative transfer simulations in complete analogy to figures 4.8 & 4.9. Note that no airborne measurements of the mineralogical composition have been performed in the vicinity of Cape Verde on this date. Since the transport routes for the lower atmospheric

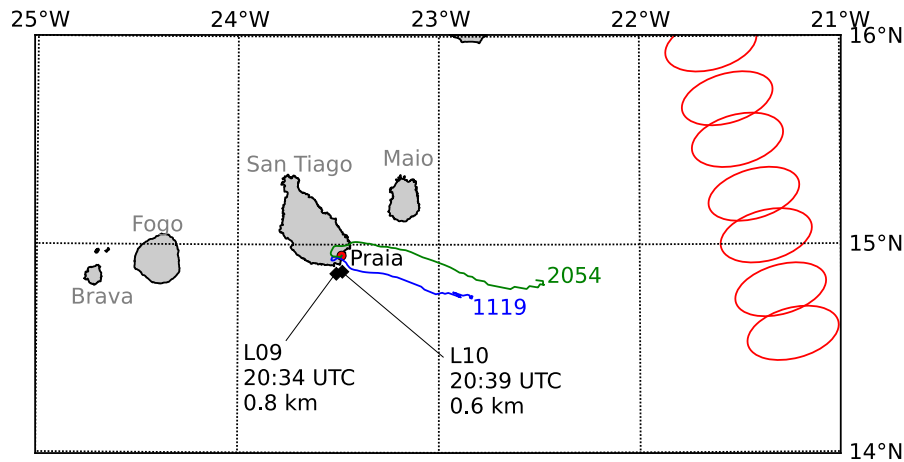


Figure 4.11: Compilation of data gathered on 29 January 2008 including a IASI overpass at 2207 UTC. Symbols are identical to figure 4.8.

layers are almost identical to those observed on 25 January 2008, the mineral composition determined from samples collected on this day are assumed to be valid for the upper dust layer on 29 January 2008, too. As the LIDAR plot in figure 4.12 (left) suggests vertically homogeneous optical properties in the lower layer, mineralogical composition and size distribution measured by Kandler et al. (2011b) at the surface are assumed to be representative for this layer.

Figure 4.13 shows a comparison of simulated and measured radiances at BOA and TOA. The upwelling radiances were averaged from 2024 UTC to 2105 UTC, thus covering the time span between airborne size distribution measurements and radiosonde ascent. The IASI observations were acquired approximately two hours later during the next MetOp overpass at 2207 UTC, which unfortunately did not cover Cape Verde. Hence the nearest pixels at the very end of the IASI swath had to be chosen. Apart from being quite far from the in-situ measurements, these observations were conducted at a zenith angle of  $58^\circ$ , where the plane-parallel approximation used in the simulations may not be an optimal choice (Illingworth et al., 2011). Taking into account the sum of these uncertainties, the agreement between measured and simulated radiances in figure 4.13 is quite good. The only exception is once more the ozone band, where the a-priori profile seemingly causes similar deviations as observed for 6 February 2008. The relatively high level of uncertainty is almost entirely attributable to variations in the averaged spectra, possibly indicating a lateral inhomogeneity in the aerosol properties. As before, an SST of 296 K yields better results than the IASI Level 2 value of 295 K (dashed curve), although none of the respective simulated spectra deviates by more than the estimated uncertainty from the measurement.

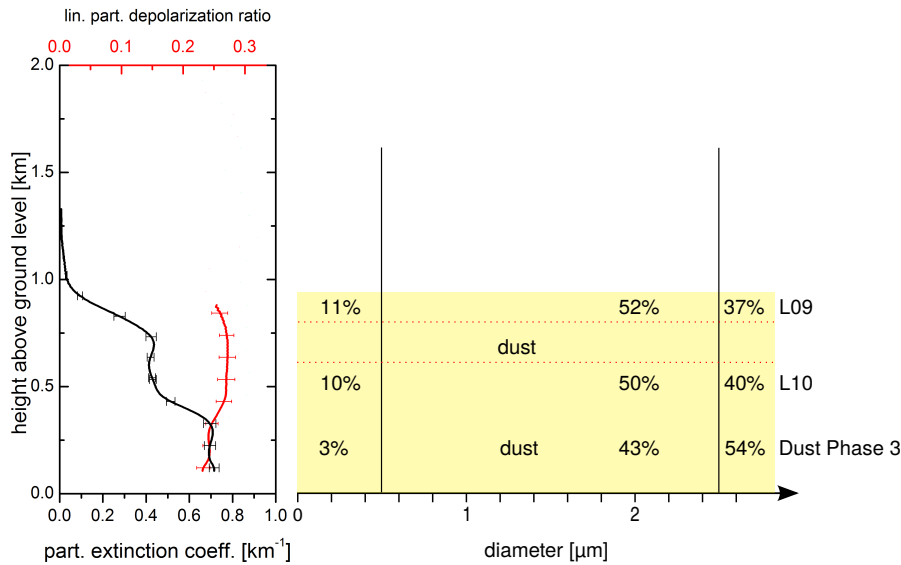


Figure 4.12: LIDAR profiles of extinction and depolarisation (left) and the derived modelled aerosol layers (right) for 29 January 2008. Annotations are identical to figure 4.8. (LIDAR plot courtesy of S. Groß)

In contrast to the measurements at TOA, the ground based measurements do not agree well with simulations. The most obvious deviation occurs between  $960\text{ cm}^{-1}$  and  $1000\text{ cm}^{-1}$ , where the measured dust emission notably exceeds its simulated counterpart. For wavenumbers greater than  $1000\text{ cm}^{-1}$  the simulated emission seems to be larger than experimentally determined. As discussed earlier, a number of uncertainties regarding the microphysical dust properties remain despite a thoroughly characterised atmospheric state. To investigate, in how far the observed deviations are attributable to these uncertainties, further simulations with modified input parameters are going to be performed. Owing to the fact, that the measured upwelling radiance is reproduced relatively well by the simulations, the discussion focuses on the downwelling radiation. Note that the small sensitivity of IASI measurements to the optical properties of low aerosols is not surprising, because any increase in dust absorption is almost entirely compensated for by additional dust emission due to the similar temperatures of dust and sea surface.

To estimate the effect of an imperfectly modelled refractive index, figure 4.14 shows the spectral dust signature (ref. chapter 4.3) obtained with various mineral dust models. These dust models are based on effective medium theory, implying that all particles of a given size are assumed to be representable in terms of a single refractive index. Apart from the internal volumetric mixture used in figure 4.13 (blue), this includes the commonly chosen refractive indices of Hess et al. (1998,

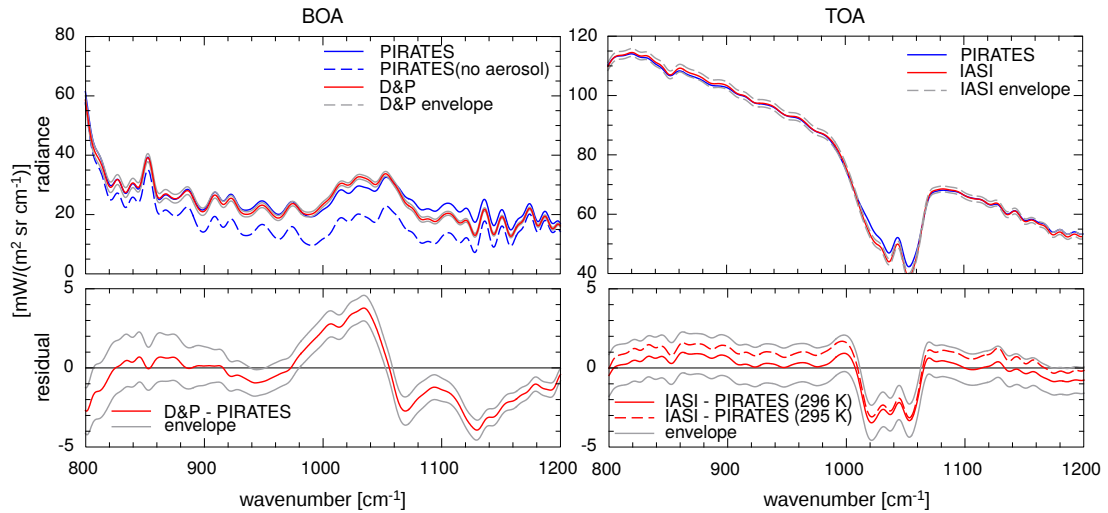


Figure 4.13: Measured (red) and simulated (blue) radiances (top row) at BOA (left) and TOA (right) along with residuals (bottom row) for 29 January 2008. Simulations are based upon the 2054 UTC radiosonde. BOA radiance measurements were averaged from 2024 UTC to 2105 UTC, while TOA observations were acquired at 2206 UTC. Annotated temperatures indicate the assumed surface temperature.

red), Shettle and Fenn (1979, green) and Volz (1973, light-blue). Except for the Shettle model, which underestimates the dust absorption over the entire atmospheric window domain, there is no clear advantage of one model over the other: while the internal mixture based on measured mineralogical composition seems to produce the best fit in the interval  $800 - 1000 \text{ cm}^{-1}$ , the Volz and OPAC models best capture the spectral behaviour at wavenumbers beyond  $1080 \text{ cm}^{-1}$ . Most importantly, however, none of the models accurately predicts the broad absorption maximum centred at  $1040 \text{ cm}^{-1}$ .

Since none of the internally mixed dust models examined above are capable of reproducing the measured signature within the estimated error, it is natural to proceed with external mixtures. An external mixture represents the aerosol in terms of particles with different refractive indices instead of pre-averaging the optical constants. Figure 4.15 displays the spectral signatures of three different external mixtures. Apart from the mineral composition used in the internal SAMUM-2 mixture (blue), the refractive indices of the bottom layer have been replaced by those measured on 25 January (red curve) and the mineral mixture measured at the surface on 29 January has been assumed for all layers (green). Obviously all three simulations lead to very similar aerosol signatures. This confirms the meteorological information, that the mineral composition on both days is almost the

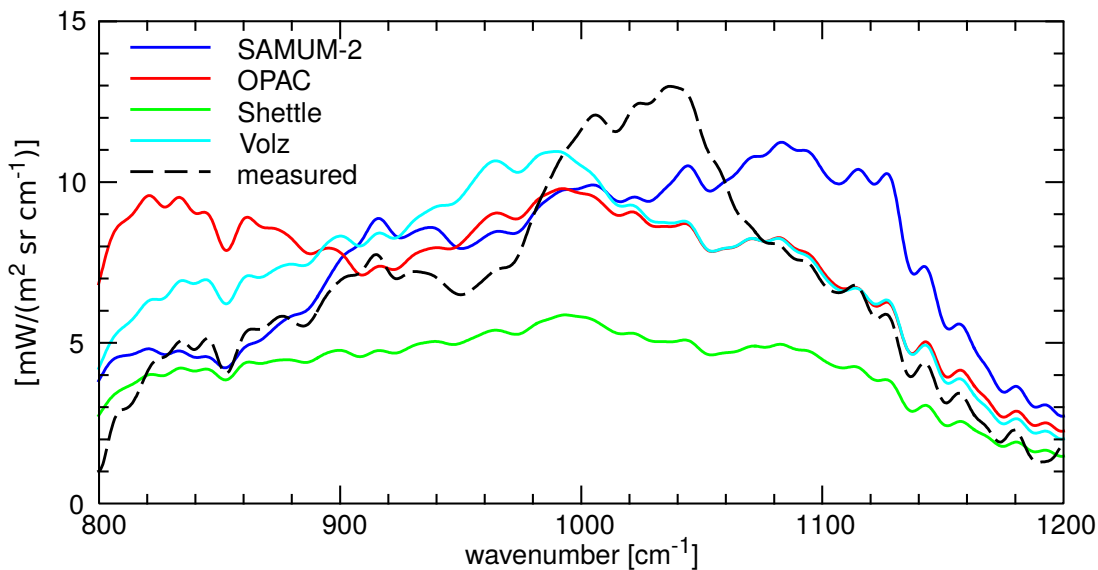


Figure 4.14: Simulated BOA aerosol signature on 29 January 2008 for an internal mixture of spherical particles with the refractive indices of OPAC (red), Shettle (green), Volz (light-blue) and based on SAMUM-2 microphysics (blue). The measured signature (dashed black) is provided as reference.

same due to similar source regions. However, the agreement with the measured dust signature improved only mildly compared to the internal mixtures, leading to the conclusion, that the refractive index is probably not the crucial parameter responsible for the poor agreement of simulation and measurement.

A closer look at figure 4.15 reveals, that the measured absorption maximum appears to be shifted compared to the simulations. Similar observations have been reported before by Thomas et al. (2009) for solar absorption measurements of mineral dust in the TIR. Hudson et al. (2008) and Mogili et al. (2008) discovered an analogous effect during laboratory studies and conclude that it is caused by non-spherical dust particles. As shown later by Kleiber et al. (2009) in a re-analysis of the same laboratory data, simulated and measured extinction spectra agree much better, if oblate spheroids with large aspect ratios (6–20, depending on the aerosol forming matter) are assumed in the simulations instead of spheres.

Unfortunately the PIRATES T-Matrix engine does not converge, if the particle shapes suggested by Kleiber et al. (2009) are used in combination with the SAMUM-2 size distribution. This is easily explained by the fact, that the particles examined within the scope of these laboratory studies were not as large as those observed during SAMUM-2. As laid out in chapter 3.1.3, it is a well-known fact, that the T-Matrix method becomes increasingly ill-conditioned with growing size

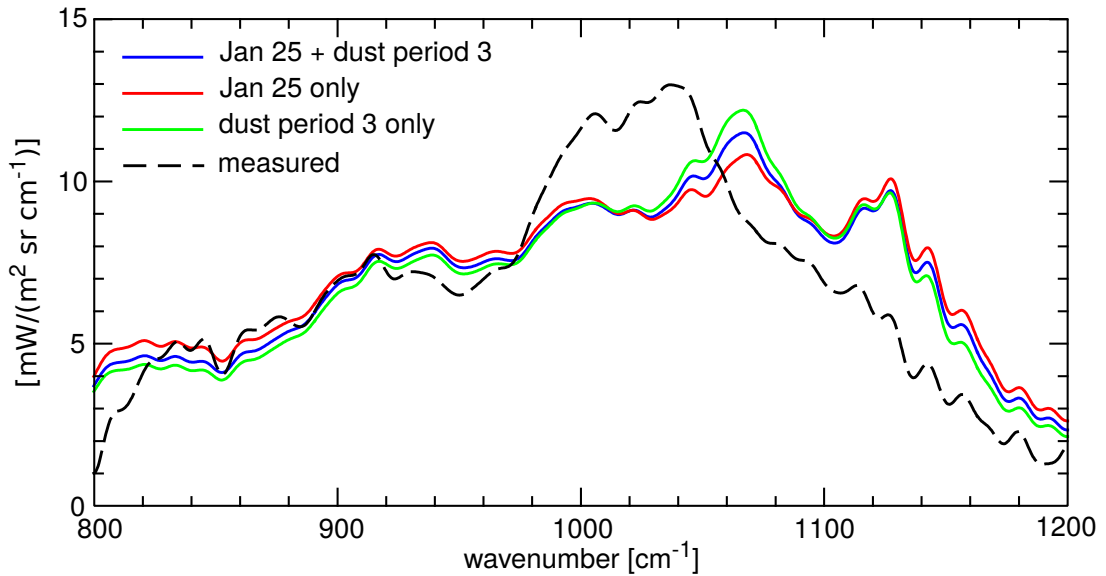


Figure 4.15: Simulated aerosol signatures for an external mixture of spherical particles using different mixtures (see text for details) compared to the measured signature (dashed black).

parameter, especially for the combination of aspect ratio and refractive index discussed here.

A possible solution to this problem has been suggested by Boer (2010), who derives dust composition and size distribution from ARIES measurements conducted within the scope of the SHADE campaign (Highwood et al., 2003). Since these airborne measurements were conducted between Sal and Dakar on 25 September 2000, they are expected to bear some resemblance to the measurements presented in the work at hand. Boer assumes a 2-modal log-normal distribution of oblate spheroids with a constant aspect ratio of 1:5 for all particles smaller than  $6.4 \mu\text{m}$  in diameter. Larger particles are neglected. This seems to be a sensible approach in light of the fact, that only one percent of the number density is omitted this way. However, a closer analysis reveals, that the truncated particles contribute approximately 13% of the total geometric cross-section. While this lack of additional cross-section is likely compensated by a higher total particle number concentration in the retrieval of Boer (2010), number density and size distribution are constrained by SAMUM-2 measurements here and thus cannot be altered.

To overcome the problem of truncation, a slightly different route is taken in the present thesis. The first modification concerns the cut-off, which is set to a fixed size parameter as opposed to a fixed radius. The cut-off is chosen as large as



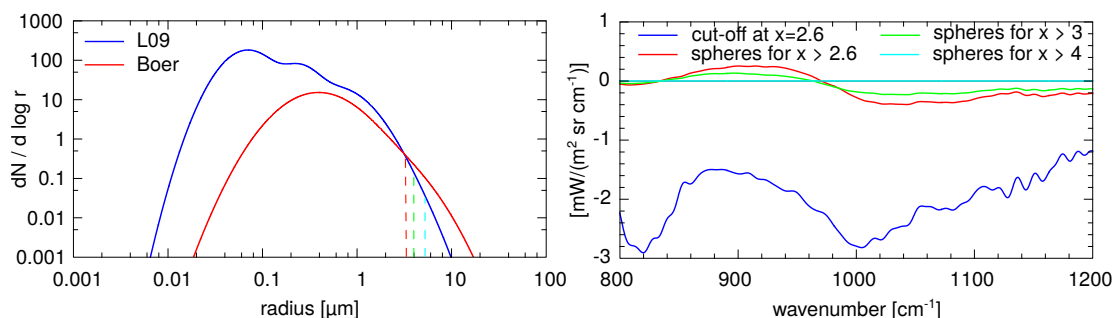


Figure 4.16: Left: Size distributions used by Boer (2010) (red) and measured on 29 January (blue). Right: Deviation of the simulated downwelling radiance at BOA for a hypothetical mixture of pure oblate quartz spheroids (aspect ratio 1:5) with respect to a simulation using spheres for  $x \geq 5$ . A simple cut-off (blue) causes significantly larger errors than a substitution with spheres.

possible such that T-Matrix computations still converge. Additionally, particles larger than the cut-off are assumed to be spherical, instead of totally neglecting them. Figure 4.16 exemplifies the effect this has with SAMUM-2 data: the size distribution assumed by Boer (2010) is plotted alongside its SAMUM-2 counterpart in the panel on the left. The sub-figure on the right shows the deviations in downwelling radiance at BOA compared to a benchmark simulation. All simulations use the SAMUM-2 size distribution and oblate quartz spheroids with aspect ratio 1:5. Particles with size parameter  $x > x_c = 5$  have been replaced by spheres for the benchmark simulation. For the other simulations, the cut-off was chosen at  $x_c = 4$  (light blue),  $x_c = 3$  (green) and  $x_c = 2.6$  (red). Furthermore the effect of completely neglecting all particles with size parameter  $x > 2.6$  (blue curve) as suggested by Boer (2010) is shown. Apparently the latter causes a significant bias in the downwelling radiance. The replacement of larger particles by spheres, however, yields acceptable results even at a rather moderate cut-off of  $x_c = 2.6$ . Increasing the cut-off further to  $x_c = 4$  yields virtually identical results to a value of  $x_c = 5$ , indicating that  $x_c = 4$  is a sufficient choice. Similar investigations lead to the choice of  $x = 0.01$  as lower threshold, below which spherical particles can be assumed without significantly altering the results.

Figure 4.17 shows a comparison of measured and simulated dust signature using oblate spheroids with aspect ratio 1:5 in the size parameter range  $0.01 \leq x \leq 4$  and spheres otherwise. The results were obtained for the same external mixture used before (blue) and for a fitted composition (red). The fit has been performed according to Boer (2010): First the aerosol signature is simulated separately for each mineral in the mixture, assuming all particles of the size distribution to consist of the respective pure material. Then the mixing ratio of each component is

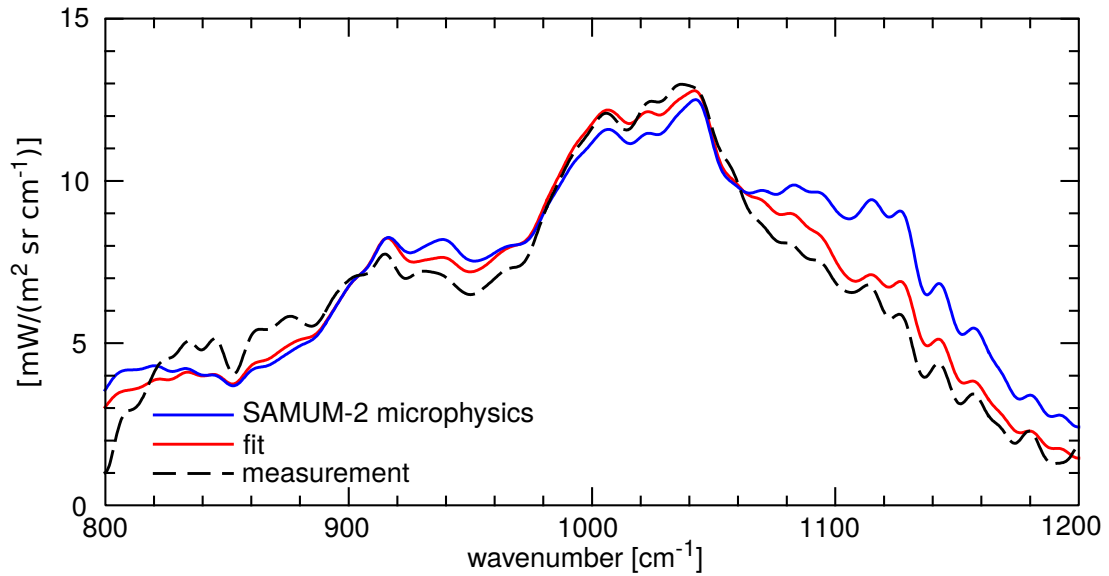


Figure 4.17: Simulated BOA aerosol signatures for 29 January 2008 obtained with an external mixture of spheroidal particles with aspect ratio 1:5. The mineralogy has been chosen based on SAMUM-2 microphysics (blue) and a least squares fit (red), respectively. The measured signature (dashed black) is provided as reference.

determined by a least-squares fit, such that a linear combination of the previously simulated aerosol signatures of the pure components best matches the measured aerosol signature. The such obtained weights are then inserted into another radiative transfer simulation to determine the bulk aerosol signature shown in figure 4.17. Note that this fit is a semi-empirical retrieval technique, as the bulk aerosol signature is assumed to be a linear combination of the pure-material signatures. Hence interactions between different aerosol constituents are neglected.

The mixture based on the measured composition (blue) clearly yields significant improvements compared to simulations using exclusively spheres (blue curves in figures 4.15 & 4.14). This is most apparent in the spectral region  $980 - 1060 \text{ cm}^{-1}$ , where the spheroids reproduce the shape of the absorption maximum very well in contrast to the spheres. However, the simulated aerosol effect is still overestimated around  $940 \text{ cm}^{-1}$  and beyond  $1060 \text{ cm}^{-1}$ . While the deviations around  $940 \text{ cm}^{-1}$  are almost within the estimated uncertainty, the deviations at wavenumbers greater than  $1060 \text{ cm}^{-1}$  are more severe.

An almost perfect agreement is obtained for the fitted mixture (red), which contains 52% illite, 22% kaolinite and 11% montmorillonite. The remaining 15% of

the particles have been omitted by the fit (i.e. the respective weight was zero). Due to the good agreement with the measured aerosol signature, it can be concluded that the assumptions of a negligible interaction between individual constituents of the mixture is valid. A comparison of the such derived mineral composition with in-situ measurements reveals some inconsistencies though: quartz, sulfates and orthoclase, all regularly identified in considerable abundance in SAMUM-2 samples remain unaccounted for by the fit. Moreover, illite particles constitute half of the fitted mixture, whereas the illite concentration in sampled material never exceeded 10%. Furthermore the total particle number concentration has to be reduced by 15% to minimise the residual. Interestingly enough, the composition retrieved here from SAMUM-2 spectra is very similar to the results reported by Boer (2010). This confirms the author's supposition, that the suggested fit is suited to effectively minimise the differences between measured and simulated aerosol signature. Unfortunately it has to be concluded, that the such derived microphysical aerosol properties do not necessarily mirror those of the real aerosol.

Striving to improve the fit between measured and simulated aerosol signature for the microphysically motivated SAMUM-2 dust composition, it is instructive to analyse the deviations in figure 4.17. As it turns out, the excess absorption beyond  $1060\text{ cm}^{-1}$  is caused by sulfates (ammonium sulfate & gypsum), quartz, orthoclase and illite. Since these are the materials for which fitted and measured composition differ the most, it is worth the effort to examine their properties a little further.

According to Kleiber et al. (2009) the measured absorption of quartz and illite is reproduced best by a mixed ensemble of spheroids with different shapes. More precisely, they report optimal results with an equally weighted mixture containing aspect ratios from 4:1 (prolate) to 1:6 (oblate) in the case of pure quartz. Their experimental results for illite are apparently matched best by an ensemble of oblate spheroids with aspect ratios between 17 and 19. For kaolinite –the dominating dust constituent during SAMUM-2– the same authors found the least distinct dependence on aspect ratio, with good results for a fixed aspect ratio of 1:5.

Applying the findings reported above to the SAMUM-2 data, the scattering properties of quartz spheroids were calculated for aspect ratios between 4:1 and 1:6. Unfortunately it was not possible to do the same for illite, since the extreme geometries caused the T-Matrix computations to diverge for a considerable fraction of larger particles contained in the SAMUM-2 size distribution. Sensitivity studies with aspect ratios of up to 1:10 did not show any significant improvements. Figure 4.18 shows the results for quartz. Although the changes compared to spheroids with a fixed aspect ratio (ref. figure 4.17) go in the right direction, their extent is too small to yield significant improvements.

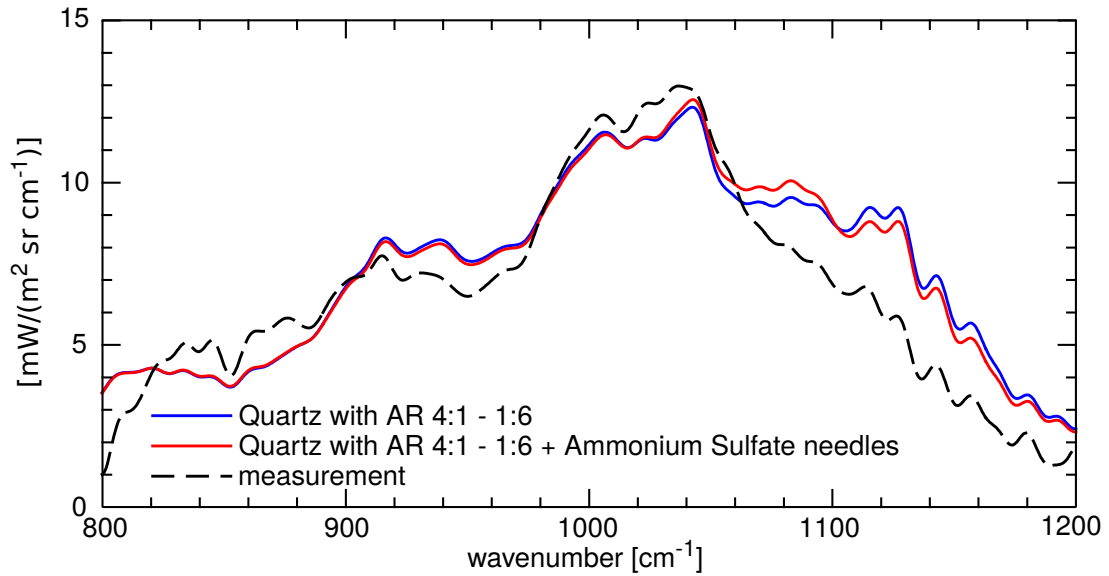


Figure 4.18: Plots similar to the blue curve in figure 4.18, but quartz particles were replaced by a distribution of spheroids with different aspect ratios from 4:1 to 1:6 (blue). Additionally sulfate particles were replaced by needle-like prolate spheroids with aspect ratio 10:1 (red).

In addition to the possible biases discussed so far, sulfates contribute significantly to the overall uncertainty budget. As mentioned previously, it was necessary to represent all sulfates by ammonium sulfate and gypsum for a lack of other optical constants in literature. This approach may be inaccurate, since Lieke et al. (2011) identify approximately half of all sulfates as sodium sulfate, while the remainder is a mixture of otherwise unspecified 'other sulfates' (i.e. neither ammonium sulfate nor gypsum). Indeed, transmission spectra of sodium sulfate and ammonium sulfate are dominated by the sulfate  $\nu_3$  band resulting in similar spectral behaviour in the TIR atmospheric window. Yet it is not clear if this holds for other sulfates as well. Zhao et al. (2006) are among the very few researchers investigating the process of sea-salt ageing with FTIR measurements. Their experiments with magnesium sulfate –apparently also abundant in aged sea salt– indicate, that depending on the relative humidity and concentration, the absorption peak of the sulfate band is shifted up to  $40\text{ cm}^{-1}$  due to the formation of polymer-like chains of contact ion pairs. Although it is tempting to attribute the deviations observed in figure 4.17 to a similar effect, it has to be stated that a shift by more than  $40\text{ cm}^{-1}$  was necessary to do so. Furthermore these results are likely limited to the (unknown) fraction of magnesium sulfate, whereas sodium sulfate absorption would remain inconsistent with the measurements.

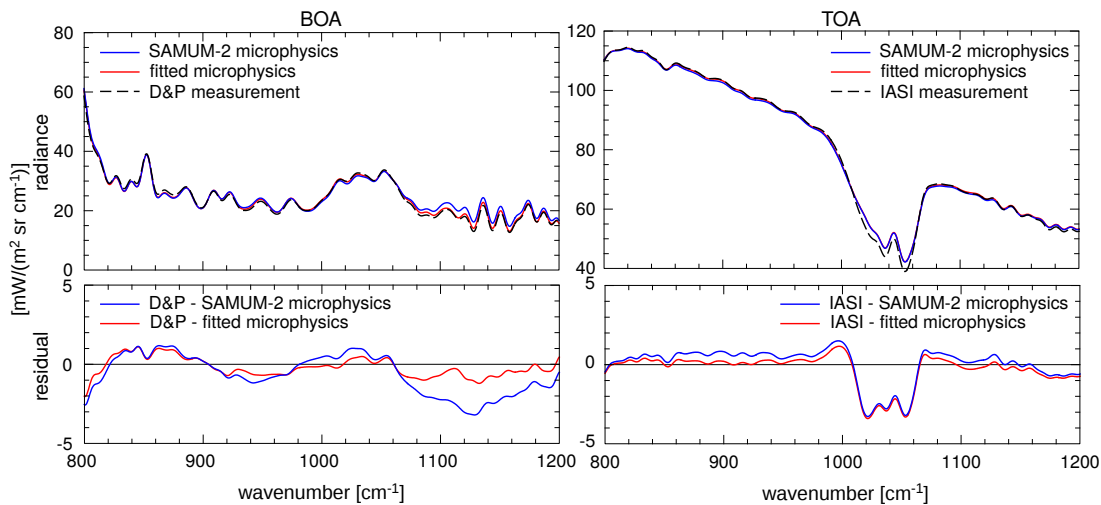


Figure 4.19: Same as figure 4.13, but simulations use oblate spheroids with aspect ratio of 1:5 instead of spheres. All simulations assume a surface temperature of 296 K.

Another possible explanation might be shape related. Kandler et al. (2011b) found sodium sulfate particles with needle-like shape and aspect ratios of up to 10 during SAMUM-2. Since sulfate particles were assumed to be spherical in the reported simulations, it is not unlikely that their simulated absorption peak is biased similar to the silicates. Using prolate spheroids as approximation to the observed needles, it was possible to compute such particles with aspect ratios up to 6:1 without having to neglect a substantial fraction of the size distribution due to divergent solutions of the T-Matrix code. These results are provided in Figure 4.18 (red) under the assumption that all sulfates are present in form of such needles. Again the modifications compared to a mixture of uniform spheroids is marginal and does not compensate for the majority of the bias. Thus it might be concluded that either more elongated particles are required or that the refractive index of a broader variety of sulfates was necessary. Unfortunately neither of these speculations can be examined further for the reasons outlined above.

Up to this point, the discussion concerning non-spherical particles has been restricted to downwelling radiances. Since an aerosol model should be capable to predict the optical properties at both BOA and TOA, some simulations addressing the issue are compiled in figure 4.19. In complete analogy to figure 4.13, it provides a comparison between simulated and measured radiances at BOA and TOA. However, a mixture of oblate spheroids with aspect ratio 1:5 has been assumed instead of spheres to produce the graphs in figure 4.19. Obviously the fitted microphysical mixture is in very good agreement with measurements of both upwelling and

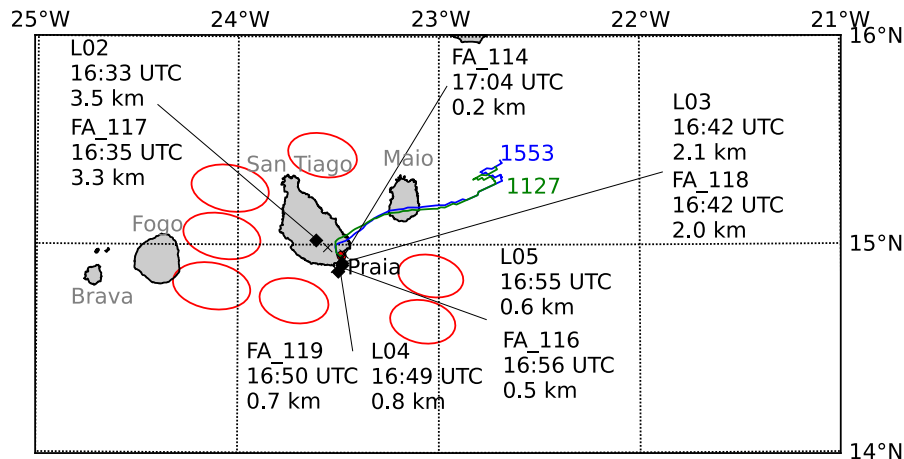


Figure 4.20: Compilation of data gathered on 25 January 2008 including a IASI overpass at 1041 UTC. Symbols are identical to figure 4.8.

downwelling radiation. The mineral mixture derived from in-situ measurements agrees not quite as well with the measurements, but it still matches the BOA measurements much better than any mixture using spherical particles. Since the residua at TOA have been small already for spherical particles, the improvements here are less pronounced but still visible. Based on these findings, it has to be concluded, that the fitted mineral mixture, although not in agreement with in-situ observations, yields a very good approximation to the aerosol optical properties in the TIR. Whether this is a coincidental result or a general trend will be analysed in the following case study.

#### 4.4.3 25 January 2008

Several dust and biomass layers were observed over Praia on 25 January 2008. Since the influences of pure dust and pure biomass have been scrutinized in the previous case studies, the data gathered on 25 January 2008 is used to verify the results gained during those studies. As before the data ingested into the radiative transfer simulations is summarised in figures 4.20 & 4.21 in graphical form. Since 25 January was dedicated entirely to column closure experiments by the SAMUM-2 consortium, a large number of in-situ observations was collected in the vicinity of Praia by the DLR Falcon aircraft. The result is a unique data set comprising all essential information required for radiative transfer simulations.

The IASI pixels displayed in figure 4.20 were recorded during an overpass at 1022 UTC at an average viewing angle of  $50^\circ$  relative to the surface normal. As

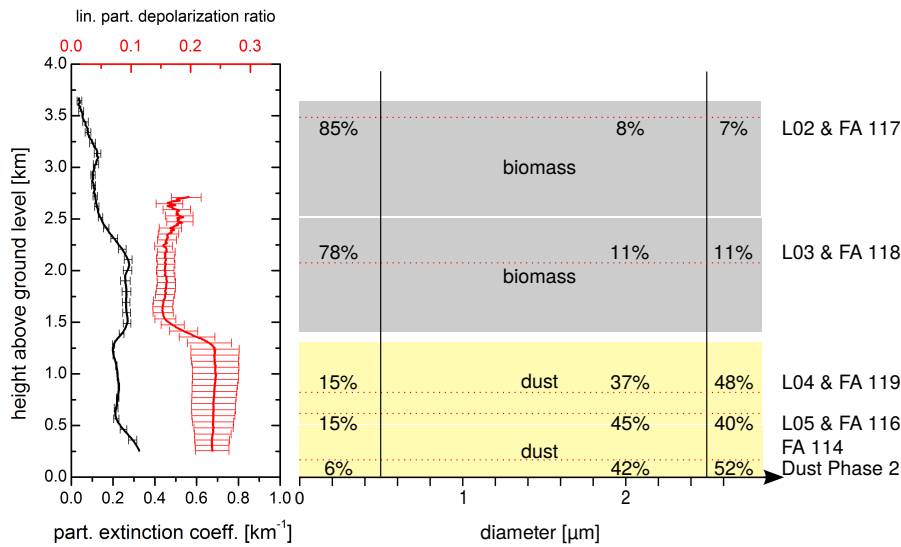


Figure 4.21: LIDAR profiles of extinction and depolarisation (left) and the derived modelled aerosol layers (right) for 25 January 2008. Annotations are identical to figure 4.8. (LIDAR plot courtesy of S. Groß)

discussed before, it is not completely clear, how accurate the plane-parallel approximation is in this case. Additionally it has to be taken into account that the time gap between overpass and sonde launch amounts to approximately one hour, during which a certain amount of solar heating is expected to occur in the lower troposphere. Even more significant is the temporal distance between overpass and in-situ observations. But since no other space-borne observations are available for this day and because LIDAR time series indicate little change in the vertical dust profiles, these measurements are included in the case study despite the imperfect circumstances.

Figure 4.22 summarises measured and simulated radiances in the same fashion introduced in previous case studies. As before, the simulations have been carried out assuming spherical model particles, to test whether this assumption yields similar deviations as observed during the case study for 29 January 2008. Since the IASI retrieved SST for the shown pixels varies between 294 K and 295 K, only one simulation for a surface temperature of 295 K is shown in the plots. Higher values did not lead to an improved agreement of simulated and measured upwelling radiances.

Apart from the usual deviations in the ozone band, simulated and measured upwelling radiances at TOA (figure 4.22, right) agree within the statistical uncertainty estimated for the IASI spectra. This is in accordance with the results

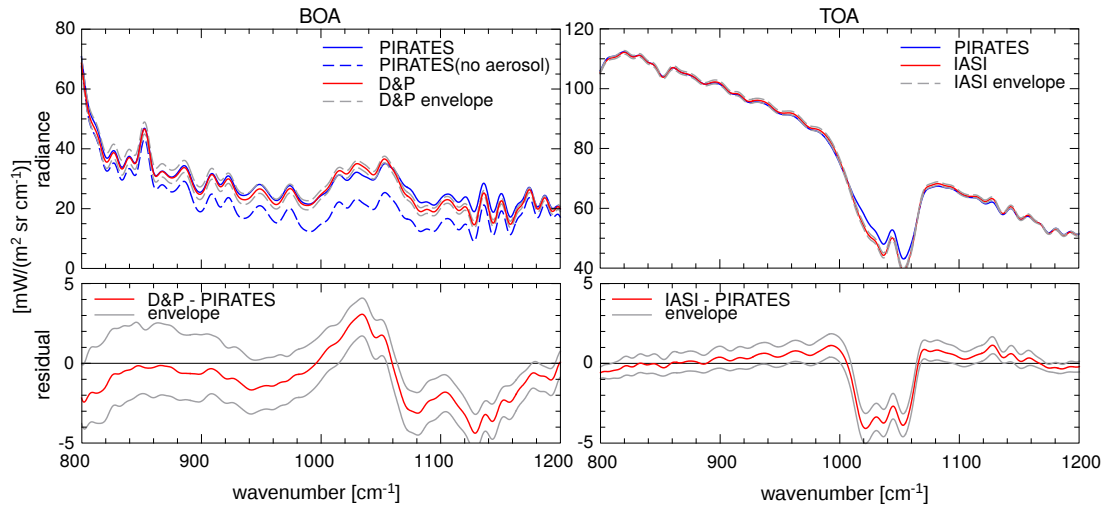


Figure 4.22: Measured (red) and simulated (blue) radiances (top row) at BOA (left) and TOA (right) along with residuals (bottom row) for 25 January 2008. BOA results are based upon the 1553 UTC radiosonde and radiance measurements averaged from 1555 UTC to 1620 UTC. TOA data include a IASI overpass at 1041 UTC and the 1127 UTC radiosonde. A surface temperature of 295 K was assumed for the simulations.

encountered before. A notable exception is the surface temperature, which is in better agreement with retrieved values compared to earlier investigations. Although the value of 295 K assumed in the simulations constitutes the upper limit of temperatures provided in the IASI Level 2 product ( $294.5 \pm 0.5$  K), it is still within the statistical uncertainty. Nonetheless, there remains a tendency towards a cold bias, even though it is less pronounced here than in previous case studies.

Regarding the downwelling radiance at BOA (figure 4.22, left), the results for 25 January 2008 are remarkably consistent with those for 29 January 2008. Comparing the residuals in figures 4.22 & 4.13 (bottom left), it becomes apparent that both are almost identical. This confirms the conclusion, that spherical particles are not well suited to model mineral dust aerosol in the TIR. Furthermore, the similarity of the results obtained by two independent measurements during different conditions underline the reliability of the calibration and correction algorithms developed for the D&P Model 102 FTIR within the scope of this thesis (ref. chapters 2.2.4 & 2.2.8). Although the instrument cannot compete with benchmark instruments in terms of spectral resolution and overall measurement uncertainty, it has still contributed invaluable data to the case studies discussed in the present chapter.

The final goal of this chapter is to verify the supposition, that spheroidal model



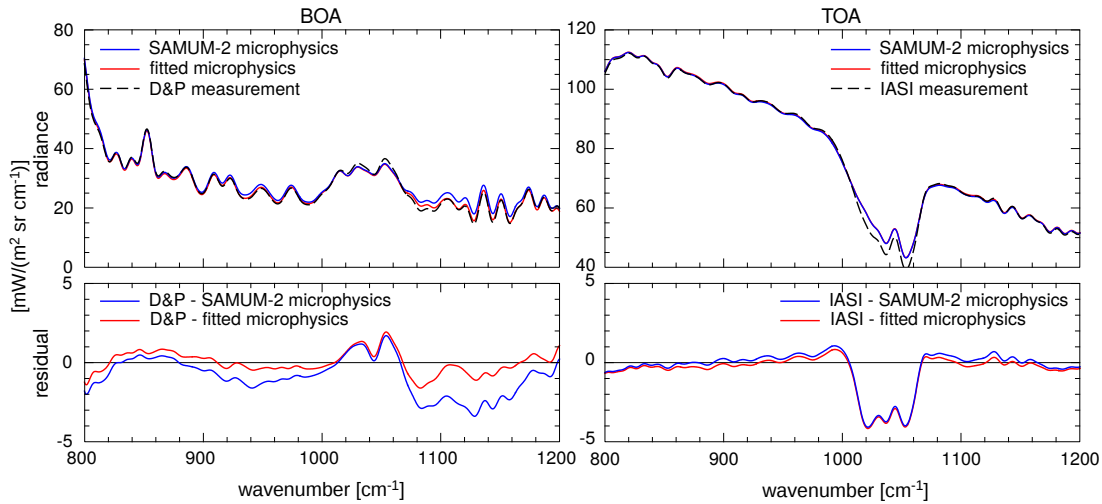


Figure 4.23: Same as figure 4.22, but simulations use oblate spheroids with aspect ratio of 1:5 instead of spheres.

particles constitute a valid approximation for mineral dust in the TIR. For this purpose the simulations discussed above were repeated using oblate spheroids with aspect ratio 1:5 instead of spheres. Additionally the mineral composition has been retrieved from the measured aerosol signature with the method of Boer (2010) discussed in the previous section. The respective computed and measured spectra are summarised in figure 4.23.

Once more the improvements achieved with non-spherical particles (blue) are most prominent in the main kaolinite absorption band around  $1040\text{ cm}^{-1}$ , where both mixtures significantly reduce the bias caused by spherical particles. As before, the overestimation of the aerosol optical depth beyond  $1100\text{ cm}^{-1}$  remains if the mineral composition is chosen based on microphysical analysis. Possible explanations for this behaviour have been discussed in the case study for 29 January 2008, where a similar effect could be observed. As discussed in this context, further investigations are required to unambiguously resolve this problem, but these are beyond the scope of this thesis.

Interestingly it is again possible to reduce the discrepancies between simulation and measurement with a modified aerosol composition. The curves shown in figure 4.23 (red) were obtained with a mixture of 30% illite, 24% kaolinite, 17% montmorillonite, 3% albite and 2% quartz. The remaining 24% of the particles were neglected. This composition bears some resemblance to the optimised mixture obtained in the case study for 29 January 2008, although the illite content found here is clearly reduced, while albite and quartz have been added. The amount of

particles neglected in the fit is somewhat larger than before. As was the case for 29 January 2008, the retrieved mixture has not much in common with the particle chemistry of aerosol samples analysed within the scope of SAMUM-2.

In accordance with the case study for 29 January 2008, simulations of the upwelling radiance at TOA assuming spheroidal model particles (figure 4.23, right) agree better with IASI observations than simulations assuming spheres (figure 4.22, right). Again it is obvious though, that the improvements are minor compared to the surface, because spherical particles already yield acceptable results at TOA.

#### 4.4.4 Discussion

Reviewing the case studies discussed above, three major conclusions can be drawn from the data. Firstly it could be clearly demonstrated, that the presence of mineral dust –be it in pure or mixed form– has a measurable impact on the radiances at BOA and TOA. While the large influence at the surface comes as no surprise, the effect exerted by mineral dust on satellite based measurements was less obvious. Nonetheless examinations of IASI spectra revealed a potential bias of up to 1 K in SST measurements due to the presence of aerosols. Further analysis of the data indicated, that the comparatively small aerosol signature can be easily mistaken for a deviation in surface temperature, leading to a conceivable pitfall in the retrieval. These findings are supported by validation studies of the IASI Level 2 SST product with drifting buoys (O’Carroll et al., 2012). Therein the authors report a global mean cool bias of 0.3 K and values around 1 K in the vicinity of Cape Verde. Regarding the high frequency of dust outbreaks in this region, these results support the theory of an aerosol induced bias.

The second result derived from the case studies concerns the shape of model particles assumed in radiative transfer simulations. The findings presented in this thesis unanimously indicate that spherical particles constitute an inaccurate model for mineral dust aerosols in the TIR. The only exception are scenarios, where the influence of dust is weak (e.g. 6 February 2008 or TOA observations). In these cases spherical particles turned out to be a good first approximation. Still it could also be shown, that non-spherical particles typically yield even better results. Stronger dust signatures, such as those measured at the surface on 29 January 2008, could be reproduced well using oblate spheroids with an aspect ratio of 1:5, whereas spheres yielded comparatively poor results. These findings agree well with recent observations obtained from field studies (Thomas et al., 2009) and laboratory experiments (Hudson et al., 2008, Mogili et al., 2008, Kleiber et al., 2009). In contrast to Kleiber et al. (2009), no significant improvements were attained using mixtures

of spheroids with diverse aspect ratios. This fact might be attributable to differences between pure crystalline matter analysed in the laboratory studies and the more inhomogeneous natural aerosol constituents encountered during SAMUM-2.

The third and final outcome is related to the mineral composition and the associated refractive index of the aerosols. In accordance with earlier studies of Boer (2010), a fitted mineral mixture was shown to be capable of minimising the residual between simulated and measured downwelling radiances. However, it is doubtful whether the such retrieved composition and particle number density are useful. Apart from a consistent underestimation of the particle number density, the abundances of retrieved mineral species were found to deviate significantly from results of in-situ samples analysed in the laboratory. When generalising these results to the work of Boer (2010), however, the different time of the year has to be considered. While SAMUM-2 took place in January and February, the measurements of Highwood et al. (2003) (analysed by Boer) were conducted in September. As pointed out by Haywood et al. (2008), altitude and transport routes of the aerosols are subject to seasonal variability due to a different location of inter-tropical convergence zone and Harmattan front. Thus it cannot be ruled out completely, that the mineral composition retrieved by Boer (2010) is accurate for the studied case. Still, observed dust signature and retrieved mineral composition display strong similarity in both studies. Hence the validity of the mineral composition retrieved by Boer (2010) has to be challenged based on the data presented here. In any case the findings underline the importance of dedicated closure studies including a variety of instrumentation for a thorough characterisation of the atmospheric state.

Although it has been demonstrated, that the such developed aerosol model yields superior results compared to spherical particles and other commonly used models, there clearly remains room for improvement. Especially the discrepancies between retrieved and measured mineral composition indicate inconsistencies in the model. These doubts are fostered by the required large aspect ratio of 5 compared to an average value of 1.6 reported by Kandler et al. (2011b) based on laboratory studies. It might be speculated, that less symmetric particles with shapes more closely related to the geometry of real dust particles could lead to even better results or that the optical anisotropy, which is quite common among dust constituents, has to be accounted for. To the best of the author's knowledge, no such investigations addressing radiative transfer in the TIR have been conducted so far.

Laboratory measurements of comparatively simple model aerosols similar to those conducted by Hudson et al. (2008) would certainly be of great interest, because they contribute important experimental reference results against which simulations can be validated. Additionally it would be helpful, if reliable measurements of the

optical constants were available for a broader variety of dust constituents. This is especially true for orthoclase and several sulfate end-members. Apart from more experimental work, advances in the numerical treatment of electromagnetic scattering theory are desirable as well, because the current approaches still constrain models to very symmetric particle shapes, neglecting e.g. the surface roughness of real-world aerosols.

# Chapter 5

## Summary and Outlook

This thesis treats the optical properties of mixed mineral dust and biomass burning aerosol in the TIR based on FTIR measurements and radiative transfer simulations. The measurements were part of the SAMUM-2 field experiment conducted from January to February 2008 at Praia, Cape Verde. The large amount of different instruments co-located at the main field site during the campaign resulted in a unique dataset comprising in-situ information and remote sensing data perfectly suited for column closure studies. In addition to the ground based instrumentation, the DLR Falcon research aircraft collected aerosol samples at different altitudes above the field site for online and offline analysis. Spaceborne measurements of the upwelling TIR radiance acquired during several IASI overpasses complete the observations. The ultimate goal of this work is to investigate the consistency of microphysical and TIR remote sensing data. This is achieved by reproducing the measured radiances at BOA and TOA with a newly developed radiative transfer model, which ingests the results of microphysical aerosol measurements performed by other SAMUM groups.

The first topic addressed in this thesis are observations of the downwelling atmospheric radiance with the D&P Model 102 FTIR (ref. chapter 2). The Model 102 is a commercial off-the-shelf instrument, which has been operated by the author to perform the ground based FTIR measurements during SAMUM-2. The such obtained data forms a fundamental building block for the studies reported on in chapter 4. Additionally, a thorough instrument characterisation has been performed to analyse the performance of the Model 102 for the designated assignment. Most notably an improved calibration method has been developed to overcome certain instrument specific deficiencies, which otherwise could have rendered the instrument useless for the intended mission. Furthermore a significant drift –likely

attributable to thermal flows inside the spectrometer— has been corrected with a novel algorithm. Although calibration and drift correction have been specifically designed for the D&P Model 102, they are general enough to be applicable to other FTIR instruments without further adaptation. Laboratory measurements of high precision NIST black bodies were employed for a characterisation of the D&P calibration source to couple the calibrated radiances to NIST standards. A comparison of atmospheric measurements with simultaneous MAERI observations has been used to validate the Model 102 for the intended application.

Radiative transfer simulations form the second building block of this thesis. These simulations are required for the analysis of the measured radiances in combination with the aerosol properties inferred by other SAMUM-2 groups. Chapter 3 describes the radiative transfer library PIRATES, a versatile tool box for radiative transfer applications developed as part of this thesis. While PIRATES has been designed primarily with TIR applications in mind, most functionality is more general in nature, such that it could be of interest in the UV/Vis spectral region as well. In contrast to most available radiative transfer models, one design goal has been parallelization from the beginning on. As a result PIRATES efficiently capitalises on the increased concurrency available on modern computer hardware. Most notable features of the library include a parallel line-by-line engine with configurable accuracy for gaseous absorption, concurrent Mie- and T-Matrix modules for the computation of spherical and non-spherical particles and a parallel discrete ordinate solver based on DISORT. PIRATES has been validated against other well proven radiative transfer models and against benchmark atmospheric measurements.

The third and final part of this thesis (chapter 4) describes the analyses of measured radiances in the context of experimental aerosol information gathered during SAMUM-2. Several case studies using PIRATES address the uncertainties in various input quantities on the simulated radiances. The ozone profile and the sea surface temperature turn out to be the most influential parameters for the upwelling radiances. The downwelling radiances are mostly sensitive to changes in temperature and relative humidity in the lower troposphere.

Examination of the downwelling radiances measured with the D&P FTIR revealed a strong impact of pure low dust layers in the TIR atmospheric window region. The associated aerosol signature has a strong peak around  $1000\text{ cm}^{-1}$ . Lofted layers composed of biomass burning aerosol and mineral dust were found to have a considerably weaker signature at the surface due to their smaller optical depth and lower temperature. In contrast to this, IASI observations above the ocean yielded weak signatures for both aerosol types. In the case of low mineral dust layers, the comparatively small aerosol effect at TOA is attributable to the small

temperature difference between particulate matter and the surface, which leads to a low contrast. In the case of lofted mixtures of mineral dust and biomass burning aerosol, the small optical depth was the reason for the weak TOA signature. Since the aerosol signature at TOA bore close resemblance to the effect of a reduced surface temperature, it has been demonstrated that SST retrievals are likely to be biased if such aerosols are neglected in the inversion. This assumption has been confirmed in the course of later investigations.

The aerosol optical properties were scrutinised in three case studies comprising a joint analysis of simulated and measured radiances. It turned out, that none of the frequently employed aerosol models with pre-defined refractive indices for mineral dust were well suited to reproduce the BOA observations. Furthermore the investigations revealed, that spherical particles generally constitute an inappropriate model for dust particles in the TIR. Oblate spheroids with aspect ratio 5, on the other hand, were demonstrated to yield optical properties in good agreement with BOA measurements. Nonetheless spheres have proven to be a valid first approximation in the case of weak aerosol signatures, although spheroids lead to even better results in most cases.

The best agreement between measured and simulated radiances was achieved, if the abundance of each mineral constituent in an external mixture was chosen based on a least squares technique. Unfortunately the such obtained aerosol composition proved to be inconsistent with the results attained from the analysis of in-situ samples. Selecting the amount of each mineral component according to the in-situ data instead of fitting it, lead to distinctively larger residuals at wavenumbers beyond  $1000\text{ cm}^{-1}$ . It has been laid out, that these deviations are possibly attributable to sulfates, which had to be modelled based on incomplete refractive index data in some cases. In other cases the shape of sulfate particles could not be modelled adequately due to the unavailability of algorithms for the computation of their corresponding optical properties.

Although this thesis provides some answers regarding the simulation of mineral dust aerosol in the TIR, several questions are left open for future studies. One of the most important topics, which apparently warrants further investigation based on the results discussed in this thesis, is the role of sulfates. Due to a lack of optical constants and a surprisingly small number of laboratory studies addressing the interaction of sulfate aerosols with TIR radiation, there remains a high level of uncertainty regarding their contribution to the bulk aerosol optical properties. In general there is a need for more reliable optical constants in the TIR, since the published data for many materials is quite old and in some cases obviously faulty. The recent inclusion of refractive indices for a few important materials into the HITRAN database is definitively considered a step in the right direction in this

regard, but the amount of data is still insufficient.

The search for optimal model geometries remains another interesting research topic. Clearly this thesis has confirmed former studies suggesting that particle shape constitutes an important parameter in the TIR. However, it is doubtful whether spheroids indeed constitute optimal model particles, since neither the refractive index nor the geometric shape leading to the best matching optical properties were in good agreement with microphysical or chemical observations. Perhaps other more irregular shapes, possibly including surface roughness should be considered in future simulation studies.

Prerequisite for such investigations is a progress in the numerical treatment of electromagnetic scattering, because currently available T-Matrix codes are not capable to handle particles of the suggested shape in the necessary size range. The required advances might be attainable either by a brute force approach employing e.g. multi-precision arithmetic or –preferably of course– via mathematical stabilisation of the ill-conditioned matrix inversion.

Another route to pursue are further studies based on the aerosol model developed in this thesis. Since the latter has been demonstrated to accurately predict the influence of mineral dust aerosols on radiances at both BOA and TOA, it could e.g. be applied to parametrise the radiative effect of mineral dust aerosols for a set of representative conditions. This type of research might be of interest for the improvement of aerosol models implemented into large scale climate simulations or for an uncertainty assessment of these models.

Finally it is possible to validate different aerosol retrieval algorithms with the help of the information compiled within the scope of this thesis. Since measured radiances are available at BOA and TOA in combination with reference data on aerosol composition and particle number concentration, the dataset comprises a demanding set of test scenarios for a variety of retrieval methods. Additional intermediate aerosol properties, such as e.g. aerosol optical depth or single scattering albedo could be readily calculated with PIRATES, which has been demonstrated to reproduce the optical properties sufficiently well in a physically consistent manner.



# Bibliography

- Abrams, M. C., Toon, G. C., and Schindler, R. A. (1994). Practical example of the correction of Fourier-transform spectra for detector nonlinearity. *Appl. Opt.*, 33(27):6307–6314.
- Ansmann, A., Petzold, A., Kandler, K., Tegen, I., Wendisch, M., Müller, D., Weinzierl, B., Müller, T., and Heintzenberg, J. (2011). Saharan Mineral Dust Experiments SAMUM-1 and SAMUM-2: What have we learned? *Tellus*, 63B(4):403–429.
- Aronson, J. R. (1986). Optical constants of monoclinic anisotropic crystals: Orthoclase. *Spectrochimica Acta*, 42A(2/3):187–190.
- Aronson, J. R. and Strong, P. F. (1975). Optical constants of minerals and rocks. *Appl. Opt.*, 14(12):2914–2920.
- Baranov, Y. I. and Lafferty, W. J. (2012). The water vapour self- and water-nitrogen continuum absorption in the 1000 and 2500  $\text{cm}^{-1}$  atmospheric windows. *Philos. Trans. R. Soc. A*, 370:2578–2589.
- Beer, R. (1991). *Remote Sensing by Fourier Transform Spectroscopy*, volume 120 of *Chemical Analysis*. John Wiley & Sons, New York, Chichester, Brisbane, Toronto, Singapore.
- Berk, A., Anderson, G. P., Acharya, P. K., Bernstein, L. S., Muratov, L., Lee, J., Fox, M., Adler-Golden, S. M., Chetwynd, Jr., J. H., Hoke, M. L., Lockwood, R. B., Gardner, J. A., Cooley, T. W., Borel, C. C., Lewis, P. E., and Shettle, E. P. (2006). Modtran5: 2006 update. *Proc. SPIE*, 6233:62331F.
- Bertie, J. E. and Lan, Z. (1996). Infrared Intensities of Liquids XX: The Intensity of the OH Stretching Band of Liquid Water Revisited, and the Best Current Values of the Optical Constants of H<sub>2</sub>O(l) at 25 °C between 15,000 and 1  $\text{cm}^{-1}$ . *Appl. Spectrosc.*, 50(8):1047–1057.
- Blumstein, D. and Fjortoft, R. (2008). Dossier de définition des algorithmes IASI. Technical Report IA-DF-0000-2006-CNE, CNES.
- Boer, G. J. (2010). *Investigation of high spectral resolution signatures and radiative forcing of tropospheric aerosol in the thermal infrared*. PhD thesis, Georgia

- Institute of Technology.
- Bohren, C. F. and Huffman, D. R. (1998). *Absorption and Scattering of Light by Small Particles*. WILEY-VCH, Weinheim.
- Bronstein, I. N., Semendjajew, K. A., Musiol, G., and Mühlig, H. (2001). *Taschenbuch der Mathematik*. Verlag Harri Deutsch, Thun, Frankfurt am Main, 5 edition.
- Cady-Pereira, K. E., Shephard, M. W., Turner, D. D., Mlawer, E. J., Clough, S. A., and Wagner, T. J. (2008). Improved Daytime Column-Integrated Precipitable Water Vapor from Vaisala Radiosonde Humidity Sensors. *J. Atmos. Ocean. Technol.*, 25:873–883.
- Clough, S., Shephard, M., Mlawer, E., Delamere, J., Iacono, M., Cady-Pereira, K., Boukabara, S., and Brown, P. (2005). Atmospheric radiative transfer modeling: a summary of the AER codes. *J. Quant. Spectrosc. Radiat. Transfer*, 91(2):233–244.
- Clough, S. A., Kneizys, F. X., and Davies, R. W. (1989). Line Shape and the Water Vapour Continuum. *Atmos. Res.*, 23:229–241.
- Cooley, J. W. and Tukey, J. W. (1965). An Algorithm for the Machine Calculation of Complex Fourier Series. *Mathematics of Computation*, 19(90):297–301.
- Das, T. M. (1988). Effect of Deposition of Dust Particles on Leaves of Crop Plants on Screening of Solar Illumination and Associated Physiological Processes. *Environ. Poll.*, 53:421–422.
- De Longueville, F., Hountondji, Y.-C., Henry, S., and Ozer, P. (2010). What do we know about effects of desert dust on air quality and human health in West Africa compared to other regions? *Sci. Tot. Environ.*, 409:1–8.
- Delamere, J. S., Clough, S. A., Payne, V. H., Mlawer, E. J., Turner, D. D., and Gamache, R. R. (2010). A far-infrared radiative closure study in the Arctic: Application to water vapor. *J. Geophys. Res.*, 115(D17106):1–17.
- Engelbrecht, S. (2010). Charakterisierung und Einsatz eines tragbaren FTIR Spektrometers. Diploma thesis, Ludwig-Maximilians-Universität München, München.
- EUMETSAT (2011). IASI Level 1 Product Guide. Technical Report EUM/OPS-EPS/MAN/04/0032, EUMETSAT, Darmstadt.
- Fiedler, L., Newman, S., and Bakan, S. (2005). Correction of detector nonlinearity in Fourier transform spectroscopy with a low-temperature blackbody. *Appl. Opt.*, 44(25):5332–5340.
- Fomin, B. A. (1995). Effective Interpolation Technique for Line-by-line Calculations of Radiation Absorption in Gases. *J. Quant. Spectrosc. Radiat. Transfer*, 53(6):663–669.

- Fowler, J. B. (1995). A Third Generation Water Bath Based Blackbody Source. *Journal of Research of the National Institute of Standard and Technology*, 100(5):591–599.
- Friedman, D. (1969). Infrared characteristics of ocean water (1.5–15  $\mu\text{m}$ ). *Appl. Opt.*, 8:2073–2078.
- Frigo, M. and Johnson, S. G. (2005). The Design and Implementation of FFTW3. *Proceedings of the IEEE*, 93(2):216–231. Special issue on ‘Program Generation, Optimization, and Platform Adaptation’.
- Glotch, T. D., Christensen, P. R., and Sharp, T. G. (2006). Fresnel modeling of hematite crystal surfaces and application to martian hematite spherules. *Icarus*, 181:408–418.
- Glotch, T. D., Rossman, G. R., and Aharonson, O. (2007). Mid IR reflectance spectra and optical constants of ten phyllosilicate minerals. *Icarus*, 192:605–622.
- Goudie, A. S. and Middleton, N. J. (2006). *Desert Dust in the Global System*. Springer, Berlin, Heidelberg, New York.
- Groß, S., Gasteiger, J., Freudenthaler, V., Wiegner, M., Greiß, A., Schladitz, A., Toledano, C., Kandler, K., Tesche, M., Ansmann, A., and Wiedensohler, A. (2011a). Characterization of the planetary boundary layer during SAMUM-2 by means of lidar measurements. *Tellus*, 63B(4):695–705.
- Groß, S., Tesche, M., Freudenthaler, V., Toledano, C., Wiegner, M., Ansmann, A., Althausen, D., and Seefeldner, M. (2011b). Characterization of saharan dust, marine aerosols and mixtures of biomass-burning aerosols and dust by means of multi-wavelength depolarization and raman lidar measurements during samum 2. *Tellus*, 63B(4):706–724.
- Hamilton, M. W. (2000). Phase Shifts in Multilayer Dielectric Beam Splitters. *Am. J. Phys.*, 68(2):186–191.
- Hansell, R. A., Liou, K. N., Ou, S. C., Tsay, S. C., Ji, Q., and Reid, J. S. (2008). Remote sensing of mineral dust aerosol using AERI during the UAE<sup>2</sup>: A modeling and sensitivity study. *J. Geophys. Res.*, 113(D18202):1–18.
- Hansell, R. A., Tsay, S. C., Ji, Q., Hsu, N. C., Jeong, M. J., Wang, S. H., Reid, J. S., Liou, K. N., and Ou, S. C. (2010). An Assessment of the Surface Longwave Direct Radiative Effect of Airborne Saharan Dust during the NAMMA Field Campaign. *J. Atmos. Sci.*, 67(4):1048–1065.
- Haschberger, P. and Tank, V. (1993). Optimization of a Michelson interferometer with a rotating retroreflector in optical design, spectral resolution and optical throughput. *J. Opt. Soc. Am. A*, 10(11):2338–2345.
- Haywood, J. M., Pelon, J., Formenti, P., Bharmal, N., Brooks, M., Capes, G., Chazette, P., Chou, C., Christopher, S., Coe, H., Cuesta, J., Derimian, Y.,

- Desboeufs, K., Greed, G., Harrison, M., Heese, B., Highwood, E. J., Johnson, B., Mallet, M., Marticorena, B., Marsham, J., Milton, S., Myhre, G., Osborne, S. R., Parker, D. J., Rajot, J.-L., Schulz, M., Slingo, A., Tanré, D., and Tulet, P. (2008). Overview of the dust and biomass-burning experiment and african monsoon multidisciplinary analysis special observing period-0. *J. Geophys. Res.*, 113(D23):1–20.
- Heintzenberg, J. (2009). The SAMUM-1 experiment over Southern Morocco: Overview and introduction. *Tellus*, 61B(1):2–11.
- Henning, T. and Mutschke, H. (1997). Low-temperature IR properties of cosmic dust analogues. *Astron. Astrophys.*, 327:743–754.
- Henry, L. G. and Greenstein, J. L. (1940). Diffuse Radiation in the Galaxy. *Annales d’Astrophysique*, 3:117–137.
- Hess, M., Koepke, P., and Schult, I. (1998). Optical Properties of Aerosols and clouds: The software package OPAC. *Bull. Am. Met. Soc.*, 79:831–844.
- Hettner, G. (1918). Über das ultrarote Absorptionsspektrum des Wasserdampfes. *Ann. Phys.*, 360(6):476–496.
- Highwood, E. J., Haywood, J. M., Silverstone, M. D., Newman, S. M., and Taylor, J. P. (2003). Radiative properties and direct effect of Saharan dust measured by the C-130 aircraft during Saharan Dust Experiment (SHADE): 2. Terrestrial spectrum. *J. Geophys. Res.*, 108(D18):8578.
- Hoidale, G. B. and Blanco, A. J. (1969). Infrared absorption spectra of atmospheric dust over an interior desert basin. *Pure Appl. Geophys.*, 74(1):151–164. 10.1007/BF00875195.
- Hollweg, H., Bakan, S., and Taylor, J. P. (2006). Is the aerosol emission detectable in the thermal infrared? *J. Geophys. Res.*, 111:D15202.
- Hudson, P. K., Gibson, E. R., Young, M. A., Kleiber, P. D., and Grassian, V. H. (2008). Coupled infrared extinction and size distribution measurements for several clay components of mineral dust aerosol. *J. Geophys. Res.*, 113:D01201.
- Hui, A. K., Armstrong, B. H., and Wray, A. A. (1977). Rapid Computation of the Voigt and Complex Error Functions. *J. Quant. Spectrosc. Radiat. Transfer*, 19:509–516.
- Illingworth, S. M., Remedios, J. J., Boesch, H., Moore, D. P., Sembhi, H., Dudhia, A., and Walker, J. C. (2011). ULIRS, an optimal estimation retrieval scheme for carbon monoxide using IASI spectral radiances: sensitivity analysis, error budget and simulations. *Atmos. Meas. Tech.*, 4(2):269–288.
- IPCC (2007). *Climate Change 2007: The Physical Science Basis. Contribution of Working Group I to the Fourth Assessment Report of the Intergovernmental Panel on Climate Change*. Cambridge University Press, Cambridge, United

- Kingdom and New York, NY, USA.
- Joint Committee for Guides in Metrology (2008). Evaluation of measurement data - Guide to the expression of uncertainty in measurement. Technical Report 100, Bureau International des Poids et Mesures.
- Kandler, K., Lieke, K., Benker, N., Emmel, C., Kuepper, M., Mueller-Ebert, D., Ebert, M., Scheuvens, D., Schladitz, A., Schuetz, L., and Weinbruch, S. (2011a). Electron microscopy of particles collected at Praia, Cape Verde, during the Saharan Mineral dust experiment: particle chemistry, shape, mixing state and complex refractive index. *Tellus*, 63B(4):475–496.
- Kandler, K., Schütz, L., Jaeckel, S., Lieke, K., Emmel, C., Müller-Ebert, D., Ebert, M., Scheuvens, D., Schladitz, A., Wiedensohler, A., and Weinbruch, S. (2011b). Ground-based off-line aerosol measurements at Praia, Cape Verde, during the Saharan Mineral Dust Experiment: Microphysical properties and mineralogy. *Tellus*, 63B(4):459–474.
- Kar, A. and Takeuchi, K. (2004). Yellow dust: an overview of research and felt needs. *J. Arid Environ.*, 59:167–187.
- Kauppinen, J. and Partanen, J. (2001). *Fourier Transforms in Spectroscopy*. Wiley-VCH, Berlin, first edition.
- Kerner, H. and von Wahl, W. (2006). *Mathematik für Physiker*. Springer, Berlin, Heidelberg, New York, first edition.
- Kleiber, P. D., Grassian, V. H., Young, M. A., and Hudson, P. K. (2009). T-Matrix studies of aerosol particle shape effects on IR resonance spectral line profiles and comparison with an experiment. *J. Geophys. Res.*, 114(D21209):1–10.
- Kleinert, A., Aubertin, G., Perron, G., Birk, M., Wagner, G., Hase, F., Nett, H., and Poulin, R. (2007). MIPAS Level 1B algorithms overview: operational processing and characterization. *Atmos. Chem. Phys.*, 7(5):1395–1406.
- Knippertz, P., Tesche, M., Heinold, B., Kandler, K., Toledano, C., and Esselborn, M. (2011). Dust Mobilization and Aerosol Transport from Western Africa to Cape Verde - A Meteorological Overview of SAMUM-2. *Tellus*, 63B(4):430–447.
- Knuteson, R. O., Revercomb, H. E., Best, F. A., Ciganovich, N. C., Dedecker, R. G., Dirkx, T. P., Ellington, S. C., Feltz, W. F., Garcia, R. K., Howell, H. B., Smith, W. L., Short, J. F., and Tobin, D. C. (2004). Atmospheric Emitted Radiance Interferometer. Part II: Instrument Performance. *J. Atmos. Ocean. Technol.*, 21(12):1777–1789.
- Koehler, C. H., Trautmann, T., and Lindermeir, E. (2009). Measurement of mixed biomass burning and mineral dust aerosol in the thermal infrared. *AIP Conference Proceedings*, 1100(1):169–172.
- Korb, A. R., Dybward, P., Wadsworth, W., and Salisbury, J. (1996). Portable

- Fourier transform infrared spectroradiometer for field measurements of radiance and emissivity. *Appl. Opt.*, 35(10):1679–1692.
- Kuntz, M. and Hoepfner, M. (1999). Efficient line-by-line calculation of absorption coefficients. *J. Quant. Spectrosc. Radiat. Transfer*, 63(1):97–114.
- Lamouroux, J., Tran, H., Laraia, A. L., Gamache, R. R., Rothman, L. S., Gordon, I. E., and Hartmann, J.-M. (2010). Updated database plus software for line-mixing in CO<sub>2</sub> infrared spectra and their test using laboratory spectra in the 1.5-2.3  $\mu\text{m}$  region. *J. Quant. Spectrosc. Radiat. Transfer*, 111:2321–2331.
- Lieke, K., Kandler, K., Scheuvens, D., Emmel, C., von Glahn, C., Petzold, A., Weinzierl, B., Veira, A., Ebert, M., and Weinbruch, S. (2011). Particle chemical properties in the vertical column based on aircraft observations in the vicinity of Cape Verde Islands. *Tellus*, 63B(4):497–511.
- Lindermeir, E. (1994). *Messung und Auswertung von Emissionsspektren im infraroten Spektralbereich*. Dissertation, Technische Universität München.
- Long, L. L., Querry, M. R., Bell, R. J., and Alexander, R. W. (1993). Optical Properties of Calcite and Gypsum in Crystalline and Powdered Form in TIR and FIR. *Infrared Phys.*, 34(2):191–201.
- Loyola, D., Koukouli, M., Valks, P., Balis, D., Hao, N., Van Roozendaal, M., Spurr, R. J. D., Zimmer, W., Kiemle, S., Lerot, C., and Lambert, J.-C. (2011). The GOME-2 Total Column Ozone Product: Retrieval Algorithm and Ground-Based Validation. *J. Geophys. Res.*, 116:D07302.
- Martin, J. H., Gordon, R. M., and Fitzwater, S. E. (1991). The case for iron. *Limnol. Oceanogr.*, 36(8):1793–1802.
- Mayer, B. and Kylling, A. (2005). Technical note: The libRadtran software package for radiative transfer calculations - description and examples of use. *Atmos. Chem. Phys.*, 5(7):1855–1877.
- Mie, G. (1908). Beiträge zur Optik trüber Medien speziell kolloidaler Metallösungen. *Ann. Phys.*, 25:377–445.
- Minnett, P. J., Knuteson, R. O., Best, F. A., Osborne, B. J., Hanafin, J. A., and Brown, O. B. (2001). The Marine-Atmospheric Emitted Radiance Interferometer: A High-Accuracy, Seagoing Infrared Spectroradiometer. *J. Atmos. Ocean. Technol.*, 18(6):994–1013.
- Mishchenko, M. I. (1991). Light scattering by randomly oriented axially symmetric particles. *J. Opt. Soc. Am. A*, 8(6):871–882.
- Mishchenko, M. I. (2002). Vector radiative transfer equation for arbitrarily shaped and arbitrarily oriented particles: a microphysical derivation from statistical electromagnetics. *Appl. Opt.*, 41(33):7114–7134.
- Mishchenko, M. I. (2011). Directional radiometry and radiative transfer: A new

- paradigm. *J. Quant. Spectrosc. Radiat. Transfer*, 112:2079–2094.
- Mishchenko, M. I. and Travis, L. D. (1998). Capabilities and Limitations of a current Fortran implementation of the T-Matrix Method for Randomly Oriented, Rotationally Symmetric Scatterers. *J. Quant. Spectrosc. Radiat. Transfer*, 60(3):309–324.
- Mishchenko, M. I., Travis, L. D., and Lacis, A. A. (2002). *Scattering, Absorption and Emission of Light by Small Particles*. Cambridge University Press, Cambridge.
- Mogili, P. K., Yang, K. H., Young, M. A., Kleiber, P. D., and Grassian, V. H. (2008). Extinction spectra of mineral dust aerosol components in an environmental aerosol chamber: IR resonance studies. *Atmos. Environ.*, 42:1752–1761.
- Mooney, T. and Knacke, R. F. (1985). Optical Constants of Chlorite and Serpentine between 2.5 and 50 $\mu$ m. *Icarus*, 64:493–502.
- Moré, J. J. (1978). The Levenberg-Marquardt algorithm: Implementation and theory. In Watson, G., editor, *Numerical Analysis*, volume 630 of *Lecture Notes in Mathematics*, pages 105–116. Springer, Berlin, Heidelberg.
- Mutschke, H., Begemann, B., Dorschner, J., Guertler, J., Gustafson, B., Henning, T., and Stognienko, R. (1998). Steps toward interstellar silicate mineralogy - III. The role of aluminium in circumstellar amorphous silicates. *Astron. Astrophys.*, 333:188–198.
- Nalli, N. R., Minnett, P. J., and van Delst, P. (2008). Emissivity and reflection model for calculating unpolarized isotropic water surface-leaving radiance in the infrared. I: Theoretical development and calculations. *Appl. Opt.*, 47(21):3701–3721.
- Norton, R. H. and Rinsland, C. P. (1991). ATMOS data processing and science analysis methods. *Appl. Opt.*, 30(4):389–400.
- O’Carroll, A. G., August, T., Le Borgne, P., and Marsouin, A. (2012). The accuracy of SST retrievals from Metop-A IASI and AVHRR using EUMETSAT OSI-SAF matchup dataset. *Remote Sens. Environ.*, 126(0):184–194.
- Oreopoulos, L., Mlawer, E., Delamere, J., Shippert, T., Cole, J., Fomin, B., Iacono, M., Jin, Z., Li, J., Manners, J., Räisänen, P., Rose, F., Zhang, Y., Wilson, M. J., and Rossow, W. B. (2012). The Continual Intercomparison of Radiation Codes: Results from Phase I. *J. Geophys. Res.*, 117(D06118):1–19.
- Otto, S. (2012). *Optische Eigenschaften nichtkugelförmiger Saharamineralstaubpartikel und deren Einfluss auf den Strahlungstransport in der Erdatmosphäre*. Dissertation, Universität Leipzig.
- Otto, S., Bierwirth, E., Weinzierl, B., Kandler, K., Esselborn, M., Tesche, M., Schladitz, A., Wendisch, M., and Trautmann, T. (2009). Solar radiative effects

- of a Saharan dust plume observed during SAMUM assuming spheroidal model particles. *Tellus*, 61B:270–296.
- Ptashnik, I. V., McPheat, R. A., Shine, K. P., Smith, K. M., and Williams, R. G. (2012). Water vapour foreign-continuum absorption in near-infrared windows from laboratory measurements. *Philos. Trans. R. Soc. A*, 370:2557–2577.
- Querry, M. R., Osborne, G., Lies, K., Jordon, R., and Coveney, R. M. (1978). Complex refractive index of limestone in the visible and infrared. *Appl. Opt.*, 17(3):353–356.
- Remedios, J. J., Leigh, R. J., Waterfall, A. M., Moore, D. P., Sembhi, H., Parkes, I., Greenhough, J., Chipperfield, M., and Hauglustaine, D. (2007). MIPAS reference atmospheres and comparisons to V4.61/V4.62 MIPAS level 2 geophysical data sets. *Atmos. Chem. Phys. Discuss.*, 7(4):9973–10017.
- Rothman, L., Gordon, I., Barbe, A., Benner, D., Bernath, P., Birk, M., Boudon, V., Brown, L., Campargue, A., Champion, J.-P., Chance, K., Coudert, L., Dana, V., Devi, V., Fally, S., Flaud, J.-M., Gamache, R., Goldman, A., Jacquemart, D., Kleiner, I., Lacombe, N., Lafferty, W., Mandin, J.-Y., Massie, S., Mikhailenko, S., Miller, C., Moazzen-Ahmadi, N., Naumenko, O., Nikitin, A., Orphal, J., Perevalov, V., Perrin, A., Predoi-Cross, A., Rinsland, C., Rotger, M., Simeckova, M., Smith, M., Sung, K., Tashkun, S., Tennyson, J., Toth, R., Vandaele, A., and Auwera, J. V. (2009). The HITRAN 2008 molecular spectroscopic database. *J. Quant. Spectrosc. Radiat. Transfer*, 110(9-10):533–572.
- Rothman, L. S., Rinsland, C. P., Goldman, A., Massie, S. T., Edwards, D. P., Flaud, J.-M., Perrin, A., Camy-Peyret, C., Dana, V., Mandin, Y.-Y., Schroeder, J. W., Gamache, R. R., Wattson, R. B., Yoshino, K., Chance, K. V., Jucks, K. W., Brown, L. R., Nemtchinov, V., and Varanasi, P. (1998). The HITRAN molecular spectroscopic database and HAWKS (HITRAN atmospheric workstation). *J. Quant. Spectrosc. Radiat. Transfer*, 60(5):665–710.
- Sakazaki, T., Fujiwara, M., Mitsuda, C., Imai, K., Manago, N., Naito, Y., Nakamura, T., Akiyoshi, H., Kinnison, D., Sano, T., Suzuki, M., and Shiotani, M. (2013). Diurnal ozone variations in the stratosphere revealed in observations from the superconducting submillimeter-wave limb-emission sounder (smiles) on board the international space station (iss). *J. Geophys. Res.*, 118(7):2991–3006.
- Schmidt, K., Wauer, J., Rother, T., and Trautmann, T. (2009). Scattering database for spheroidal particles. *Appl. Opt.*, 48(11):2154–2164.
- Sekera, Z. (1952). Legendre Series of the Scattering Functions for Spherical Particles. Technical Report ASTIA No. AD-3870, Dept. of Meteorology, University of California, Los Angeles.
- Shettle, E. P. and Fenn, R. W. (1979). Models for the Aerosols of the Lower Atmosphere and the Effects of Humidity Variations on Their Optical Properties.



- Technical Report AFGL-TR-79-0214, AFGL.
- Shinn, E. A., Smith, G. W., Prospero, J. M., Betzer, P., Hayes, M. L., Garrison, V., and Barber, R. T. (2000). African Dust and the Demise of Caribbean Coral Reefs. *Geophys. Res. Lett.*, 27(19):3029–3032.
- Sokolik, I., Toon, O. B., and Bergstrom, R. W. (1998). Modeling the radiative characteristics of airborne mineral aerosols at infrared wavelengths. *J. Geophys. Res.*, 103:8813–8826.
- Stamnes, K., Tsay, S., Jayaweera, K., and Wiscombe, W. (1988). Numerically stable algorithm for discrete-ordinate-method radiative transfer in multiple scattering and emitting layered media. *Appl. Opt.*, 27:2502–2509.
- Stamnes, K., Tsay, S.-C., and Laszlo, I. (2000). *DISORT, a General-Purpose Fortran Program for Discrete-Ordinate-Method Radiative Transfer in Scattering and Emitting Layered Media: Documentation and Methodology*.
- Sutherland, R. A. and Khanna, R. K. (1991). Optical Properties of Organic-based Aerosols Produced by Burning Vegetation. *Aerosol. Sci. Technol.*, 14:331–342.
- Sutter, H. (2005). The free lunch is over. *Dr. Dobb's Journal*, 30(3).
- Swap, R., Garstang, M., Greco, S., Talbot, R., and Källberg, P. (1992). Saharan dust in the Amazon Basin. *Tellus*, 44B:133–149.
- Tesche, M., Gross, S., Ansmann, A., Müller, D., Althausen, D., Freudenthaler, V., and Esselborn, M. (2011a). Profiling of Saharan dust and biomass burning smoke with multiwavelength polarization Raman lidar at Cape Verde. *Tellus*, 63B(4):649–676.
- Tesche, M., Müller, D., Gross, S., Ansmann, A., Althausen, D., Freudenthaler, V., Weinzierl, B., Veira, A., and Petzold, A. (2011b). Optical and microphysical properties of smoke over cape verde inferred from multiwavelength lidar measurements. *Tellus*, 63B(4):677–694.
- Theocharous, E., Usadi, E., and Fox, N. P. (2010). CEOS comparison of IR brightness temperature measurements in support of satellite validation. Part I: Laboratory and Ocean surface temperature comparison of radiation thermometers. NPL Report OP 3, NPL.
- Thomas, M. and Gautier, C. (2009). Investigations of the March 2006 African dust storm using ground-based column-integrated high spectral resolution infrared (8–13  $\mu\text{m}$ ) and visible aerosol optical thickness measurements: 2. Mineral aerosol mixture analyses. *J. Geophys. Res.*, 114:D14209.
- Thomas, M., Gautier, C., and Ricchiazzi, P. (2009). Investigations of the March 2006 African dust storm using ground-based column-integrated high spectral resolution infrared (8–13  $\mu\text{m}$ ) and visible aerosol optical thickness measurements: 1. Measurement procedures and results. *J. Geophys. Res.*, 114:D11202.

- Toon, O. B., Pollock, J. B., and Khare, B. N. (1976). The optical constants of several atmospheric aerosols species: ammonium sulfate, aluminum oxide and sodium chloride. *J. Geophys. Res.*, 81:5733–5748.
- Turner, D. D. (2008). Ground-based infrared retrievals of optical depth, effective radius, and composition of airborne mineral dust above the Sahel. *J. Geophys. Res.*, 113:D00E03.
- Van Vleck, J. H. and Huber, D. L. (1977). Absorption, emission, and linebreadths: A semihistorical perspective. *Rev. Mod. Phys.*, 49(4):939–959.
- Volz, F. E. (1973). Infrared Optical Constants of Ammonium Sulfate, Sahara Dust, Volcanic Pumice, and Flyash. *Appl. Opt.*, 12:564–568.
- Wagner, W. and Pruß, A. (2002). The IAPWS Formulation 1995 for the Thermodynamic Properties of Ordinary Water Substance for General and Scientific Use. *J. Phys. Chem. Ref. Data*, 31(2):387–535.
- Wang, J., Zhang, L., Dai, A., Immler, F., Sommer, M., and Vömel, H. (2012). Radiation Dry Bias Correction of Vaisala RS92 Humidity Data and Its Impacts on Historical Radiosonde Data. *J. Atmos. Ocean. Technol.*, 30(2):197–214.
- Waterman, P. C. (1965). Matrix Formulation of Electromagnetic Scattering. *Proc. IEEE*, 53(8):805–812.
- Weinzierl, B., Sauer, D., Esselborn, M., Petzold, A., Veira, A., Rose, M., Mund, S., Wirth, M., Ansmann, A., Tesche, M., Groß, S., Freudenthaler, V., Tesche, M., Ansmann, A., and Wirth, M. (2011). Microphysical and optical properties of dust and tropical biomass burning aerosol layers in the Cape Verde region - An overview of the airborne in-situ and lidar measurements during SAMUM-2. *Tellus*, 63B(4):589–618.
- Wiscombe, W. J. (1980). Improved Mie scattering algorithms. *Appl. Opt.*, 19(9):1505–1509.
- Wiscombe, W. J. (1996). Mie Scattering Calculations: Advances in Technique and Fast, Vector-Speed Computer Codes. Technical Report NCAR/TN-140+STR, NCAR, Boulder, Colorado.
- Yaroslavsky, L. P. (2003). Boundary effect free and adaptive discrete signal sinc-interpolation algorithms for signal and image resampling. *Appl. Opt.*, 42(20):4166–4175.
- Zdunkowski, W., Bott, A., and Trautmann, T. (2007). *Radiation in the Atmosphere*. Cambridge University Press, New York.
- Zhao, L.-J., Zhang, Y.-H., Wei, Z.-F., Cheng, H., and Li, X.-H. (2006). Magnesium Sulfate Aerosols Studied by FTIR Spectroscopy: Hygroscopic Properties, Supersaturated Structures, and Implications for Seawater Aerosols. *J. Phys. Chem. A*, 110:951–958.

# Symbols

<b>Notation</b>	<b>Description</b>
$B$	radiance emitted by an ideal black body (Planck function)
$c$	speed of light in vacuum
$c_i$	volume mixing ratio of species $i$
$C_{\text{abs}}$	absorption cross section
$C_{\text{sca}}$	scattering cross section
$\mathbf{E}$	electrical field vector
$\epsilon_0$	permittivity of free space
$f$	frequency
$\Phi$	radiative flux
$h$	Planck constant
$I$	irradiance, $I =  \langle \mathbf{S} \rangle $
$i$	imaginary unit, $i^2 = -1$
$k_{\text{sca}}$	volume scattering coefficient
$k$	imaginary refractive index
$k_{\text{abs}}$	volume absorption coefficient
$k_B$	Boltzmann constant
$k_{\text{ext}}$	volume extinction coefficient
$L$	radiance
$\lambda$	wavelength

<b>Notation</b>	<b>Description</b>
$\mu_0$	permeability of free space
$\mathcal{N}$	complex refractive index, $\mathcal{N} = n + ik$
$n$	real refractive index
$N_A$	Avogadro constant
$\nu$	wavenumber, $\nu = \lambda^{-1}$
$\omega_0$	single scattering albedo
$\mathcal{P}$	scattering phase function
$\hat{\mathbf{q}}$	unit vector specifying a direction
$Q_{\text{abs}}$	absorption efficiency
$Q_{\text{sca}}$	scattering efficiency
$\mathbf{r}$	3-dimensional position vector
$\mathbf{S}$	Poynting vector
$S^2$	surface of the 3-dimensional unit sphere
$T$	temperature
$t$	time
$\tau$	optical depth
$\hat{\mathbf{x}}$	unit vector in x-direction
$\hat{\mathbf{y}}$	unit vector in y-direction

# Acronyms

ADC	analog to digital converter
AERI	atmospheric emitted radiance interferometer
AMMA	African monsoon multidisciplinary analysis
AOD	aerosol optical depth
API	application programming interface
ARIES	airborne research interferometer evaluation system
ARM	Atmospheric Radiation Measurement
BOA	bottom of the atmosphere
BT	brightness temperature
BTD	brightness temperature difference
CEOS	Committee for Earth Observation Satellites
CIRC	Continual Intercomparison of Radiation Codes
CNES	Centre National d' Études Spatiales
DFG	German Research Foundation
DIRAC	Database for the Index of Refraction of Aerosol Components
DLR	German Aerospace Center
DRE	direct radiative effect
EUMETSAT	European Organisation for the Exploitation of Meteorological Satellites

FFT	fast Fourier Transform
FOV	field of view
FTIR	Fourier Transform infrared spectrometer
FTS	Fourier Transform spectroscopy
FWHM	full width at half maximum
HDF5	Version 5 of the Hierarchical Data Format
HITRAN	high-resolution transmission molecular absorption database
HWHM	half width at half maximum
IASI	Infrared Atmospheric Sounding Interferometer
IFOV	instantaneous field of view
InSb	indium antimonide
IPCC	Intergovernmental Panel on Climate Change
LIDAR	Light detection and ranging
MAERI	Marine Atmospheric Emitted Radiance Interferometer
MCT	mercury cadmium telluride
MIROR	Michelson Interferometer with Rotating Retroreflector
MODIS	Moderate Resolution Imaging Spectroradiometer
MOPD	maximum optical path difference
MTCKD	Mlawer-Tobin-Clough-Kneizys-Davies
NESR	noise equivalent spectral radiance
NIR	near infrared
NIST	United States National Institute of Standards and Technology
PFORTE	PIRATES Forward Radiative Transfer Engine
PIRATES	Programmer's Interface to Radiative Transfer algorithmS

RSMAS	Rosenstiel School of Marine and Atmospheric Science
RT	radiative transfer
RTE	radiative transfer equation
SAMUM	SAharan Mineral dUst experiMent
SST	sea surface temperature
TIR	thermal infrared
TOA	top of the atmosphere
UKMO	United Kingdom Met Office
UTC	universal time coordinated
UV	ultraviolet
UV/Vis	ultraviolet and visible spectral domain
WGCV	Working Group on Calibration and Validation
ZPD	zero (optical) path difference





# Danksagung

Diese Dissertation wäre nicht ohne die moralische und fachliche Unterstützung einer Vielzahl von Personen entstanden, denen ich an dieser Stelle danken möchte.

Als erstes ist hier Thomas Trautmann zu nennen, der nicht nur das Thema der Arbeit gestellt hat sondern mir stets mit Rat und Tat als Betreuer zur Seite stand. Weiterhin gilt mein Dank Erwin Lindermeir dafür, dass er mich in die Geheimnisse der Fourierpektroskopie und der C++ Programmierung eingeführt hat. Auch Walter Zimmer bin ich dankbar für viele kleine und große Tipps rund um das Thema Software Entwicklung. Bernd Aberle gebührt großes Lob für die Bereitstellung und Wartung einer mustergültigen IT Infrastruktur, in der Programmieren und Simulieren großen Spaß gemacht haben. Franz Schreier bin ich für das Teilen seiner Expertise im Bereich der Atmosphärenspektroskopie ebenfalls zu Dank verpflichtet. Außerdem habe ich sehr die lebhaften Diskussionen zum Thema elektromagnetische Streutheorie genossen, die ich während eines Kurzbesuchs in Neustrelitz mit Tom Rother, Karsten Schmidt und Jochen Wauer führen durfte und in denen ich viel gelernt habe.

Des weiteren habe ich sehr von der Unterstützung der Partner im SAMUM-2 Projekt profitiert, auf deren Daten diese Arbeit aufbaut. Explizit erwähnt seien hier Konrad Kandler, Kerstin Lieke, Silke Groß, Bernadett Weinzierl und Matthias Tesche, die jederzeit geduldig Auskunft über die Details ihrer Messungen gegeben haben. Darüber hinaus habe ich mich über die Begleitung von Willem Vreeling auf verschiedenen Messkampagnen gefreut, der sowohl fachlich als auch menschlich sehr zum Gelingen dieser Expeditionen beigetragen hat.

Schließlich danke ich Peter Haschberger, dass er mir bei der Ausübung meiner Tätigkeiten immer den nötigen Freiraum für die Fertigstellung dieser Dissertation gelassen hat. Zu guter Letzt möchte ich nicht versäumen, mich bei den Kollegen von MF-EXV und MF-ATP für die gesellige Atmosphäre und die vielen anregenden Gespräche bei Mittagessen und Kaffee zu bedanken, die immer wieder hilfreiche Impulse gegeben haben.

Auf privater Seite bin ich zunächst meiner Familie zu großem Dank verpflichtet, allen voran meinen Eltern, die mich in all den Jahren auf verschiedenste Art unterstützt haben und somit einen maßgeblichen Anteil zur Promotion beigesteuert haben. Last but not least danke ich natürlich Nicole, dass sie viel Verständnis für meine Arbeit aufgebracht hat und sich selbst oft zurückgenommen hat. Ohne Deine moralische Unterstützung und Liebe wäre ich längst 'eingestürzt'.